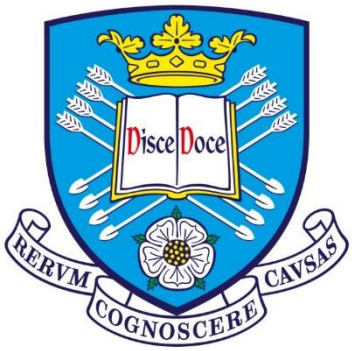

The University Of Sheffield.

Uncovering novel drug therapies and targets for amyotrophic lateral sclerosis (ALS) using artificial intelligence (AI)

Monika Adriana Myszczyńska

Registration number: 160267545

A thesis submitted in partial fulfilment of the requirements for the degree of Doctor of Philosophy

The University of Sheffield

Faculty of Medicine, Dentistry and Health

Department of Neuroscience

Sheffield Institute for Translational Neuroscience (SITraN)

February 2021

Preface

This thesis presents work conducted as a part of a collaboration between The University of Sheffield and BenevolentAI, a biotechnology company specialising in applying machine learning to data and literature mining methods in order to unveil novel targets and treatments for disorders for which few or no effective therapies yet exist. In this project, amyotrophic lateral sclerosis (ALS) was the subject of the investigation. All experimental work described in Chapters 3 and 4, unless otherwise stated, has been conducted by myself, Monika Myszczynska.

Chapter 1 introduces clinical and pathological manifestations, and genetic determinants of ALS. Portion of the chapter 1 is devoted to discussion of the current developments in the field of artificial intelligence applied to drug discovery efforts. Chapter 2 describes in detail materials and methods used in Chapters 3 and 4. The first results chapter, Chapter 3, characterises the effect of a non-small cell lung cancer therapeutic called gefitinib on induced neural progenitor cell (iNPC)-derived ALS patient astrocytes. Here, I describe the effect of gefitinib on astrocyte cell numbers, cell morphology, and its engagement with its targets EGFR and Abl1, and demonstrate gefitinib's ability to reduce hallmarks of TDP-43 proteinopathy in astrocytes and induce autophagy in HEK293 cells and control astrocytes. Given the effect of gefitinib on Abl1, a binding partner of several mitochondrial genes, mitochondrial network of astrocytes treated with gefitinib was also characterised. Result chapter 2, Chapter 4, follows the same pattern of experiments as Chapter 3, applied to a chronic myelogenous leukaemia (CML) drug called nilotinib.

Finally, chapter 5 provides a discussion on the results chapters, linking the results together and elaborating on future directions.

Abstract

ALS is a devastating neurodegenerative disorder characterised by the death of motor neurons in the motor cortex and spinal cord. Astrocytes have been implicated as important drivers of the motor neuronal death. The pathogenic mechanisms of ALS are many and varied, ~97% of all patients carry hallmarks of TDP-43 proteinopathy. There are currently no disease course-altering drug therapies available for ALS.

Developments in the field of artificial intelligence (AI) have shown a potential to uncover novel therapies for ALS in a short space of time, as AI algorithms can identify links between a disease and potential beneficial compounds after a thorough scan of the scientific literature, omics databases, chemical libraries and other public sources. One such effort by a biotechnology company BenevolentAI identified two cancer drugs, gefitinib and nilotinib, as having repurposing opportunities for ALS. They have also highlighted the importance of Abl1 as a target in ALS, which both drugs modulate. The function of gefitinib and nilotinib in ALS astrocytes, as well as their engagement with Abl1, was investigated in this study.

In this project, astrocytes obtained from patient donors through direct conversion of fibroblasts to induced neural progenitor cells were used. Having resulted in a rescue of motor neuronal survival in a co-culture model of ALS, gefitinib caused a mild cell staticity in astrocytes, whilst nilotinib had no effect on cell numbers. Drugs also had a mild effect on cellular morphology. Astrocytes showed significantly upregulated levels of total Abl1, which gefitinib targeted transcriptionally, whilst nilotinib inhibited Abl1 phosphorylation.

Astrocytes have been found to recapitulate aspects of TDP-43 pathology in ALS, such as increased levels of TDP-35 cleavage product, nuclear loss, and accumulation of pTDP-43. Of the two compounds, gefitinib had a positive effect on alleviation of TDP-43 proteinopathy, whilst nilotinib targeted sALS astrocytes to a limited extend. Ability to induce autophagy was tested in both drugs as a mechanism behind the reduction of TDP-35 fragment levels. Gefitinib caused autophagic flux in all tested cells, with nilotinib showing a much milder effect. Drugs had a differential effect on mitochondrial numbers and membrane potential, where nilotinib's performance suggests a role in supporting mitochondrial function.

Acknowledgments

First and foremost, I would like to thank the MND patients who have generously donated their tissue for use in SITraN-based studies. Your contribution is impossible to overstate and without it, this work – and many other projects - would not see the light of day.

I would like to express my biggest gratitude for the tireless support of my supervisor Dr Laura Ferraiuolo. Thank you for looking after me these past several years. If I have gotten anywhere near to becoming a good scientist, it's all thanks to you. To Dr Guillaume Hautbergue, Dr Richard Mead and Dr Peter Richardson for their supervision, feedback, great ideas and stimulating discussions. Thank you to Dr Adrian Higginbottom, Dr Lydia Castelli and Dr Ya-Hui Lin for valuable technical support (and friendship).

Huge thank you to the entire team at BenevolentAI involved in the ALS project since its inception in 2016, especially Dr Dave Sheppard, Dr Mark Rackham, Dr Peter Cox, Dr Linda Kitching, Dr Anne Phelan, Dr Povilas Norvaisas and Dr Poojitha Ojamies. Thank you for letting me be a part of this fascinating collaboration.

A massive thank you to the great army of people that is the Ferraiuolo lab past and present: Matt, Noemi, Chloe, Allan, Andre, Sophie, Nora, Cleide, Janny, Lai Mei, Marco and Ana. I am so lucky to have gotten to work with you all. Thank you for all the good times, bad times, long shift times, and urgently-need-a-drink times. You are all outstanding scientists and working alongside you was a privilege.

Thank you to my fellow PhD students. It was such a pleasure working with you all and I wish you all the best in your future endeavours. To all my colleagues and friends I made at SITraN, especially Kat, Simo, Joe, Marga and Simon, who took care of my sanity when I could not be trusted with it.

To my entire family for their support and patience. Mamie i Tacie, za wyrozumiałość i cierpliwość. Dziękuję, że posterowaliście mnie w tym kierunku. Nobla z tego nie będzie, ale warto było spróbować.

And finally to my flatmate of 3 years and brother of the past 22 – Maciej, hero absolute and oatmeal cookie baker extraordinaire. Thank you for always waiting for me with a hot cup of tea.

I would like to dedicate this work to three important people. Firstly, to my nieces, Nina and Luna. If I could pull this off, you girls can conquer the world.

To my grandfather Kazimierz (1935-2021), for being my biggest champion since day one, whose pride and faith in me, words of support, and unending kindness lifted me up whenever carrying on did not seem like an option. Life will never be the same.

“I leave Sisyphus at the foot of the mountain. (…) The struggle itself toward the heights is enough to fill a man's heart. One must imagine Sisyphus happy.”

Albert Camus, *The Myth of Sisyphus*

List of contents

Table of Contents

List of abbreviations

Abl1 - Abelson murine leukemia viral oncogene homolog 1

AD - Alzheimer's disease

ADMET – (drug) absorption, distribution, metabolism, excretion, toxicity

AI - artificial intelligence

ALS - amyotrophic lateral sclerosis

ANN - artificial neural network

ATP – adenosine triphosphate

BBB - blood brain barrier

BCA - bicinchoninic acid assay

BCR-Abl - breakpoint cluster region-Abelson murine leukemia

BCRP - breast cancer resistance protein

BDNF - brain neurotrophic factor

bFGF - basic fibroblast growth factor

BSA - bovine serum albumin

C9orf72 - chromosome 9 open reading frame 72

CCCP - carbonyl cyanide m-chlorophenyl hydrazone

CCNG2 – cyclin G2

cDNA - complementary DNA

CK – casein kinase

CML - chronic myelogenous leukaemia

CMTD – Charcot-Marie-Tooth disease

CNS - central nervous system

CRKL – CRK-like protein

CSF - cerebrospinal fluid

C-terminal – carboxy-terminal

DMEM - Dulbecco's Modified Eagle's Medium

DMSO - dimethyl sulfoxide

CNTF - ciliary neurotrophic factor

DPR - dipeptide repeat protein

DRP1 - dynamin-1-like protein

ECL - enhanced chemiluminescence

EGFR - epidermal growth factor receptor

ELISA - enzyme-linked immunosorbent assay

ER – endoplasmic reticulum

ETC – electron transport chain

fALS - familial amyotrophic lateral sclerosis

FBS - fetal bovine serum

FDA – Food and Drug Administration

FTD – frontotemporal dementia

FUS - fused in sarcoma

GABA – gamma aminobutyric acid

GDNF - glial cell line-derived neurotrophic factor

GFP - green fluorescent protein

Hb9 – homebox 9

HEK293 – human embryonic kidney 293

HRP - horseradish peroxidase

iAstrocyte - induced astrocyte

iNeuron - induced neuron

iNPC - induced neural progenitor cell

iPSC - induced pluripotent stem cells

IRAK1 - interleukin 1 receptor associated kinase 1

IRAK4 - interleukin 1 receptor associated kinase 4

JNK - c-Jun N-terminal kinase

LC3 - microtubule-associated proteins 1A/1B light chain 3B

LDH – lactate dehydrogenase

LINCS - Library of Integrated Network-based Cellular Signatures

LIF - leukemia inhibitory factor

mEB - mouse embryoid body

mESC - mouse embryonic stem cell

mRNA - messenger RNA

mTOR - mammalian target of rapamycin

ML - machine learning

MMP – mitochondrial membrane potential

MN - motor neuron

MND - motor neuron disease

MS - multiple sclerosis

MTA – material transfer agreement

N-terminal – amino-terminal

NFκB – nuclear factor kappa B

NGS - next generation sequencing

NSCLC – non-small cell lung cancer

NUP – nuclear transport protein

p62 - nucleoporin p62

pAbl1 - phosphorylated Abelson murine leukemia viral oncogene homolog 1

PBS - phosphate buffered saline

PCA - principal component analysis

PD - Parkinson's disease

pEGFR - phosphorylated epidermal growth factor receptor

PGP – p-glycoprotein

PLA – proximity ligation assay

PNS - peripheral nervous system

Poly-GR – poly-glycine-arginine

Poly-PR – poly-glycine-proline

QSAR – quantitative structure-activity relationship

RFP – red fluorescent protein

RNA – ribonucleic acid

ROS – reactive oxygen species

RRM – RNA recognition motifs

RT-qPCR - reverse transcription quantitative polymerase chain reaction

sALS - sporadic amyotrophic lateral sclerosis

shRNA - short hairpin RNA

SOD1 - superoxide dismutase 1

SMA – spinal muscular atrophy

SQSTM1 - sequestosome 1

SVM - support vector machine

TBST - tris buffered saline with Tween-20

TDP-43 - TAR DNA-binding protein 43

TKI – tyrosine kinase inhibitor

TMRM - tetramethylrhodamine, methyl ester

UPS – ubiquitin proteasome system

List of tables

List of figures

1 Introduction

1.1 ALS

Amyotrophic lateral sclerosis (ALS), also known as motor neuron disease (MND) or Lou Gehrig's disease, is a fatal, multifactorial neurodegenerative disease, in which loss of upper motor neurons in the brain and brainstem and lower motor neurons in the spinal cord causes progressive muscle weakness and wasting. Characterised by fast progression and poor prognosis, ALS leads to death 2-3 years post-diagnosis, most commonly as a result of respiratory failure (Kiernan et al., 2021). There are currently only two Food and Drug Administration (FDA) -approved drug-based therapies available for ALS. Riluzole, first introduced in the mid-1990s, offers a very modest improvement to patient survival, often not extending it beyond 3 months (Miller, Mitchell & Moore, 2012). An intravenous drug edaravone was approved in 2017 after a clinical trial which showed its ability to slow down patient decline (Abe et al., 2017). However, it is estimated that approximately only 7% of ALS patients would be eligible to take edaravone (Hardiman & van den Berg, 2017). Therefore, identification of new drug treatments for ALS remains an urgent matter.

1.1.1 Clinical manifestation

Degeneration of lower motor neurons manifests itself in muscle fasciculation caused by spontaneous activity of motor axons, muscle weakness and muscle atrophy. Involuntary muscle contractions known as clonus, overexaggerated tendon reflexes, and positive Babinski (lower extremity) and Hoffman (upper extremity) signs are hallmarks of the upper motor neuron degeneration (Rowland & Shneider, 2001). ALS is usually diagnosed based on the presence of both symptom classes simultaneously, which distinguishes this subgroup of MND patients from other conditions such as progressive muscular atrophy (PMA), which presents as a lower motor neuron disorder, or primary lateral sclerosis (PLS), where only upper motor neuron symptoms are observed (Rowland & Shneider, 2001). In the clinic, typically, ALS patients present unilateral limb muscle weakness or dysfunction of muscles innervated by the brainstem via the cranial nerves, also known as bulbar dysfunction, which affects the throat, facial muscles, and tongue (Van Damme et al., 2017).

ALS was considered a disorder of the motor system only, however incidence of frontotemporal dementia (FTD) in a genetic subset of patients points to cognitive impairment

as a symptom of the disease, albeit classically uncharacteristic (Ferraiuolo et al., 2011; Uchino et al., 2015). Estimated 49% of FTD patients have been found to carry mutations in the ALS-associated gene guanine nucleotide exchange chromosome 9 open reading frame 72 (C9orf72) and transactivation response DNA binding protein 43 (TDP-43) with characteristic cytoplasmic inclusions (Geser et al., 2011), thus implying that FTD and ALS lay on the same pathological and epidemiological disease spectrum (Couratier et al., 2017). Recent investigation of twins where one co-twin was suffering with ALS showed the cells of the affected twin to be epigenetically older, thus suggesting that premature ageing is a feature of ALS and could explain the incidence of FTD, which is normally associated with old age (Young et al., 2017). Moreover, as some rare cases of ALS also affect sensory and autonomic systems as well as the cerebellum, the growing consensus recognises ALS as a multisystem disorder (Swinnen & Robberecht, 2014).

1.1.2 Epidemiology and genetics

Current data suggests that the median age of ALS symptoms development is 64, with 50% of disease cases occurring in the 7^{th}-9^{th} decade of life (Bruijn et al., 2004; Kiernan et al., 2021). Current estimated lifetime risk of developing ALS is approximated at 1 in 400, with an incidence of 2 and prevalence of 4 individuals per 100,000 per year in the Western world (Johnston et al., 2006; Logroscino et al., 2010). ALS is predominantly a sporadic disease, with 90% of all cases having no family history of the disorder, while, in its inherited form, ALS is an autosomal dominant disorder (Brown & Al-Chalabi, 2017). Both sporadic (sALS) and familial ALS (fALS) are clinically indistinguishable and are speculated to share a number of mechanistic and pathological features (Brown & Al-Chalabi, 2017). The number of genes known to be mutated in ALS is currently estimated at 25 though the number rises annually (Brown & Al-Chalabi, 2017). Those genes presently account for circa 68% of all fALS and 11% of sALS cases (Al Sultan et al., 2016). Table 1.1 provides a summary of examples of ALS-associated genes.

Table 1.1 Pathway alterations in ALS and their genetic causes.

Pathway	**Gene (protein)**	**Inheritance** (*AD – autosomal dominant, AR – autosomal recessive, XD – X-linked*)	**Reference**
Autophagy and RNA metabolism	*C9orf72* (Guanine nucleotide exchange	AD	(DeJesus-Hernandez et al., 2011;

	chromosome 9 open reading frame 72)		Renton et al., 2011)
RNA metabolism	*TARDBP* (TAR DNA-binding protein 43, TDP-43)	AD	(Kabashi et al., 2009; Rutherford et al., 2008; Sreedharan et al., 2008)
	ANG (Angiogenin)	AD	(Greenway et al., 2006)
	FUS (RNA-binding protein FUS)	AD or AR	(Kwiatkowski et al., 2009; Vance et al., 2009)
	ATX2 (Ataxin 2)	AD	(Elden et al., 2010)
	HNRNPA1 (Heterogeneous nuclear ribonucleoprotein A1)	AD	(Kim et al., 2013)
	MATR3 (Matrin 3)	AD	(Johnson, Pioro, et al., 2014)
Mitochondrial function	*CHCHD10* (Coiled-coil-helix-coiled-coil-helix domain-containing 10)	AD	(Johnson, Glynn, et al., 2014)
Oxidative stress	*SOD1* (Superoxide dismutase 1)	AD or AR	(Rosen et al., 1993)
Endosomal trafficking/ Endoplasmic reticulum stress	*ALS2* (Alsin)	AR	(Shinji Hadano et al., 2010)
	FIG4 (Polyphosphoinositide phosphatase)	AD	(Chow et al., 2009)
	CHMP2B (Charged multivesicular body protein 2B)	AD	(Cox et al., 2010)
	VAPB (Vesicle-associated membrane protein-associated protein B/C)	AD	(Chen et al., 2010; Gkogkas et al., 2008; Nishimura et al., 2004)
Autophagy/ Ubiquitin-proteasome system	*OPTN* (Optineurin)	AD or AR	(Maruyama et al., 2010)
	VCP (Valosin-containing protein)	AD	(Johnson et al., 2010)
	SQSTM1 (Sequestosome 1)	AD	(Fecto et al., 2011)
	TBK1 (Serine/threonine-protein kinase TBK1)	Unknown	(Freischmidt, Wieland, et al., 2015)

	UBQLN2 (Ubiquilin-2)	XD	(Deng et al., 2011)
	SIGMAR1 (Sigma non-opioid intracellular receptor 1)	AD	(Al-Saif et al., 2011; Luty et al., 2010)
Cytoskeleton	*PFN1* (Profilin 1)	AD	(Wu et al., 2012)
	TUBA4A (Tubulin α4A)	AD	(Smith et al., 2014)
Neuronal development	*ERBB4* (Receptor tyrosine-protein kinase erbB 4)	AD	(Takahashi et al., 2013)

1.1.2.1 SOD1

Mutations in Cu-Zn superoxide dismutase 1 (SOD1) were the first identified genetic cause of ALS (Rosen et al., 1993) and to date account for 20% of fALS, or 2% of all cases of the disease (Meyerowitz et al., 2011). SOD1 protein is composed of 154 amino acids and, with 153 mutations described and linked to ALS thus far, mutations have been observed in nearly all positions of SOD1's primary sequence. However, it is not known if all of these mutations are pathogenic (Felbecker et al., 2010). Of those mutated SOD1 apoforms whose pathogenic function is known, several cause mitochondrial dysfunction by changing mitochondrial protein conformation (Li et al., 2010) and interfering with mitochondrial intermembrane space (Sheng et al., 2012). Early reports demonstrated that SOD1 mutations in ALS result in a toxic gain of function, as motor dysfunction was not observed in SOD1-deficient mice (Reaume et al., 1996).

Under normal physiological conditions, SOD1 is a soluble enzyme, which resides in the cytoplasm and is involved in the antioxidant response. Its enzyme activity breaks free superoxide radicals into hydrogen peroxide and oxygen by binding copper and zinc ions. A nuclear role of this protein has also recently been unveiled, as SOD1 is speculated to act as a transcription factor for other antioxidant genes (Tsang et al., 2014). Mutations in SOD1 gene cause the resulting protein to misfold and form cytoplasmic aggregates. One of the hypotheses in the field links soluble, oligomeric mutant SOD1 species to aggregate formation, hence making them the main drivers of SOD1-ALS pathology (Matus et al., 2014). SOD1 misfolding has previously been linked to oxidative damage, which occurs through exacerbated release of reactive oxygen species (ROS). In this context, SOD1 binding of a Ras-related C3

botulinum toxin substrate 1 (Rac1) GTPase leads to continual activation of NADPH oxidase 2 (Nox2), which in turn results in ROS production (Harraz et al., 2008). Moreover, misfolded SOD1 has been shown to affect mitochondrial electron transport chain activity, which also results in ROS production (Li et al., 2010). This is further supported by a decrease in ATP production in SOD1 mice, which drives the disease onset (Israelson et al., 2010).

SOD1 mutants have also been demonstrated to impact the ubiquitin proteasome system (UPS). Studies have linked the presence of misfolded SOD1 to a decrease in proteasomal function (Urushitani et al., 2002), which ultimately exacerbates the motor neuronal death in ALS (Kitamura et al., 2014). Overall, dysfunction in the cell's energy production, oxidative stress, and changes in the protein turnover appear to be amongst the drivers of motor neuronal death in the presence of misfolded SOD1.

1.1.2.2 TDP-43

TARDBP is one of the genes affected by point mutations, as well as truncation mutations, which can result in the formation of ubiquitinated, detergent-resistant cytoplasmic inclusions in the brains of patients and loss of TDP-43 from the nucleus (Elden et al., 2010). These cytoplasmic inclusions are also observed in ALS patients without mutations in TDP-43. TDP-43 protein is encoded for by *TARDBP* gene, contains 414 amino acid residues and its highly conserved structure includes amino-terminal (N-terminal) and glycine-rich carboxy-terminal (C-terminal) domains on either side of RNA recognition motifs (RRM) RRM1/RRM2 (Hanspal et al., 2017; Kametani et al., 2009; Li et al., 2015). C-terminal is the site of the clear majority of recognised TDP-43 point mutations occurring in ALS and FTD (Harrison & Shorter, 2017). Although far fewer ALS/FTD-associated mutations have been observed in the N-terminal domain, it has been shown that their occurrence causes protein misfolding and dramatically alters the ability of TDP-43 to perform its native function (Mompeán et al., 2017).

The occurrence of TDP-43 inclusions in neurodegeneration is collectively referred to as TDP-43 proteinopathy (Highley et al., 2014). Incorrect RNA splicing, sequestration of RNA molecules and functional RNA-binding proteins (RBPs), leading to translation as well as RNA transport impairments in motor neurons, are some of the toxic mechanisms proposed for TDP-43 proteinopathy (Kametani et al., 2016; Li et al., 2015). Apart from 95% of all ALS cases (Mitra et al., 2019), aberrant TDP-43 pathology is also observed in FTD, Lewy body disease, Niemann-Pick type C lysosomal disease and Alzheimer's disease (Cykowski et al., 2017; Dardis

et al., 2016). Interestingly, TDP-43 accumulation is also observed in normal aging population, with the current incidence rate estimate based on post-mortem studies reaching 40% (Geser et al., 2011; Uchino et al., 2015); however, the aggregates mostly present themselves as dystrophic neurites, not as classical cytoplasmic inclusions (Uchino et al., 2015). Moreover, post-mortem studies have shown ALS patients suffering the fastest cognitive decline to have the highest burden of TDP-43 aggregates in the brain (Cykowski et al., 2017). Furthermore, TDP-43 has been found to play a role in splicing of other known ALS genes, such as *ATXN2*, *FUS* and *C9orf72* (Highley et al., 2014). TDP-43 also affects splicing of a broader range of RNA species, including long non-coding RNAs and miRNAs (Cirillo et al., 2013), making its potential impact even more widespread. It remains to be fully elucidated why TDP-43 proteinopathy is seen in a vast majority of ALS cases. However, it is not unlikely that certain prolonged or repeated environmental stressors such as oxidative, osmotic or heat stress may cause stress granules, whose formation is reversible in healthy condition once the stressor is removed, to become a permanent cytoplasmic feature (Scotter, Chen & Shaw, 2015). The potential impact of TDP-43 proteinopathy on ALS pathogenesis and pathophysiology will be discussed in more details in section 1.1.3.3.

1.1.2.3 C9orf72

In 2011, the field of ALS research was widened by a landmark discovery of a GGGGCC (G_4C_2) hexanucleotide repeat expansion in the first intron of the C9orf72 gene (DeJesus-Hernandez et al., 2011). C9orf72 is the most common genetic cause of ALS, observed in both fALS and sALS cases (Conlon et al., 2016), currently accounting for 45% of fALS and 5-10% of sALS cases (Brown & Al-Chalabi, 2017). Physiologically, healthy individuals can carry up to 23 copies of G_4C_2 expansion, however, possessing more than 23 copies is pathogenic (Renton et al., 2011). However, no clear relationship exists between the length of the expansion and the severity of the disease (Van Mossevelde et al., 2017).

While the full spectrum of its physiological functions is still being investigated, the role of C9orf72 protein has been linked to initiation of autophagy (Webster et al., 2016), vesicle formation and trafficking (Aoki et al., 2017). C9orf72 is a member of the differentially expressed in normal and neoplastic cells (DENN) domain proteins, which have been described as regulators of the Rab GTPases (Marat et al., 2011). These proteins have also been linked to regulation of membrane trafficking (Zhang et al., 2012). Indeed, *in vitro* studies have

identified a defect in vesicular trafficking and vesicle assembly in cells harbouring the C9orf72 mutation (Iyer et al., 2018). Importantly, evidence points towards the importance of C9orf72 protein in autophagy initiation (Sellier et al., 2016).

1.1.2.3.1 RNA toxicity

Long chains of expanded repeats containing RNA and RBPs can adhere to one another, leading to formation of inclusions called RNA foci (Rizzu et al., 2016). Predominantly nuclear RNA foci are observed in all neuronal cells in the CNS, but in neurons to a much larger extent than astrocytes, microglia, or oligodendrocytes (Mizielinska et al., 2013). Burden of nuclear RNA foci has been documented as detrimental to cell survival via apoptotic pathway activation (Lee et al., 2013). Others demonstrated that RNase A administration abolishes RNA foci and treatment with antisense oligonucleotides, which activate the RNase H-mediated degradation of RNA foci, improves cell survival (Donnelly et al., 2013; Jiang et al., 2016). RNA foci have been speculated to also contribute to neurodegeneration by binding RBPs such as heterogeneous nuclear ribonucleoprotein A3 (hnRNPA3) (Mori et al., 2016), heterogeneous nuclear ribonucleoprotein A1 (hnRNPA1) and transcription factor Pur-alpha 1 (Pur-α) (Sareen et al., 2013), heterogeneous nuclear ribonucleoprotein A2 (hnRNPA2) (Kwon et al., 2014), and heterogeneous nuclear ribonucleoprotein H1 (hnRNPH1) (Conlon et al., 2016), thus contributing to a widespread disruption of RNA metabolism.

1.1.2.3.2 Dipeptide repeat proteins

RNA foci can undergo repeat-associated non-ATG-mediated (RAN) translation, producing dipeptide repeat proteins (DPRs) found in the cytoplasm (DeJesus-Hernandez et al., 2011; Gendron et al., 2013). These polydipeptides also actively contribute to neurodegeneration in ALS (see section 1.1.3.2; Conlon et al., 2016). Depending on the dominant amino acid sequence, DPRs can vary in toxicity. Indeed, evidence suggests that DPRs are more neurotoxic than RNA foci (Tran et al., 2015). Recent evidence showed the importin family of nuclear import receptor to directly bind glycine–arginine (poly-GR) and proline–arginine (poly-PR) DPRs (Hutten et al., 2020). As importin α and β shuttle TDP-43 to the nucleus, arginine-rich DPR binding of importins prevents TDP-43 nuclear import. This not only leads to TDP-43 accumulation in the cytoplasm, but also increased TDP-43 insolubility (Hutten et al., 2020). Moreover, mice induced to carry the C9orf72 expansion developed not only the RNA foci,

DPRs, and motor deficits, but also accumulated pTDP-43 inclusions in the cytoplasm not observed in their wild-type littermates (Chew et al., 2015).

1.1.2.3.3 C9orf72 protein haploinsufficiency

Previously, haploinsufficiency was considered to be one of the causes of C9orf72 ALS. However, studies have shown that ablation of C9orf72 in mice has not resulted in onset of motor neuron disease and the absence of astrogliosis, thus suggesting that loss of protein function on its own is not a driving mechanism of C9orf72 pathology (Koppers et al., 2015). Rather, haploinsufficiency and gain of toxic function driven by RNA foci and DRPs work in tandem. Furthermore, deletion of C9orf72 in roundworm (*Caenorhabditis elegans*; *C. elegans)* carrying the TDP-43^{A315T} mutation was more detrimental to the organism survival than the TDP-43^{A315T} mutation alone (Therrien et al., 2013). Moreover, defects observed in vesicle trafficking in C9orf72 induced pluripotent stem cell (iPSC)-derived motor neurons were reversed upon restoration of C9orf72 to its physiological levels (Aoki et al., 2017).

1.1.2.4 Other familial ALS genes

As previously mentioned, ALS is predominantly a disease associated with ageing. However, a subset of autosomal recessive familial cases carries a deletion mutation within the amyotrophic lateral sclerosis 2 (ALS2) gene on chromosome 2q33, which results in a juvenile onset of the disease (Hadano et al., 2001; Otomo et al., 2003). ALS2 protein, also known as alsin, is truncated in the disease, resulting in diminished protein function, consequently leading to death of upper motor neurons (Otomo et al., 2003). Alsin has been linked to the endosomal function as a guanine nucleotide exchange factor for guanosine triphosphate enzymes Rac1 and Rab5, which are responsible for actin function and endosomal trafficking (Yamanaka et al., 2006). Similarly, sigma non-opioid intracellular receptor 1 (SIGMAR1) mutation also results in a juvenile ALS onset, with endoplasmic reticulum (ER) stress and UPS function identified as its functions (Al-Saif et al., 2011; Luty et al., 2010).

Fused in sarcoma (FUS) mutation present in 4.1% fALS cases (Al-Sultan et al., 2016) forms inclusions which co-label with stress granule markers, which in itself could contribute to ALS pathology (Bentmann et al., 2012). In a healthy system, FUS acts as RBPs during transcription, splicing, miRNA regulation and nuclear mRNA transport (Bentmann et al., 2012). Dysregulation of RNA processing and metabolism have been recognised as pathological

mechanisms involved in ALS, FUS being recognised as one of the key genes implicated (Walsh et al., 2015).

1.1.2.5 Sporadic ALS

Approximately 90% of all ALS cases are classed as sporadic, i.e. having no family history of the disease. Due to lack of *in vivo* models and relatively recent emergence of iPSC technology utilising patient biopsies, sALS remains critically understudied compared to fALS. sALS and fALS are indistinguishable in the clinic, which suggest a presence of overlapping pathological mechanisms. Indeed, several genetic mutations observed in fALS have also been identified as causative factors in sALS (Brown & Al-Chalabi, 2017). This subset of genes, described frequently as ALS genetic risk factors, are most often identified in genome-wide association studies (GWAS) (van Rheenen et al., 2016). Of these, cytoskeletal proteins MOBP and C21orf2, and protein homeostasis regulators UNC13A, SCFD1, are important examples (Brown & Al-Chalabi, 2017).

sALS patients often suffer a delay in diagnosis, as clinical symptoms at very early stages of the disease often resemble other neurodegenerative disorders (Freischmidt et al., 2015). Studies showed that transplantation of post-mortem astrocytes from sALS patients caused motor neuronal death in the spinal cord of wild-type mice accompanied by neuroinflammation (Qian et al., 2017).

1.1.3 ALS pathogenesis and pathophysiology

ALS is known to be a multimechanistic disorder. The pathogenic process and mechanism of disease onset and progression remain poorly understood, though dysregulation of RNA processing and metabolism (splicing, nuclear export and translation), glutamate excitotoxicity, oxidative stress, axonal transport impairment, and mitochondrial dysfunction are some of the well-described factors (Ferraiuolo et al., 2011; Walsh et al., 2015). In the following sections, I have focussed on the contributions of three pathophysiological processes to ALS – protein misfolding, formation of DPRs in C9orf72 ALS, and TDP-43 proteinopathy, as these are of particular relevance to the aims of this thesis.

1.1.3.1 Protein misfolding

In order to fulfil its protein function correctly, the amino acid chain must be folded in ER into a three-dimensional structure with an aid of molecular chaperones to assume a correct conformation. Protein misfolding refers to a process where protein synthesis does not

culminate in a protein assuming conformation that allows it to fulfil its biological functions. Protein misfolding can be a result of genetic mutations as well as environmental factors. Under baseline conditions, misfolded proteins undergo degradation via UPS, via autophagy (see section 1.3.3), or are cleared to the extracellular space (Sweeney et al., 2017). In disease, however, misfolded protein species accumulate in the cytoplasm and often sequester other cytosolic proteins into their aggregates, exacerbating the resulting cell death. These cytoplasmic inclusions often serve as pathological hallmarks of the disease. For example, TDP-43 inclusions with and without mutations in *TARDBP* are observed in 97% of all non-SOD1 or FS ALS cases (see section 1.1.3.3; (Brettschneider et al., 2012; Neumann et al., 2006). Cytoplasmic aggregates of FUS have also been observed in ALS cases driven by a mutation *FUS* gene (Kwiatkowski et al., 2009).

Presence of misfolded proteins causes chronic cellular stress. Such triggers induce the expression of pro-autophagy chaperones BAG cochaperone 3 (Bag3) and heat shock protein beta-8 (HspB8) (Cascella et al., 2017; Guilbert et al., 2018). Indeed, Crippa et al. (2013) observed a transcriptional upregulation of these co-chaperones in transgenic $SOD1^{G93A}$ mice where misfolded SOD1 is seen to accumulate, but not in wild-type control or wild-type SOD1 mice.

The reasons behind widespread protein misfolding in ALS and other neurodegenerative disorders have not yet been fully elucidated. Studies have linked mitochondrial dysfunction and aberrant mitochondrial protein homeostasis to misfolded SOD1 aggregation (Jordi Magrané et al., 2012), whereas chronic ER stress has been shown to lead to TDP-43 aggregation (Hicks et al., 2020a). Misfolded proteins have been observed in CNS neurons and glia alike (Parakh & Atkin, 2016), suggesting that an underlying mechanism of protein misfolding in ALS does not target one specific type of cells.

1.1.3.2 Dipeptide repeat proteins

Even though the C9orf72 repeat is intronic and should not get transcribed, it does undergo transcription. Moreover, some RNA foci molecules are transported out of the nucleus and can still be translated via RAN translation (Ash et al., 2013). Indeed, recent efforts have identified a CUG start codon with a Kozak consensus sequence, which allows for this process to occur (Sonobe et al., 2018). Resulting DPRs accumulate in the cytosol and have been observed to cause chronic cellular stress that can lead to cell death (Sonobe et al., 2018). This appears to

be a self-perpetuating cycle, where chronic stress conditions favour translation of toxic protein, thereby keeping the production of DPRs constant (Green et al., 2017).

There are five recognised species of DPRs, each differing in structure, toxicity, and known interactions. Poly-glycine-proline (poly-GP) and poly-proline-alanine (poly-PA) DPRs, although abundant, have not been recognised as toxic (Freibaum & Taylor, 2017). Poly-GR and poly-PR both interact with ~150 proteins, have a highly charged and polar coil structure, and have been reported to be the most toxic species of DPRs (Freibaum & Taylor, 2017). Poly-glycine-alanine (poly-GA) DPRs, due to their formation of very compact aggregates, are readily seen in ubiquitinated, $p62^{+}$ inclusions in the patient post-mortem CNS tissue (Mori et al., 2013; May et al., 2014). DPRs can be translated from both sense [$(G_4C_2)_n$ – poly-GA, poly-GR, poly-GP] and antisense [$(C_4G_2)_n$ – poly-PA, poly-GP, poly-PR] sequences, although there does not seem to be a link between a starting RNA sequence and DPR toxicity. Moreover, although present in glia and neurons alike, motor neurons carry a much larger burden of DPRs in ALS than glial cells (Dafinca et al., 2016).

As discussed in section 1.1.2.3.2, DPRs interact with TDP-43 to further exacerbate cell death. Impaired nucleocytoplasmic transport resulting from the C9orf72 repeat expansion and a presence of some species of arginine-rich DPR proteins has been described in ALS and FTLD (Rizzu et al., 2016). Poly-GA DPRs, which co-localise with TDP-43 cytoplasmic inclusions in various cell models of ALS, have been linked to the inhibition of nuclear import of TDP-43. This effect can be reversed by upregulation of nuclear transport proteins (NUPs) NUP62 and NUP54 and re-entry of poly-GA into the nucleus (Khosravi et al., 2017).

1.1.3.3 TDP-43 cytoplasmic aggregation and nuclear loss

TDP-43 in healthy individuals is located mostly in the nucleus where it acts as an RBP and a DNA-binding protein, an exon splicing factor, mRNA biosynthesis mediator, and is also involved in inhibition of retroviral replication (Barmada et al., 2010). In times of cellular stress, TDP-43 shuttles to the nucleus where it incorporates into stress granules, temporary cytoplasmic inclusions whose aim is sequestration of only the most essential mRNA molecules for translation in order for the cell to survive the stress event (Anderson & Kedersha, 2008; Khalfallah et al., 2018). However, nuclear export/loss, lack of nuclear import, protein cleavage and phosphorylation of the C-terminal domain may cause TDP-43 to remain in the cytoplasm and form aggregates (Li et al., 2015b; Zhang et al., 2009; Hutten et al., 2020). Loss of nuclear

TDP-43, cytoplasmic accumulation, phosphorylation (figure 1.1) and its association with stress granules is observed under conditions of chronic oxidative stress or heat shock response (Li et al., 2017; Meyerowitz et al., 2011).

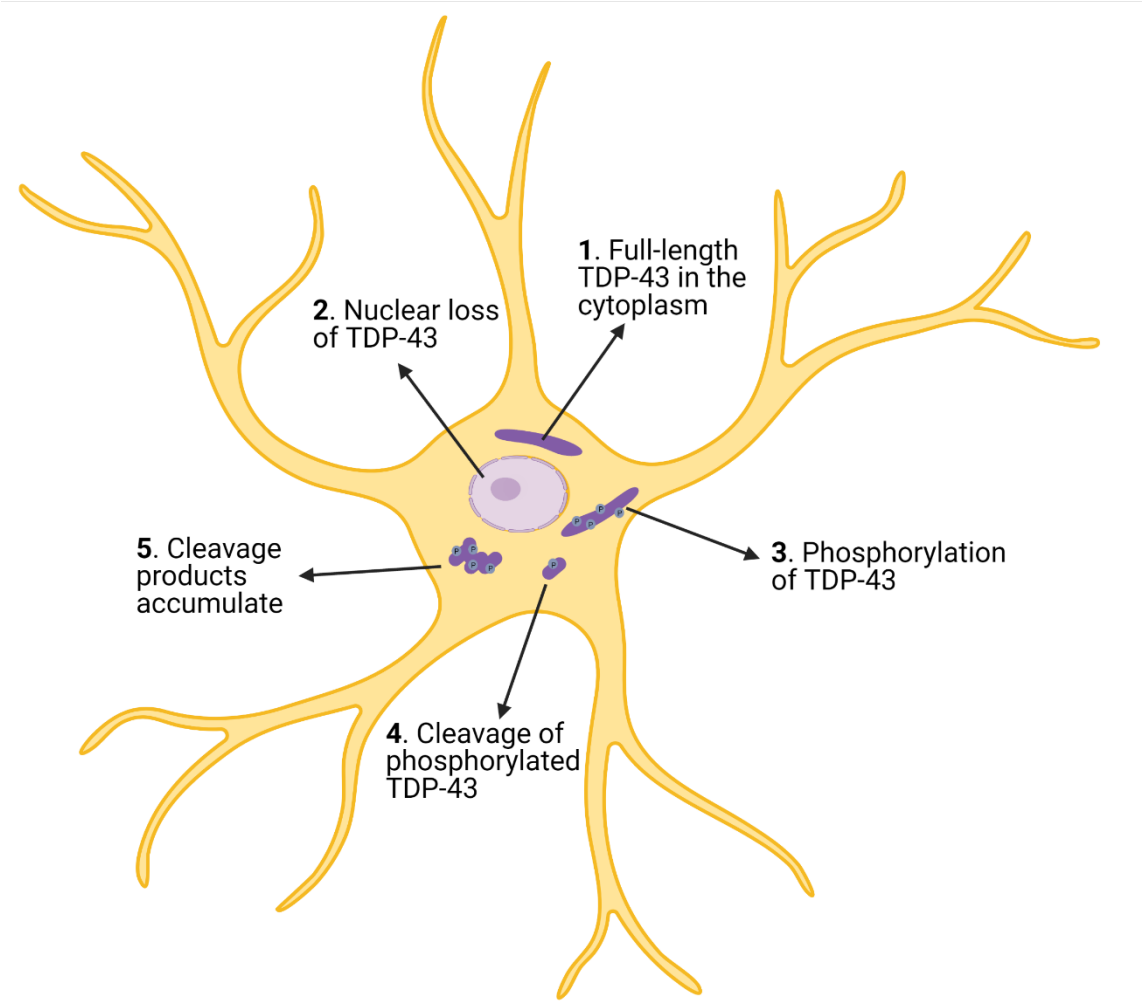

Figure 1.1 TDP-43 proteinopathy dynamics

Under basal conditions, TDP-43 resides in the nucleus (1). Under cellular stress, it shuttles to the cytoplasm. In ALS, a permanent loss of TDP-43 from the nucleus occurs (2). Once in the cytoplasm, TDP-43 is phosphorylated (3) and cleaved (4). Its cleavage products accumulate, forming cytoplasmic aggregates (5), which often also include full-length TDP-43.

The precise mechanism triggering the mislocalisation and aggregation of TDP-43 remains unknown, though several hypotheses have been postulated, including axotomy, prolonged cell stress, and neuroinflammation (Correia et al., 2015).

Current hypotheses state that depletion of nuclear TDP-43 can have its consequences either in the form of loss of its nuclear function or a gain of cytoplasmic function (Winton et al., 2008). Loss of TDP-43 nuclear function from motor neurons has been shown before to cause age-dependent degeneration and neuron loss in mice (Iguchi et al., 2013). When lost from the nucleus, TDP-43 leads to an accumulation of DNA double strand breaks and a deficiency in the DNA damage repair mechanism (Mitra et al., 2019). Consistently with its role as an mRNA biosynthesis mediator, loss of nuclear TDP-43 from lower motor neurons resulted in dysregulation of RNA splicing, found in transcriptomic studies as a differential expression of a range of RNA splicing-related genes (Highley et al., 2014). Little is yet known about the precise mechanisms behind which TDP-43 nuclear loss occurs, but reports seem to suggest a mechanism independent of traditional stress granule dynamics as a response to transient stress (Gasset-Rosa et al., 2019). Studies conducted on cell lines expressing exogenous TDP-43 aggregates observed a loss of endogenous TDP-43 from the nucleus and its cytoplasmic accumulation, suggesting a need for an exogenous cellular stress (Budini et al., 2015). Moreover, it has been suggested that nuclear loss of TDP-43 gets worse as the cytoplasmic aggregates attract more TDP-43 and become insoluble (Budini et al., 2015).

TDP-43 found in the cytoplasm of ALS patients is truncated into fragments containing its C-terminal domain, which are often phosphorylated or ubiquitinated, or both (Correia et al., 2015). Phosphorylation of TDP-43 is considered one of the main triggers of the protein's mislocalisation and aggregation. Multiple TDP-43 phosphorylation sites are phosphorylated by members of the casein kinase (CK) family. For instance, overexpression of truncated CK1ð was identified as the main factor causing TDP-43 nuclear loss and cytoplasmic accumulation (Nonaka et al., 2016).

Several other species of TDP-43, such as 45, 35, and 18-25 kDa fragments are also found within the inclusions (Kametani et al., 2016). TDP-43 possesses two caspase-3 cleavage sites, including one at TDP-43's nuclear localisation signal (NES) site (figure 1.2). Once in the cytoplasm, cleavage leads to C-terminal fragmentation and formation of 35 kDa and 25 kDa TDP-43 fragments (Chiang et al., 2016; Elden et al., 2010; Meyerowitz et al., 2011). Studies have proposed that these smaller species, especially the 35 kDa fragment, act as a seed and sequester TDP-43 for further accumulation (Che et al., 2015; Shimonaka et al., 2016; Tanaka et al., 2016). It is speculated that as the inclusions grow, they trap other RNA species, thus

further increasing in size, preventing said RNAs from executing their function, and making the clearance of the inclusions increasingly difficult (Walsh et al., 2015). A recent mass spectrometry analysis of the insoluble cytoplasmic TDP-43 inclusions from post-mortem ALS and FTD samples has described regional discrepancies in the composition of the inclusions. TDP-43 aggregates in the brains of patients express high levels of the C-terminal fragments, whereas aggregates found within the spinal cord are both N- and C-terminal positive, suggesting that the protein cleavage sites are located within non-core terminal regions and proteolytic enzyme-mediated cleavage can occur distally (Kametani et al., 2016). The study has also linked the RRM2 and the glycine-rich portion of the C-terminal as critical elements for prion-like aggregate formation, confirming previous studies (Nonaka et al., 2016; Wang et al., 2016). However, it appears that TDP-43 association with stress granules is a mechanism independent of pathogenic aggregate formation, as inhibition of c-Jun N-terminal kinase (JNK), shown to play a role in stress granule formation, does not affect the nuclear loss of TDP-43 or its fragmentation. Moreover, inhibiting caspase, which is crucial for C-terminal cleavage, blocks 35 kDa fragment aggregation, but does not have an effect on TDP-43 accumulation in stress granules (Meyerowitz et al., 2011; Wobst et al., 2017). Also, not all stress granules are TDP-43-positive and pathogenic TDP-43 aggregates are negative for classical markers of stress granules such as TIAR1 and G3BP1 (Hicks et al., 2020b). Lines of evidence also state that it is the full-length TDP-43 that induces cell death in ALS, not the C-terminal fragments, as the mutated full-length TDP-43 has a longer half-life than its wild-type counterpart (Li et al., 2015). In fact, slow protein turnover can play a particularly important role in generating cell toxicity in post-mitotic cells, such as neurons, and in cells with limited ability to proliferate, such as astrocytes, as the pool of non-degraded proteins does not dilute sufficiently over time (Toyama et al., 2014) and can result in toxic aggregate formation. Though the mutant TDP-43 protein turnover rate is slower than that of the non-mutant, wild-type TDP-43 can still have a toxic effect on cells in other genetic subtypes of ALS and in sporadic patients. For example, since the UPS plays a vital role in degradation of TDP-43 (Scotter et al., 2015), aberrant proteasomal function may prolong the turnover of wild-type TDP-43, which could be relevant to the sporadic ALS patients (Kabashi et al., 2012). Dysfunctions in the proteasome have previously also been observed in SOD1 ALS patients (Kitamura et al., 2014), thus suggesting that impaired protein degradation plays a role in disease pathogenesis.

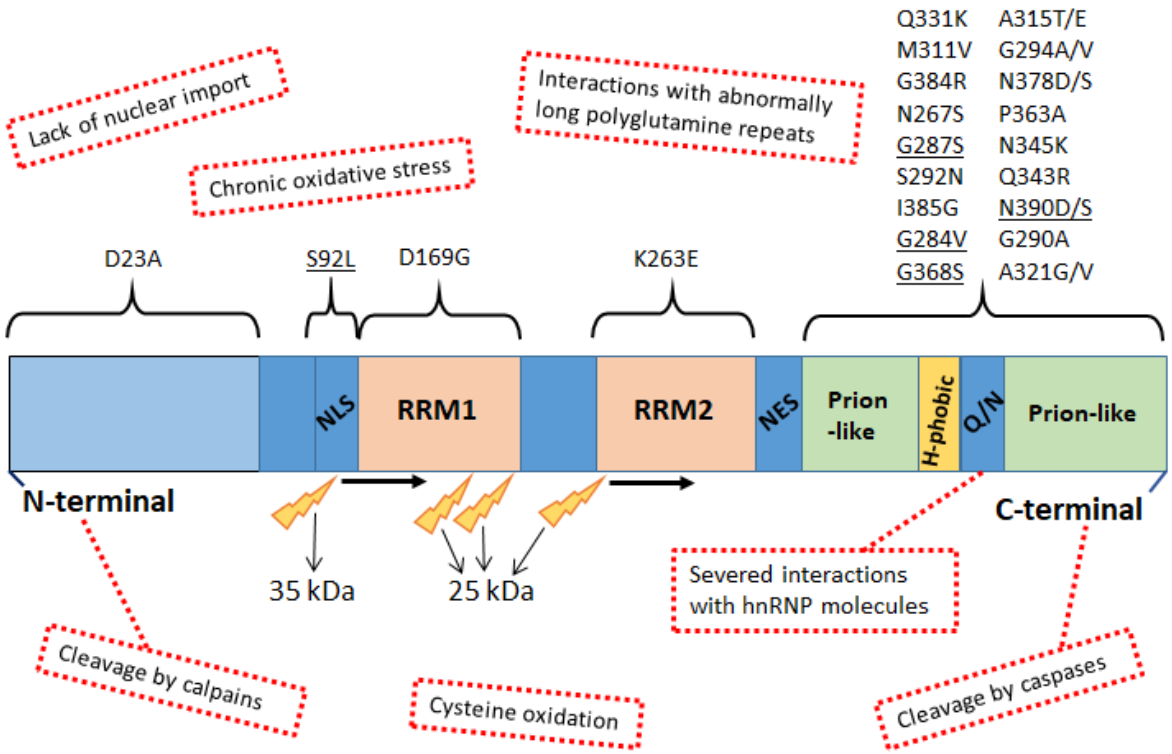

Figure 1.2 Structure of TDP-43 protein and known mechanisms of proteinopathy

TDP-43 protein consists of an N-terminal and C-terminal at both ends and two RNA recognition motifs (RRM). Mutations at several of TDP-43 residues have been identified and a selection of them shown here above each region they occur here. Highlighted mutations have also been identified in healthy controls. Cleavage of TDP-43 at the level of nuclear localisation signal (NLS) causes a formation of a 35 kDa fragment, whereas cleavage at the level of RRMs prior to nuclear export signal (NES) results in formation of the 25 kDa fragments. Several mechanisms have been shown to play a role in formation of TDP-43 aggregates, most of which are presented in red dotted boxes. Some of these mechanisms have been linked to particular regions of the TDP-43 protein. For example, cleavage of the N-terminal by endoplasmic reticulum-bound calpains, as well as caspases-mediated cleavage of the C-terminal contribute the proteinopathy. Moreover, disrupted interactions between the Q/N rich region of the C-terminal, located next to the hydrophobic portion of the C-terminal, and hnRNP molecules has been shown to cause cytoplasmic aggregation of TDP-43.

Interestingly, Barmada et al. (2010) have found the formation of cytoplasmic TDP-43 inclusions not to correlate with cell death, suggesting rather that cell survival can also be affected by diffuse TDP-43. This supports the idea that TDP-43 aggregates per se are not pathological, but they are rather a sign of pathology. Furthermore, Ala-315-Thr missense

mutation seen in familial TDP-43 forms of ALS has been shown to exacerbate cell death due to an increase in TDP-43 mislocalisation (Gitcho et al., 2009), indicating that nuclear loss might be the principal mechanism driving pathology.

Recent efforts yielded many significant findings, which shed a light on the types of cellular processes and targets needing a modulation in order to restore normal TDP-43 function. Williamson et al. (2019) pointed to overexpression of an antioxidant protein oxidation resistance protein 1 (*Oxr1*) in motor neurons as a key to rid the cells of cytoplasmic TDP-43 burden and improve the neuromuscular junction (NMJ) and muscle health. Similarly, White et al. (2019) rescued the motor neuron, NMJ, and cortical spine degeneration in TDP-43 mouse model by knocking out sterile alpha and TIR motif containing 1 (*Sarm1*), which is associated with axonal degeneration. Prevention of TDP-43 phosphorylation may also be beneficial, as studies have described a reduction of soluble and insoluble TDP-43 inclusions in cells treated with CK1 inhibitors without affecting cell viability (Hicks et al., 2019), suggesting that stopping the phosphorylation of full-length TDP-43 has a beneficial and potentially therapeutic effect to be explored.

Removal of existing TDP-43 aggregates found in the cytoplasm and prevention of further aggregation have been a subject of a substantial debate. Both autophagy and UPS systems of aberrant cargo degradation are affected in ALS, exacerbating the cytoplasmic aggregate burden and contributing to cell death. Modulation of these processes can help clear cytoplasmic inclusions and lead to improved cell survival. Current evidence suggests that smaller fragments of TDP-43, such as TDP-25, are primarily degraded by autophagy (Crippa et al., 2016).

It remains unclear if TDP-43 proteinopathy is a causative factor or rather a manifestation of the disease (Kametani et al., 2016). It is also yet to be uncovered if it is the nuclear loss of TDP-43 or its gain of function in the cytoplasm that is toxic to motor neurons in ALS (Dardis et al., 2016).

1.1.4 Non-cell autonomous component of ALS

Since motor neurons are the cell type that perishes in ALS, significant research momentum has been put behind studying it. However, efforts stemming from research conducted in mid- and late-2000s has implicated other cell types as contributors to the disease, most

importantly the glial cells, thus proving ALS to be a non-cell autonomous disorder (Ferraiuolo et al., 2011; Serio et al., 2013). Moreover, recent studies show the ratio of glial cells to neurons in the brain to be 1:1, hence studying these cells is important to understand the full profile of neurodegenerative diseases (von Bartheld et al., 2017).

1.1.4.1 Role of astrocytes in ALS

Astrocytes constitute 20-40% of all glial cells in the brain (Verkhratsky & Butt, 2013). They have long been considered a support cell type, aiding the normal function of neurons by providing trophic support, removing toxic factors from the intracellular space and excess neurotransmitters from the synaptic cleft, providing essential metabolites, aiding vasomudulation, and regulating levels of extracellular K^+ to prevent undue axon depolarization.

The role of astrocytes as drivers of ALS pathology became of interest in mid-2000s thanks to studies which used primary neonatal astrocytes and motor neurons from mutant SOD1, as well as motor neurons derived from mouse embryonic stem cells (mESCs) harbouring the same mutations (Di Giorgio et al., 2007; Nagai et al., 2007). These studies described an exacerbated death of motor neurons grown on mutant astrocytes. Importantly, they also determined through conditioned medium experiments that mutant SOD1 astrocytes release factors that are selectively toxic towards motor neurons (Nagai et al., 2007).

Recent evidence speculates that death and atrophy of astrocytes in ALS patients might occur before neuronal degeneration and manifestation of clinical symptoms (Liu et al., 2017), although more evidence is needed to support this notion. Nevertheless, glia are an attractive target for drug therapies aiming to prevent neuronal death. For example, riluzole has been found to target excessive glutamate excitotoxicity caused by a downregulation of excitatory amino acid transporter 2 (EAAT2), which associates with astrocytes (Wang et al., 2004). Indeed, lack of a robust glutamate clearance by these transporters and reduction of gamma aminobutyric acid (GABA) neurotransmitter in the cortex with degeneration of inhibitory circuits, have previously been linked to hyperexcitability observed in ALS patient motor and cortical neurons (Raiteri et al., 2005; Young et al., 2017).

Despite the research efforts focussing on uncovering the factors which determine astrocyte neurotoxicity, there is no consensus on what factor(s) exactly are responsible for neuronal

death. Several hypotheses, however, have been put forward, including a release of toxic factors, lack of metabolic flexibility and metabolic support towards motor neurons (Allen et al., 2019; Ferraiuolo et al., 2007).

In addition, compelling evidence indicates that astrocyte toxicity is due at least in part, if not completely, to the release of soluble factors (Nagai et al., 2007; Rojas et al., 2015). Recently, studies of extracellular vesicles released by astrocytes differentiated from C9orf72 patient-derived iPSCs (Birger et al., 2019) and induced neural progenitor cells (Varcianna et al., 2019) has highlighted not just the toxicity of astrocytes against motor neurons via soluble factors, but also a decreased secretion of important antioxidant proteins (Birger et al., 2019) and release of miRNA species regulating axonal guidance (Varcianna et al., 2019). Moreover, conditioned medium from C9orf72 iPSC-derived astrocytes was able to induce an autophagy dysfunction in wild-type cells (Madill et al., 2017). Taken together, these findings help solidify the crucial pathogenic role played by astrocytes in ALS.

1.1.4.2 Role of other glial cells

Oligodendrocytes and Schwann cells are CNS glia responsible for myelination, or production and ensheathment of axons in myelin sheath, to ensure fast signal conduction. These highly specialised glia are chiefly associated with diseases featuring axon demyelination, such as multiple sclerosis (MS). However, oligodendrocytes have been shown to be affected in ALS. Evidence from $SOD1^{G93A}$ mice showed death of oligodendrocytes to occur before motor neuron degeneration, and a failure of these cells to provide trophic support and perform myelination (Philips et al., 2013). Oligodendrocyte precursors have been shown to proliferate faster in young $SOD1^{G93A}$ mice than wild-type controls, and to atrophy much earlier, leading to myelin dysfunctions and demyelination of grey matter region of the CNS (Kang et al., 2013). Interestingly, knockdown of mutant SOD1 from these cells rescued the motor phenotype observed in the transgenic mice. Similarly, recent efforts have identified oligodendrocytes as carriers of toxicity against motor neurons in C9orf72, SOD1 and sporadic ALS (Ferraiuolo et al., 2016). Although evidence of their involvement in ALS is limited, oligodendrocytes of the periphery known as Schwann cells, have been thus far described as having the opposite effect on motor neuron survival when mutant SOD1 is knocked down (Lobsiger et al., 2009).

Microglia, resident macrophages of the CNS, provide the first line of immune response to a variety of insults. At resting state, microglia are ramified, and their extending processes are

sensing changes in the microenvironment (Kreutzberg, 1996). Upon detection of such insults, the processes retract, microglia proliferate and release pro-inflammatory cytokines such as interferon gamma (IFN-γ), tumour necrosis factor alpha (TNF-α), and a variety of interleukins, which in turn help recruit other microglia to the site of the insult or pathogen activity (Brown & Vilalta, 2015). While this effect helps fight infections in the CNS and microglial anti-inflammatory function can help speed up the recovery of CNS tissue and provide growth factors to healthy neurons, microglia can also assume a chronic pro-inflammatory phenotype. In SOD1 mice, microglia start assuming an activated phenotype just before or at disease onset, though it has not been clarified if it is a symptom of underlying inflammatory changes or a cause of progressive neurodegeneration. Microglia have been identified as key players in formation of a chronic pro-inflammatory environment observed in ALS, which manifests itself in an active phagocytosis of axons by microglia, irrespective of axon health (Brown & Vilalta, 2015). Inhibition of microglial activation, either via cyclooxygenase 2 (COX-2) inhibition (Drachman et al., 2002) or pharmacologically (Kriz et al., 2002; Van Den Bosch et al., 2002), has showed neuroprotection and improved survival in transgenic SOD1 mice. In a landmark study by Boillée et al. (2006), targeted knock-down of mutant SOD1 burden in microglia of LoxSOD1^{G37R}/CD11b-Cre^{+} mice, has not decreased microglial activation, but resulted in improved survival. Indeed, survival of mutation-harbouring motor neurons can be rescued in systems where surrounding glia lack the mutation and, consequently, astrogliosis and microgliosis are absent (Clement et al., 2003).

Inflammation seems to be the main pathway involved in microglia neurotoxic action. In fact, studies aiming to reduce or deplete activation of inflammation through nuclear factor kappa B (NFκB) knockdown showed that NFκB inhibition in astrocytes alone does not improve the disease phenotype. Targeting microglia, however, resulted in a rescue of motor neuronal survival in SOD1^{G93A} mice and downregulation of microgliosis without affecting SOD1 expression levels. Conversely, constitutive activation of NFκB in wild-type mice led to motor neuronal degeneration, thus confirming the important role of neuroinflammation signalling in ALS (Frakes et al., 2014). Further studies focusing on NFκB suppression in both microglia and astrocytes not only slowed down ALS onset, but also delayed the disease progression (Frakes et al., 2017).

Other glial cells of the CNS, ependymal glia of the choroid plexus involved in cerebrospinal fluid (CSF) production, have not been extensively studied in the context of ALS (Payne, 2009; Smith et al., 2015), hence their involvement in the disease, if any, remains unknown.

1.2 ALS modelling

First landmark discoveries made on the pathophysiological hallmarks and mechanisms of ALS were made in patient post-mortem samples. Due to unavailability of patient CNS material during the course of the disease and with post-mortem samples representing the disease end-stage only, ALS researchers rely substantially on disease models to help them unravel the pathogenic mechanisms of ALS. Numerous *in vitro* and *in vivo* models have now been introduced to facilitate the discoveries.

1.2.1 *In vitro* models

Cells of neuronal origin such as **Neuro2a** (N2a) and **SH-SY5Y** neuroblastoma cell lines, provide a favourable environment to study diseases of the CNS, as they can be propagated *ad infinitum* and differentiated into neurons (Kovalevich & Langford, 2013). Such cells can be efficiently transfected with disease-specific mutations to model the disease *in vitro*. One of the first such approaches applied to ALS investigated G37R, G41D and G85R SOD1 mutations in differentiated N2a cells (Pasinelli et al., 1998). Similarly, SH-SY5Y cell line helped clarify the role of C9orf72 protein, linking the pathogenic expansion to aberrant endosomal trafficking and autophagy dysfunctions in ALS patients (Farg et al., 2014). Other neuron-like cell types, such as NSC-34, are widely used in ALS research. They have recently been used to deconvolute the dynamics of TDP-43 inclusion formation (Hicks et al., 2020) and to assess the clearance of TDP-43 aggregates by UPS and autophagy (Cascella et al., 2017).

For studies where a function and pathogenic mechanism of a given genetic mutation is to be investigated, immortalised cell lines transfected with either a mutant human gene construct or an overexpression construct have been widely studied. Most commonly used lines such as **HeLa** and human embryonic kidney cell line (**HEK293T**) prove reliable for that purpose. HEK293T cells have been used to elucidate the process of mutant TDP-43 (M337V and A382T) aggregation in ALS, especially the formation of the detergent-insoluble cytoplasmic inclusions (Furukawa et al., 2011). Similarly, HEK293T cells have been used to confirm the post-mortem observation of vesicle-associated membrane protein-associated protein B/C (VAPB) cytoplasmic aggregation in the overexpression model (Mitne-Neto et al., 2011). These models

remain widely popular and keep providing useful mechanistic insights into ALS. Importantly, HEK293 cells express neuronal markers and present a neuronal phenotype thanks to the neural crest ectodermal origin of the adrenal medulla from which they originate (Lin et al., 2014; Shaw et al., 2002).

Stem cells and their pluripotent properties were first tested with the aim of implementing therapies capable of repairing damaged CNS tissue, especially at the sites of marked cell loss (Nikkhah et al., 1994). Their use proved more versatile for research purposes as differentiation protocols for different cell types were devised. Neurons were first differentiated from human stem cells in 2001 (Zhang et al. 2001), thus marking a new era of *in vitro* research which ALS researchers also benefited from. Stem cell technology was first utilised in ALS research in a form of mESCs derived from the $SOD1^{G39A}$ mouse model (Di Giorgio et al., 2007). The study also demonstrated a decrease in mESCs-derived motor neuron survival in a co-culture with $SOD1^{G93A}$ primary cortex glia. For example, human embryonic stem cells (hESCs) differentiated into motor neurons were used in a co-culture system with primary foetal astrocytes transfected with mutant $SOD1^{G37R}$ transgene (Marchetto et al., 2008). Not only were the astrocytes found to exhibit an inflammatory phenotype, they have also caused motor neuron death in a co-culture system. These findings helped establish lack of cell autonomy as a feature of ALS, elevating astrocytes to a position of active drivers of neurodegeneration. Use of cells of human embryonic origins is no longer widely implemented as their sourcing poses many ethical issues and more suitable alternatives have been identified.

With the dawn of the cellular reprogramming technology, which has introduced iPSCs, it has become easier to study disease mechanisms during the patient's lifetime. Fibroblasts obtained from patient skin biopsies were the first (Takahashi et al., 2007) and remain the most common starting point for cellular reprogramming, but other somatic cell types such as adipocytes (Taura et al., 2009), keratinocytes (Aasen et al., 2008) and blood mononuclear cells (Ustyantseva et al., 2020) are also used. Cells are then transfected with a set of reprogramming factors, i.e. Oct4, Sox2, Klf4 and c-Myc or Lin28 (often referred to as Yamanaka factors or Thompson factors depending on the set), which forces them to revert to an embryonic stage, where cell fate has not yet been determined. These stem cells can be differentiated into any cell type of the human body.

Motor neurons derived from patient iPSCs were first used to study ALS in 2008, when Dimos et al first investigated the feasibility of using iPS-derived motor neurons to unravel the pathogenic mechanisms involved in ALS. The use of this technology has since helped ALS research grow from strength to strength. Motor neurons have been differentiated from ALS8 patient-derived iPSCs to assess the levels of VAPB protein levels in a study that confirmed the VAPB downregulation status of ALS8 patients, whilst also noting the lack of cytoplasmic aggregation of this protein previously observed in patient post-mortem samples (Mitne-Neto et al., 2011). Although the majority of efforts focused on studying iPSC-derived motor neurons in ALS, glial cells can also be studied in this *in vitro* system. iPSC-derived astrocytes from patients with TDP-43^{M337V} mutation showed cytoplasmic TDP-43 inclusions (Serio et al., 2013), thus confirming previous post-mortem findings. Moreover, ectopic expression of mutant TDP-43 in control astrocytes reproduced the phenotype of the M337V mutant protein (Serio et al., 2013).

iPSC technology, however, is not without its caveats. Due to its reliance on reverting the cells back to an embryonic stage, the epigenome of reprogrammed cells does not reflect the changes that have occurred in the body of the donor over their lifetime. This poses a significant issue for neurodegenerative disease research, as age is the main risk factor for the vast majority of these disorders, including ALS. Moreover, not all iPSC-based *in vitro* models manage to recapitulate all pathophysiological features of ALS. iPSC-derived motor neurons with TDP-43^{M337V} mutation, despite showing increased TDP-43 levels, failed to show mislocalisation or aggregation observed post-mortem (Bilican et al., 2012) and astrocytes from the same mutant line did not show toxicity against motor neurons in a co-culture system (Serio et al., 2013), further suggesting that the reprogramming process modifies the cell epigenome.

To circumvent this limitation, direct reprogramming bypasses the stem cell stage of its iPSC-based predecessor and produces a single cell type. These cells retain their aging phenotype with no clonal variability (Mertens et al., 2015). However, an important caveat of direct reprogramming is a poor reprogramming efficiency of 1-5%.

Although answering many caveats of the iPSC technology, directly reprogrammed neurons are a finite resource. They are post-mitotic and cannot be cryopreserved for further research purposes, increasing the need for a constant supply of patient fibroblasts. Induced neural

progenitor cells (iNPCs) introduced by Meyer and Ferraiuolo (2014) provide an alternative to directly reprogrammed cells. This technology yields tripotent progenitor cells limited to the neural lineage only, but the proliferating iNPCs can be cryopreserved. Further differentiation of these progenitors into neuronal cells of interest is much faster when compared to iPSC differentiation (Meyer et al., 2014). Moreover, just like their directly reprogrammed counterparts, cells differentiated from iNPCs retain their ageing phenotype (Gatto et al., 2021). Importantly, iNPCs recapitulate important pathophysiological features of ALS, such as patient astrocyte toxicity in a co-culture system (Stopford et al., 2019), TDP-43 mislocalisation, fragmentation and aggregation, discussed later in Chapter 3 of this work.

Although *in vitro* models helped us uncover many pathological mechanisms of ALS, a remaining caveat of *in vitro* modelling is the fact that only one cell type can be studied at one time. In a co-culture scenario, since neurons are grown on an astrocyte feeder layer, temporal interplay between original and secondary events is masked (Rojas et al., 2015). Moreover, many overexpressing or constitutively active models do not reflect faithfully the pathology of ALS, as one specific feature of the disease is exaggerated in any given model. This means that relatively low expression levels of certain pathological hallmarks of ALS might be too low to detect at an endogenous level, as antibodies and commercial kits are often tailored to perform well in overexpressing models. To that end, a creation of a co-culture modelling system which could accommodate several disease cell types at once and expressing levels of targets of interest at an endogenous level would allow for a more thorough approach to model a disease in a dish.

1.3 Common mechanisms in neurodegeneration

Although vastly different in terms of their aetiologies, symptoms, genetics, cellular pathologies, clinical manifestations, outcomes, and treatments needed, mechanistic domains of many neurodegenerative diseases overlap. The following section will discuss some of the most common pathophysiological mechanisms observed in CNS disorders: neuroinflammation, protein aggregation, autophagy dysfunction, and disruption to normal mitochondrial function.

1.3.1 Inflammation

Neuroinflammation is characterised by a change in phenotype of microglia from anti-inflammatory (M2) to pro-inflammatory (M1). This shift can be a result of a direct insult or

injury to the CNS tissue, such as the one occurring in stroke. Several lines of evidence, however, implicate microglial pro-inflammatory phenotype as a cause of numerous neurodegenerative diseases. Change of microglial size to hypertrophic microglia has been observed pre-symptomatically at sites of marked cell loss in *in vivo* models of Alzheimer's disease (AD), Parkinson's disease (PD), and ALS, suggesting that inflammation of the nervous tissue is an event pre-dating the disease onset (Cooper-Knock et al., 2012). Whilst it can be a sign of a healthy system responding to an infection, chronic inflammation leads to further cell damage and loss. Moreover, astrocytes are also active contributors to neuroinflammation, primarily via the release of numerous pro-inflammatory cytokines.

1.3.2 Protein aggregation

Aberrant protein homeostasis has been described as a feature of multiple neurodegenerative diseases. The resulting protein misfolding often leads to formation of cytoplasmic aggregates, which overburden the cell and may contribute to cell death. Cytoplasmic aggregation of TDP-43, described in section 1.1.3.3, is a pathological feature of the ALS-FTD disease spectrum. In AD, amyloid beta (Aβ) and tau protein deposits are observed in both neurons and glia, whereas α-synuclein protein deposits form characteristic Lewy bodies in PD. Large cytoplasmic inclusions of mutant huntingtin protein are also observed in Huntington's disease (HD; Carty et al., 2015). These disease hallmarks posed an attractive therapeutic target for many years. Numerous pieces of evidence, however, show that presence of these aggregates or their removal does not prevent neuronal cell death, improve motor or cognitive functions, or disease prognosis (Barmada et al., 2010; Schneider, 2019). Instead, modulation of underlying mechanisms causing protein aggregation might be a promising therapeutic strategy (Singh, Dutta & Modi, 2017).

1.3.3 Autophagy

As described in the previous section (1.3.2), protein aggregation occurring in disease can have detrimental effects on normal cell function and has in several cases been linked directly to cell death causation. Lack of appropriate clearance of aggregated or misfolded proteins can further exacerbate this effect. Two pivotal cargo clearance mechanisms in the cell, autophagy and UPS work in synergy to ensure cell health by degrading aberrant proteins, mitochondria and other organelles. It is not uncommon, however, for either or both of these processes to become dysfunctional in neurodegeneration.

Autophagy (figure 1.3), also known as programmed cell death II, is a cell's internal housekeeping process designed to target aberrant cargo for lysosomal degradation. In a healthy organism, rough ER structure known as an omegasome is a site of phosphatidylinositol 3-phosphate (PI3P) activation, which subsequently recruits autophagy effector proteins. Conversion of microtubule-associated proteins 1A/1B light chain 3B (LC3) from a soluble (LC3-I) into a lipidated (LC3-II) form marks the start of the autophagophore formation, a membranous structure which expands around and envelops the sequestered cargo. The autophagy receptor p62 binds to the cargo and LC3-II, serving as a scaffold for the autophagophore formation. Fully formed autophagophores, called autophagosomes, fuse with degradation enzymes-containing lysosomes. Thusly formed autolysosomes are a contained site of cargo degradation.

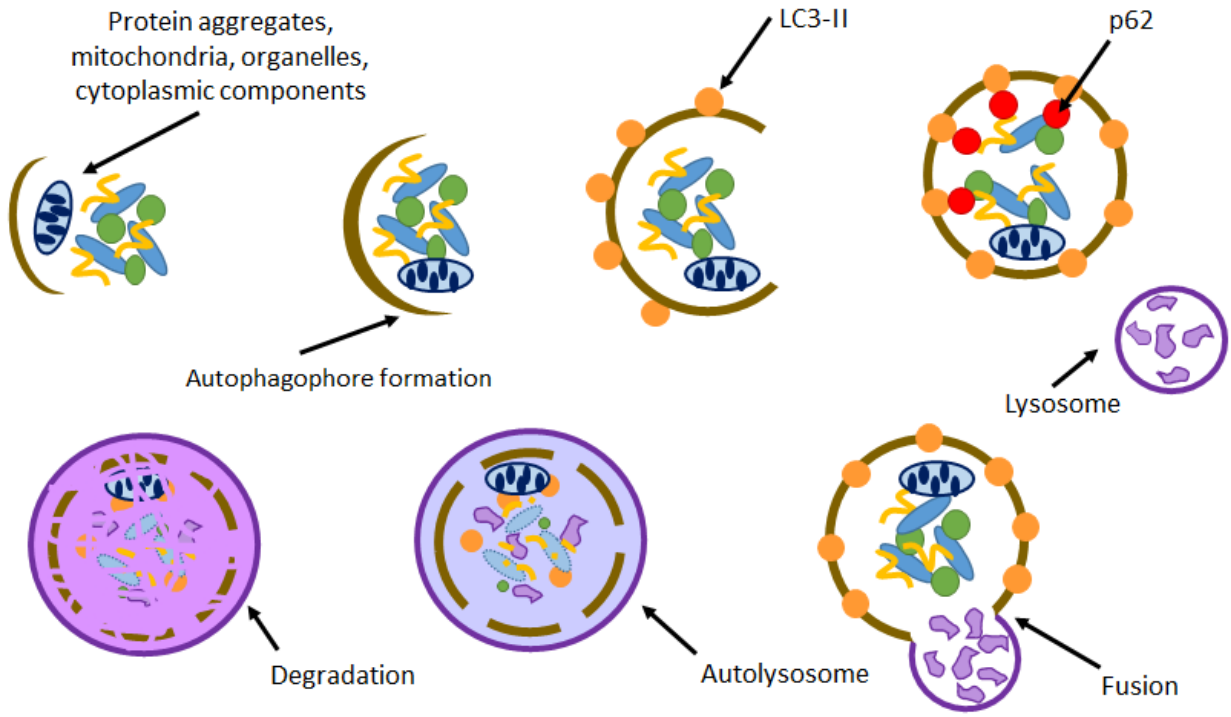

Figure 1.3 Autophagy cascade in healthy cells

Upon induction of an autophagic flux, a structure named autophagophore begins to envelop the cargo to be degraded. Autophagophore membrane undergoes elongation as LC3-I undergoes conversion to LC3-II, which in turn lines the phagophore membrane. The resulting autophagophore also contains p62, which is an autophagy receptor binding to both the cargo and LC3-II. Under basal conditions, autophagophore forms an autolysosome by fusing with lysosomes. It is in that final structure that degradation of the cargo takes place.

It is challenging to say whether targeted autophagy induction has a clear, stand-alone effect on disease pathogenesis, as, apart from protein catabolism, autophagy also plays a role in mitochondrial turnover (via a process called mitophagy, see section 1.3.3.1) and in global cellular energy balance (Laplante & Sabatini, 2012). The multifaceted aspects of this biological process make autophagy an important player and potential therapeutic target in ALS and many other neurodegenerative diseases.

Interestingly, previous lines of evidence from transgenic mice and neuronal *in vitro* models of HD gave rise to a speculation that neurons have a limited capacity to perform autophagy (Fox et al., 2010; Tsvetkov et al. 2010; Roscic et al., 2011). Moreover, autophagy function in neurons might be regulated via non-cell autonomous mechanisms, as glia conditioned medium had a pro-autophagy effect in HD transgenic mice (Perucho et al., 2013), and the opposite effect in *in vitro* ALS models (Madill et al., 2017), thus indicating that therapeutics aiming at modulating autophagy are likely to have an effect through non-neuronal cells.

To date, multiple lines of evidence have shown cytoplasmic α-synuclein deposits (Lee et al., 2004; Gao et al., 2019) in PD and cytoplasmic TDP-43 fragments and aggregates to be cleared via autophagy in neurons and neuronal cells in ALS (Barmada et al., 2014). Indeed, repair of autophagy dysfunction in ALS has been shown to be beneficial for progression, survival (Staats et al., 2013), and presence of pathological hallmarks in mutant SOD1 animals (Li et al., 2015) and in a *Drosophila* model of TDP-43 pathology (Cheng, Lin & Shen, 2015).

1.3.4 Mitochondrial dysfunction

Mitochondria are the cell's resident producers of adenosine triphosphate (ATP) via the process of oxidative phosphorylation, are involved in calcium homeostasis, phospholipid biogenesis and apoptosis (Smith et al., 2019). Post-mitotic cells such as neurons, which last an individual's lifetime, have a high metabolic rate and are vulnerable to accumulation of stressors and damage. Therefore, healthy mitochondria are essential for their survival. Disruptions in the normal mitochondrial function can lead to or exacerbate neurodegeneration. Several mitochondrial genes have to date been identified as carrying mutations resulting in CNS disorders. Perhaps the most well-known example, parkin, currently accounts for 50% cases of familial PD (Pickrell & Youle, 2015).

Thus far, only one genetic mutation linked to ALS has been shown to have an exclusively mitochondrial function. CHCHD10 (table 1.1) is located between the inner and the outer membrane of the mitochondria. The mutation affects the structure of cristae and is characterised by a severe bioenergetic deficit and an impaired activity of all electron transport chain (ETC) complexes (Bannwarth et al., 2014; Genin et al., 2016). However, changes in the cristae structure are also observed in C9orf72, TDP-43^{A513T} and SOD1^{G93A} mutants (Genin et al., 2016) and activity of all ETC complexes was found to be reduced in post-mortem spinal cord tissue of sALS patients (Borthwick et al., 1999; Wiedemann et al., 2002), indicating widespread phenotypic and functional changes in mitochondria of ALS patients regardless of a genetic mutation. Furthermore, mitochondrial membrane potential (MMP) is increased in sALS (Kirk et al., 2014) and C9orf72-patient fibroblasts (Onesto et al., 2016), which might be a compensatory mechanism aiming to counteract the decrease in ATP production. However, the opposite was observed in iPSC-derived motor neurons of C9orf72 patients (Onesto et al., 2016) and in HEK293 cell lines overexpressing wild-type TDP-43 (Deng et al., 2015).

Round, swollen mitochondria were amongst the first pieces of evidence for mitochondrial damage in patient motor neurons (Atsumi, 1981; Sasaki & Iwata, 2007). Indeed, further studies showed that transgenic TDP-43^{M337V}, TDP-43^{Q331K} and TDP-43^{A315T} mice carry fragmented, aggregated mitochondria (Magrané et al., 2014). Similar mitochondrial phenotype was observed in motor neurons of SOD1^{G93A} mice (De Vos et al., 2007), as well as in early symptomatic SOD1^{G37R} and SOD1^{G85R}, where mitochondrial clusters along the length of the axon were also found (Vande Velde et al., 2011). iPSC-derived motor neurons of C9orf72 patients also presented a rounded, swollen mitochondrial phenotype (Dafinca et al., 2016), indicating a universal disruption of mitochondrial structure in ALS.

Mitochondrial fission and fusion are natural processes and are controlled by dynamin-related protein 1 (DRP1) and mitochondrial fission 1 (Fis1), mitofusin-1 (Mfn1), mitofusin-2 (Mfn2) and optic atrophy protein 1 (Opa1) proteins respectively. Fragmented appearance might be a result of exacerbated fission, which has been observed in several ALS models. SH-SY5Y and NSC-34 cells expressing SOD1^{G93A} expressed increased levels of DRP1 and decreased expression of Opa1 (Ferri et al., 2010). Similar findings were described in spinal cord tissue of mice carrying the same mutation, although their levels Fis1 and DRP1 phosphorylated at its serine 616 site, which is responsible chiefly for mitochondrial fission orchestration, were

unchanged (Liu et al., 2013). Fibroblasts of TDP-43^{A38T} patients also showed a trend towards an increase in fission, whereas the opposite was true for C9orf72 fibroblasts, whose increased Mfn2 levels despite clear mitochondrial fragmentation might indicate a compensatory mechanism (Onesto et al., 2016).

Production of ROS, which is a natural by-product of oxidative phosphorylation, becomes exacerbated in ALS. Markers of ROS damage were found in CSF and serum of sALS patients and their post-mortem tissue (Bogdanov et al., 2000; Mitsumoto et al., 2008; Simpson et al., 2004; Smith et al., 1998). In SOD1^{G93A} mice, oxidation of ETC complexes and ATP synthase mRNAs was observed prior to motor neuron degeneration (Chang et al., 2008). This suggests that the inability of mitochondria to meet the energy demands of neurons is one of the causes of motor neuronal death in ALS.

Several lines of evidence report interaction of ALS-associated proteins with mitochondria, which appear to be an important driver of mitochondrial damage. Poly-GR species of DPRs were found to bind to ribosomal proteins of mitochondria (Lopez-Gonzalez et al., 2016), whilst isolation of a cell mitochondrial fraction found it to be enriched in C9orf72 protein (Blokhuis et al., 2016), whilst SOD1 accumulates in the intermembrane space and reduces ETC activity (Ferri et al., 2006; Vijayvergiya et al., 2005). ALS-associated mutations in optineurin, a mitophagy receptor, prevents autophagosome formation, causing mitophagy dysfunction and subsequent accumulation of damaged mitochondria (Moore & Holzbaur, 2016). Moreover, mutant SOD1 aggregates have been found to sequester optineurin, thus preventing the autophagic flux (Tak et al., 2020). In models harbouring TDP-43 mutations, TDP-43 accumulates in mitochondria and binds to complex 1 subunits mRNA, eventually leading to their disassembly, which is caused by specific sequences in TDP-43 which target mitochondria (Wang et al., 2016). This consequently leads to exacerbated ROS production, decreased oxygen consumption, increased MMP and decreased ATP release (Wang et al., 2016). Whether the binding of pathogenic ALS protein to mitochondria precedes mitochondrial dysfunction or is a result of it, is still a subject of investigation.

TDP-43 is ubiquitinated by parkin, which promotes its nuclear translocation. Interestingly, loss of TDP-43 from the nucleus and its cytoplasmic aggregation in spinal cord motor neurons of sALS patients lead to a decrease in total parkin levels (Lagier-Tourenne et al., 2012), suggesting a close mutually regulatory mechanism. Other proteins, such as Abelson murine

leukaemia viral oncogene homolog 1 (Abl1, also known as cAbl), which have recently been found to be overexpressed in ALS patients, serve as a substrate for parkin and their relationship in ALS warrants a closer investigation.

1.3.5 Abl1 activation

Although not canonically described as a contributor to neurodegeneration, Abl1 is a member of Abl non-receptor tyrosine kinases belonging to a group of Src/Brc proto-oncogenes. Alongside its orthologue Arg (Abl2), it is involved in signalling pathways regulating cytoskeletal dynamics, cell proliferation, and membrane trafficking (Khatri et al., 2016). Its role in several types of carcinomas, chiefly stomach cancers, has been well described. Recent reports have implicated Abl1 as a player in neurodegeneration. Inhibition of active, phosphorylated Abl1 (pAbl1) has resulted in an improved motor function of MPTP animal model of parkinsonism whilst restoring levels of available dopamine precursors, a finding which has stimulated a currently ongoing clinical trial (ClinicalTrials.gov identifier number NCT02954978) for repurposing of Abl1 inhibitor compounds for PD (Karuppagounder et al., 2014). Since parkin is a direct substrate of Abl1 (Ko et al., 2010), modulation of Abl1 signalling has been shown to be beneficial for mitochondrial function in PD (Abushouk et al., 2018).

Abl1 is involved in cytoskeleton remodelling via phosphorylation of tau. Interplay with tau made Abl1 an obvious exploratory target for AD. Vargas et al. (2014) has found Abl1 to be abundant in dendritic spines, suggesting a role in synaptic function. Importantly, synaptic damage caused by Aβ oligomers observed in AD was found to be directly mediated by an interplay between Abl1 activation and ephrin type-A receptor 4 (EphA4) activation. EphA4 activation has later been shown to be detrimental in $SOD1^{G93A}$ mice and its knockdown improved motor neuronal survival, which also translated to an improved motor performance (Zhao, Cooper, Boyd, & Bartlett, 2018). Ephrine signalling, which includes proteins responsible for axon guidance and dendritic structure, has other of its members showing alteration in ALS. Ephrin type-B receptor 1 has been shown to be upregulated in diseased motor neurons (Tyzack et al., 2017), whereas a reduction in ephrin-A5 worsens ALS progression (Rué et al., 2019). Abl1 inhibition in AD transgenic mice has resulted in a rescue of synaptic loss in the hippocampi of these animals (Estrada et al., 2016; Vargas et al., 2014). In summary, using Abl1 inhibitors to target the ephrin signalling pathway may help rescue motor neuronal survival.

A landmark study by Imamura et al (2017) has focused on repurposing Src/Brc inhibitors, most of which directly target Abl1, for ALS. The high-throughput drug screening of these compounds on directly reprogrammed motor neurons has noted an improved survival of neurons and improved axonal and dendritic morphology upon Abl1 inhibition. Moreover, this drug treatment has resulted in correction of several pathological and mechanistic hallmarks of ALS, including TDP-43 proteinopathy and autophagy regulation, thus suggesting that Abl1 might be a promising therapeutic target for ALS.

1.4 AI in drug discovery and repurposing

Development of new drugs is a costly and time-consuming process (Williams et al., 2015). Drug repurposing, a method of applying existing drugs to new diseases, poses an attractive alternative to novel molecule discovery thanks to the approved safety profiles and significantly shortened development times (Ashburn & Thor, 2004). However, validation of a new repurposing candidate in a context of a different disease can also pose many challenges from a clinical and cost-related perspective (Li et al., 2017). Both the discovery of new drugs and drug repurposing processes could greatly benefit from an automated system that identifies a biological process to be targeted and analyses the docking sites of a given target to create a specific drug. Moreover, as the current data indicates, most clinical trials fail at stages II and III, with low therapy efficacy and lack of understating of the drug action being cited as the main reason for those failures (Harrison, 2016; Townsend & Arron, 2016). Indeed, ALS drug discovery also has been plagued by many clinical trial failures (Mitsumoto et al., 2014; Petrov et al., 2017). Thorough exploration of the drug's downstream, upstream, and off-target effects can help avoid those issues at a much earlier stage.

1.4.1 *In silico* drug modelling

As early as 1869, Alexander Crum Brown described a physiological response of and to a chemical compound as being a function of its chemical constitution, thus giving rise to the idea that properties of compounds can be predicted without a need to synthesise them (Sellwood et al., 2018). Indeed, the most important question in molecular design remains 'what type of chemical structure will produce a compound with a desired list of properties?'. Machine learning algorithms have shown to be of use in new molecule design, aiming to model a new drug around a known disease target faster and more efficiently (King et al.,

1992). Supervised machine learning algorithms can be applied to quantitative structure-activity relationship methods (QSAR; Hansch et al., 1962) where, based on a set of labels within the dataset, AI can predict the polypharmacological profile of the compound. This then allows for a multiparameter optimisation, i.e. an evolution and optimisation of chemical structures in accordance with a set of defined objectives (Klucznik et al., 2018; Segler et al., 2018). It can also allow for minimisation of toxic side effects by making the molecule receptor-specific, more soluble, and activating key molecule targets at higher rates (Chao et al., 2014).

Binding of a peptide or a drug to a chosen target can be modelled using AI systems via docking simulation, which then automatically selects the best hits (Nishiyama, 2017). Such docking simulations and target-based virtual screenings (Qingliang Li & Shah, 2017) are based around creating a 3D structure of the intended target and using algorithms to predict drugs' binding affinities (Scarpino et al., 2018). Machine learning methods can improve upon this established model by making associations between a target and group of drugs with similar structures, thus predicting drug-target interactions faster and more efficiently. This has led to a creation of methods such as KronRLS (Pahikkala et al., 2015).

Moreover, AI systems can model release behaviour of biodegradable nanoparticles of varying concentrations and sizes in various media and emulsions, thus allowing for a better understanding of such molecules' behaviour in a human organism (Baghaei et al., 2017). Artificial neural networks (ANNs) built around such systems can also predict the response of an organism to the given concentration of particles depending on individual genetic differences, allowing for a study of novel therapeutic approaches on a personalised medicine basis (Baghaei et al., 2017). It is important, however, to highlight that reliable prediction of important drug properties, chiefly its biological activity, remains an issue. Some methods, such as computer-aided synthesis planning (Vléduts, 1963), can help prioritise a design of drugs which are more readily synthesisable, or find alternative ways of creating a desired chemical (Sellwood et al., 2018).

The field of drug repurposing has also benefited significantly from *in silico* drug modelling approaches. A recently described AI tool termed 'process pharmacology' puts disease and its biology at the fore of drug research and therapy, treating identified targets as a link between the disease and the drug. Based on the genetic factors that play a part in the process to be pursued, an association is made between a drug and the biological process of interest (Lötsch

& Ultsch, 2016). This and similar methods utilise databases of patient information, disease biology, and drugs currently available on the market, allowing for an exploration of new therapies using drugs already approved for a use in humans (Lötsch & Ultsch, 2016). Such application of AI to medical research has a potential to significantly improve the efficacy of novel therapeutics discovery, especially because the question of compound toxicity on the patients has been addressed.

Although very promising, applications of process pharmacology and other *in silico* drug modelling are still in their infancy in terms of practical applications and readiness for use in clinical scenarios. Nevertheless, the technological challenges should be resolved with an increased utilisation of the methods described here, as AI algorithms learn and improve with time.

1.4.2 Drug synergy

The wealth of literature and datasets available can help AI systems build algorithms essential for understanding not only drug metabolism and behaviour in the organism, but also interactions between different molecules, which can result in adverse reactions. One such model studied drug-drug interactions based on known adverse compounding drug effects, e.g. aspirin and warfarin taken together may result in bleeding. This method, termed Causal Association Rule Discovery, has been found to be more efficient that previously used association rule mining algorithms (Cai et al., 2017). Beyond studying drug synergy to avoid side effects, AI can also be used to identify drug combinations based on their polypharmacological profiles to increase their therapeutic potential. Although this approach is still in its infancy, one such study used an AI-powered Therapeutic Performance Mapping System to find a neuroprotective treatment for nerve trauma (Romeo-Guitart et al., 2018). Out of a total of 5440 drugs and resulting 15 billion possible combinations, computational tools have selected acamprostate (used to treat alcohol dependency) and ribavirin (an anti-viral compound) co-treatment in *in silico* tests as the best candidate. Indeed, pre-clinical *in vivo* studies confirmed their beneficial synergistic effect on nerve regeneration and anti-inflammatory action on sirtuin 1 (Romeo-Guitart et al., 2018).

Such AI applications to medicine and pharmacology are important not just from the side effect avoidance point of view, but also as a tool decreasing the patient waiting time for a treatment and can lead to an introduction of new therapies where there previously were few or none.

Moreover, *in silico* modelling of a drug mode of action (MOA) in the context of a new disease or a drug synergy avoids costly and time consuming *in vitro* and *in vivo* experiments on multiple candidates, not all of which will be successful.

1.4.3 AI-powered literature screening

Research output across multiple disciplines that is published on a daily basis surpasses by far our ability to ingest and make sense of all available information. Access to a machine learning system that scans available published information and extracts relevant data, would be of great help in the research community. Such a system would not only help create a comprehensive picture of discoveries as they are being made but would also open an opportunity to make new ones by drawing our attention to previously unconsidered connections and patterns within published data. However, published scientific literature is in its native form made to be read by humans only and is thus classed as an unstructured data source for machine learning algorithms (Winograd, 1971). Natural language processing (NLP) technology in AI provides a solution to this issue by transforming written language into a modality that is readily analysed by AI algorithms (Rindflesch & Fiszman, 2003). This technology is undergoing constant refinements to increase the rate of scientific discoveries. For example, a large-scale knowledge network created by NLP, known as the Semantic MEDLINE Database (Kilicoglu et al., 2012), serves as a *bona fide* interpreter of the scientific literature for machine learning purposes. It has recently been utilised to predict the types of data necessary to evaluate the repurposing opportunities for compounds (Mayers et al., 2019), which in the future can help increase the efficiency and speed of drug repurposing processes further.

Although of significant use in drug discovery, AI-powered literature screening can also be used to unveil new pathophysiological or genetic components of diseases. IBM's AI system, Watson®, has been used to help predict novel RBP-ALS associations based on a bulk of data published after 2013 (Bakkar et al., 2018). IBM Watson® was able to scan the breadth of published literature, extract and match any RBPs of interest to ALS. Based on this initial documentation, Watson® developed a conceptual semantic data model for the known RBP-ALS connections and subsequently applied this model to the set of identified novel candidates. IBM Watson® successfully validated a set of RBPs with a well-established role in ALS, such as TDP-43 and FUS, and, conversely, RBPs identified as the least likely to contribute

to ALS were indeed found to have no association with the disease based on a further literature search (Bakkar et al., 2018). Novel promising findings were validated in ALS patient tissue samples and successfully identified caprin-1 as a new RBP associated with ALS. Coincidentally, this finding was independently investigated and described by Blokhuis et al. (2016) as the Watson study was taking place, which nevertheless highlights the benefits of the system.

Although based on existing knowledge, mining existing literature and resources contained within databases can help unveil non-obvious connections between diseases, targets, and drugs, hence improving the efficacy and speed of drug discovery and repurposing. Machine learning systems can facilitate those improvements.

1.4.4 Use of OMICS data

Data with various OMICS modalities presents a wealth of information on diseases and drug modes of action that is unparalleled. Increasingly, this data is converted into structured information, such as databases, which makes the information readily accessible and readable by machine learning algorithms, as each described variable, such as gene name, has another variable assigned to it, such as a fold change. With a set of simple commands, a list of gene perturbations caused by a drug can be interrogated to extrapolate meaningful relationships between a target of interest and a drug, as well as unexpected interactions that might lead to side effects. Specialist computational analysis platforms have been created in order to make the most of the gene expression profiling data available. One of such resources, DrugGenExnet, aims to improve the process of drug repurposing by aiming to predict drug polypharmacology in the context of a specific disease based not just on the primary drug target, but all predicted biological processes involved (Issa et al., 2016). Several recent studies have utilised available transcriptomic data to find repurposing candidates for various diseases of the CNS. Zhao & So (2018), for example, used a machine learning algorithm trained in identifying drug-gene-disease relationships outside of the drug's established MOA and applied it to a set of transcriptomics profiles to identify repurposing candidates for schizophrenia, depression, and other anxiety disorders. This is especially important when a repurposing candidate is a drug previously used in cancer cells, as its effect in the CNS might be different due to different levels of target expression or presence (or indeed absence) of important receptors necessary for the drug to exert its function.

Outside the realm of drug discovery, transcriptomic profiles have been interrogated by machine learning technologies to explore the links between proteins encoded for by genes associated with neurodegenerative diseases in order to build a comprehensive picture of the overlap between molecular connections in CNS disorders (Garcia-Vaquero et al., 2018). This cross-disease analysis approach has, for example, confirmed the molecular similarities between ALS and SMA (Garcia-Vaquero et al., 2018).

1.4.4.1 Cancer transcriptomics

Field of cancer research pioneered the use of transcriptomics data obtained from cell lines and human tissue to not only better understand the genetic and molecular underpinnings of tumorigenesis and cancer progression, but also in oncology compound discovery (Sirota et al., 2011). Early use of cancer genomics for drug discovery purposes has, for example, seen an introduction of BCR-Abl and EGF receptor inhibitors onto the market (Clarke et al., 2001). Drug efficiency screenings conducted on cancer cell lines and the abundance of transcriptomic datasets they created have been amassed into publicly available databases which now serve as a valuable resource for further studies. Recently, for example, such datasets of cancer cell line transcriptomes have been used to assess drug toxicity based on landmark genes and pathways affected (Li, Tong, Roberts, Liu, & Thakkar, 2020).

Drug discovery in cancer remains notoriously challenging even with the use of transcriptomics, as every cancer entity differs dramatically at the transcriptomic level due to a variety of genetic and environmental factors (Clarke et al., 2001). Nevertheless, advancements in cancer transcriptomics helped inform drug discovery and repurposing studies across a variety of diseases and provided an invaluable tool for future trials.

1.4.4.2 Using transcriptomics data to uncover drug modes of action

Understanding the MOA of a drug in one specific disease can help make educated assessments with regards to drug repurposing. Computational polypharmacology platforms, which rely on existence of robust cell gene expression profiles, have established that drug indications for diseases can be predicted from disease-specific genetic signatures of other disorders, as they unveil target and biological processes in need of modulation (Gottlieb et al., 2011). Other platforms, which operate on an increasingly high-throughput basis, aim to improve upon the standard drug discovery methods by including transcriptional profiling of

cells before and after treatment with various perturbagens at an ever decreasing cost (Ye et al., 2018).

1.5 Summary of aims

The non-cell autonomous component of ALS pathology has been well-described, significantly implicating astrocytes as drivers of ALS progression. The fundamental hypothesis driving this project relies on the astrocyte toxicity contributing to motor neuron death in ALS and the drugs' ability to dampen that toxic effect, thus rescuing motor neuron survival. In the patient, this effect may translate into slowing of disease progression and/or delay in symptom onset.

Unfortunately, two drugs currently marketed for ALS, riluzole and edaravone, offer very modest extension in survival (2-3 months on average) and patients often report unpleasant side effects, which frequently drive them to abandon the treatment. From around 60 molecules investigated during clinical trials for ALS in the last 23 years, the vast majority have failed due to lack of significant improvement to patients' condition, safety concerns, or lack of biomarkers to determine whether the drug had even reached the target. Due to the aggressive and devastating nature ALS, overcoming these issues is of primary importance.

With the aim to overcome at least some of these issues, we have set up a collaboration with BenevolentAI, a biotech company which specialises in application of machine learning technologies to find novel targets and treatments for diseases which currently have limited or no pharmacological interventions available.

Through this collaboration we have identified 2 drugs, gefitinib and nilotinib, which indeed had neuroprotective effects in our *in vitro* model of ALS (described in sections 3.1.2 and 4.1.2).

The underlying hypothesis of this project is that AI can identify drugs targeting disease-relevant pathways in ALS.

In order to test our hypotheses, I will address the following aims:

Aim 1: to uncover the function of gefitinib in iAstrocytes and its mode of action in ALS.

Aim 2: to identify the function of nilotinib in iAstrocytes and its mode of action in ALS.

Aim 3: to compare the polypharmacological profiles of gefitinib and nilotinib in relation to their effectiveness in our *in vitro* model of ALS.

2 Materials and Methods

2.1 Materials

All plastics for cell culture were purchased from Greiner Bio One, unless otherwise specified.

All other reagents and chemicals were purchased as follows:

2.1.1 General reagents

Table 2.1 General reagents and stock solutions.

Reagent	Supplier
(4-(2-hydroxyethyl)-1-piperazineethanesulfonic acid) (HEPES)	Sigma
Acetic acid	Fisher Chemicals
Acrylamide, 30%	Geneflow
Ammonium persulphate (APS)	Sigma
β-mercapthoethanol, pH 6.8 (50 mM)	Sigma
Bicinchoninic acid (BCA) assay kit	Thermo Fisher
BLUeye pre-stained protein ladder	Geneflow
Bovine serum albumin (BSA), powder	Sigma
Bromophenol blue	Fisher
Cell lysis buffer 10X	Cell Signalling Technologies
Diethyl Pyrocarbonate (DEPC)	BioChemica
Dithiothreitol (DTT)	Invitrogen
Dried skimmed milk	Marvel
Duolink® *In Situ* Orange Starter Kit Mouse/Rabbit	Sigma-Aldrich
Ethanol, 100%	Fisher Chemicals
Ethylenediaminetetraacetic acid (EDTA)	Thermo Fisher
EZ-ECL Enhanced Chemiluminescence Detection Kit	Biological Industries
Glycerol	Fisher Chemicals
Glycine	Fisher Chemicals
Hoechst 33342 Trihydrochloride, Trihydrate, 20 nM	Life Technologies
Methanol, 100%	Fisher Chemicals
Normal horse serum	Gibco
Nuclease-free water	Ambion
Paraformaldehyde, 40%	Fisher Chemicals
PathScan® phospho-c-Abl (panTyr) Sandwich ELISA kit	Cell Signalling Technologies
PathScan® Phospho-c-Abl (Tyr412) Sandwich ELISA Kit	Cell Signalling Technologies
Phenylmethanesulfonyl fluoride (PMSF)	Sigma
Phosphate buffered saline (PBS)	Oxoid
PhosSTOP™	Roche
cOmplete™ proteinase inhibitor cocktail (PIC)	Roche
Protein assay dye concentrate	BioRad
ProtoGel 30% (w/v) Acrylamide: 0.8% (w/v) Bis-Acrylamide Stock Solution	GeneFlow
Sodium azide	Thermo Fisher
Sodium chloride (NaCl)	Fisher Chemicals

Sodium dodecyl sulfate (SDS)	Fisher Chemicals
2x SYBR Green qPCR Master Mix	Bimake
SYPRO® Ruby protein stain	Thermo Fisher
Trisaminomethane hydrochloride (Tris-HCl)	Melford
Triton™ X-100	Sigma
Trizma®	Fisher Chemicals
Tween®20, pH 7.6	Sigma

2.1.2 Cell culture and reagents

Table 2.2 Tissue culture reagents.

Reagent	Supplier
Accutase™	Gibco Life Technologies
β-mercapthoethanol, pH 6.8	Sigma
B-27 supplement (50X)	Gibco Life Technologies
Bafilomycin A1	Alfa Aesar
Brain-derived neurotrophic factor (BDNF)	PeproTech
Carbonyl cyanide m-chlorophenyl hydrazine (CCCP)	Sigma
Cilliary neurotrophic factor (CNTF)	PeproTech
N-[N-(3,5-Difluorophenacetyl)-L-alanyl]-S-phenylglycine t-butyl ester (DAPT)	Tocris
Dimethyl sulfoxide, anhydrous, ≤99.9% (DMSO)	Sigma Aldrich
Dulbecco's Modified Eagle's Medium (DMEM) (4500 mg/ml glucose, L-glutamine, sodium bicarbonate)	Sigma
Dulbecco's Modified Eagle's Medium/F-12 (1:1) + GlutaMAX-I (DMEM/F-12)	Gibco Life Technologies
DNase I	Sigma
Embryonic stem cell serum	Gibco Life Technologies
F-12 medium	Gibco Life Technologies
Foetal bovine serum (FBS)	Life Science Products
Forskolin	Sigma
Gefitinib	Cayman Chemicals
Glial cell-derived neurotrophic factor (GDNF)	PeproTech
Glucose powder	Sigma
Human fibroblast growth factor, basic (bFGF)	PeproTech
Human plasma fibronectin	Millipore
Iscove's Modified Dulbecco's Medium (IMDM)	Gibco Life Technologies
KnockOut DMEM	Gibco Life Technologies
KnockOut serum replacement	Gibco Life Technologies
L-glutamine (200 mM)	Gibco Life Technologies
Leukaemia inhibitory factor (LIF)	Millipore
Minimum Essential Medium Non-Essential Amino Acids (MEM NEAA) (100X)	Gibco Life Technologies
Minimum Essential Medium (1X), Phenol red-free	Gibco Life Technologies
N2 supplement (100X)	Gibco Life Technologies
Nilotinib	Sigma
Papain	Sigma
Penicillin (5000 Units/ ml) –Streptomycin (5000 Units/ ml) (PS)	Lonza BioWhittaker

Phosphate buffered saline (PBS)	Oxoid
Rapamycin	Cayman Chemicals
Retinoic acid (RA)	Sigma
Smoothened agonist (SAG)	Millipore
Sodium pyruvate (100 mM)	Sigma
Tetramethylrhodamine methyl ester (TMRM)	Invitrogen
Torin 1	Tocris
Trypsin (10X)	Gibco Life Technologies

2.1.3 Cell lines

Table 2.3 Induced neural progenitor cell (iNPC) lines.

Sample	Mutation	Sex	Ethnicity	Age at biopsy collection	Onset to death (months)
CTR_AG08620	-	F	Caucasian	64	-
CTR_CS-14	-	F	Caucasian	52	-
CTR_155	-	M	Caucasian	40	-
CTR_155v2	-	M	Caucasian	40	-
CTR_161	-	M	Caucasian	31	-
CTR_3050	-	M	Caucasian	55	-
C9_78	C9orf72	M	Caucasian	66	31.7
C9_183	C9orf72	M	Caucasian	50	27
C9_201	C9orf72	F	Caucasian	66	19.4
sALS_009	sALS	F	Caucasian	61	21
sALS_12	sALS	M	Caucasian	29	90
sALS_17	sALS	M	Caucasian	47	72

2.1.4 Real-time quantitative polymerase chain reaction (RT-qPCR) primers

Table 2.4 Primers used for RT-qPCR. All primers listed were used at a final concentration of 250 nM.

Gene name	Gene symbol	Sequence (5' – 3')	Species	Supplier
Beta-actin	β-ACTIN	F: TCCCCCAACTTGAGATGTATGAAG	Human	Sigma
		R: AACTGGTCTCAAGTCAGTGTACAGG		
Abelson Tyrosine-Protein Kinase 1	ABL1	F: CTTCAGCGGCCAGTAGCAT	Human	Sigma
		R: GTGCAACGAAAAGGTTGGGG		

Epidermal growth factor receptor	EGFR	F: CGCAGTTGGGCACTTTTGAA R: TCCCAAGGACCACCTCACA	Human	Sigma
Cyclin-G2	CCNG2	F: GATCGTTTCAAGGCGCACAG R: CAGGTATCGTTGGCAGCTCA	Human	Sigma

2.1.5 Primary and secondary antibodies

Table 2.5 Antibodies used for Western blotting immunofluorescence.

Protein	Species	Stock conc.	Dilution	Blocking	Membrane	Supplier, catalogue number
β-actin	Mouse	2.2 mg/ml	1:10,000	5% milk	Nitrocellulose	Abcam, ab6276
c-Abl	Rabbit	1 mg/ml	1:1000	5% milk	Nitrocellulose	Cell Signalling Technology, 2862
TDP-43 (C-terminal)	Rabbit	1µg/150µl	1:1000	5% milk	Nitrocellulose	ProteinTech, 12892-1-AP
DRP1	Mouse	1 mg/ml	1:1000	5% milk	Nitrocellulose	Abcam, ab56788
Phospho-DRP1 (ser616)	Rabbit	1 mg/ml	1:1000	5% BSA	Nitrocellulose	Cell Signalling Technology, 3455
Phospho-c-Abl (Tyr412)	Rabbit	1 mg/ml	1:1000	5% BSA	PVDF	Cell Signalling, 247C7
p62	Mouse	250µl/ml	1:800	5% milk	Nitrocellulose	BD Biosciences, 610833
LC3	Rabbit	1 mg/ml	1:1000	5% milk	Nitrocellulose	Novus Biologics, 2220
EGFR	Rabbit		1:1000	5% milk	Nitrocellulose	Cell Signalling, 4267
Phospho-EGFR (Tyr1068)	Rabbit		1:1000	5% BSA	Nitrocellulose	Cell Signalling, 3777

Table 2.6 Horseradish peroxidase (HRP)- conjugated secondary antibodies used for Western blotting immunofluorescence.

Secondary antibody	Stock concentration	Dilution (in 5% milk)	Supplier, catalogue number
HRP-conjugated α-mouse IgG (H+L)	1 mg/ml	1:5000	Promega, W402B

HRP-conjugated α-rabbit IgG (H+L)	1 mg/ml	1:5000	Promega, W401B

Table 2.7 Primary antibodies used for immunocytochemistry.

Protein name	Species	Stock concentration	Dilution	Supplier, catalogue number
Vimentin	Chicken	1 mg/ml	1:1000	Millipore, ab5733
TDP-43 (C-terminal)	Rabbit	1µg/150µl	1:200	ProteinTech, 12892-1-AP
Cleaved caspase-3	Rabbit	1 mg/ml	1:500	Millipore, AB3623
Phosphorylated TDP-43 (Ser409)	Mouse	1 mg/ml	1:100	Affinity Biologicals, AF7365
Ki67	Rabbit	1.04 mg/ml	1:1000	Abcam, ab15580

Table 2.8 Secondary antibodies used for immunocytochemistry.

Antibody	Species	Dilution	Supplier, catalogue number
Alexa Fluor α –chicken 488 IgG (H+L)	goat	1:1000	Thermo Fisher, Invitrogen, A-11039
Alexa Fluor α –rabbit 568 IgG (H+L)	goat	1:1000	Thermo Fisher, Invitrogen, A-11011
Alexa Fluor α –rabbit 488 IgG (H+L)	donkey	1:1000	Thermo Fisher, Invitrogen, A-21206
Alexa Fluor α –mouse 568 IgG (H+L)	donkey	1:1000	Thermo Fisher, Invitrogen, A-10037
Alexa Fluor α –mouse 488 IgG (H+L)	donkey	1:1000	Thermo Fisher, Invitrogen, A-21202

Table 2.9 Short hairpin RNAs (shRNAs) used for target knockdown experiments.

Target	Transgene	Backbone	Promoter	Viral titre	Tag	Targeting sequence	Supplier
Abl1	Human *ABL1* shRNA	Adenovirus	U6	9.6×10^9 PFU/ml	RFP	GCTGAAATCCACCAA GCCTTT	Vector Biolabs
RFP	DsRed2	Adenovirus	CMV	1×10^{10} IFU/ml	RFP	-	Vector Biolabs

2.2 Methods

2.2.1 Induced neural progenitor cell (iNPC) culture, maintenance and differentiation

Cell culture procedures were performed in class II microbiological cabinets, under sterile conditions. All cell types described below were grown at 37°C in a humidified incubator with 5% CO_2.

Prof. Pamela Shaw provided control (CS-14, 155, 155v2, 161, 3050) and C9orf72 patient fibroblast samples used for iNPC reprogramming from the University of Sheffield (study number STH16573, Research Committee reference 12/YH/0330). Prof Stephen J. Kolb provided sALS patient fibroblast samples from the ALS/MND Clinic, Department of Neurology, Ohio State University (OSU), Wexner Medical Center, Columbus, Ohio (Ethics number 04304AR). Control AG08620 fibroblast line was purchased from the Coriell Institute biobank under material transfer agreement (MTA). Informed consent was obtained from all subjects before sample collection.

2.2.1.1 iNPC culture

iNPCs were obtained via direct reprogramming of patient fibroblasts, according to the published protocol (Meyer et al., 2014) and were already available from previous work carried out by Dr Laura Ferraiuolo and Mr Allan Shaw.

iNPCs were grown as an adherent culture in a serum-free medium containing bFGF (see Table 2.10). During the regular maintenance, a medium change was performed once every 48 hours to replenish the bFGF and nutrients. iNPCs were passaged upon reaching 90% confluence and their maintenance was performed by myself, Mr Allan Shaw and Miss Lai Mei Wan.

Table 2.10 Composition of iNPC culture medium.

Reagent	Volume	Final concentration
DMEM/F-12 1X	500 ml	
B27 Supplement 50X	5 ml	0.5X
N2 Supplement 100X	5 ml	1X
FGFb, 4 mg/ ml	5 µl	40 ng/ ml

To passage iNPCs, 10cm TC-treated culture dish was incubated for a minimum of 5 minutes at room temperature (RT) in PBS containing 3 µg/ml human plasma fibronectin. The growth medium was removed from the ongoing culture dish and 1 ml of warm Accutase™ enzyme was added. Cells were incubated for 5 minutes at 37°C. Detached cells were collected in 3 ml of PBS, transferred to a 15 ml falcon, and centrifuged for 4 minutes at 200g to pellet the cells. The supernatant was removed and the resulting pellet resuspended in iNPC culture medium

according to its size. Homogenous cell suspension was obtained by gentle trituration with P1000 Gilson pipette tip. The PBS was then aspirated from the previously prepared fresh 10 cm plate and replaced with 10-12 ml of warm iNPC medium (volume added was dependant on the known proliferation rate of the cells, i.e. faster growing cells would be seeded in a larger volume of medium). About 500,000 cells (or volume equivalent) were then added to prepared fresh culture plate and a new passage number noted. Any leftover cell suspension was used for further differentiation into iAstrocytes or iNeurons (see sections 2.2.1.2 and 2.2.1.3) or frozen in medium and 10% DMSO. The prepared and labelled cryovials were then transferred to a freezing system container (Corning® CoolCell™) with a metal core at RT and left at -80°C for a minimum of 2 hours.

When thawing iNPCs stored at -80°C or in liquid nitrogen dewars, a cryovial was immediately placed in a 37°C water bath. After 1.5-2 minutes, the thawed cryovial contents were placed in warm iNPC medium in a fresh 10 cm plate prepared as before and monitored daily, with media change after 24h to remove the DMSO and subsequently typically every 48h or when medium was depleted and until ready for first passaging.

2.2.1.2 Differentiation of iNPCs into iAstrocytes and drug treatment

Tissue culture plates or dishes were coated with 1.5 µg/ml human plasma fibronectin in PBS for minimum of 5 minutes at RT. Fibronectin was then replaced with 10 ml of warm iAstrocyte differentiation medium (Table 2.11). Once the iNPC pellet was resuspended, about 200,000 cells were seeded per prepared iAstrocyte differentiation plate. During the seven-day differentiation protocol, one medium change was performed at day 4 to replenish the nutrients. If a drug treatment was to be applied at day 5 during the process, the medium change at day 4 was not performed (see section 2.2.1.4). To transfer iAstrocytes to 96- or 384-well plates, cells had their culture medium removed and were washed once with PBS. Cells were then incubated for 5 minutes at 37°C with 1 ml Accutase™. Following the incubation, cells were collected in 4 ml of PBS and centrifuged for 4 minutes at 200g. The cell pellet was resuspended in iAstrocyte culture medium and cells counted. Density at which iAstrocytes were plated in fibronectin-coated optical 96- or 384-well plates varied between experiments, which is detailed in relevant individual sections of this chapter.

For an overview of iAstrocyte differentiation and drug or virus treatments involved, see Figure 2.1. Throughout this chapter, treatment times are referred to as 'iAstrocytes differentiation day X', please refer to Figure 2.1. for clarity.

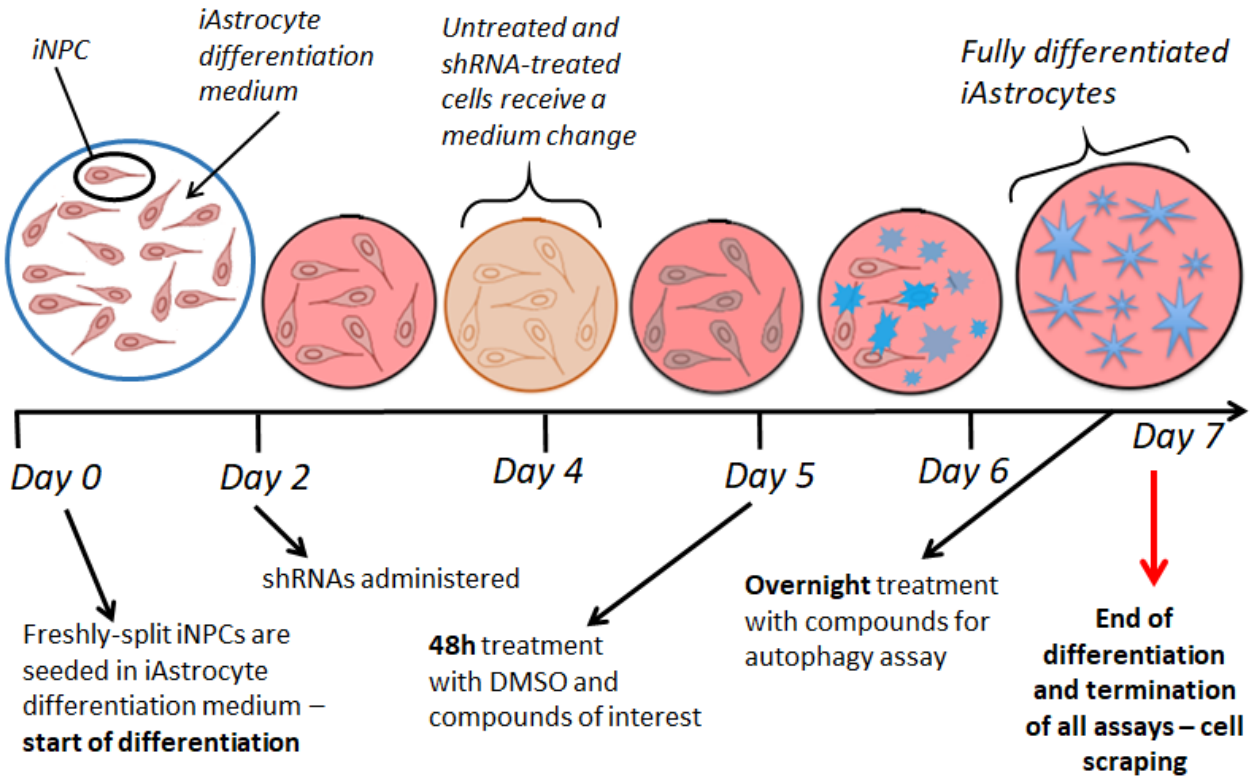

Figure 2.1 Timeline of induced astrocyte (iAstrocyte) differentiation and drug treatments

iNPCs – induced neural progenitor cells; shRNA – short hairpin RNA; DMSO – dimethyl sulfoxide.

Table 2.11 Composition of iAstrocyte differentiation medium.

Reagent	Volume	Final concentration
DMEM	500 ml	
FBS	50 ml	10%
PS	5 ml	50 units Penicillin/ml 50 units Streptomycin/ml
N2 Supplement 100X	1 ml	0.18X

2.2.1.3 Target knockdown with shRNA

iAstrocytes on day 2 of differentiation were used for experiments where expression levels of a selected target were knocked down. For that purpose, shRNA adenoviruses expressing a selected transgene under either a cytomegalovirus (CMV) or U6 promoter were purchased (Vector Biolabs). Each viral construct also contained red fluorescent protein (RFP) under a CMV promoter. Calculations for multiplicity of infection (MOI) of 10, 7.5, 5, 2.5 and 1 of both the transgene of interest and RFP-only control were made and appropriate shRNA volumes diluted in iAstrocyte culture medium. iAstrocytes were incubated with shRNAs for 48 hours, after which their culture medium was replaced. Transfection efficiency was investigated by initial quality control examination of RFP expression under a fluorescence filter, after which target knockdown levels were measured via western blotting.

2.2.1.4 Differentiation of iNPCs into iNeurons

TC-treated 6-well plates were coated with 1 ml/well of fibronectin (3 µg/ml in PBS). After 5 minutes at RT, fibronectin was replaced with 2 ml/well of iNPC culture medium. Once the iNPC pellet had been resuspended, about 150,000 cells/well (adjustable to growth rate of the cells) were seeded and plates transferred to the incubator. When cells reached 70% confluence, typically 48 hours after seeding, the iNPC medium was removed and replaced with iNeuron differentiation medium (see Table 2.12), supplemented with 2.5 µM small molecule γ-secretase inhibitor (DAPT) to promote cell cycle exit and formation of post-mitotic neurons. The following day, 1 ml of medium was added per well to replenish nutrients. On day 4 of differentiation, half of the volume in each well was removed and replaced with iNeuron differentiation medium supplemented with 1 µM SAG agonist of hedgehog signalling to promote ventralisation, 1 µM RA to promote caudalisation, and 2.5 µM forskolin, which directly activates adenylyl cyclase, thus resulting in an increase of cyclic adenosine monophosphate (cAMP) levels in the cell. cAMP is an important second messenger involved in many signal transduction pathways, including activation of protein kinase A, and has been found to favour neuronal maturation.

Supplementation of differentiation drugs, as described above, was repeated daily for four days, at which point cells were washed gently with PBS to remove the debris and harvested by scraping in PBS, and centrifuging for 1 minute at 17,000g. The cell pellets were stored at -80°C before processing. For an overview of the iNeuron differentiation process, see Figure 2.2.

Table 2.12 Composition of iNeuron differentiation medium.

Reagent	Volume	Final concentration
DMEM/F-12 1X	50 ml	
B27 Supplement 50X	1 ml	1X
N2 Supplement 100X	500 µl	1X
PS	500 µl	5 Units Penicillin/ml 5 Units Streptomycin/ml

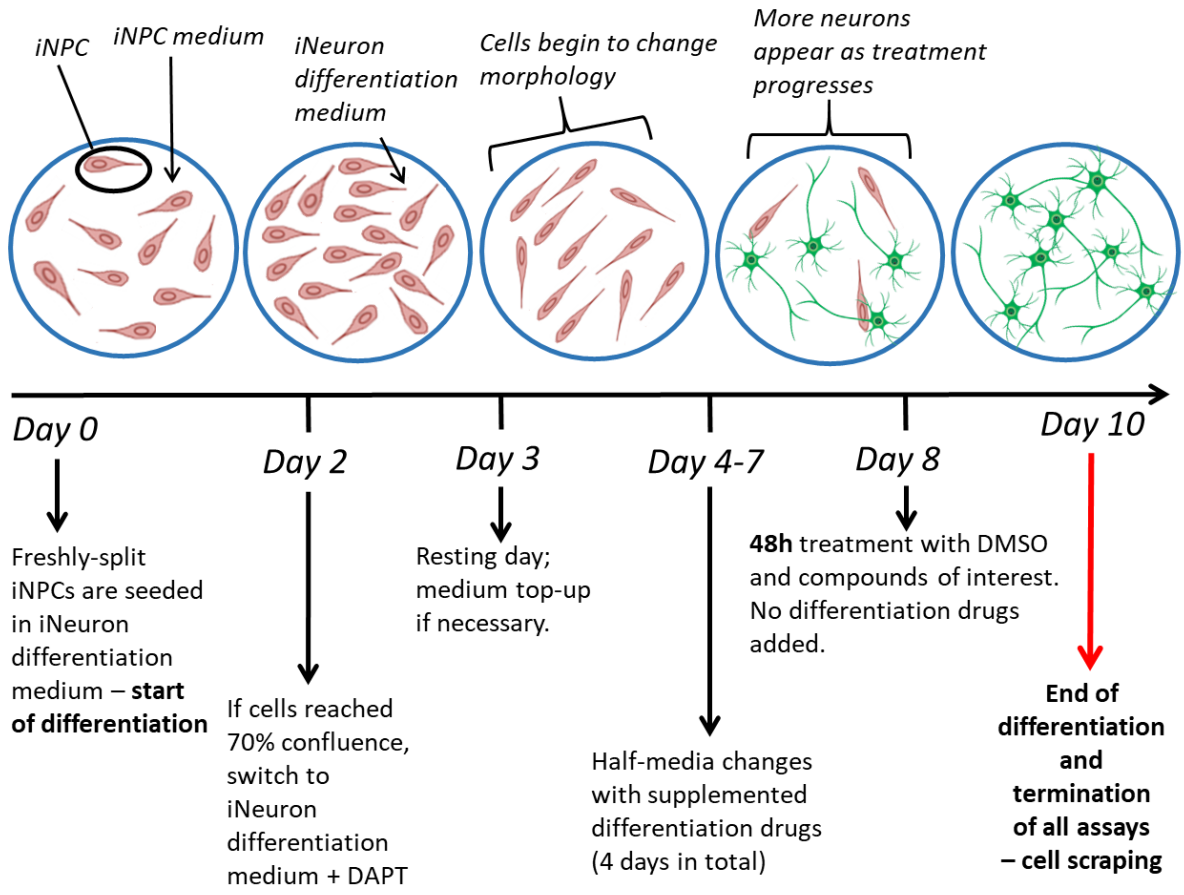

Figure 2.2 Timeline of induce neuron (iNeuron) differentiation and drug treatments

iNPCs – induced neural progenitor cells; DAPT - (2S)-N-[(3,5-Difluorophenyl)acetyl]-L-alanyl-2-phenyl]glycine 1,1-dimethylethyl ester; DMSO – dimethyl sulfoxide.

2.2.1.5 iAstrocyte and iNeuron drug treatment

Unless otherwise stated, both iAstrocytes and iNeurons were treated with drugs for the last 48 hours of their differentiation. For that purpose, medium was removed from the culture plates and replaced with fresh corresponding differentiation medium containing gefitinib or nilotinib. Every experiment also included a subset of cells treated with 0.1% (v/v) of DMSO drug vehicle as a negative control. After 48 hours, medium was removed, cells washed once with PBS to remove residual serum and/or cellular debris and scraped in 1 ml PBS. Cells were then pelleted by centrifugation at 17,000g for 1 minute in a cold ultracentrifuge. Supernatant and residual PBS were removed before storage at -80°C.

2.2.1.5.1 Drug preparation

Drugs investigated in this work were gefitinib (Cayman Chemical) and nilotinib (Sigma). Both gefitinib (446.902 g/mol) and nilotinib (529.5245 g/mol) were stored in powder form under inert nitrogen at 0.5 pound per square inch (PSI), >12% oxygen and 5% relative humidity conditions (MultiPod™, Roylan Developments) to eliminate destabilisation caused by water contamination and oxidisation. Each compound was reconstituted in anhydrous DMSO (≥99.9%) to 10 mM concentration in accordance with the following formula:

$$\text{Volume (µl) of DMSO added} = \frac{mass\ in\ mg}{molecular\ weight\ in\ g/mol \div 1000} \text{ x } 100$$

Once reconstituted, compounds were stored for short-term use in moisture-depleted conditions of a desiccator and discarded after one month. Gefitinib solution was prepared and kept at a stock concentration of 10 mM and diluted 1:1000 for treatment, giving the final working concentration of 10 µM. Nilotinib solution was further diluted in DMSO to a final stock concentration of 1 mM and diluted 1:1000 for treatment, giving the final working concentration of 1 µM.

2.2.2 Murine embryonic stem cell (mESC) culture and motor neuron-iAstrocyte co-culture

2.2.2.1 Hb9-GFP mESC passage and maintenance

Murine embryonic stem cells (mESC) expressing green fluorescent protein (GFP) under the motor neuron-specific homebox protein HB9 (Hb9) promotor were a kind gift from Prof. Thomas Jessell and their routine maintenance was conducted by Dr Matthew Stopford, Miss Chloe Allen, Mr Marco Destro or myself. 10 cm culture plates were coated with 1.5 µg/ml human plasma fibronectin in PBS for minimum of 5 minutes at RT and mouse embryonic fibroblasts (mEFs, Merck) were thawed onto them and cultured in complete iAstrocyte

culture medium (see table 2.11) to act as a feeder layer for mESCs. The following day, the medium was changed to mESC culture medium (Table 2.13) supplemented with 100 units/ml of leukaemia inhibitory factor (LIF). To passage mESCs, culture medium was removed, cells were washed once with PBS, and incubated in 1ml of trypsin 1X for 5 minutes at 37°C. Trypsin was quenched with 9 ml of complete mESC culture media and cells triturated vigorously using a 10 ml stripette, whilst pressing the stripette nozzle against the plate in order to break cell clusters under pressure. The resulting single cell suspension was incubated in a TC-treated 10 cm plates for 30 minutes at 37°C, which allowed for any remaining mEFs to adhere to the dish, leaving mESCs in suspension. Following the incubation, cells from multiple plates were pooled in a 50 ml falcon and centrifuged for 4 minutes at 200g. Once the supernatant was removed, the pellet was re-suspended in mESC culture medium, gently mixed with a 1 ml pipette tip, and filtered through a 70 µm mesh filter to remove any residual mEFs. Approximately 300,000 cells were replated onto previously prepared fresh mEFs to re-propagate the culture. Medium was replenished every 24 hours for 3 days before a next passage.

Table 2.13 Composition mESC culture medium.

Reagent	Volume	Final concentration
KnockOut DMEM	400 ml	80%
Embryonic stem cell serum	75 ml	15%
MEM NEAA (100X)	5 ml	1X
PS	5 ml	50 Units Penicillin/ml 50 Units Streptomycin/ml
L-glutamine (200 mM)	5 ml	2 mM
β-mercaptoethanol (50 mM)	3.6 µl	0.36 µM

2.2.2.2 Motor neuron differentiation from mouse embryoid bodies (mEBs)

Following a split, approximately 1,000,000 mESCs were plated for motor neuron differentiation and grown in mouse embryoid bodies (mEBs) culture medium (Table 2.14) as a non-adherent culture in uncoated non-tissue culture treated 10 cm plates. Contents of each culture plate were transferred gently into 50 ml falcons 24 hours after the initial seeding and cells allowed to precipitate for 10 minutes at RT. Supernatant was then removed and medium replaced. 24 hours later, 1 µM SAG and 2 µM RA were added to the fresh medium to start

mEBs differentiation in motor neurons. This drug treatment was performed every day for a total of 6 days, after which resulting mEBs were examined for their GFP expression by assessing their intensity under a fluorescent filter, in order to assess the motor neuron differentiation efficiency.

Table 2.14 Composition mESC culture medium.

Reagent	Volume	Final concentration
KnockOut DMEM	220 ml	44%
F12	220 ml	44%
KnockOut serum replacement	50 ml	10%
N2 supplement 100X	5 ml	1X
PS	5 ml	50 Units Penicillin/ml 50 Units Streptomycin/ml
Glucose (1 M)	2.5 ml	5 mM
L-glutamine	2.5 ml	1 mM
β-mercaptoethanol	4 µl	0.4 µM

2.2.2.3 Motor neuron dissociation and co-culture with iAstrocytes

On the final day of motor neuron differentiation, mEBs were collected in a 50 ml falcon and centrifuged at RT for 4 minutes at 200g. Supernatant was collected and mEBs re-suspended and triturated in 2.75 ml enzyme dissociation buffer (Table 2.15) with 250 µl papain 10X (10 units/ml final concentration). mEBs were then incubated at 37°C (water bath) for 10 minutes, with agitation every 3 minutes. Following the incubation, cells were gently triturated, 2 ml of fresh dissociation buffer added, and the cell suspension was centrifuged at RT for 5 minutes at 300g. During centrifugation, 2.7. ml of the dissociation buffer, 300 µl FBS and 150 µl DNase I (60 µg/ml final concentration) were mixed together in a 15 ml falcon. After the centrifugation, supernatant was aspirated, and cells were triturated in 3 ml of the DNase I-containing solution. 5 ml of FBS was added to a separate 15 ml falcon and the cell suspension was carefully dispensed on top of it, making sure not to agitate the interface between the FBS and the cell suspension. The resulting cells suspension on top of the FBS cushion were centrifuged for at RT for 6 minutes at 100g, with the accelerator/decelerator 'brake' setting switched off. Pellet of dissociated motor neurons were resuspended in motor neuron culture

medium (mEB culture medium [Table 2.14] supplemented with BDNF, CNTF and GDNF, 20 ng/ml each) and counted.

Mouse embryonic motor neuron-human iAstrocyte co-culture was assembled as previously described (Stopford et al., 2019). Briefly, prior to motor neuron dissociation, iAstrocytes on day 5 of differentiation were plated at a density of 10 000 cells/well in 96-well plates or 6000 cells/well in 384-well plates, as described in section 2.2.1.3. To set up an iAstrocyte-Hb9-GFP motor neuron co-culture, motor neurons were plated on a layer of iAstrocytes (day 7 of differentiation) at a density of 10,000 cells/well in 96-well plates, or at 1500 cells/well in 384-well plates. The resulting co-culture plate was scanned using the INCell 2000 imaging system (GE Healthcare) 24 hours after seeding (co-culture day 1) and 48 hours after the first scan (co-culture day 3). Acquired images were analysed using Columbus software (Perkin Elmer), collecting the following parameters: cell bodies, cell bodies with neurites, neurite length.

Importantly, the 48h drug treatment applied to iAstrocytes throughout this work has been selected as it corresponds to the co-culture day 1 (section 2.2.2.3), where initial effect of drugs on astrocytes and motor neurons is observed.

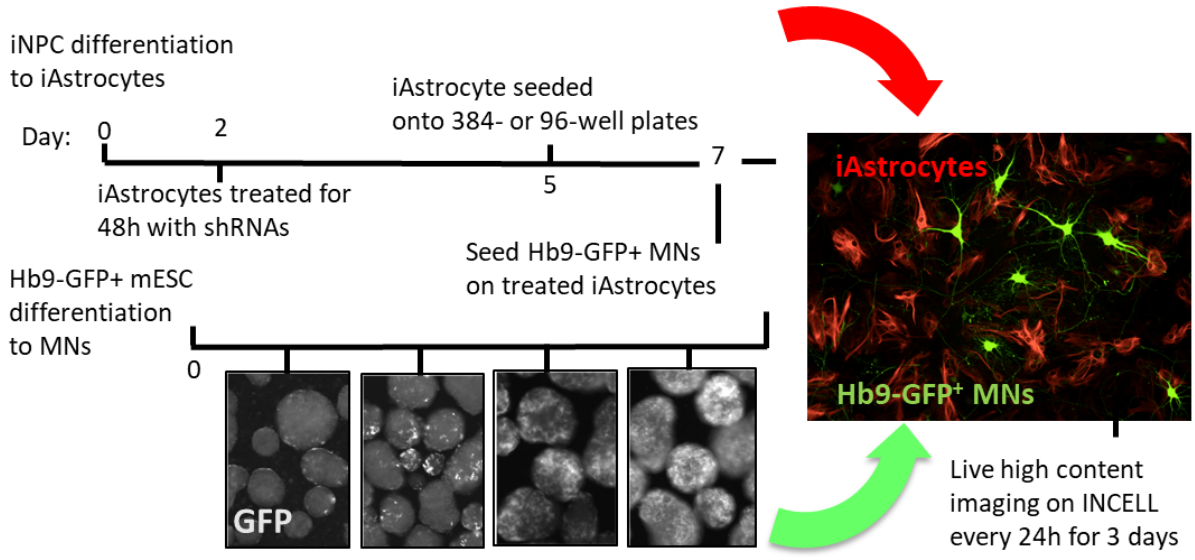

Figure 2.3 Summary and timeline of Hb9-GFP mouse embryonic motor neurons (HB9-GFP+ MNs)/induced astrocytes (iAstrocyte) co-culture experiments

iNPC – induced neural progenitor cell; shRNA – short hairpin RNA; mESC – mouse embryonic stem cell.

Table 2.15 Composition of motor neuron dissociation buffer (for 40 ml final volume).

Reagent	Volume (ml)	Final concentration (mM)
NaCl	4.64	116
KCl	0.216	5.4
$NaHCO_3$	1.04	26
NaH_2PO_4	0.4	1
$CaCl_2$	0.6	1.5
$MgSO_4$	0.4	1
Glucose	1	25
EDTA	0.04	0.5
dH_20	31.472	-
Cysteine	0.192	1

2.2.3 Autophagy assay

2.2.3.1 Human embryonic kidney 293 (HEK293) cell culture

The procedure described in this section was conducted by Dr Emma Smith and Dr Rebecca Cohen of Dr Kurt de Vos lab at SITraN.

Human embryonic kidney 293 (HEK293) cells were cultured in 10 ml of their culture medium (see Table 2.16) in 10 cm plates in a 37°C / 5% CO_2 incubator. HEK293 cells were split every 3-4 days. To split the HEK293 cells, the media was removed, and cells were washed in PBS. 1 ml 1X trypsin was added to the cells, and cells were returned to incubator for 4mins. The plate was tapped to dislodge trypsinised cells from the plate, and 9 ml of medium was added. Cells were resuspended, and 1 ml cell suspension was added to a new 10 cm plate. Supplemented DMEM was added to a final volume of 10 ml.

Table 2.16 Composition of HEK293 cells culture medium.

Reagent	Volume	Final concentration
DMEM	500 ml	-
FBS	50 ml	10%
PS	5 ml	50 units Penicillin/ml, 50 units Streptomycin/ml
Sodium pyruvate (100 mM)	5 ml	1 mM

2.2.3.2 Treatment conditions

HEK293 cells were seeded into 12-well plates and cultured for 3 days until 80% confluence. Media was removed from HEK293 cells, and 1 ml media was added per well, containing either DMSO only, 10 µM gefitinib, 1 µM nilotinib, 500 nM rapamycin (Cayman Chemicals), 100 nM bafilomycin A1 (Alfa Aesar), or a combination of the above, at 1 well per treatment condition. Media always contained 0.1% (v/v) of the drug-vehicle anhydrous DMSO. Cells were incubated for 6 h, medium removed, and cells washed with PBS. LC3 and p62 protein expression was investigated by western blotting, as described in section 2.2.4.

2.2.3.3 Autophagy assay in iAstrocytes

iNPCs were seeded in iAstrocyte differentiation medium in three 6-well plates per cell line. Cells received a medium change on day 4. On day 6 of differentiation, culture medium was replaced with fresh medium containing either DMSO only, 10 µM gefitinib, 1 µM nilotinib, 250 nM torin 1 (Tocris), 100 nM bafilomycin A1, or a combination of the above, 3 well per treatment condition. Torin 1 is an autophagy activator used here as a positive control, whereas bafilomycin A1 is an autophagy inhibitor, used as a negative control. Media always contained 0.1% (v/v) of the drug-vehicle anhydrous DMSO. Cells were incubated for 16 h, medium removed, and cells washed with PBS. LC3, p62, and TDP-43 protein expression was investigated by Western blotting, as described in section 2.2.4.

2.2.4 Western blotting

2.2.4.1 Preparation of the soluble proteins

Cell pellets were lysed by trituration in IP lysis buffer (see Table 2.17) supplemented with 1X PIC and 1X PhosStop. Volume of IP lysis buffer used was adjusted per pellet and varied between 10 µl and 100 µl. Following a 15-minute incubation on ice, lysates were centrifuged at 4°C for 5 minutes at 17,000g to pellet insoluble proteins. Lysates were transferred to fresh 1.5 ml tubes and kept on ice for the remainder of the procedure. The leftover pellet could then be subjected to further processing to extract detergent insoluble proteins (see section 2.2.4.1.1).

Table 2.17 Composition of IP lysis buffer.

Reagent	Final concentration
Sodium chloride (NaCl)	150mM
HEPES	50mM
EDTA	1mM
DTT	1mM
Triton™ X-100	0.5% (v/v)
PIC, 100X	1X
PhosSTOP, 10X	1X

Bradford assay for protein quantification was performed by adding 1 µl of each sample to 1 ml of Protein assay dye concentrate diluted 1:5 in ddH_2O, mixing well by shaking and transferring to a 10 x 4 x 45 mm couvette (Sarstedt). After a blank measurement was recorded, protein concentration of each sample was measured by reading their absorbance value at 595 nm with S1200 Diode Array Spectrophotometer (WPA). In accordance with Beer-Lambert law (OD595nm = εcl; where ε = 1/15, and l = 1 cm), each 595 nm optical density value was multiplied by 15 to obtain a protein concentration in mg/ml. Once loading calculations were made, samples mixed with 4X laemmli loading buffer (see Table 2.18) were boiled at 95°C for 5 minutes to linearize the proteins, then loaded onto a previously prepared gel (see section 2.2.4.2).

2.2.4.1.1 Preparation of insoluble proteins

Once the IP lysis buffer-soluble protein fraction was transferred to fresh 1.5 ml Eppendorf tubes, the remaining precipitate pellet was resuspended in 500 µl ice-cold RIPA buffer (150 nM NaCl, 50 nM Tris, 1% v/v Triton X-100, 0.5% w/v SDS, 0.5% w/v deoxycholate, pH 8.0 [Sigma]) supplemented with PIC 1X and sonicated on ice for 10 seconds (30% Amp). Samples were then incubated on ice for 15 minutes and centrifuged at 17,000g for 30 minutes at 4°C. Supernatant was transferred to a fresh 1.5. ml Eppendorf tube. The pellet was resuspended in 500 µl RIPA buffer with PIC 1X and centrifuged at 17,000g for 15 minutes at 4°C. The

supernatant was removed and transferred to a fresh 1.5 ml tube. This step was subsequently repeated. Residual RIPA buffer was removed and the final pellet was resuspended in 10 µl Urea buffer (7 M Urea [Fisher], 2 M Thiourea [Sigma], 1 mM EDTA, 30 mM Tris, pH 8.5). 9 µl of the Urea-soluble fraction was mixed with 3 µl laemmli buffer (Table 2.15). 16µl of RIPA-soluble fraction was mixed with 4 µl laemmli buffer and boiled at 95°C for 5 minutes. Urea fraction was loaded onto gels unboiled.

Table 2.18 Composition of 4X laemmli loading buffer.

Reagent	Final concentration
Tris-HCl	228mM
Glycerol	38% (v/v)
SDS	277mM
Bromophenol blue	0.038% (w/v)
β-mercaptoethanol, pH 6.8	5% (v/v)

2.2.4.2 SDS-PAGE

Depending on the kilodalton (kDa) weight of the protein of interest, three different gel densities were used (see Table 2.19 for composition and applications). Once the resolving gel was set, 1.5 ml of 5% stacking gel was dispensed on top and a 15- or 10- lane comb was inserted. The comb was removed once the stacking gel was set. The gel was encased in a cassette and placed into Mini-PROTEAN® Tetra System tank (BioRad).

Table 2.19 Composition of gels used for Western blotting and their applications.

Reagent	5% stacking gel	8% resolving gel	12% resolving gel	15% resolving gel
dH_20	5.8 ml	4.9 ml	3.5 ml	2.5 ml
30% (w/v) Acrylamide	1.7 ml	2.6 ml	4 ml	5 ml
Resolving buffer (1.5 M Trizma®, 13.9 mM SDS, pH 8.8, filtered)	-	2.5 ml	2.5 ml	2.5 ml
Stacking buffer (0.5 M Trizma®, 13.9 mM SDS, pH 6.8, filtered)	2.5 ml	-	-	-
10% (w/v) APS	50 µl	50 µl	50 µl	50 µl
TEMED	20 µl	20 µl	20 µl	10 µl
Resolution	-	100 ≤ kDa proteins	80 ≥ kDa proteins	30 ≥ kDa proteins

Once the apparatus was set up, running buffer (Table 2.20) was poured inside the gel cassette. Samples were loaded inside the lanes alongside 2 µl BLUeye pre-stained protein ladder. Gels were run initially at 50 V for 30 minutes, using PowerPAC™ Basic (BioRad) to ensure correct stacking of the proteins, after which the voltage was increased to 150 V for 1-1.2 hours depending on gel density. Once the run was complete, gels were removed from the glass cassette and transferred onto a nitrocellulose or PVDF membrane incubated in methanol for 1 minute (both GE Healthcare) in semi-dry Biometra Fastblot™ (Analytik Jena AG) transfer with transfer buffer (Table 2.21) for 1 hour at 250 V (0.15 milliamperes [mA] per gel), using PowerPAC™ HD (BioRad). Note, PVDF membranes required an incubation in methanol for 60 seconds prior to immersion in transfer buffer.

Table 2.20 Composition of running buffer.

Reagent	Final concentration
Tris	25mM
SDS	3.5mM
Glycine	20mM

Table 2.21 Composition of transfer buffer.

Reagent	Final concentration
Tris	47.9mM
Glycine	38.6mM
SDS	1.38mM

Upon completion of the transfer, membranes were stained with Ponceau S (0.1% w/v Ponceau S powder, 5% (v/v) acetic acid, ddH_2O) by incubation on a shaker for 1 minute. Membranes were then cut to size as needed and blocked on a roller for 1 hour at RT in 5% (w/v) low-fat milk powder (Marvel) in Tris-buffered saline, 0.1% (v/v) Tween 20 (TBST; see Table 2.19 for composition) or 5% BSA (w/v) (further details in Table 2.5). Membranes were then incubated in primary antibody overnight at 4°C on a roller. Note, β-actin, a loading control for most SDS-PAGE experiments, was often blotted following chemiluminescence capture for TDP-43. Blots were first incubated on a roller at RT for 1 hour with 25 nM sodium azide, to destroy HRP activity of the secondary antibody to TDP-43. This is because of similarities in molecular weight between β-actin and TDP-43 (42 and 43 kDa respectively).

Table 2.22 Composition of TBST, pH 7.6.

Reagent	Final concentration
Tris	20mM
NaCl	137 mM
Tween® 20, pH 7.6	0.2% (v/v)

Following an incubation with primary antibodies, membranes were washed three times for 5 minutes in TBST and incubated in HRP-conjugated secondary antibody (see Table 2.6). Membranes were then washed again three times for 5 minutes in TBST prior to capture.

2.2.4.3 SYPRO® Ruby stain

The following steps were performed at RT on a plate shaker at 50 rpm. After the transfer of urea- and RIPA-soluble protein gels, nitrocellulose membranes were incubated for 15 minutes at RT in a mixture of 7% (v/v) acetic acid and 10% (v/v) methanol diluted in ddH_2O. Membranes were subsequently washed in deionised water 4 times for 5 minutes. SYPRO Ruby® was added onto the membrane, using enough volume to fully immerse it, and incubated for 15 minutes. Membranes were then washed with deionised water 5 times for 1 minute. Membranes were allowed to air dry before image capture. Once imaged, membranes were used for protein detection.

2.2.4.4 GeneSnap immunofluorescence capture

Membranes were incubated with EZ-ECL Enhanced Chemiluminescence Detection Kit for 1 minute and imaged using GBOX imaging system (Syngene). Intelli-Chemi images were viewed in real time using GeneSnap software (Syngene). For membranes stained with SYPRO® Ruby, images were obtained on in 'classic' mode, using UV epi-illumination setting.

2.2.4.5 GeneTools protein quantification

GeneSnap-associated files containing the intelli-Chemi images were opened in GeneTools software (Syngene) and the raw fluorescence value was calculated automatically once the bands were identified. Subsequently the protein concentration was calculated relative to β-actin loading control or as a ratio of two associated protein cleavage products or isoforms (used for TDP-43 and LC3). The 'n' numbers in figures presenting Western blotting data represent experimental replicates.

2.2.5 Enzyme-linked immunosorbent assay (ELISA)

2.2.5.1 K562 leukaemia cell line culture

Human bone marrow-derived chronic myelogenous leukaemia cell line K562 was provided by collaborators at BenevolentAI, Babraham Research Campus, under MTA.

K562 cell line was grown as a suspension culture in complete culture medium (Table 2.23), using Corning® T-75 flasks. During regular maintenance, medium was refreshed every 48h by centrifugation of cells for 4 minutes at 200g (accelerator and decelerator settings switched off), removal of the supernatant and replacement with the equivalent volume of fresh media. Cultures were re-propagated every 4 days at a density of $1x\ 10^5$ cells/ml. During each routine medium replacement, a fraction of cells was treated with 0.1% v/v DMSO, 10 µM gefitinib or 1 µM nilotinib for 48h.

Table 2.23 Composition K562 cell line culture medium.

Reagent	Volume	Final concentration
Iscove's Modified Dulbecco's Media (IMDM)	500 ml	
FBS	50 ml	10%
PS	5 ml	50 Units Penicillin/ml 50 Units Streptomycin/ml
L-glutamine	5 ml	2 mM

2.2.5.2 Sample preparation

iAstrocytes and K562 cells treated with gefitinib, nilotinib or DMSO as described in sections 2.2.1.4 and 2.2.5.1 had their culture medium removed at day 7 of differentiation for iAstrocytes and day 4 of culture for K562 cells. iAstrocyte culture plates were placed on ice and washed with cold PBS. K562 cells were resuspended in PBS and pelleted by centrifugation at 17,000g for 1 minute at 4°C. Once PBS was removed, cells were scraped and collected in 1.5 ml Eppendorf tubes with residual PBS. Following a centrifugation at 17,000g for 1 minute at 4°C and removal of the supernatant, the cell pellet was triturated in 500 µl of cold lysis solution containing cell lysis buffer 1X (Cell Signalling Technologies), 1X PIC, 1X PhosStop and 1 µM PMSF, Sigma. Lysing cells were incubated on ice for 10 minutes, followed by a centrifugation for 10 minutes and 14,000g and 4°C. Supernatants were transferred to fresh 1.5 ml Eppendorf tubes and stored immediately at -80°C until ready for processing.

2.2.5.3 Bicinchoninic acid (BCA) assay and interpolation of unknown protein samples

Standards with a working protein concentration range of 20 – 2000 µg/ml (plus blank) were prepared by adding an appropriate volume of BSA to a diluent solution. Protein samples of interest were diluted 1:50 in their lysis buffer. 10 µl of the standards and diluted protein samples were added per well of a 96-well non-optical plate. Bicinchoninic acid (BCA) assay working reagent master mix was prepared by adding one part of BCA reagent B per 50 parts of BCA reagent A, assuring sufficient volumes to cover all standards and unknowns in triplicate. 200 µl of BCA working solution was then added to each standard and sample-containing well and the plate incubated for 30 minutes at 37°C. Following the incubation, the plate was imaged immediately using PHERAstar to determine absorbance values at 560 nm. Protein standard replicates were averaged, and values fitted onto a standard curve trend line

to obtain a linear equation. Unknown protein concentrations were determined by interpolating the absorbance values of replicate averages onto the standard curve and multiplying by the dilution factor.

2.2.5.4 Enzyme-linked immunosorbent assay

ELISA for p-c-Abl was optimised using PathScan® phospho-c-Abl (panTyr) Sandwich ELISA kit (Cell Signalling Technologies) at Babraham Research Institute-based branch of BenevolentAI, under the supervision of Dr Linda Kitching. Unless otherwise specified, the reagents listed below are a part of the aforementioned kit.

Samples of interest were left to thaw on ice. ELISA plate with a desired number of wells coated with c-Abl antibody (rabbit) was brought to RT. Once loading calculations were conducted for 30 mg of protein per samples and each sample diluted in PBS as necessary, 100 µl of the lysate mixture was loaded in duplicate onto the ELISA plate, plate sealed and incubated overnight at 4°C. The following day, the supernatant was removed and washed four times with 200 µl of ELISA wash buffer 1X (20X in ddH_2O) using Multidrop Combi (Thermo Fisher Scientific). The plate was inverted on tissue paper between each wash to absorb the residual liquid. Following the washes, 100 µl of phosphor-tyrosine detection antibody (mouse mAb) was added per well, plate sealed and incubated for 1 hour at 37°C. The detection antibody was then removed, four washes performed as described before, and 100 µl of HRP-conjugated antibody (mouse IgG) added per well. Plate was then resealed and incubated for 30 minutes at 37°C. After the incubation, secondary antibody was removed and plate washed as before. The plate was resealed and 100 µl of TMB substrate solution was added per well and incubated for 10 minutes at 37°C. 100 µl of the STOP solution was then added per well and the absorbance at 450 nm was measured using PHERAstar no later than 30 minutes after the addition of the STOP solution.

2.2.6 Immunocytochemistry

2.2.6.1 Cell preparation and fixing

Cells were cultured as described in section 2.2.1.2. On day 4 of iAstrocyte differentiation, cells were removed from their culture dish using Accutase™. Following a pellet resuspension, 10 µl of suspension was used for cell counting with a 0.100 mm hemocytometer (Neubauer). Calculations were made for seeding 4000 cells/well, in 100 µl medium/well, and cells transferred to a fibronectin-coated black optical 96-well plates. The following day, medium

was removed and replaced with medium containing 0.1% (v/v) DMSO, 10 µM gefitinib, or 1 µM nilotinib. Cells were cultured for further 48 hours, after which they were washed gently with PBS and incubated for 10 minutes at RT with 80 µl/well of 4% paraformaldehyde (PFA). Wells were washed with 160 µl PBS and stored in 200 µl PBS at 4°C, ready for further use.

2.2.6.2 Immunofluorescent staining

Non-specific binding sites were blocked in 70 µl 5% normal horse serum with 0.5% Triton® (all in PBS) for 1 hour. Blocking solution was removed. Cells were incubated in 70 µl primary antibodies diluted in the solution used for blocking overnight at 4°C (see Table 2.8 for a list of antibodies used). The following morning, primary antibodies were removed and cells are washed 3 times for 5 minutes in 100 µl PBS with 0.2% Tween®20. After the last wash, secondary antibodies diluted in PBS were added for 30 minutes at RT. Following this incubation, secondary antibodies were removed and Hoescht stain solution diluted 1:10,000 in PBS was added for 5 minutes to label nuclei, followed by two 5-minute washes in PBS. Stained plates were imaged using Opera Phenix™ High Content Screening System (Perkin Elmer) and analysed using associated Harmony software (v4.8, Perkin Elmer).

2.2.6.3 Analysis

Images captured on Opera Phenix™ are automatically stored on Harmony server, from which assay files can be uploaded onto Columbus Data Storage and Analysis System (Perkin Elmer).

For each immunofluorescence staining plate, two technical repeat wells, containing 20 random fields per well per experimental condition at 40X magnification, were imaged and analysed. An average of technical repeats per plate was treated as an experimental n=1 and each microscopy-based experiment was brought to at least n=3 experimental repeats. When n=2 only was obtained due to cell unavailability, the experimental duplicate was averaged and pooled together with average values of other n=2 datasets from the same genotype (indicated in the figure legend). The same approach was applied to proximity ligation assay (section 2.2.7) and tetramethylrhodamine methyl ester live stain (section 2.2.8).

2.2.7 Proximity ligation assay (PLA)

To study an interaction between two proteins of interest via a proximity ligation assay (PLA), a commercially available Duolink® *In Situ* Orange Starter Kit Mouse/Rabbit (Sigma-Aldrich) kit was used. Unless otherwise specified, the reagents listed below are a part of the aforementioned kit.

iAstrocytes on day 4 of differentiation were plated into 96-well optical plates, treated with compounds the next day and fixed with 4% PFA after 48 hours of treatment as described in section 2.2.6. Following a PBS wash, non-specific binding sites were blocked in 50 µl of PLA Blocking Buffer 1X for 30 minutes at 37°C. Primary antibodies were then diluted in PBS and added to the wells, ensuring that sufficient controls are in place (single antibody only and no antibody as negative controls, and LC3+p62 as a positive control). Cells were incubated in primary antibodies overnight at 4°C. The following day, plates were washed twice with Wash Buffer A for 5 minutes on a plate shaker set to no more than 50 rpm. Mouse and Rabbit Secondary Probes were diluted in the Antibody Diluent and 40 µl of the mix added to each well following the washes and incubated for 1 hour at 37°C. Wells were then washed twice with Wash Buffer A as described above. Following the incubation, wells were washed twice with Wash Buffer A as before, and incubated in 40 µl/well of ligation mix (dH_2O, Ligation Stock Solution, Ligase Enzyme) for 30 minutes at 37°C. Next, cells were washed again with Wash Buffer A and incubated for 100 minutes at 37°C in 40 µl/well of amplification mix (dH_2O, Amplification Stock Solution, Polymerase Enzyme). After the amplification incubation, wells were washed twice with Wash Buffer B 1X for 5 minutes on a plate shaker set to no more than 50 rpm. Wash Buffer B 0.01X was prepared by diluting Wash Buffer B in dH_2O and Hoescht was diluted 1:6000 in the new solution. Wells were then incubated in the Wash Buffer B + Hoescht mix for 5 minutes at RT. Lastly, cells were washed twice with Wash Buffer B 0.01X and images acquired on Opera Phenix imaging system. Images were analysed using Columbus software.

2.2.8 Tetramethylrhodamine methyl ester (TMRM) live stain

2.2.8.1 Cell preparation

To visualise the mitochondrial network, iAstrocytes on day 5 of differentiation were lifted and plated in 96-well optical plates at a density of 3000 cells/well as described in section 2.2.6. Cells with a high proliferation rate were plated at a density of 2000 cells/well, whereas cells exhibiting slower proliferation rate were plated at 4000 cells/well. After 24 hours, cells were treated with either 0.1% v/v DMSO, 10 µM gefitinib, or 1 µM nilotinib. After 24 hours of treatment, cells underwent TMRM staining as described below.

2.2.8.2 TMRM staining

On day 7 of iAstrocyte differentiation, cells were washed twice with phenol red-free minimum essential medium (MEM) at RT. TMRM dye was diluted in phenol red-free MEM to a final

concentration of 80 nM with or without 10 µM carbonyl cyanide m-chlorophenyl hydrazone (CCCP), so that each DMSO, gefitinib and nilotinib treated fraction of cells was treated with TMRM alone and with TMRM+CCCP. Cells were then incubated for 1 hour at 37°C and 5% CO_2. After the incubation, TMRM and CCCP were removed and cells washed twice with 100 µm phenol red-free MEM, then imaged.

2.2.8.3 Image acquisition and analysis

Prepared plates were imaged live on Opera Phenix imaging system, with 5% CO_2 and 37°C plate heater settings enabled to maintain conditions under which cells were cultured. Once acquired, images were analysed using Columbus software, collecting the following parameters: cell number, number of mitochondria, mitochondrial intensity.

Images uploaded into Columbus software, showing TMRM in the Cy3 channel and DAPI-positive nuclei (Fig. 2.4 A), had 'Find Image Region' function applied to them to find the TMRM-positive cell region as the cell region of interest (Fig. 2.4 B). TMRM-positive cell regions were then converted into Spots, Edges, and Ridges (SER) Gaussian derivative images using 'Filter Image' function (Fig. 2.4 C), which allow for identification of textured features in the image and detection of objects of interest within said textured region. Here, 'SER Ridge' feature was selected. Next, 'Find Spots' function was applied to the TMRM-positive image region to identify mitochondria from the calculated SER Ridge textured features (Fig. 2.4 D). From the identified spots, the population was enriched in spots bigger than 15 pixels and mean region (i.e. TMRM/Cy3-positive) staining intensity higher than 1900 (arbitrary units), using the 'Select Population' function (Fig. 2.4 E). Spots passing these criteria appear in green (Fig. 2.4 F) and are used a readout for mitochondrial numbers. To calculate the intensity of the mitochondria, 'Calculate Intensity Properties' function was applied to the population of selected mitochondria (Fig. 2.4 G), followed by 'Calculate Morphology Properties', which allowed for calculation of the mitochondrial area in μm^2, roundness (on a scale from 0 to 1, where 1 = circle), and ration of width to length. Similarly, intensity and area (in μm^2) of the whole TMRM-positive image region was calculated, values of which were used to calculate the mitochondrial membrane potential (MMP) (Fig. 2.4 H). Normalisation of the mean intensity of the TMRM-positive image region per image area in pixels was used as a readout for the MMP. The mitochondrial network size was calculated as the number of mitochondria

per TMRM-positive image area. The number of mitochondria per cell was calculated by dividing the total number of mitochondria per image by the number of DAPI-positive nuclei.

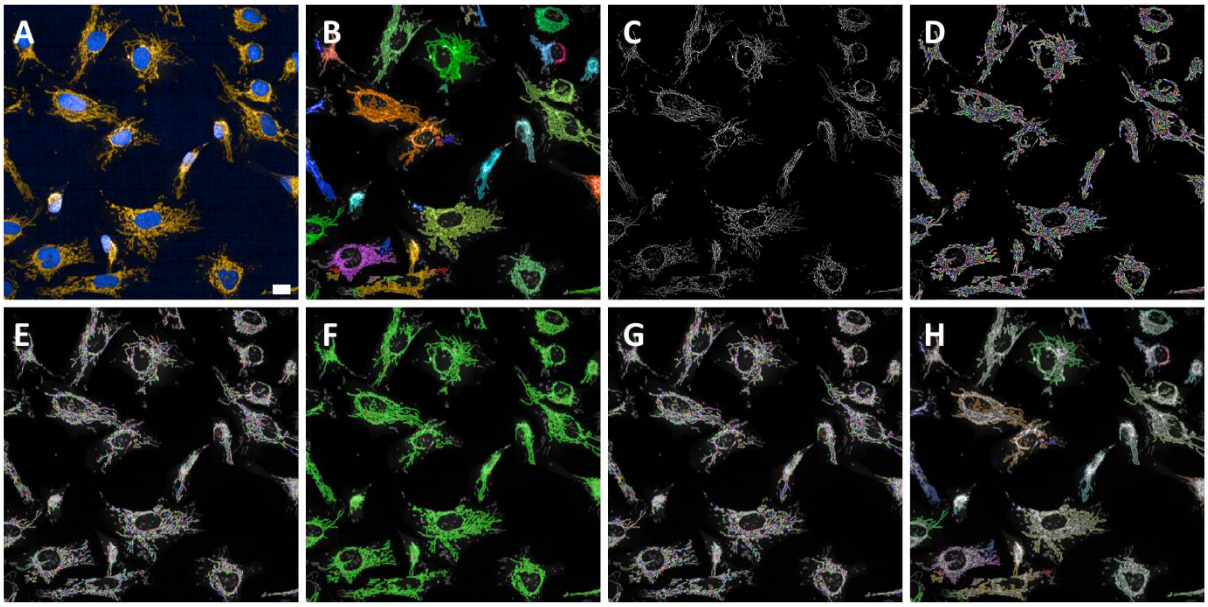

Figure 2.4. Analysis of mitochondrial network using Columbus image analysis software

(A) Input image showing tetramethylrhodamine methyl ester (TMRM) in Cy3 channel and DAPI-positive nuclei. **(B)** 'Find Image Region' highlights the TMRM-positive image region. **(C)** 'Filter Image' function converts TMRM-positive image region into Spots, Edges and Ridges (SER) image, which allows for calculation of texture properties within the image region. **(D)** 'Find Spots' function select spot features within the textured region calculated in C. **(E)** Within spots identified in D, 'Select Population' function filters out spots smaller than 15 pixels and with mean TMRM intensity lower than 1900 (arbitrary units). **(F)** The output of the 'Select Population' step, showing spots passing the threshold criteria in green and those below in red. **(G)** Selected spots, i.e. mitochondria, are subjected to 'Calculate Intensity Properties' and 'Calculate Morphology Properties' to obtain mitochondrial staining intensity, size (in um^2), roundness (0 to 1, where 1 = circle) and width to length ratio. **(H)** Calculate Intensity Properties' and 'Calculate Morphology Properties' are applied to the TMRM-positive cell region. Scale: 20 µm.

2.2.9 Real time quantitative polymerase chain reaction (RT-qPCR)

2.2.9.1 RNA isolation

Frozen cell pellets stored at -80°C were transferred to RT and 700 µl of PureZOL™ RNA isolation reagent (BioRad) was added, mixing cells thoroughly and incubating them for 10

minutes at RT. The RNA isolation was then performed using the Direct-zol™ RNA Miniprep Kit (Zymo Research) in accordance with the manufacturer's protocol.

2.2.9.2 RNA quantification

Extracted RNA stored on ice was subsequently quantified using a NanoDrop ND-1000 Spectrophotometer (Thermo Fisher) and its associated software (ND-1000 v3.8.1). The blank value was obtained from nuclease-free water. 1 µl of each sample was then used to determine RNA quantity in ng/µl. 260 nm /280 nm ratio was examined to check for RNA quality and presence of impurities; the desired 260 nm /280 nm value ranges around 2.

2.2.9.3 Reverse transcription

cDNA synthesis was performed using High-Capacity cDNA Reverse Transcription Kit (Thermo Fisher) according to manufacturer's instructions. Typically, 1 mg of RNA was used for reverse transcription. When this amount of RNA could not be obtained due to low concentration of RNA, the amount was adjusted to accommodate the sample with the lowest RNA concentration and applied to samples within further experimental repeats.

2.2.9.4 Real time quantitative polymerase chain reaction

RT-qPCR master mix was prepared by combining 7 µl of nuclease-free water, 1 µl of 5 µM forward primer (final concentration 250 nM), 1 µl of 5 µM reverse primer (final concentration 250 nM), and 10 µl 2x SYBR Green qPCR Master Mix for a final concentration of 1x SYBR green. Master mix volumes were calculated for duplicate technical repeats of all samples and duplicate wells per primer pair as non-template negative controls, plus 10% extra volume to account for pipetting errors. 19 µl of master mix was dispensed per well of thin wall low-profile 96 x 0.2 ml plate (Appleton Woods), followed by 1 µl of sample per well. Wells were covered with optical flat 8-cap strips (BIOplastics).

RT-qPCR reaction was run on Mx3000p (Stratagene) or CFX96™ Reverse-Transcription System (BioRad) qPCR machines, using the thermal profile described in Table 2.24. Primers used for this work are listed in Table 2.4. β-actin was used as a housekeeping gene in all RT-qPCR experiments due to its stability and resistance to changes after drug treatments tested in this project.

Table 2.24 Thermal profile programme used for RT-qPCR.

Segment		Temperature	Time	Cycles
1: initial denaturation		95°C	10 minutes	1
2:	denaturation	95°C	30 seconds	40
	annealing	x	x	
	extension	60°C	60 seconds	
3: final extension		95°C	60 seconds	1
		55°C	30 seconds	
		95°C	30 seconds	

2.2.9.5 Analysis

Raw cycle threshold (Ct) values for technical replicates were averaged. For each sample, average Ct values for gene of interest were subtracted from corresponding average Ct values for housekeeping gene to obtain ΔCt value. ΔCt value for a control sample was then subtracted from ΔCt values of all samples to obtain ΔΔCt. Calculations were performed on logarithmic scale base 2, hence to obtain fold change values, $2^{-\Delta\Delta Ct}$ function was calculated.

2.2.10 Statistical analysis

All experiments, unless otherwise stated, were performed at least in triplicate. When a triplicate could not be collected, duplicate values were averaged and pooled together with other samples from the same genotype to provide a readout for the whole genotype group and allow for statistical analyses to be performed (see figure legends for more detail).

All statistical analysis was conducted using GraphPad Prism software (versions 7, 8 and 9). **Paired t-test** was used to compare two paired groups, e.g. a drug treatment to its vehicle control (bafilomycin A1 + gefitinib/nilotinib vs bafilomycin A1 treatments in autophagy assays, in experiments comparing DMSO and gefitinib or nilotinib treated conditions in an individual cell line, or in experiments comparing shRNA-RFP to shRNA-ABL1). **Unpaired t-test** was used to compare two unpaired groups, e.g. control to ALS patient iAstrocyte samples in western blotting datasets. **One-sample t-test** was used in qPCR and western blot experiments to compare the delta between samples when the vehicle control or the untreated sample control was set to 100 or 1. **Mann-Whitney test** was used to compare groups with two two variables where one variable represent 1 or 100 and does not possess a standard deviation, e.g. the same conditions as described above but across a dataset with multiple such pairings,

e.g. TDP-43 and TDP-35 western blotting data comparing DMSO to gefitinib or nilotinib. **One-way ANOVA with Tukey's multiple comparisons** was used to compare groups characterised by three variables e.g. healthy control and ALS patient iAstrocytes, as well as their corresponding treatments. **One-way ANOVA with Šidák's multiple comparisons** was used to compare to compare groups characterised by two variables across multiple lines e.g. drug treatment to its DMSO vehicle across multiple cell lines or genotypes. **Kruskal-Wallis test** was used to analyse datasets where one condition (usually untreated) was set to 100 with no SD. **Two-way ANOVA with multiple comparisons** was used to compare groups characterised by two variables, e.g. control and patient samples and drug treatments simultaneously. Statistical significance is delineated throughout this work as follows: *P<0.05, **P<0.005, ***P<0.001, ****P<0.0001.

3 Uncovering the mode of action of gefitinib in ALS

3.1 Introduction

Traditional *de novo* drug discovery approaches are costly and time consuming, taking on average 10-17 years to complete and resulting in millions of dollars of expenditure (Ashburner & Thor, 2004). Moreover, these efforts do not always culminate in the introduction of new compounds onto the market, as clinical trials can fail due to safety and/or efficacy concerns (Cummings, Morstorf, & Zhong, 2014). Neurodegenerative diseases (Cummings, 2018; Gordon & Meininger, 2011; Hiroshi Mitsumoto et al., 2014) and indeed ALS have been particularly affected by these failures (Petrov et al., 2017), hence new approaches need to be adopted.

Drug repurposing could offer a new, more efficient way of exploring potential targets and treatment candidates for disease. The repurposing pipeline bypasses the need for costly and time-consuming target selection and lead optimisation procedures, involving a myriad of *in vitro*, *in vivo* and *ex vivo* screenings, as well as a polypharmacological characterisation that needs to be performed for novel molecules. Since drug bioavailability and absorption, distribution, metabolism, excretion, and toxicity (ADMET) (van de Waterbeemd & Gifford, 2003) have already been characterised, drug repurposing takes advantage of molecules with a proven safety profile and an approval for a use in humans (Ashburner & Thor, 2004). However, it is important to remember that all the biosafety profiling has been conducted in the context of the original disease that the compound was in the use for, therefore drug repurposing candidates would still need to be subjected to clinical trials. It is especially critical to consider the array of side effects that might occur. If the compound was initially used for a disease of the periphery, side effects in patients with CNS disorders need to be fully understood in order to appreciate the balance between the costs and potential benefits of the compound in a different disease environment (Ashburner & Thor, 2004). Of crucial importance for neurodegenerative disorders is the CNS permeability of the drug, which might not have been a subject of prior investigations. Drug repurposing pipelines must thus take into account any necessary methods of increasing the bioavailability of the molecule in the CNS if the drug is to be approved for use in a new cohort of patients.

Lack of knowledge of the mode of action of a compound is one of the main overlooked factors leading to failures of phase 2 clinical trials (Cummings, Morstorf & Zhong, 2014). Therefore,

understanding the mechanisms through which a drug exerts its function in the disease is of a paramount importance for generation of new therapies. This chapter aims to uncover the mechanism of action of gefitinib, a drug identified as having a repurposing potential in ALS.

3.1.1 Identification of gefitinib using AI

Gefitinib was identified as a drug with a repurposing opportunity for ALS in a high-throughput data scan conducted on Precede system by our collaborators at BenevolentAI, with an aim to build a comprehensive *knowledge graph* (figure 3.1) based on the literature search. This system, driven by a combination of deep learning and natural language processing, is capable of reading, processing and ultimately "understanding" scientific literature and patents. To create a meaningful *knowledge graph*, Precede semantically integrates information from 'structured' (public chemical databases, transcriptomic databases, etc) and 'unstructured' (PubMed, Web of Knowledge) data sources. It also assigns a probability score of 0 to 1 to rank how good of an association there is between two generic terms of interest, for example "ALS" and "TDP-43" would receive a score of 1 (i.e. there is a real link between them, they do not just appear in the same sentence).

The search was able to return 100 compounds showing a repurposing promise after a 20-minute literature scan. Compounds were subsequently reviewed in terms of their disease relevance, CNS penetrance ability, relevance of molecular targets, and signalling pathways involved. Top 20 compounds with satisfactory profiles were subjected to deep investigation and hypothesis generation using a Scaffold Query Tool (SQT) workflow (figure 3.1). SQT requires a person to build a knowledge graph based on elements of interest, such as diseases, genes or proteins, pathways, specific processes, or known drugs. Some elements of the workflow may be concrete (e.g. disease: ALS, gene/protein: SOD1, pathway: p53-signalling pathway) and other parts of the workflow may be left as unknowns for the system to 'fill in' by finding suitable suggestions. Once the connection is established, any of the elements can be blanked out to check if the connection still appears, thus allowing for further validation to be performed. Moreover, further elements can be added to expand the knowledge graph, such as downstream/upstream targets, cell types, specify if you want the connection to be novel or already established etc.

The SQT hypothesis validation and in-depth review of the known mechanisms of action of the top 20 compounds resulted in a selection of 5 final compounds with the best polypharmacological profiles and CNS relevance being taken forward for an *in vitro* validation in a co-culture model of ALS.

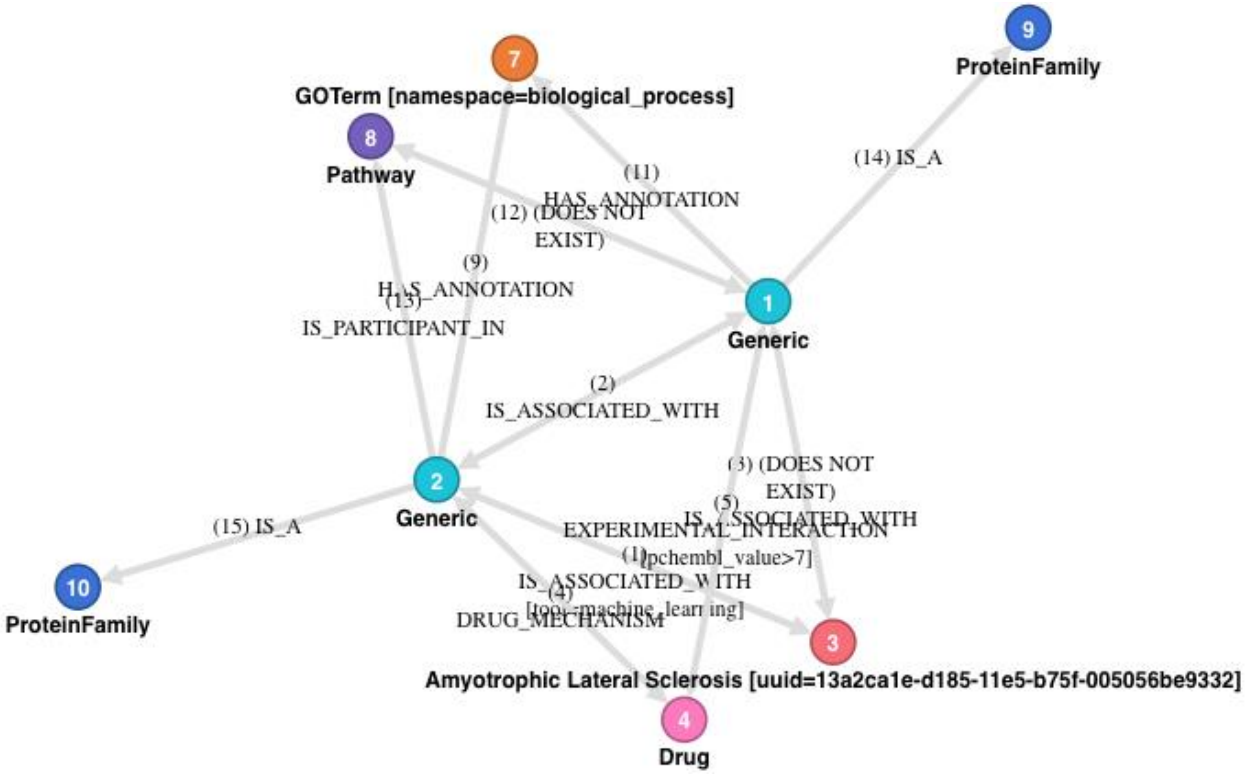

Figure 3.1 Scaffold Query Tool

A method of building a knowledge graph and generating scientific hypotheses, it allows for an exploration of multiple queries based on a battery of simple commands. Image courtesy of Dr Mark Rackham of BenevolentAI.

3.1.2 Gefitinib: use, properties, and function

Lung cancer constitutes the main cause of death worldwide, of which non-small cell lung cancer (NSCLC) represents approximately 80% of all deaths. 15% of all NSCLC patients harbour a mutation in epidermal growth factor receptor (EGFR; Xin et al., 2020). In an effort to combat EGFR-driven NSCLC, a generation of chemotherapy compounds targeting EGFR, erlotinib and gefitinib, was introduced in the mid-2000s. Gefitinib (figure 3.2), marketed as Iressa®, was first approved by the FDA in 2005. Over the years, its usage in cancer has extended beyond NSCLC to colon and breast cancers (Kazandjian et al., 2016). Amongst its proposed mechanisms of action in NSCLC cell lines are autophagic flux induction, p65 regulation, cell

growth and migration inhibition (Pan et al., 2015; Rothschild et al., 2006). Gefitinib is not currently in use for diseases other than cancer.

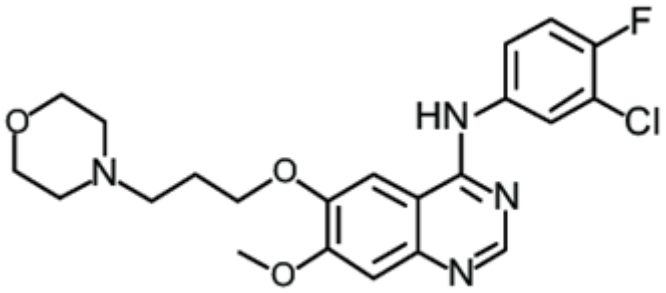

Figure 3.2 Molecular structure of gefitinib

Source: (Yuan et al., 2014).

3.1.3 Results leading up to this study

Unless stated otherwise, all work described in the following section was conducted by Dr Matthew Stopford.

The above described AI-driven methods resulted in a selection of 5 compounds for an *in vitro* validation: ambroxol, erlotinib, gefitinib, siramesine, and RTA408. These compounds were validated in a pathophysiologically-relevant high-throughput co-culture model of ALS, which models the endogenous ALS astrocyte toxicity against motor neurons. As previously published, iAstrocytes express vimentin (see figures 3.9 and 3.10), cell surface glycoprotein CD44, EAAT2, glial fibrillary acidic protein (GFAP) (Gatto et al., 2021), aquaporin 4 and S100 calcium binding protein B (S100β) (Meyer et al., 2014), and do not express cytoplasmic nestin or nuclear paired box 6 (Pax6) markers of neuronal progenitors which are richly expressed in iNPCs (Meyer et al., 2014). Wild-type mESC-derived motor neurons were plated on control and ALS iAstrocytes, treated either with a compound of interest or vehicle 24h prior. The co-culture plates were screened once every 24h for 3 days, and the final readout of the experiment was the rescue of motor neuronal survival with the drug compared to vehicle only. Figure 3.3 summarises the co-culture screening workflow.

Of the 5 tested compounds, gefitinib consistently resulted in a significant rescue of motor neurons cultured on 3 out of 3 C9orf72 and 2 out of 3 sALS iAstrocyte lines (figure 3.4).

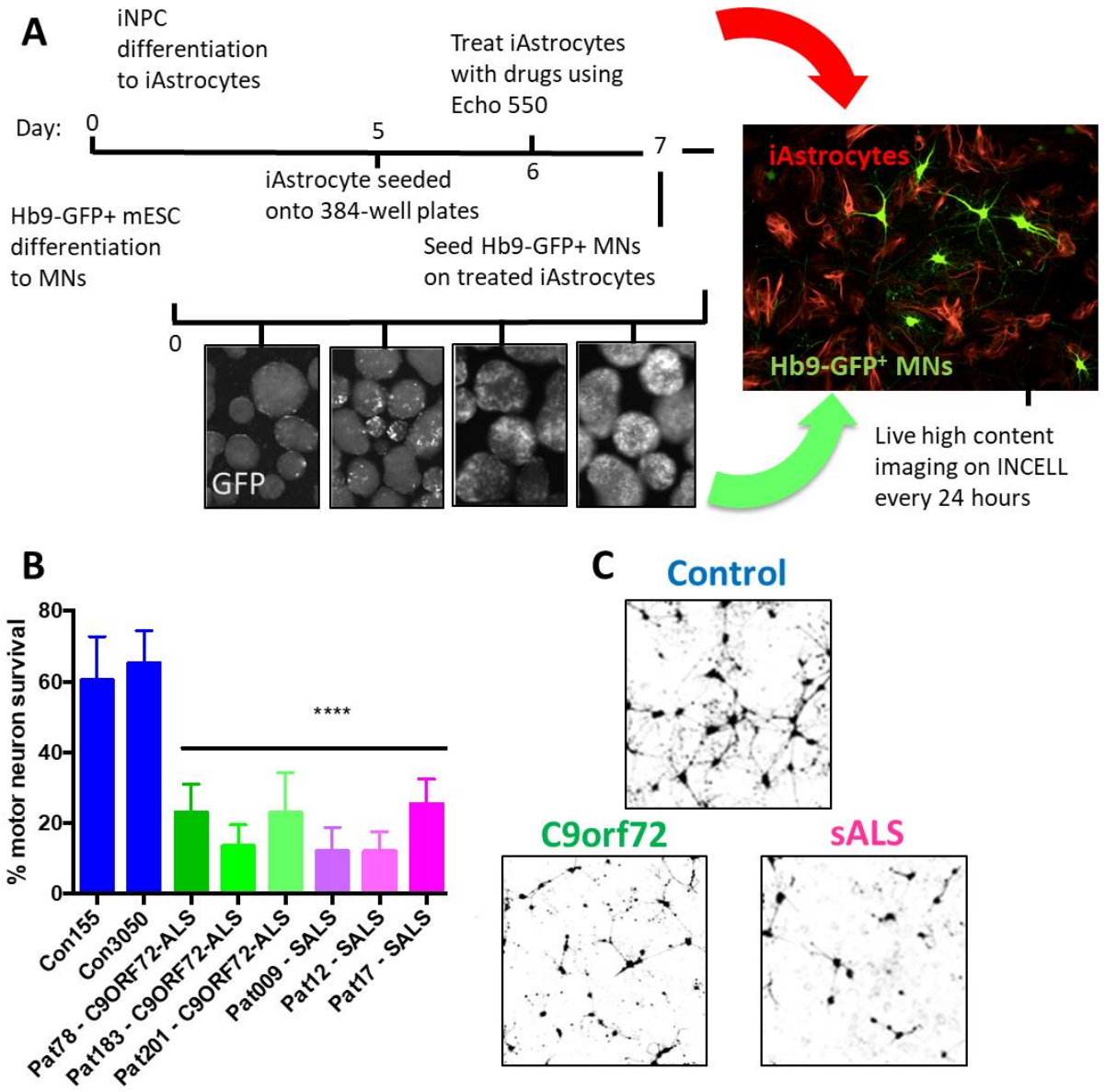

Figure 3.3 High-throughput co-culture screening model

iAstrocyte differentiation from iNPCs and differentiation of MNs from Hb9-GFP^{+} mESC take place simultaneously over a 7-day period. (**A**) iAstrocytes are seeded onto screening plates on day 5 of differentiation and treated with compound of interest the following day. MNs are plated on top of treated iAstrocytes on day 7. **(B)** The resulting co-culture system is screened for 3 days once every 24h This pathophysiologically-relevant model of ALS recapitulates the non-cell autonomous component of the disease. Data courtesy of Dr Matthew Stopford. **(C)** In contrast with controls, MNs cultured on untreated ALS iAstrocytes show a significant decrease in cell numbers. Images courtesy of Dr Matthew Stopford.

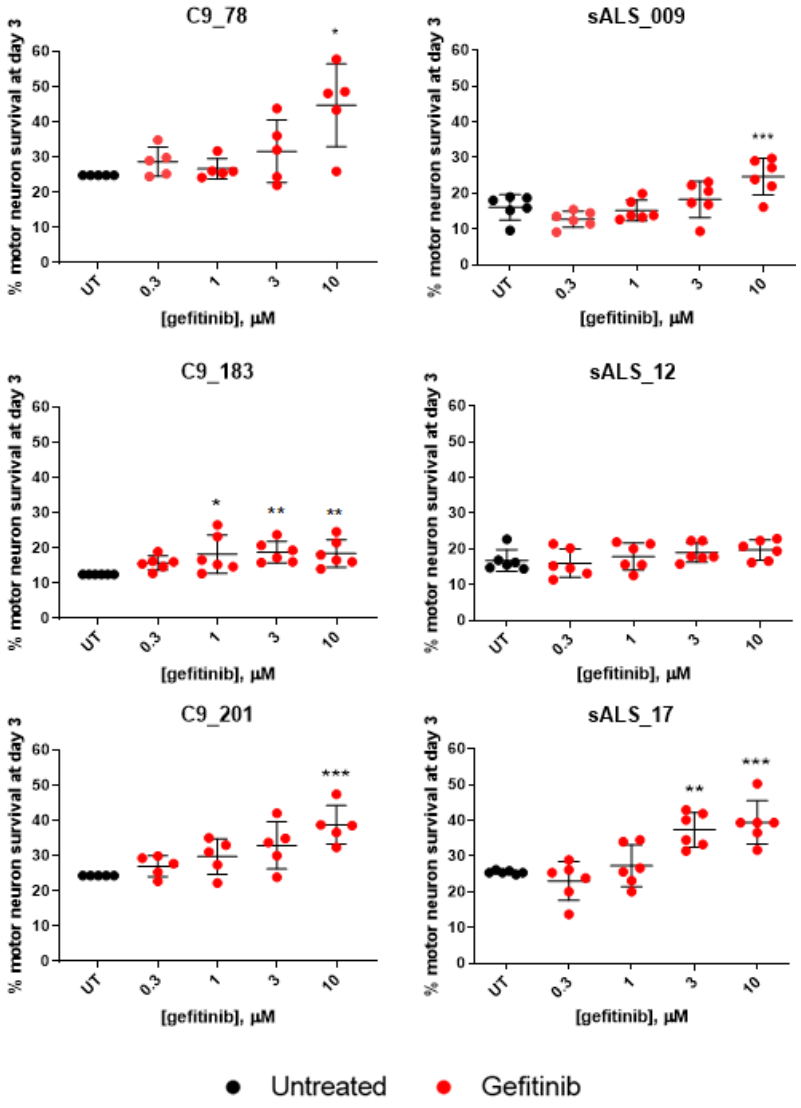

Figure 3.4 Results of the co-culture screening with gefitinib

A rescue of motor neuron survival after drug treatment in 5 out of 6 ALS iAstrocyte lines was observed. *P<0.05; **P<0.01; ***P<0.001. Kruskal-Wallis test with Dunnett's multiple comparisons post-hoc test; n=6, experimental replicates. Data courtesy of Dr Matthew Stopford.

Marketed primarily as an EGFR inhibitor, gefitinib targets multiple kinases. A collaborative effort led by BenevolentAI and Eurofins Cerep (Dundee) resulted in a kinome screening revealing target kinases and the potency with which gefitinib engages them (table 3.1).

Table 3.1 Top 10 kinases targeted by gefitinib, in order of binding affinity.

Kinase name	Kinase symbol	pKd
epidermal growth factor receptor	EGFR	9.3
cyclin G associated kinase	GAK	7.9
interleukin 1 receptor associated kinase 1	IRAK1	7.2
ABL proto-oncogene 1, non-receptor tyrosine kinase	ABL1	6.6
mitogen-activated protein kinase kinase kinase 19	YSK4	6.6
MAP kinase interacting serine/threonine kinase 1	MKNK1	6.5
homeodomain interacting protein kinase 4	HIPK4	6.5
erb-b2 receptor tyrosine kinase 4	ERBB4	6.4
casein kinase 1 epsilon	CSNK1E	6.4
serine/threonine kinase 10	LOK	6.3

The lack of understanding of the mechanisms involved in astrocyte toxicity in ALS makes it difficult to identify what pathways are involved in neuroprotection. For this reason, the focus of this first chapter is to interrogate gefitinib's mechanism(s) of action involved in the motor neuron rescue in the co-culture system.

The aims of this chapter are:

1. To unveil the effect of gefitinib treatment on ALS iAstrocytes;
2. To uncover the mechanism of action of gefitinib in ALS by mapping out its effect on TDP-43 proteinopathy;
3. To determine the changes in autophagy and mitochondrial function in iAstrocytes following a treatment with gefitinib.

3.2 Results

3.2.1 Gefitinib-driven changes in iAstrocyte numbers and morphology

As described in section 3.1.3, treatment of ALS iAstrocytes with gefitinib resulted in a rescue of motor neuronal survival in a co-culture screening. However, this result did not convey any specific information regarding the effect of the drug on iAstrocytes themselves. This section will describe the effect of gefitinib on iAstrocytes in terms of cytotoxicity, cell numbers, proliferation, and cell morphology.

3.2.1.1 Cell number analysis

3.2.1.1.1 Cell number

Given the use of gefitinib in chemotherapies, where the goal is to stop the abnormal growth of hyperproliferative tumour cells, the effect of gefitinib on iAstrocyte cell number was measured. For this purpose, iAstrocytes were plated in fibronectin-coated 96-well optical plates on day 4 of differentiation and treated with 0.1% DMSO (v/v) or 10 µM gefitinib the following day. Cells were fixed with 4% PFA 48 hours after treatment and stained for a nuclear marker DAPI. The cell number was determined by automated quantification of nuclei in the DMSO and gefitinib-treated wells, using Columbus image analysis software. An example of a nuclear mask applied for this quantification can be found in figure 3.8.

Since the same number of cells was plated per well, gefitinib-treated cells were compared to their vehicle-treated counterparts to determine the effect of the drug on iAstrocyte numbers. Gefitinib treatment resulted in a significant reduction in iAstrocyte cell numbers in CTR_155v2, C9_78, sALS_009 and sALS_12 (figure 3.6 A). The effect of gefitinib on CTR_AG08620, C9_183, C9_201, and sALS_17 was not significant, possibly due to variability in the dataset. When iAstrocyte lines within each genotype were pooled together, the cytostatic effect resulted in a statistical significance for both the control and sALS lines (figure 3.6 B).

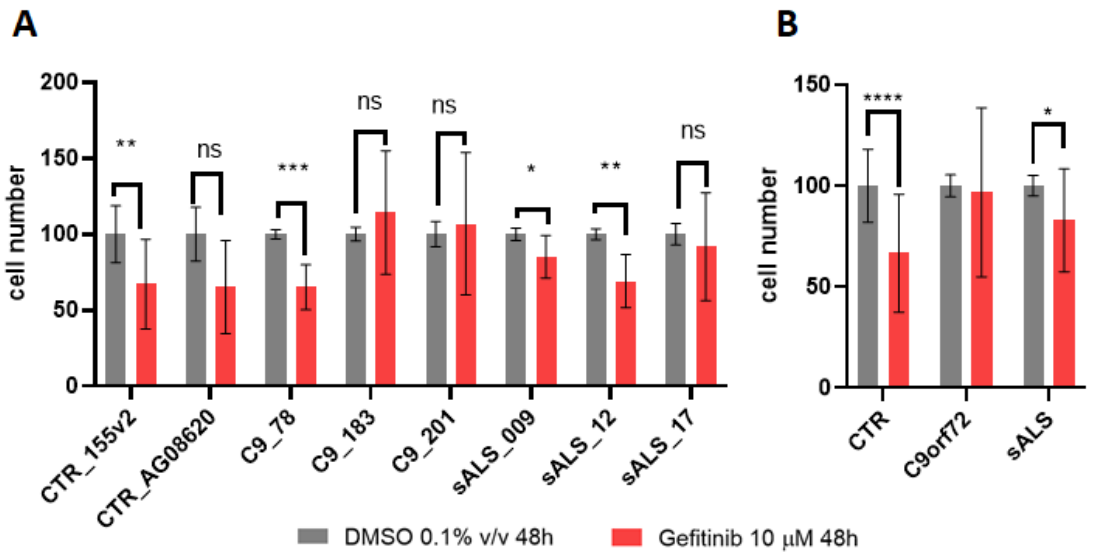

Figure 3.5 Effect of gefitinib on iAstrocyte cell numbers

(A) Quantification of iAstrocyte cell numbers in individual cell lines; n=3-6 experimental repeats; mean ± SD; data normalised to DMSO=100; *P<0.05; **P<0.01; ***P<0.001; **(B)** Quantification of iAstrocyte cell numbers per genotype; n=3 per genotype; CTR includes CTR_155v2 mean from n=5 experimental repeats, CTR_AG08620 mean from n=3 experimental repeats and CTR_3050 mean from n=2 experimental repeats; mean ± SD; data normalised to DMSO=100; *P<0.05; ****P<0.0001; drug treatment effect: ****P<0.0001; two-way ANOVA with Tukey's multiple comparisons.

3.2.1.1.2 LDH assay

The cytostatic effect of gefitinib was investigated further by Dr Matthew Stopford in a lactate dehydrogenase (LDH) assay. Briefly, this colorimetric assay measures levels of LDH released by the cells, which acts as a direct measurement of apoptosis (figure 3.6). 10 mM of sodium azide cytotoxin was used as a positive control for cell death, whilst a cell lysate, obtained by treating cells with a cell lysis buffer in the assay plate, was used as a direct readout for a maximum LDH release and apoptosis. Cytotoxicity values were calculated as a percentage of the cell lysate values (=100%).

iAstrocytes used for the initial co-culture experiments with gefitinib, C9_78, were used in the LDH assays at two time points, 24h (figure 3.5 A) and 72h (figure 3.5 B). At both treatment timepoints, 10 µM gefitinib carried approximately 30% cytotoxicity.

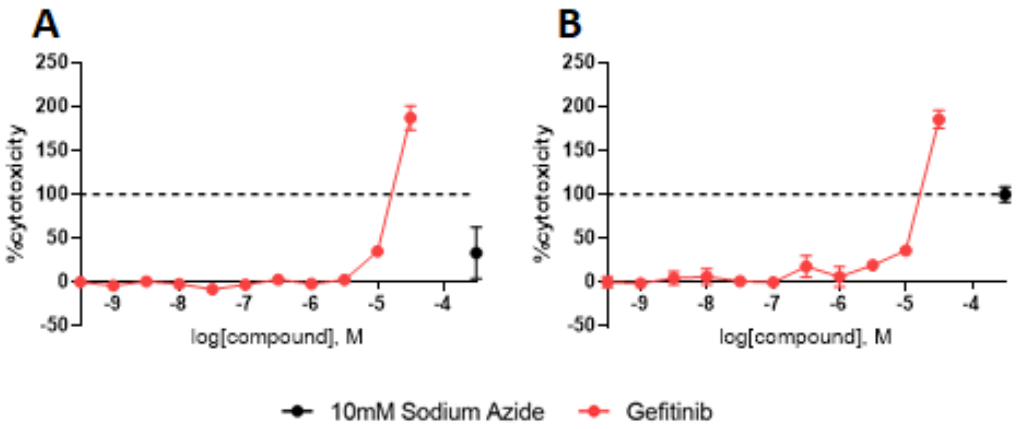

Figure 3.6 LDH cytotoxicity assay in C9_78 iAstrocytes

(A) iAstrocytes were treated with various concentrations of gefitinib for 24 hours or **(B)** 72 hours. 10 mM sodium azide was used as a positive control for cytotoxicity. Cell lysis buffer was applied as a positive control for cytotoxicity (i.e. 100% cytotoxicity). n=3-7; data relative to cell lysis; data are mean ± SD.

3.2.1.1.3 Cell proliferation

To determine if gefitinib affects cell proliferation in our model, iAstrocytes were stained for the proliferation marker protein Ki-67 (Ki67) 48h post-gefitinib or DMSO treatment (representative image of staining in figure 3.7 A). ICC-stained images were analysed for presence of nuclear Ki67 foci using Columbus image analysis software and a percentage of nuclei with Ki67 foci was calculated against the total cell number.

With an exception of CTR_155v2, which showed an increase in the number of Ki67-positive nuclei, and C9_78 where a decrease in the number of Ki67-positive nuclei was observed, gefitinib did not have a significant effect on the proliferation rate of iAstrocytes (figure 3.7 B).

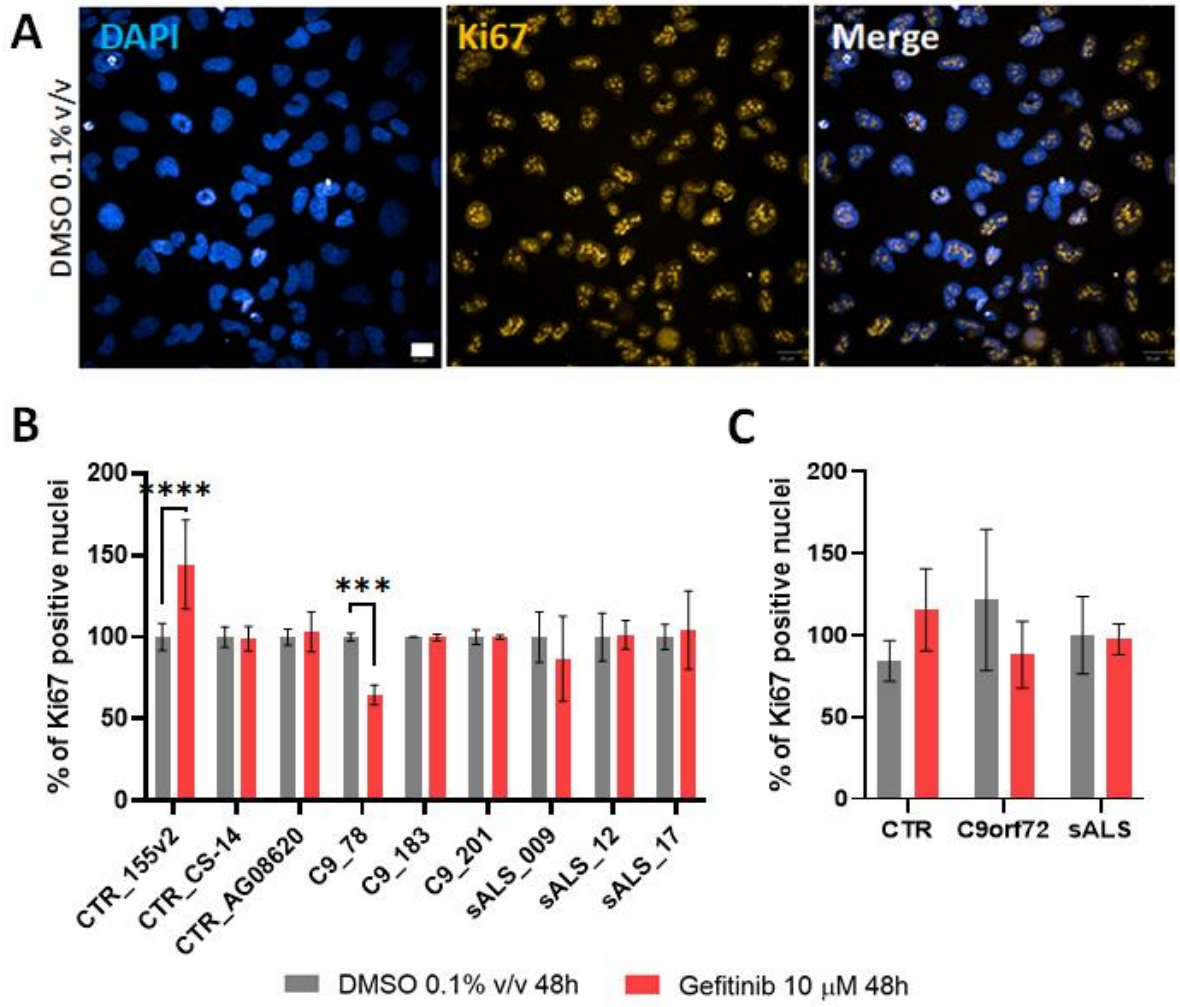

Figure 3.7 Expression of nuclear Ki67 in iAstrocytes

(A) Representative images of the staining, as observed in C9_183 cells. Scale: 20 µm. **(B)** Quantification of % of Ki67-positive nuclei after treatment with 10 µM gefitinib for 48h. n=3-6 experimental repeats (except CS-14 n=2); mean ± SD, normalised to DMSO=100; two-way ANOVA with Šidák's multiple comparisons; ***P<0.001; ****P<0.0001; cell line effect ****P<0.0001, cell-drug interaction ****P<0.0001, drug effect ns; **(C)** Quantification of % of Ki67 positive cells per genotype after treatment with 10 µM gefitinib for 48h; n=3 per genotype; CTR includes CTR_155v2 mean from n=6 experimental repeats, CTR_AG08620 mean from n=4 experimental repeats and CTR_CS-14 mean from n=2 experimental repeats; mean ± SD, normalised to DMSO=100; two-way ANOVA with Šidák's multiple comparisons; ns.

3.2.1.2 Cell morphology

Among its important functions in lung carcinomas, gefitinib has been reported to regulate cytoskeletal remodelling pathways, which result in an increased susceptibility of tumour cells

to slow proliferation or succumb to apoptosis (Pan et al., 2015). Cytoskeletal remodelling manifests itself in changes of cell shape and size. In order to examine the effect of gefitinib on cellular morphology, iAstrocytes were stained for a cytoskeletal marker vimentin and their morphology was measured in terms of cell roundness and cell area. In order to do so, a cytoplasmic mask was applied to images using Columbus image analysis software (figure 3.8) and the selected parameters were calculated automatically. Cell roundness parameter was set from 0 to 1, where 1 represented a circle. Cell area was measured in μm^2. Example images of C9orf72 and sALS iAstrocytes stained with vimentin before and after treatment are shown in figures 3.9 and 3.10 respectively.

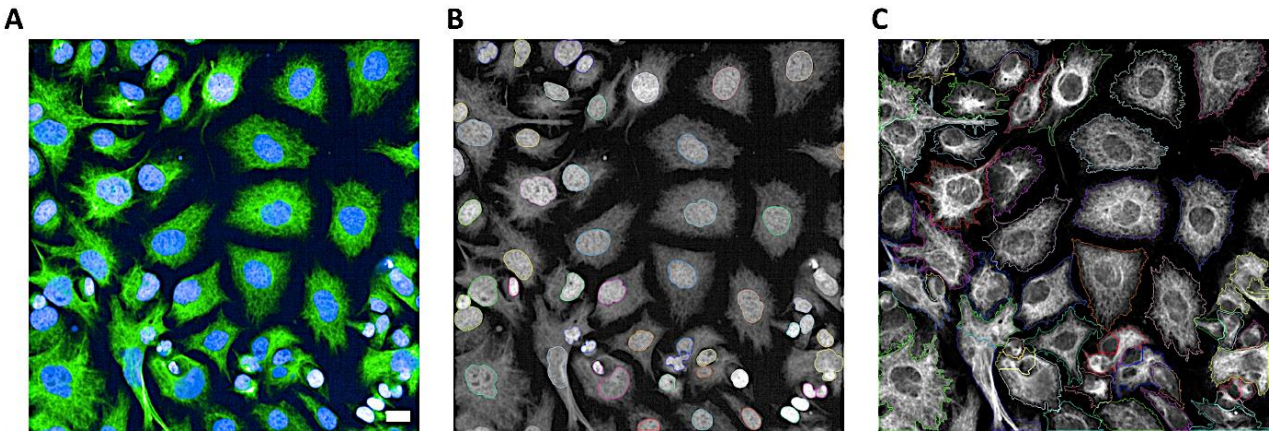

Figure 3.8 Columbus image analysis parameters used to calculate iAstrocyte morphology

Given a vimentin-stained image **(A)**, Columbus was prompted to automatically select DAPI-stained nuclei **(B)**. This process was also used to determine cell numbers, as shown in figure 3.7. Once provided the information on the fluorescence channel covering the cytoplasmic staining, the software drew approximate outline around the cytoplasm **(C)**, which was then used to automatically determine the cell roundness (0 to 1, with 1 representing a circle), and cell area in μm^2. Scale: 20 µm.

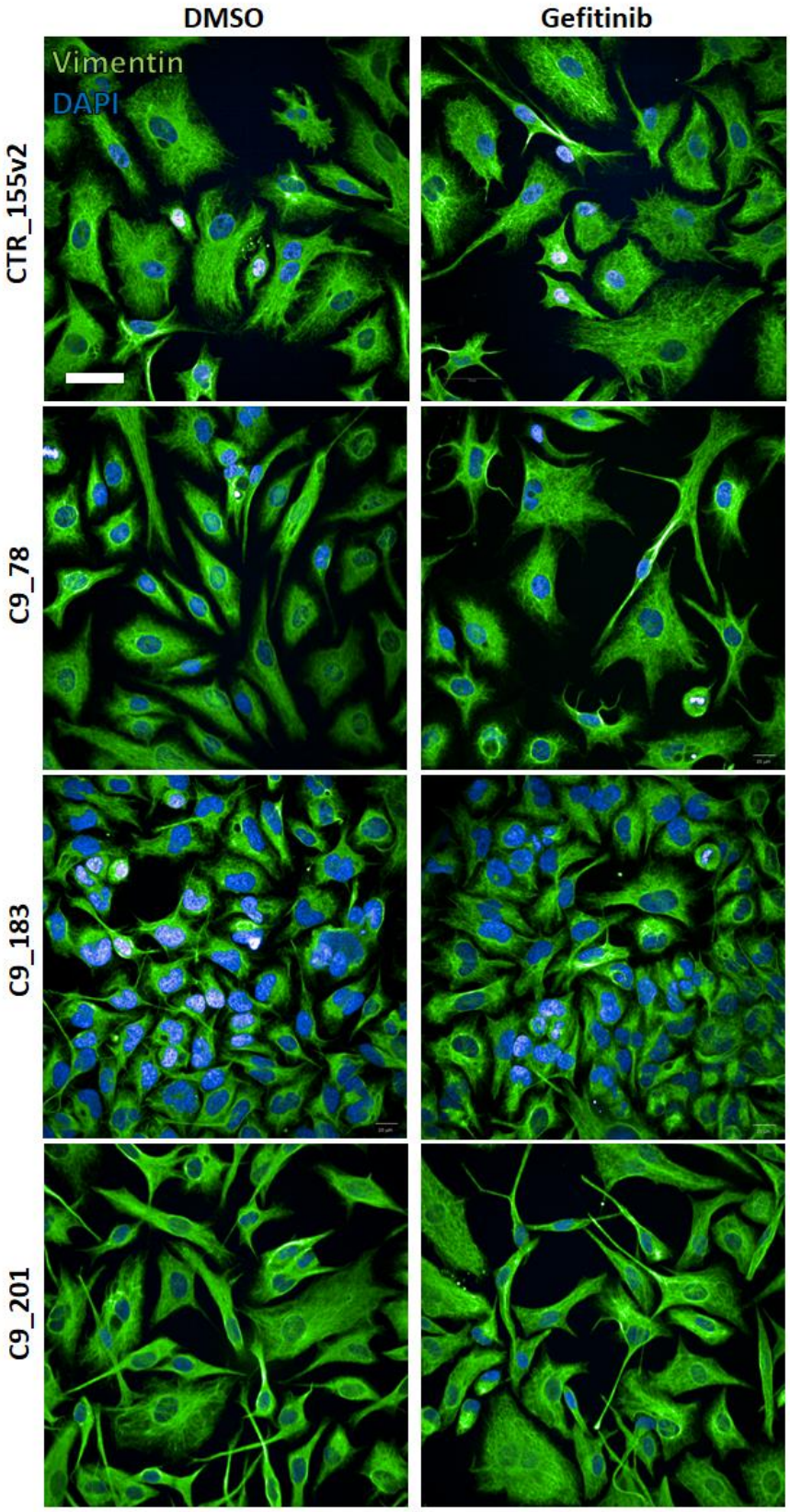

Figure 3.9 Representative images of control and C9orf72 iAstrocytes

Cell morphology after treatment for 48h with 0.1% v/v DMSO or 10 µM gefitinib. Scale: 50 µm.

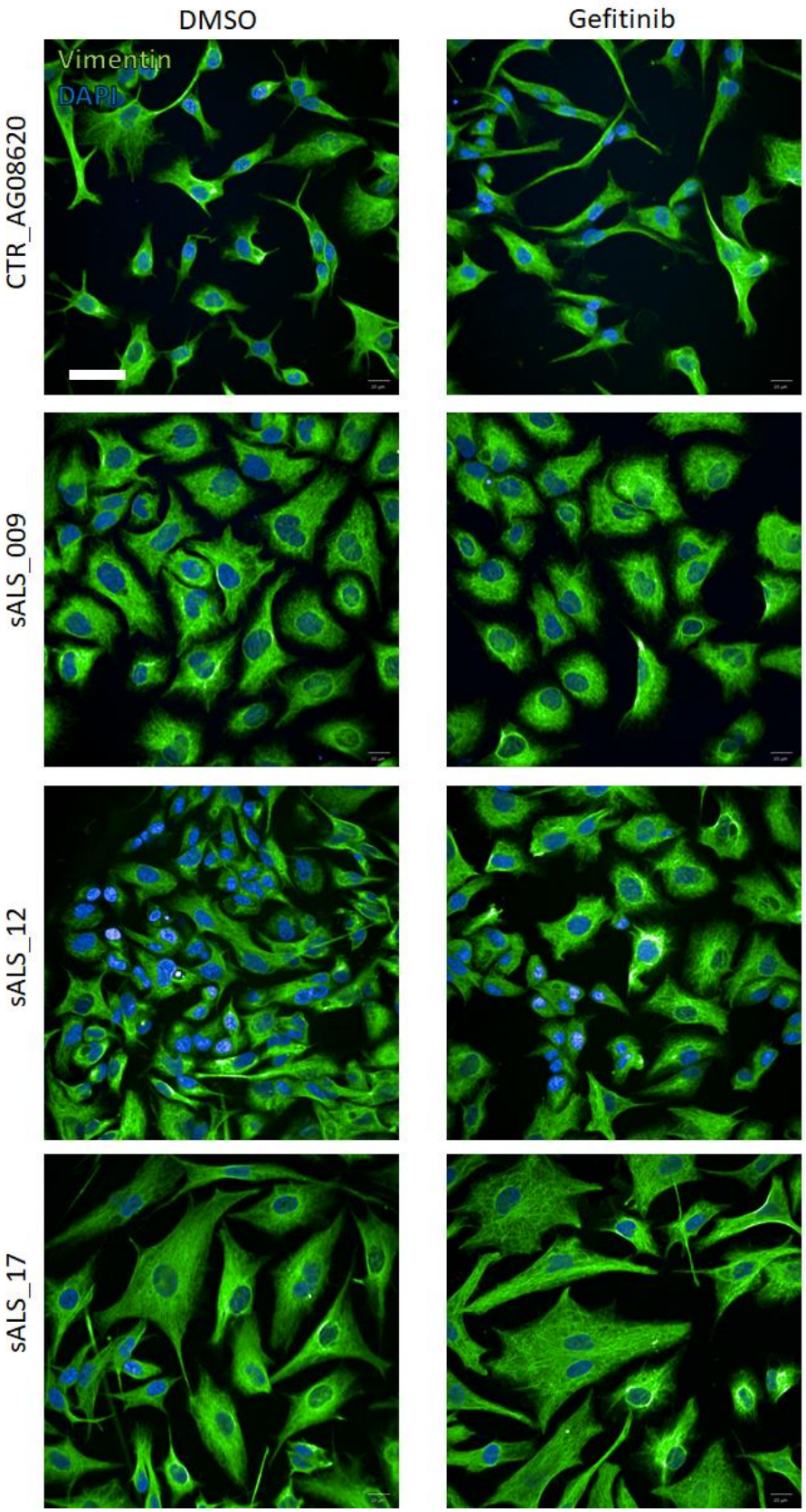

Figure 3.10 Representative images of control and sALS iAstrocyte

Cell morphology after treatment for 48h with 0.1% v/v with DMSO or 10 µM gefitinib. Scale: 50 µm.

When analysing the effect of gefitinib treatment on each individual line, drug treatment resulted in a significant increase in cell roundness only in sALS_009 and sALS_17, while in the other cell lines only a trend was observed (figure 3.11 A). However, upon pooling together all cell lines within the same genotype, it became clear that gefitinib leads to an overall significant increase in cell roundness in iAstrocytes from all genotypes (figure 3.11 B). Gefitinib had no effect on overall iAstrocyte cell area at neither individual cell line nor genotype basis (figure 3.11 C).

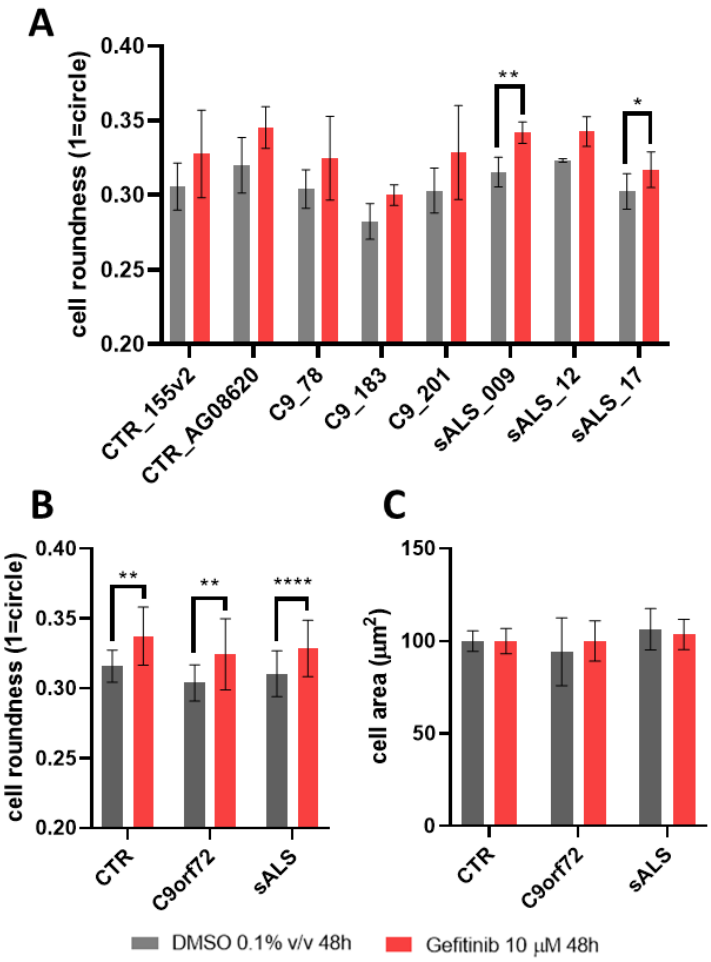

Figure 3.11 Changes in iAstrocyte morphology upon treatment with DMSO or gefitinib

(A) Quantification of cell roundness in individual lines; n=3-4 experimental repeats; mean ± SD; two-way ANOVA with Šidák's multiple comparisons test; *P<0.05, **P<0.005. (**B**) Quantification of cell roundness per genotype; n=3 per genotype; CTR includes CTR_155v2 mean from n=5 experimental repeats, CTR_AG08620 mean from n=3 experimental repeats and CTR_3050 mean from n=2 experimental repeats; mean ± SD; two-way ANOVA with Šidák's multiple comparisons test; **P<0.005,

***P<0.0005, ****P<0.0001. (**C**) Quantification of cell area per genotype after drug treatment; n=3 per genotype; CTR includes CTR_155v2 mean from n=5 experimental repeats, CTR_AG08620 mean from n=3 experimental repeats and CTR_3050 mean from n=2 experimental repeats; mean ± SD; data relative to DMSO=100; two-way ANOVA with Šidák's multiple comparisons test; ns.

3.2.1.3 Target engagement

Cell number and morphology assessments of iAstrocytes highlighted that gefitinib does have a mild effect on their growth and shape. These parameters might be affected by target engagement with gefitinib's primary target, i.e. EGFR (Rothschild et al., 2006, Pan et al., 2015), thus next I moved to investigate gefitinib's on-target efficacy. Gefitinib's on-target efficacy was measured by interrogating levels of *EGFR* mRNA via RT-qPCR and pEGFR/EGFR protein dynamics were analysed via western blotting. For this set of experiments, C9_78 and its age- and sex-matched control CTR_3050 were selected based on C9_78's consistent positive response to gefitinib, as observed in co-culture experiments.

3.2.1.3.1 Transcriptional regulation of EGFR

RNA was isolated from cell pellets treated for 1h, 6h, 12h and 24h with 10 µM gefitinib (to measure changes in *EGFR* levels over time), 0.1% (v/v) DMSO vehicle, or untreated, and retrotranscribed as described in section 2.2.6. Each qPCR plate contained C9_78 and CTR_3050, as well as an untreated condition from the same lines, in order to determine the baseline expression of *EGFR* transcript in ALS iAstrocytes.

Upon normalisation of C9_78 EGFR level to that of CTR_3050, it was determined that C9_78 iAstrocytes express significantly lower levels of *EGFR*. In C9_78, gefitinib treatment had no effect on *EGFR* levels at any of the tested timepoints, while in CTR_3050, *EGFR* expression was significantly reduced at 12h post-treatment (figure 3.12).

3.2.1.3.2 EGFR and pEGFR protein levels

Having failed to demonstrate a robust *EGFR* perturbation at mRNA level, the next step was to investigate EGFR protein levels and phosphorylation, as gefitinib is known to act as a kinase inhibitor. Here, all three C9orf72 lines were used, together with their matched controls.

Similar to the transcript validation, significantly lower levels of EGFR and pEGFR were observed in 2 out of 3 C9orf72 iAstrocytes in comparison with controls. Gefitinib treatment resulted in decreased levels of pEGFR in all treated lines (figure 3.13).

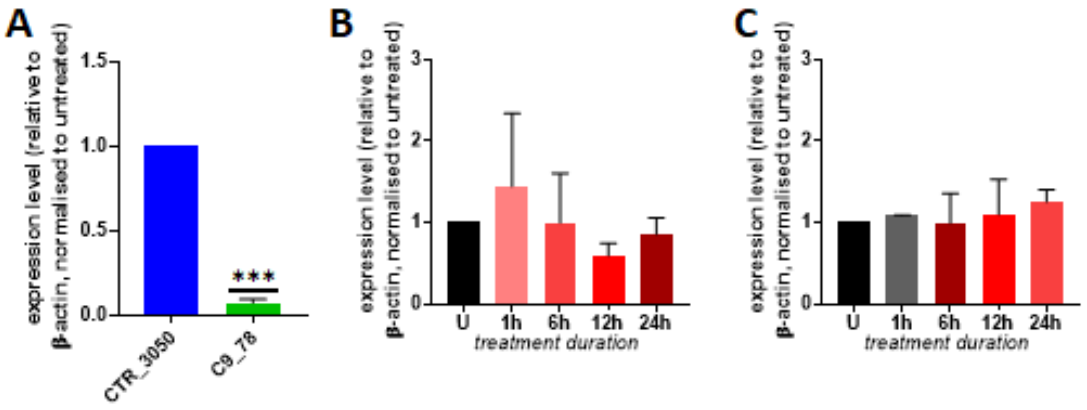

Figure 3.12 EGFR expression levels in iAstrocytes

Cells were treated with 10 µM gefitinib for 1h, 6h, 12h and 24h. **(A)** Baseline levels of *EGFR* in C9_78 compared to CTR_3050 (set to represent 1); n=3 experimental repeats; mean ± SD; one-sample t-test; ***P<0.0005. **(B)** Effect of gefitinib treatment on *EGFR* in CTR_3050; n=3 experimental repeats (except 1h n=2); mean ± SD; data relative to *EGFR* levels in untreated (U) cells; Kruskal-Wallis test; ns. **(C)** Effect of gefitinib treatment on *EGFR* in C9_78; n=3 experimental repeats (except 1h n=2); mean ± SD; data relative to *EGFR* levels in untreated (U) cells; Kruskal-Wallis test; ns

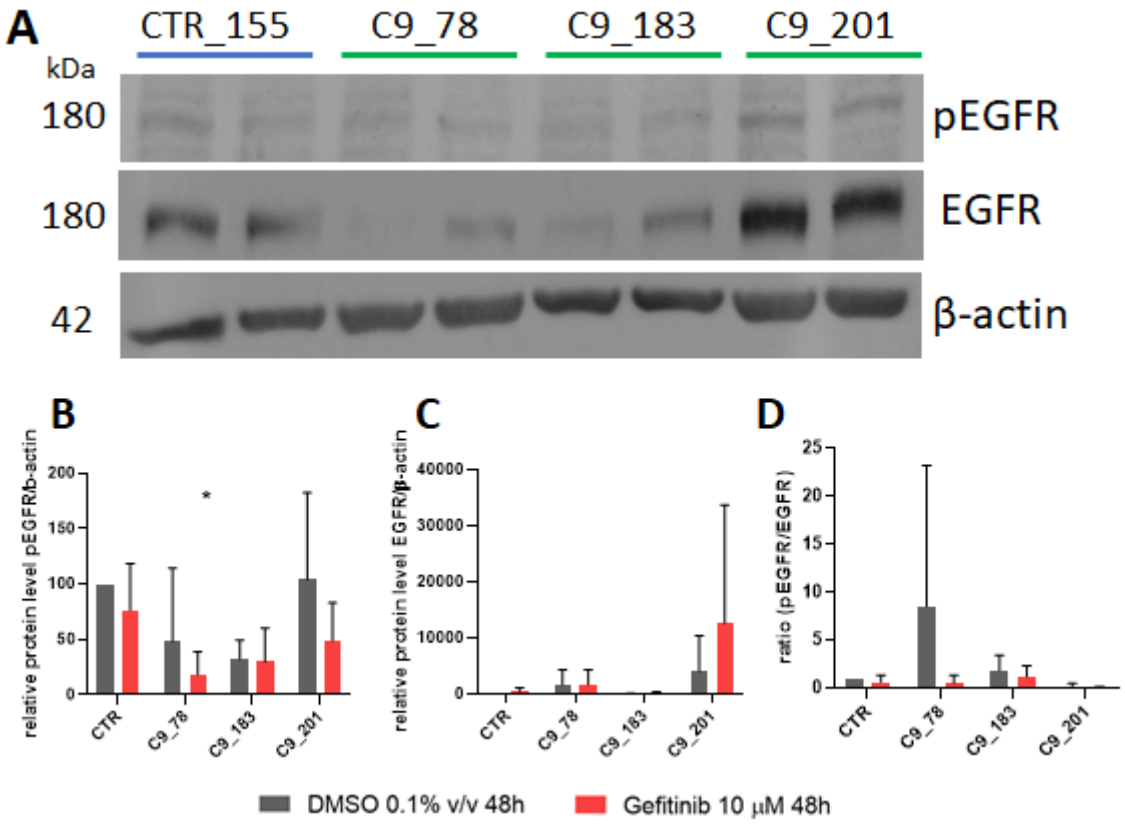

Figure 3.13 Expression of pEGFR and total EGFR protein in 3 controls and 3 C9orf72 iAstrocytes

(A) Representative western blotting image. **(B)** Quantification of pEGFR level; n=3-4 experimental repeats; CTR includes mean results of CTR_155 from n=3 experimental repeats and CTR_3050 mean from n=2 experimental repeats; mean with SD; two-way ANOVA with Tukey's multiple comparison test, drug effect *P<0.05. **(C)** Quantification of EGFR levels. **(D)** Quantification of pEGFR/EGFR ratio; n=3-4 experimental repeats; CTR includes mean results of CTR_155 from n=3 experimental repeats and CTR_3050 mean from n=2 experimental repeats; mean with SD; two-way ANOVA with Tukey's multiple comparison test, all comparisons ns (applicable to C and D).

3.2.1.3.3 Cyclin G2 regulation

In the absence of EGFR upregulation or hyperphosphorylation across the majority of C9orf72 iAstrocyte lines, I concluded that the beneficial effect of gefitinib in co-culture was unlikely to derive from EGFR signalling inhibition. I, therefore, set out to test other known gefitinib targets. For that purpose, the Library of Integrated Network-Based Cellular Signatures (LINCS) database and cancer transcriptomics datasets contained within were interrogated for a suitable candidate. Since gefitinib had a consistent cytostatic effect on C9_78 iAstrocytes and the kinome screening data showed gefitinib's high binding affinity to GAK, a protein kinase

associated with cyclin G family of cyclins, cyclin G2 (CCNG2) was selected as a validation candidate. As with the *EGFR* transcript, CTR_3050 and C9_78 iAstrocytes were used.

Baseline expression results show no significant change in the levels of *CCNG2* in C9_78 compared to the control (figure 3.14). Both lines, however, show a clear trend towards a gradual increase in *CCNG2* expression as the treatment duration increased (not statistically significant). This data is consistent with previously published results, including transcriptomic analyses of a variety of cancer cell lines found in LINCS, thus confirming *CCNG2* to be a reliable target engagement marker for gefitinib in iAstrocytes at a transcript level. This result is also consistent with an expression profile expected from an unconventional cyclin such as CCNG2, whose expression increases as cell cycle arrest progresses. Moreover, I observed a decrease in cell numbers and the proliferation rate of C9_78 after gefitinib treatment (figures 3.6 and 3.7 respectively), which further complements the transcriptional changes in *CCNG2*.

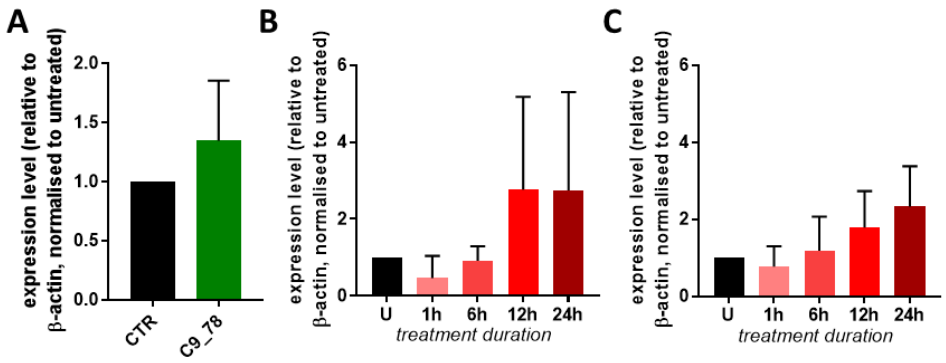

Figure 3.14 CCNG2 expression levels measured in control and C9orf72 iAstrocytes

(A) Quantification of baseline *CCNG2* expression in C9_78 compared to healthy control iAstrocytes; n=3 experimental repeats; CTR includes mean results of CTR_3050 from n=3 experimental repeats; mean ± SD; One sample t test, ns. **(B)** Quantification of *CCNG2* levels in CTR_3050; n=3 experimental repeats; mean ± SD. **(C)** Quantification of *CCNG2* levels in C9_78. n=3 experimental repeats; mean ± SD; One sample t test, all comparisons ns.

3.2.2 Gefitinib treatment effect on TDP-43 proteinopathy

As mentioned before, approximately 97% of all ALS patients show hallmarks of TDP-43 proteinopathy. iNPC-derived iAstrocytes used in this project recapitulate the endogenous TDP-43 proteinopathy hallmarks observed in post-mortem patient tissue. Amongst them are

the increased levels of TDP-43 cleavage product of 35 kDa (henceforth referred to as TDP-35; Neumann et al., 2006) in ALS patients compared to controls (figure 3.15), loss of nuclear TDP-43 signal in ALS patients (figure 3.16 B) and increased numbers of cells carrying the burden of pTDP-43 cytoplasmic inclusions (figure 3.16 C). No other *in vitro* (Berning & Walker, 2019; Van Damme et al., 2017) or indeed *in vivo* models (Ebstein et al., 2019; Watanabe et al., 2020; White et al., 2019) successfully recapitulate the full array of TDP-43 proteinopathy hallmarks, making iAstrocytes a useful model to study TDP-43 dynamics in ALS.

Since TDP-43 proteinopathy has been linked to cell toxicity and motor neuron death in ALS, a therapeutic intervention capable of mitigating this pathology is highly desirable. This section characterises the effect of gefitinib on TDP-43 proteinopathy in iAstrocytes in terms of TDP-35 burden, nuclear localisation of TDP-43, as well as presence of phosphorylated cytosolic inclusions, henceforth referred to as pTDP-43. TDP-35 burden and gefitinib's effect on it were also measured in induced neurons (iNeurons).

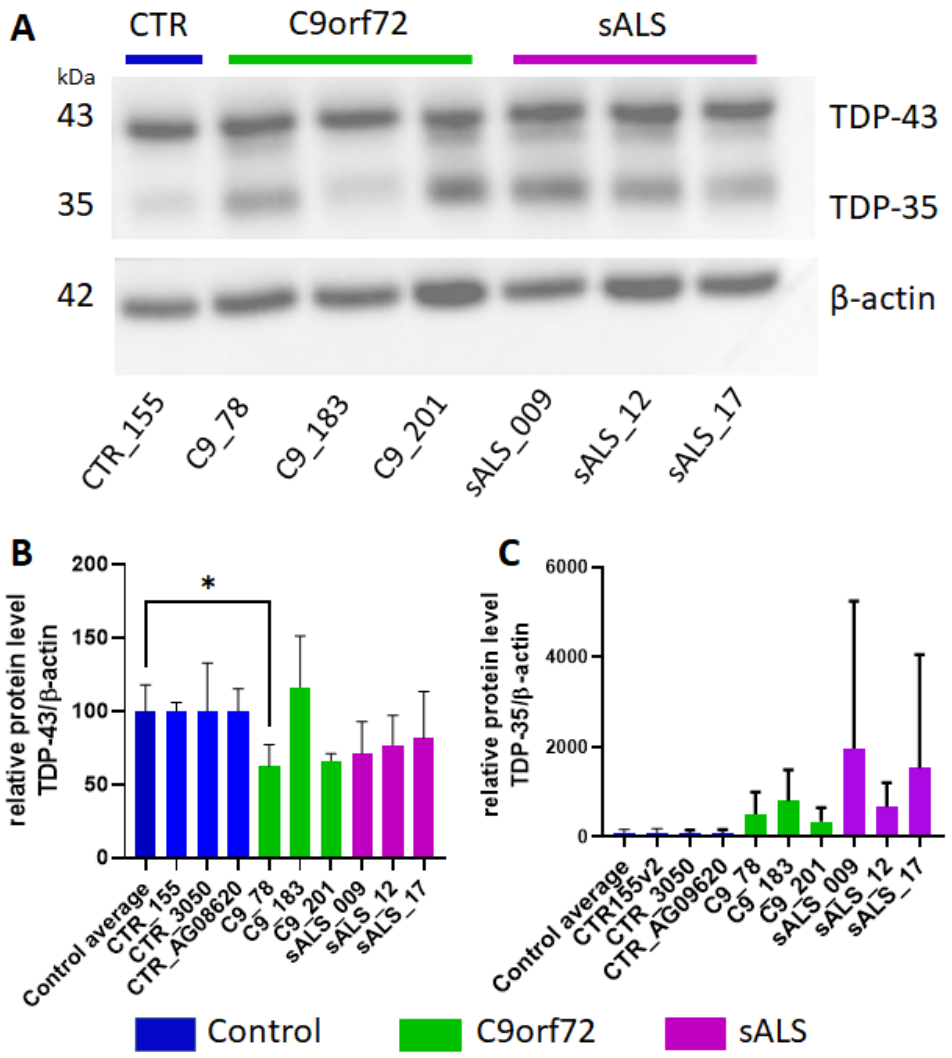

Figure 3.15 Baseline levels of TDP-43 fragmentation in iAstrocytes

(A) A representative western blot showing TDP-43 and TDP-35 levels in ALS patient iAstrocyte. **(B)** Quantification of TDP-43 levels; n=3-6 experimental repeats; mean ± SD; data relative to CTR=100; One-way ANOVA with Dunnett's multiple comparison's test (relative to control average), *P<0.05. **(C)** Quantification of TDP-35 levels; n=3-6 experimental repeats; mean ± SD; data relative to CTR=100; One-way ANOVA with Dunnett's multiple comparison's test (relative to control average), ns.

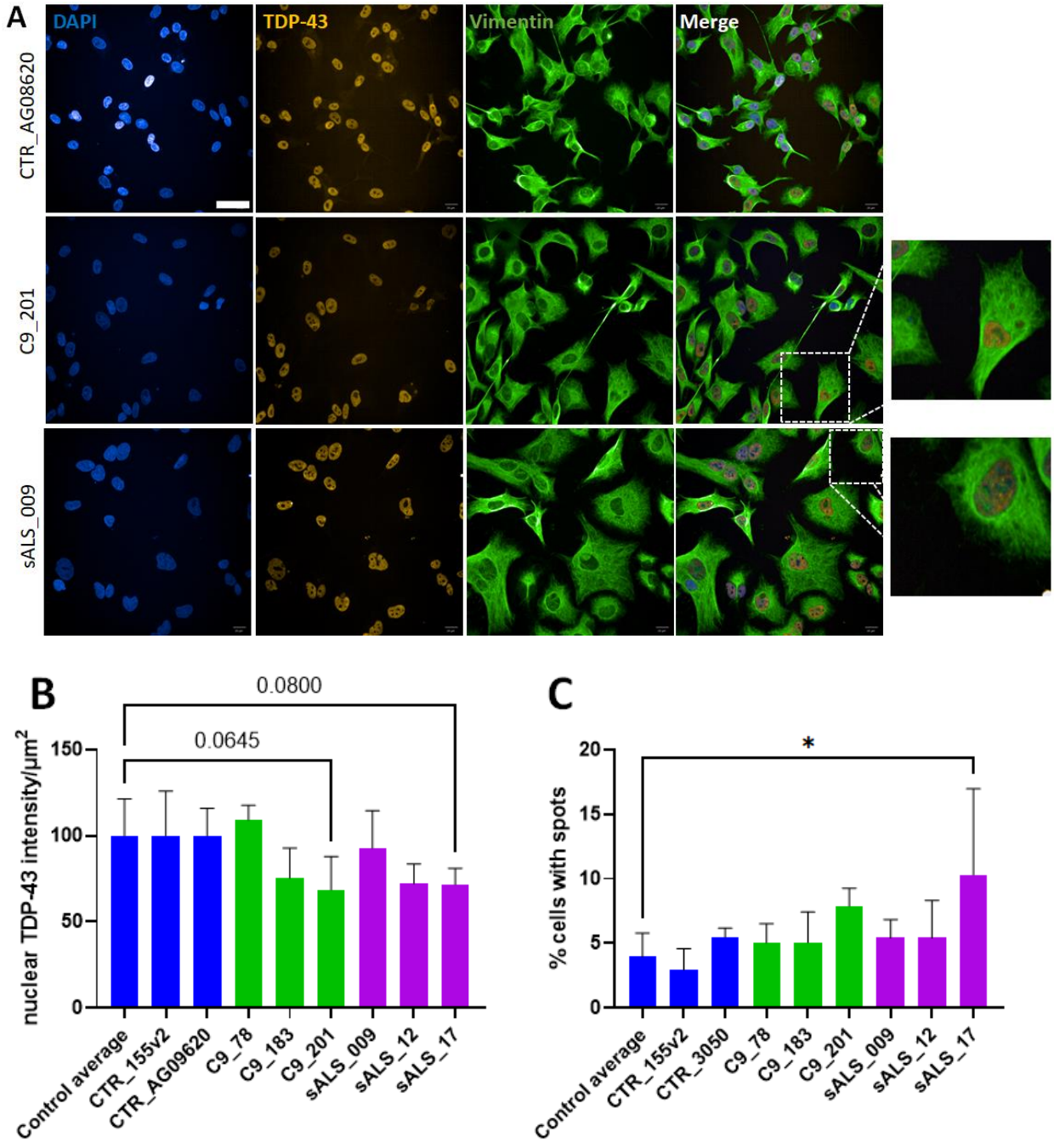

Figure 3.16 Examples of TDP-43 proteinopathy observed in iAstrocytes

(A) Representative images of TDP-43 nuclear loss and pTDP-43 accumulation in iAstrocytes. Scale: 50 µm. **(B)** Quantification of nuclear TDP-43 signal (intensity per μm^2); n=3-7 experimental repeats; mean ± SD, data relative to control average=100. One-way ANOVA with multiple comparisons. **(C)** Quantification of % of iAstrocytes with pTDP-43 spots; n=3-5 experimental repeats (except CTR_3050 n=2); mean ± SD; One-way ANOVA with multiple comparisons, *P<0.05.

3.2.2.1 TDP-43 proteinopathy in iAstrocytes after gefitinib treatment

To measure the effect of gefitinib treatment on TDP-43 fragmentation, iAstrocytes were treated with 10 µM gefitinib or 0.1% (v/v) DMSO vehicle. After 48h, cells were scraped and processed for immunoblotting with anti-TDP-43 C-terminal antibody (figure 3.17 A). The C-terminal-specific antibody was selected as all major pathological cleavage products of TDP-43, including TDP-35, contain the C-terminal region.

Because of the variability between different blots and to better visualise the delta in protein expression, all DMSO controls were set at 100 and gefitinib-treated conditions are presented as relative to DMSO (figure 3.17 B and C).

Firstly, levels of full-length TDP-43 were quantified and were found to show a trend towards an increase in TDP-43 levels after treatment, with C9_78 and sALS_009 showing a statistically significant increase (figure 3.17 B).

Levels of TDP-35 after treatment with DMSO were comparable to those at baseline, shown in figure 3.15. Gefitinib-treated cells, on the other hand, showed a significant reduction in TDP-35 levels, an effect observed in almost all lines, including the control cases which carried the least fragmentation at baseline (figure 3.17C).

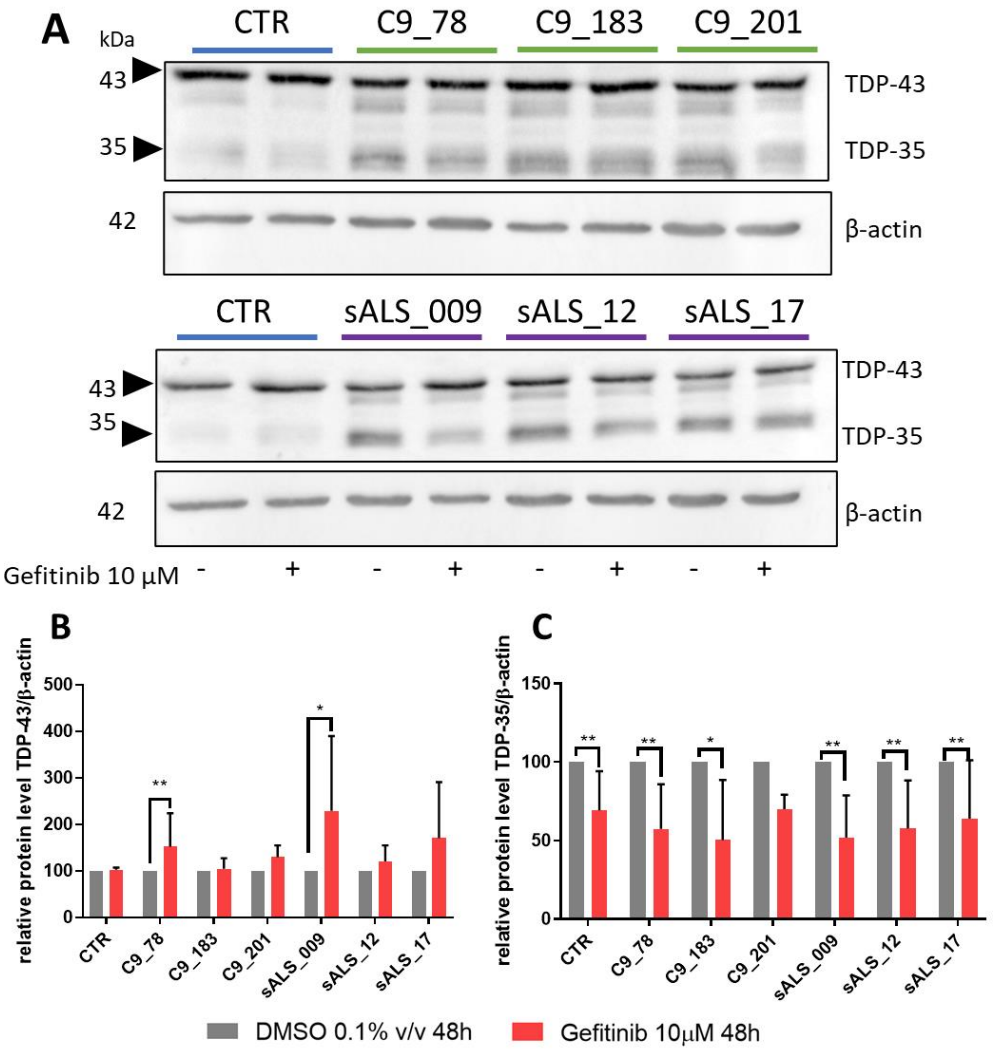

Figure 3.17 The effect of gefitinib treatment on TDP-43 fragmentation

(**A**) Representative TDP-43 western blot in ALS iAstrocytes after gefitinib treatment. (**B**) Quantification of TDP-43 levels in gefitinib-treated iAstrocytes; n=3-6 experimental repeats; CTR includes mean results of CTR_155 from n=4 experimental repeats, CTR_3050 mean from n=4 experimental repeats and CTR_AG08620 mean from n=2 experimental repeats; data are mean ± SD; all DMSO=100; Mann-Whitney test, *P<0.05, **P<0.005. (**C**) Quantification of TDP-35 levels in gefitinib-treated iAstrocytes. n=3-6 experimental repeats; CTR includes mean results of CTR_155 from n=4 experimental repeats, CTR_3050 mean from n=4 experimental repeats and CTR_AG08620 mean from n=2 experimental repeats; data are mean ± SD; all DMSO=100; Mann-Whitney test. *P<0.05, **P<0.005.

3.2.2.1.1 Effect of prolonged treatment with gefitinib on TDP-35 levels

Encouraged by the effectiveness with which gefitinib reduced the levels of TDP-35 in ALS iAstrocytes, it was investigated whether serial administration of gefitinib resulted in a further decrease and ultimately a complete ablation of TDP-35 fragments. For that purpose, an

experiment was designed where C9_78 iAstrocytes were treated on days 2, 4 and 6 (d2-6), days 4 and 6 (d4-6), and day 5 alone (d5) of their 7-day differentiation protocol. Levels of TDP-43 and TDP-35 were subsequently investigated through immunoblotting as described in the previous section.

As shown in figure 3.18, each treatment condition resulted in a significant decrease in TDP-35 levels compared to vehicle-only conditions. However, no further reduction was observed upon multiple treatments. Therefore, a single treatment of gefitinib for 48h was deemed sufficient to reduce the levels of TDP-35 and the observed results represent the maximal possible effect in C9_78 iAstrocytes. No other lines were tested.

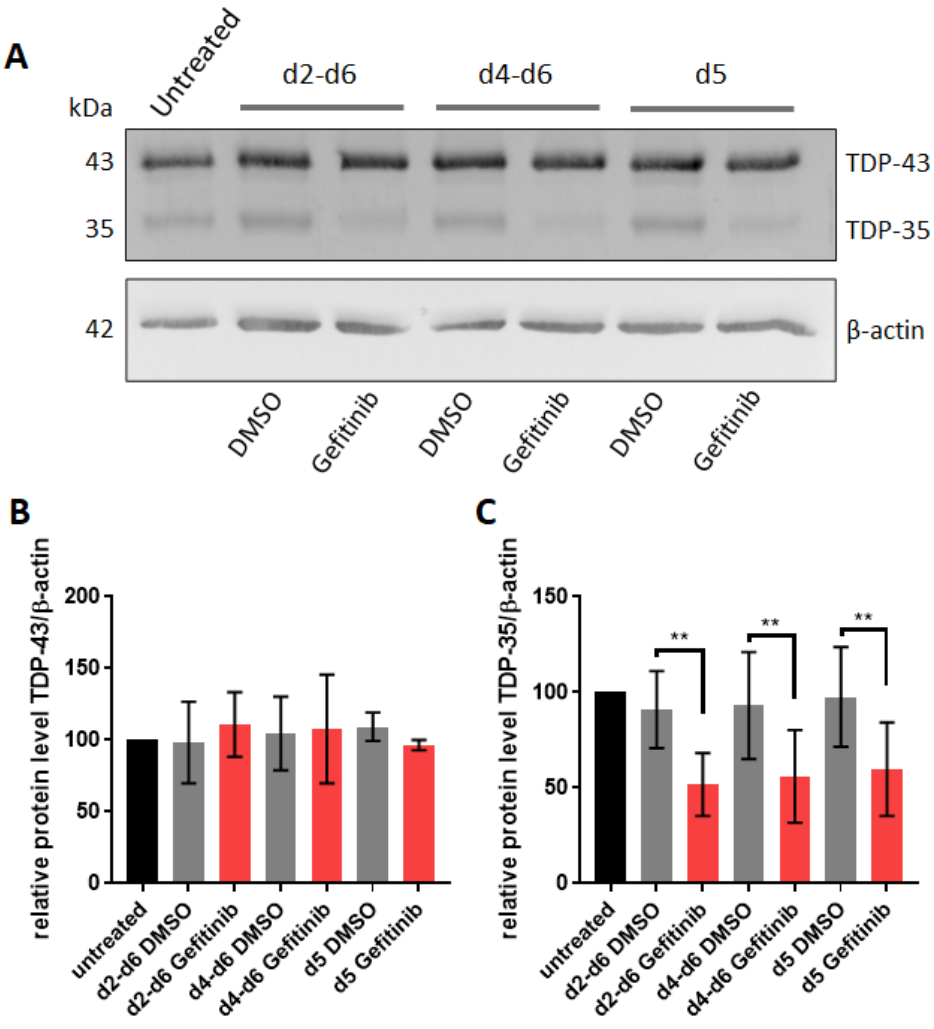

Figure 3.18 Effect of multiple treatments with gefitinib on TDP-35 in iAstrocytes

C9_78 iAstrocytes were treated with 10 µM gefitinib on days 2, 4 and 6 of differentiation (d2-6), days 4 and 6 (d4-6) and day 5 (i.e. the standard 48h) only (d5). (**A**) Representative western blot image. (**B**)

Quantification of TDP-43 levels; n=3 experimental repeats; data are mean ± SD; untreated=100; two-way ANOVA with Tukey's multiple comparisons, ns. (**C**) Quantification of TDP-35 levels. n=3 experimental repeats; data are mean ± SD; untreated=100; two-way ANOVA with Tukey's multiple comparisons, **P<0.005.

3.2.2.1.2 Effect of gefitinib treatment on insoluble TDP-43 and TDP-35 in iAstrocytes

Encouraged by the consistent decrease in TDP-35 in iAstrocytes after gefitinib treatment, the detergent-insoluble fraction of TDP-43, which is not detectable via the standard SDS lysis-based western blotting, was investigated next. Insoluble TDP-43 fragments are found in ALS patient brain tissue and were previously shown to act as a seed for further fragment aggregation of different cleavage products of full-length TDP-43 (Furukawa et al., 2011; Nonaka et al., 2013). The cell pellet remaining after the separation of the soluble proteins was incubated in urea buffer and sonicated to increase its solubility. The resulting protein lysates were run on SDS-PAGE gel as normal. Prior to blotting for TDP-43, the membrane was incubated in SYPRO Ruby reagent to stain all proteins (figure 3.19 A). The total SYPRO Ruby staining intensity of each loaded lane was used as a normaliser, as no β-actin was detectable in the urea-soluble protein fraction, as expected.

TDP-43 antibody produced a comparable signal in the urea-soluble fraction as in the standard western blotting (figure 3.19 B). Upon normalisation to untreated CTR_3050 iAstrocytes, it became apparent that both tested C9orf72 patients, C9_78 and C9_183, carried a smaller burden of insoluble TDP-43 (figure 3.19 C) and TDP-35 (figure 3.18 D) than the control, and both gefitinib and DMSO vehicle treatments increased their levels. Moreover, SYPRO Ruby staining intensity was higher in some of the patient conditions than controls, and we were unable to determine if that was a result of a real, higher burden of insoluble proteins in these samples, or loading of unequal amounts of protein lysates onto the gel. It is not unlikely, however, that an unequal loading contributed to this effect, as, in order to assure reliable Bradford assay data is collected, urea buffer must be added to the assay blank. Due to further issues with reliable normalisation, further efforts to detect the effect of gefitinib on insoluble TDP-43 were abandoned.

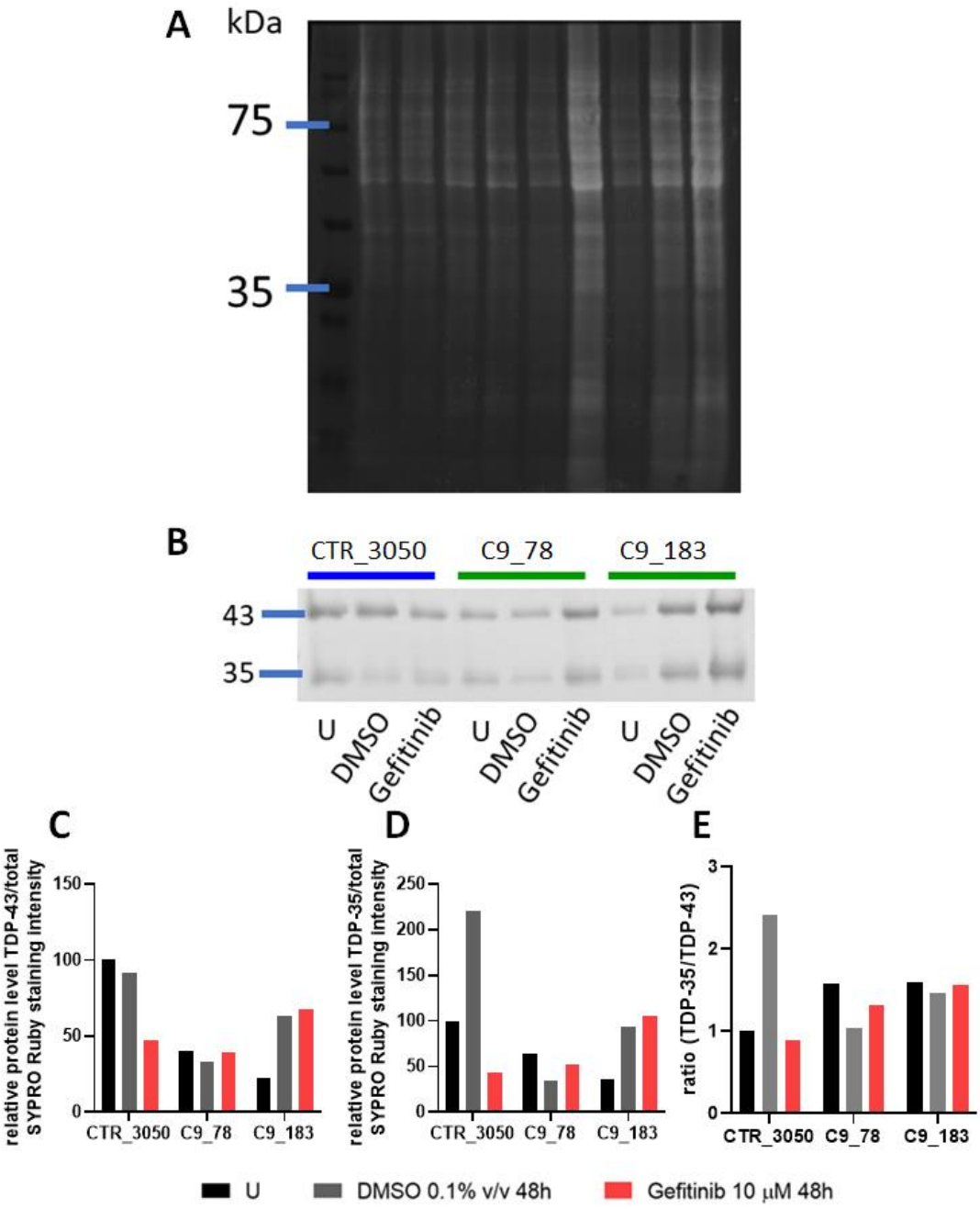

Figure 3.19 Detection of insoluble TDP-43 in iAstrocytes

(A) Representative image of SYPRO Ruby stained membrane. **(B)** After washing SYPRO Ruby off, the membrane was blotted for TDP-43 (**B**) Representative western blotting image of the insoluble protein fraction. (**C**) Quantification of TDP-43 levels. (**D**) Quantification of TDP-35 levels. **(E)** Quantification of TDP-35/TDP-43 ratio. All data n=1 experimental repeat, all data normalised to CTR_3050 DMSO (=100).

3.2.2.2 TDP-43 proteinopathy and gefitinib treatment in iNeurons

TDP-43 is widespread in all CNS cells (Ou et al., 1995), though its importance in neurodegeneration is studied primarily in motor neurons, as the overdue burden of TDP-43 proteinopathy is lethal to post-mitotic motor neurons more than glial cells, which retain a capacity to proliferate (Toyama et al., 2014). Therefore, alleviating the TDP-43 proteinopathy burden of neuronal cells is of paramount importance.

To test the hypothesis that gefitinib can be used in neurons as well as glial cells, iNPCs were differentiated into iNeurons as described in section 2.2.1.3 and illustrated in figure 2.2. Due to the differentiation drugs used, the protocol, based on a previously published study (Hester et al., 2011), results in a population of cells positive for neuron-specific class III β-tubulin (Tuj1), but not choline acetyltransferase (ChAT), and hence these cells are defined as spinal neurons. One line per genotype was selected for validation purposes on the basis of proteinopathy carried by their iAstrocyte counterparts and the reduction in TDP-35 caused by gefitinib.

As before, cells were treated with 10 µM gefitinib for 48h. The effect of the drug treatment on full-length TDP-43 was identical to the one observed in iAstrocytes, showing a trend towards an increase in levels without statistical significance (figure 3.20 B). Similar to iAstrocytes, levels of TDP-35 observed in iNeurons after gefitinib treatment were significantly reduced (figure 3.20 C).

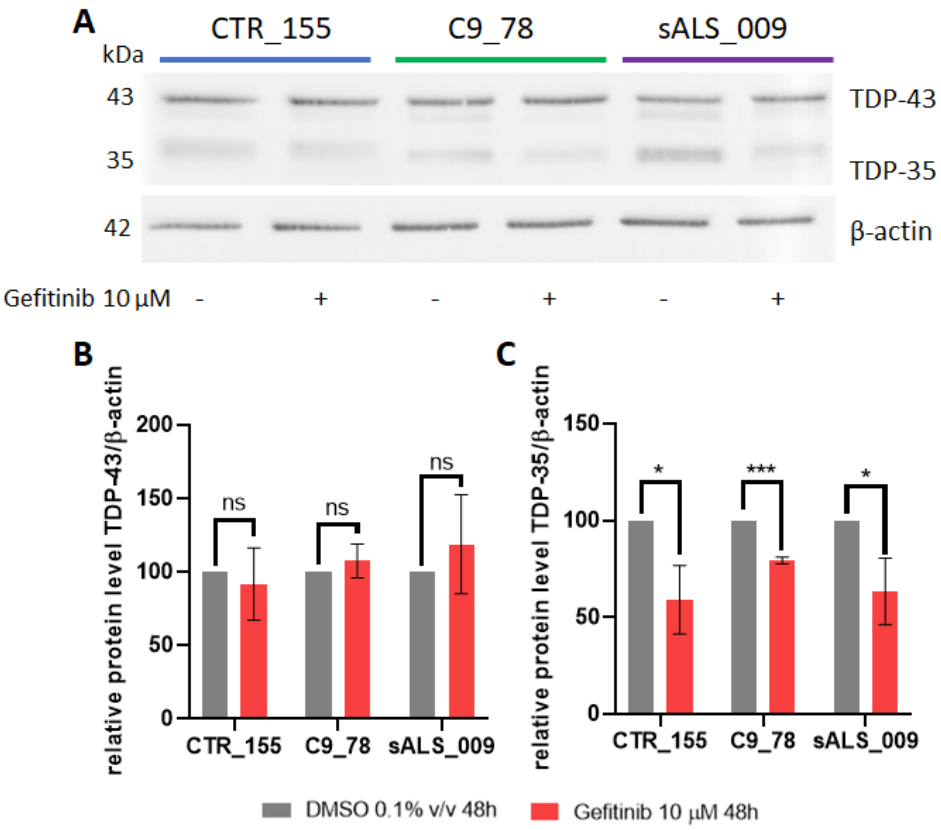

Figure 3.20 Effect of gefitinib treatment on TDP-43 fragmentation in iNeurons

(**A**) Representative western blotting image of TDP-43 expression in iNeurons. **(B)** Quantification of full-length TDP-43 levels in iNeurons; n=4 experimental repeats; data are mean ± SD; data relative to all DMSO=100, Mann-Whitney test, ns. (**C**) Quantification of TDP-35 levels in iNeurons. n=4 experimental repeats; data are mean ± SD; data relative to all DMSO=100; Mann-Whitney test, *P<0.05; ***P<0.0005.

3.2.2.3 TDP-43 localisation after gefitinib treatment

Having observed a decrease in TDP-43 fragmentation in iAstrocytes and iNeurons after treatment with gefitinib via western blotting, I hypothesised that gefitinib can rescue the loss of nuclear TDP-43. For that purpose, iAstrocytes were processed for immunocytochemistry as described before and treated with gefitinib or DMSO vehicle for 48h. Average TDP-43 staining intensity per nuclear area (in μm^2) was measured automatically using Columbus image analysis software after applying a nuclear mask to images (figure 3.8). Due to the staining intensity value of a true-positive TDP-43 nuclear signal in a control line being variable between each experimental repeat, no staining intensity threshold was applied to quantify

the number of nuclei exhibiting nuclear loss. For representative images of nuclear TDP-43 staining, see figure 3.16 A.

As presented before in figure 3.16 B, DMSO-treated iAstrocytes, except C9_78, recapitulated a nuclear loss of TDP-43 signal when compared to controls (figure 3.21). Overall, most iAstrocyte lines, with an exception of C9_78, show a trend towards an increase in nuclear TDP-43 signal following a treatment with gefitinib. The statistical analysis detected an overall significant effect of the drug treatment on the cells.

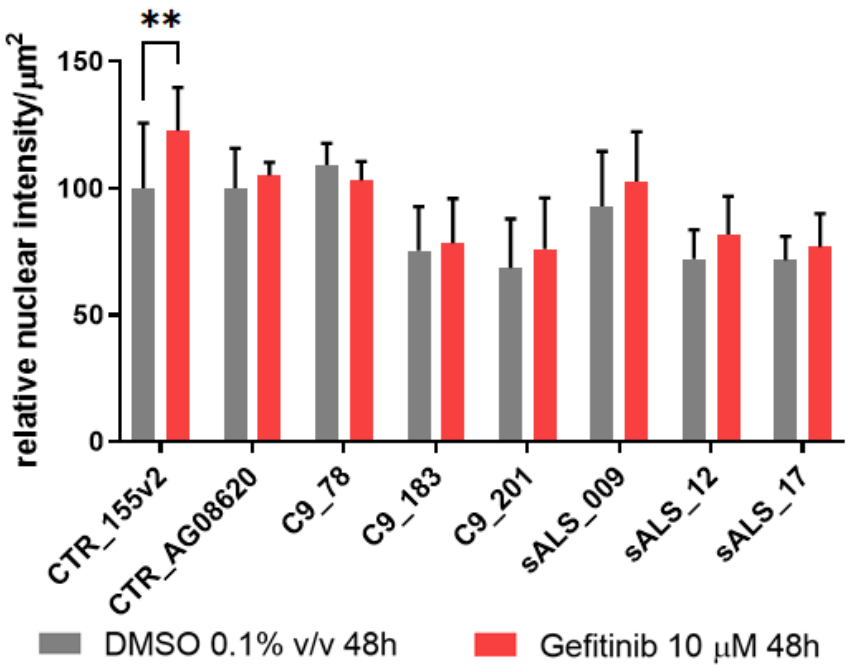

Figure 3.21 Gefitinib treatment effect on nuclear localisation of TDP-43.

n=3-5 experimental repeats; mean ± SD; data relative to CTR DMSO=100; two-way ANOVA with Šídák's multiple comparisons; **P<0.005; cell line factor: **P=0.0012; drug treatment factor: **P=0.0032

3.2.2.4 Cytoplasmic aggregation of pTDP-43 after treatment with gefitinib

Having observed a decrease in TDP-35 fragments, gefitinib's ability to decrease the levels of pTDP-43 was investigated next. For this purpose, iAstrocyte lines were stained for pTDP-43 and vimentin. Cytoplasmic protein aggregates are sequestered to the aggresome by the cell by enveloping them in vimentin filaments (Johnston, Ward, & Kopito, 2012; Lee et al., 2019). Therefore, presence of a vimentin cage around a pTDP-43-positive inclusion was used as a quality control measure. Due to issues with an automated image analysis pipeline, pTDP-43

inclusions data was obtained by blinded manual counts performed by me and Ms Lai Mei Wan.

There was no statistically significant difference between the % of cell with pTDP-43 spots in the control and any of the patient lines, although patients show a trend towards elevated % of cells with spots (figure 3.22 A). Datasets showing the percentage of cells with spots (figure 3.22 B) and a number of spots per cell (figure 3.22 C) showed a near identical trend towards a decrease in pTDP-43 spot numbers in C9orf72 cells after gefitinib treatment.

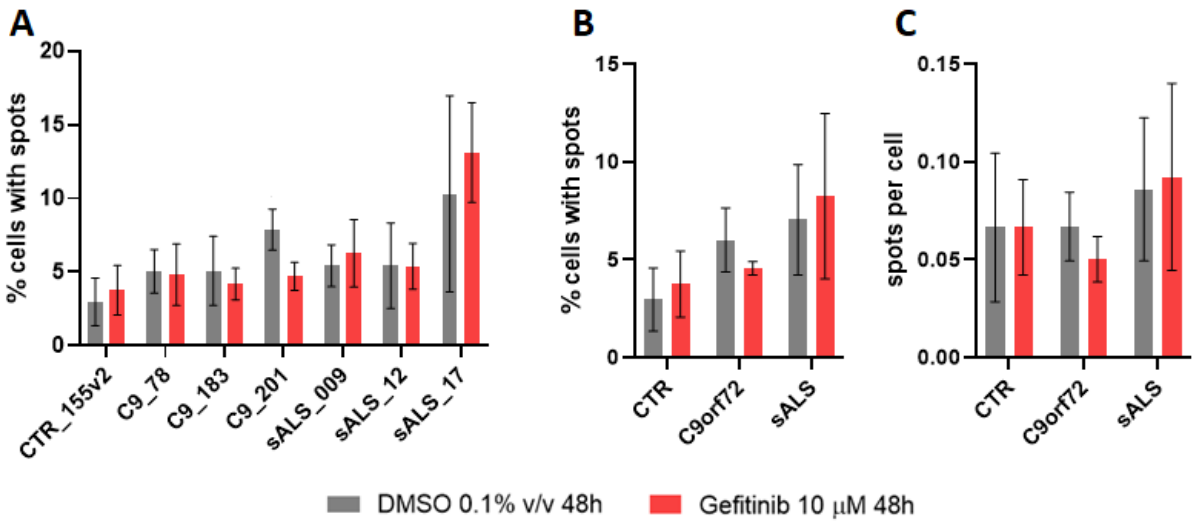

Figure 3.22 Gefitinib treatment effect on cytoplasmic accumulation of pTDP-43 inclusions

(A) Quantification of the % of cells carrying a pTDP-43 burden per individual cell line; n=3-5 experimental repeats; data are mean ± SD; data relative to CTR DMSO=100; two-way ANOVA with Šídák's multiple comparisons; cell line factor: **P=0.0031; Drug treatment factor: ns. (**B**) Quantification of the % of cells carrying a pTDP-43 burden per genotype; n=3; CTR includes mean values of CTR_155v2 from n=3 experimental repeats, CTR_3050 from n=2 experimental repeats, CTR_AG08620 from n=2 experimental repeats; data are mean ± SD; data relative to CTR DMSO=100; two-way ANOVA with Šídák's multiple comparisons; ns. (**C**) Quantification of the average number of spots per total cell number after DMSO or gefitinib treatment per genotype. n=3; CTR includes mean values of CTR_155v2 from n=3 experimental repeats, CTR_3050 from n=2 experimental repeats, CTR_AG08620 from n=2 experimental repeats; data are mean ± SD; data relative to CTR DMSO=100; two-way ANOVA with Šídák's multiple comparisons; ns

3.2.2.5 Cleavage of TDP-43 by caspase-3

Gefitinib has decreased the level of TDP-35 C-terminal fragments, increased the levels of full-length TDP-43 and led to a modest increase in nuclear TDP-43 levels. I have also observed a promising trend towards a decrease in the number of pTDP-43 inclusions in the cytoplasm, which, albeit not statistically significant at present, is worth investigating further. As explained earlier, TDP-35 is a cleavage product of phosphorylated TDP-43 being cleaved by caspase-3 (Furukawa et al., 2011). Strength of the interaction between TDP-43 and caspase-3 was measured via a proximity ligation assay (PLA). PLA shows a physical interaction between two proteins of interest as a fluorescent punctum. We hypothesised that gefitinib treatment decreases the cleavage of TDP-43 by caspase-3, thus resulting in a decrease in the interaction between in TDP-43 and caspase-3 that can be measured via the PLA.

C9_183 and sALS_009 were selected for this experiment, as gefitinib treatment in those lines led to a robust and large delta in TDP-35 expression. An interaction between LC3 and p62 was used as a technical positive control in the assay (representative images 3.23 C, D), due to the known interaction between the two proteins. Results of the positive control in this assay are presented in figure 3.29 and discussed separately in section 3.2.3.2. Cells stained with no antibodies were used as a negative control. Overall, there was no statistically significant effect of the gefitinib treatment on the strength of TDP-43/caspase-3 interaction (figure 3.23 F).

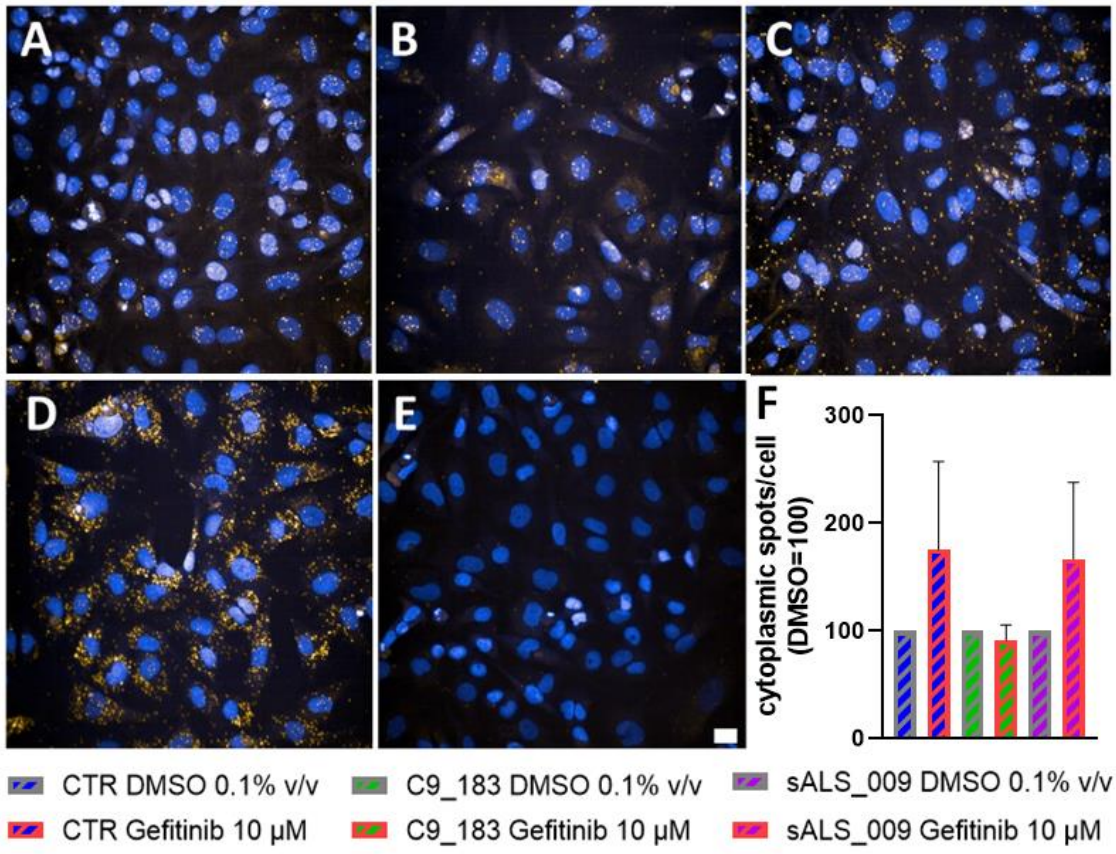

Figure 3.23 Proximity ligation assay to detect TDP-43-caspase-3 interaction in iAstrocytes

Representative PLA images of CTR_161 (**A** – TDP-43-caspase-3 with DMSO; **B** – TDP-43-caspase-3 with gefitinib; **C**- LC3+p62 with DMSO; **D** – LC3+p62 with gefitinib; **E** – no antibodies). Scale: 20 µm. **(F)** Quantification of PLA signal spots in the cytoplasm. Data are relative to DMSO=100; n=3 experimental repeats; data are mean ± SD; Mann-Whitney test, ns.

3.2.3 Effect of gefitinib on autophagy function in ALS iAstrocytes

The effect of gefitinib on TDP-43 proteinopathy in ALS iAstrocytes provides an important indication of a potential usefulness of this drug as a repurposing candidate. The mechanism behind these findings, however, remained unknown, as it could not be associated with a significant reduction in nuclear loss or fragmentation. The current literature consensus describes the clearance of TDP-35 and other smaller TDP-43 C-terminal fragments such as TDP-25 as happening via autophagy (Brady et al., 2011). Previous studies on a variety of cancer cell lines have described gefitinib as an autophagy activator (Han et al., 2011). This section explores the ability of gefitinib to induce autophagy in iAstrocytes.

3.2.3.1 Autophagy assay in HEK293 cells

As the results between different cancer cell lines across publications are variable, the ability of gefitinib to activate autophagy in a healthy cell line was investigated first. The objective of

this assay was to measure the autophagy induction in an immortalised human embryonic kidney 293 (HEK293) cell line, using a previously published protocol (Webster et al., 2016). Briefly, a 6h treatment with DMSO vehicle, 10 µM gefitinib, 500 nM rapamycin (an autophagy activator – positive control), 100 nM bafilomycin A1 (an autophagy inhibitor – negative control), or a combination of bafilomycin A1 with a positive control and gefitinib was set up. For clarity, figure 3.22 summarises the dynamics of bafilomycin A1 autophagy inhibition. Cells collected after the 6h treatment were processed for a western blot and immunoblotted for LC3 and p62.

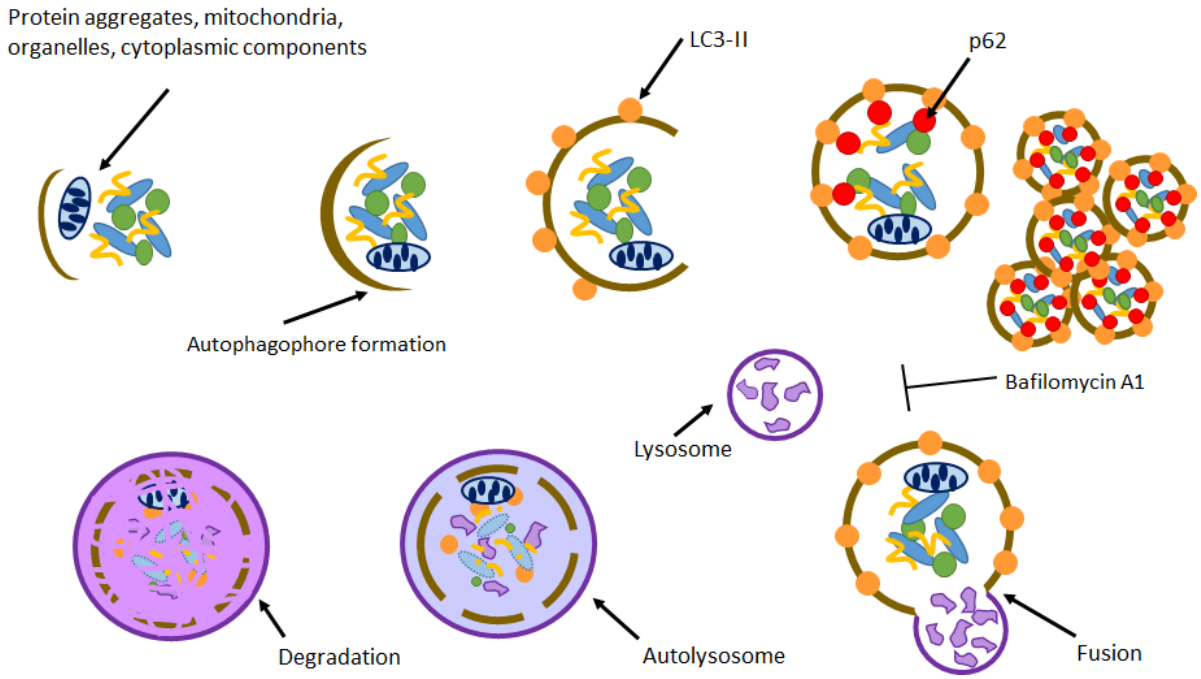

Figure 3.24 Autophagy process and inhibition with bafilomycin A1.

Upon initiation of autophagy, a structure named phagophore begins to envelop the cargo to be degraded. Phagophore membrane undergoes elongation as LC3-I undergoes conversion to LC3-II, which in turn lines the phagophore membrane. The resulting autophagophore also contains p62, which is an autophagy receptor which binds to both the cargo and LC3-II. Under basal conditions, autophagophore forms an autolysosome by fusing with lysosomes. It is in that final structure that degradation of the cargo takes place. Upon addition of bafilomycin A1, however, lysosomal fusion is blocked, resulting in an accumulation of autophagophores.

Compared to the DMSO control (=100), neither gefitinib nor rapamycin treatment had a discernible effect on the levels of LC3-I, whereas addition of bafilomycin A1 in all treatment conditions increase LC3-I expression (figure 3.23 B). Increased levels of LC3-II were observed after treatment with gefitinib alone, indicating an autophagic flux. Addition of bafilomycin A1 onto the cells resulted in a significant elevation of LC3-II levels, whilst the bafilomycin A1 + gefitinib co-treatment led to a further significant increase in LC3-II, which is consistent with gefitinib's role as an autophagy activator (figure 3.23 C). A similar pattern of response was observed when a ratio of LC3-II to LC3-I was calculated (figure 3.23 D). Neither gefitinib nor rapamycin increased the levels of p62 compared to the DMSO vehicle, confirming their ability to induce autophagy. Increase in p62 expression after the addition of bafilomycin A1, observed alongside the elevated LC3-II levels described earlier, is consistent with autophagy inhibition (Yang et al., 2019). In summary, the increase in LC3-II expression between bafilomycin A1 treatment alone and bafilomycin + gefitinib co-treatment indicated a simultaneous activation and inhibition of autophagy – LC3-II levels are driven by an autophagophore formation and inhibition of lysosomal fusion occurring simultaneously.

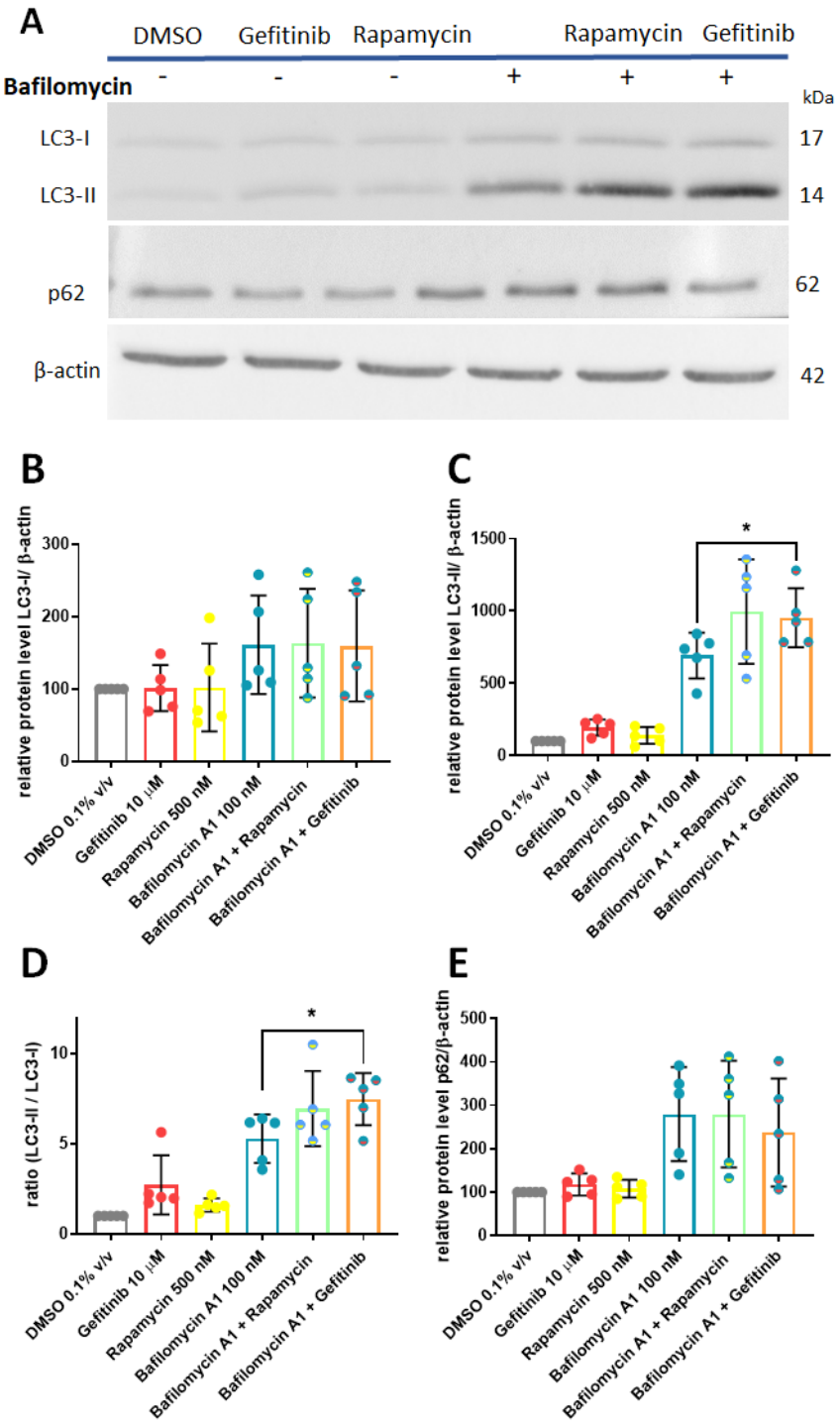

Figure 3.25 Gefitinib induces autophagy in HEK293 cell line

(A) Representative western blotting images. **(B)** Quantification of LC3-I levels in HEK293 cells; n=5. **(C)** Quantification of LC3-II levels in HEK293 cells; n=5 experimental repeats; data are mean ± SD, normalised to DMSO =100; *P<0.05; paired t-test, bafilomycin vs gefitinib + bafilomycin. **(D)** Quantification of LC3-II/LC3-I ratio; n=5; mean ± SD, normalised to DMSO =1; *P<0.05; paired t-test, bafilomycin vs gefitinib + bafilomycin. **(E)** Quantification of p62 levels; n=5 experimental repeats; data are mean ± SD, normalised to DMSO =100.

3.2.3.2 Autophagy function in iAstrocytes

Having demonstrated gefitinib's capacity to induce autophagy in HEK293 cell line, a protocol was optimised to measure the ability of gefitinib to activate autophagy in iAstrocytes. Having tested 6h, 12h and 16h of treatment, 16h was optimal to observe a reliable and consistent increase in LC3-II levels after treatment with bafilomycin A1. Anticipating a need for a more robust positive control, informed by experiments conducted by Ms Camilla Boschian, rapamycin was replaced with torin 1, due to torin's ability to inhibit both mTORC1/2 complexes, whilst rapamycin inhibits mTORC1 only (Park et al., 2016).

The first aim of this experiment was to replicate HEK293 cell line findings in healthy control iAstrocytes. In all three tested control iAstrocyte lines, no changes in LC3-I were observed (figure 3.26 B), a significant increase in LC3-II levels was observed in bafilomycin + gefitinib treated condition compared to bafilomycin alone (figure 3.26 C), which is consistent with HEK293-based experiments. The same pattern of expression was observed when LC3-II to LC3-I ratio was calculated, albeit no statistical significance was reached (figure 3.26 D). p62 expression followed a similar pattern to that seen in HEK293 cells (figure 3.26 E).

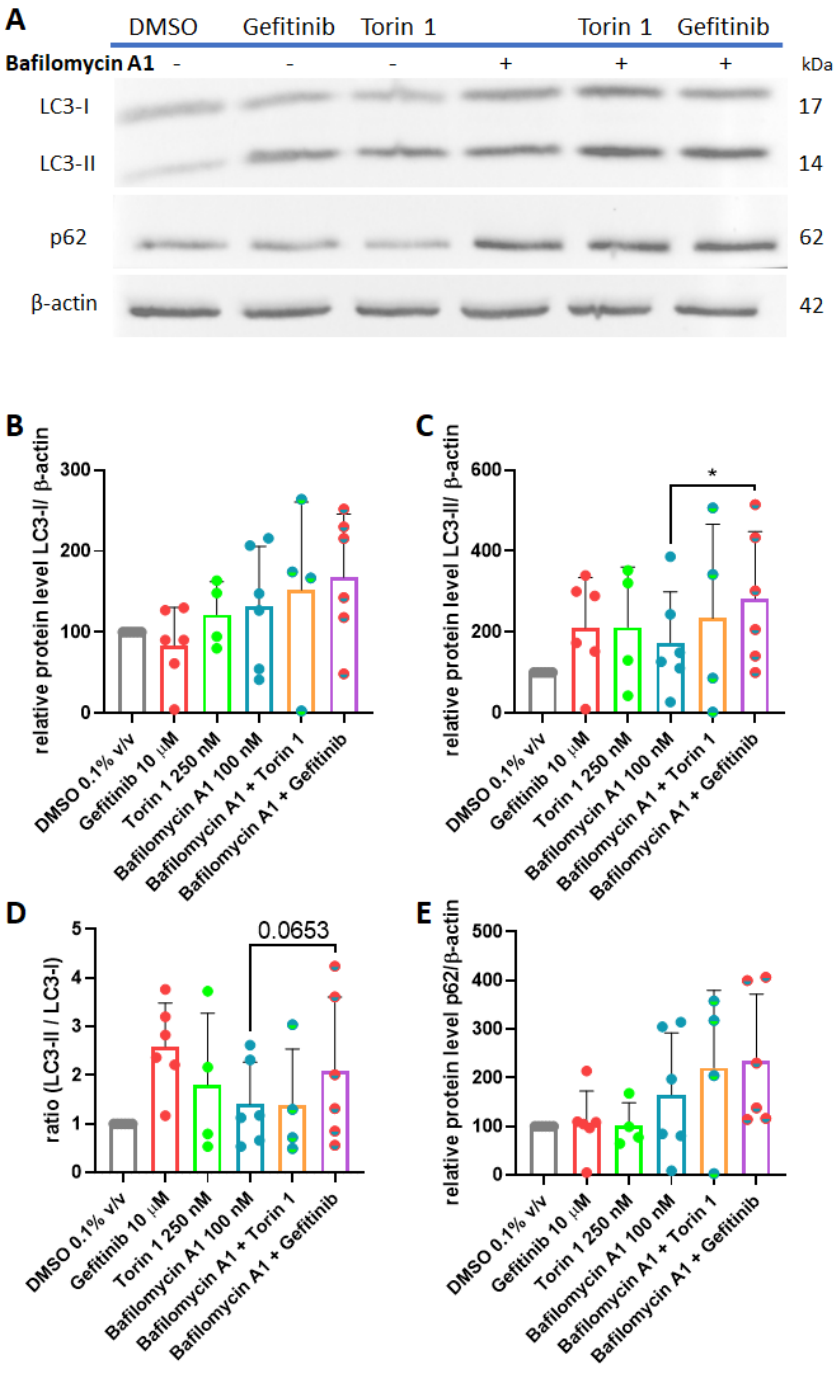

Figure 3.26 Gefitinib activates autophagy in control iAstrocytes

(A) Representative western blot. **(B)** Quantification of LC3-I levels. **(C)** Quantification of LC3-II levels; n=6 experimental repeats; data are mean ± SD; DMSO vehicle =100; paired t-test bafilomycin vs bafilomycin + gefitinib; *P<0.05. **(D)** Quantification of LC3-II/LC3-I ratio; n=6 experimental repeats; data are mean ± SD; DMSO vehicle = 1; paired t-test bafilomycin vs bafilomycin + gefitinib, ns. **(E)** Quantification of p62 levels. All data are mean ± SD; n=6, experimental repeats (CTR_161 n=2, CTR_AG08620 n=2, CTR_CS-14 n=2).

Next, the protocol described above was applied to C9_78 iAstrocytes. Following multiple attempts, no robust and consistent activation of autophagy was observed in these cells, even upon treatment with torin 1 (figure 3.27 B-E).

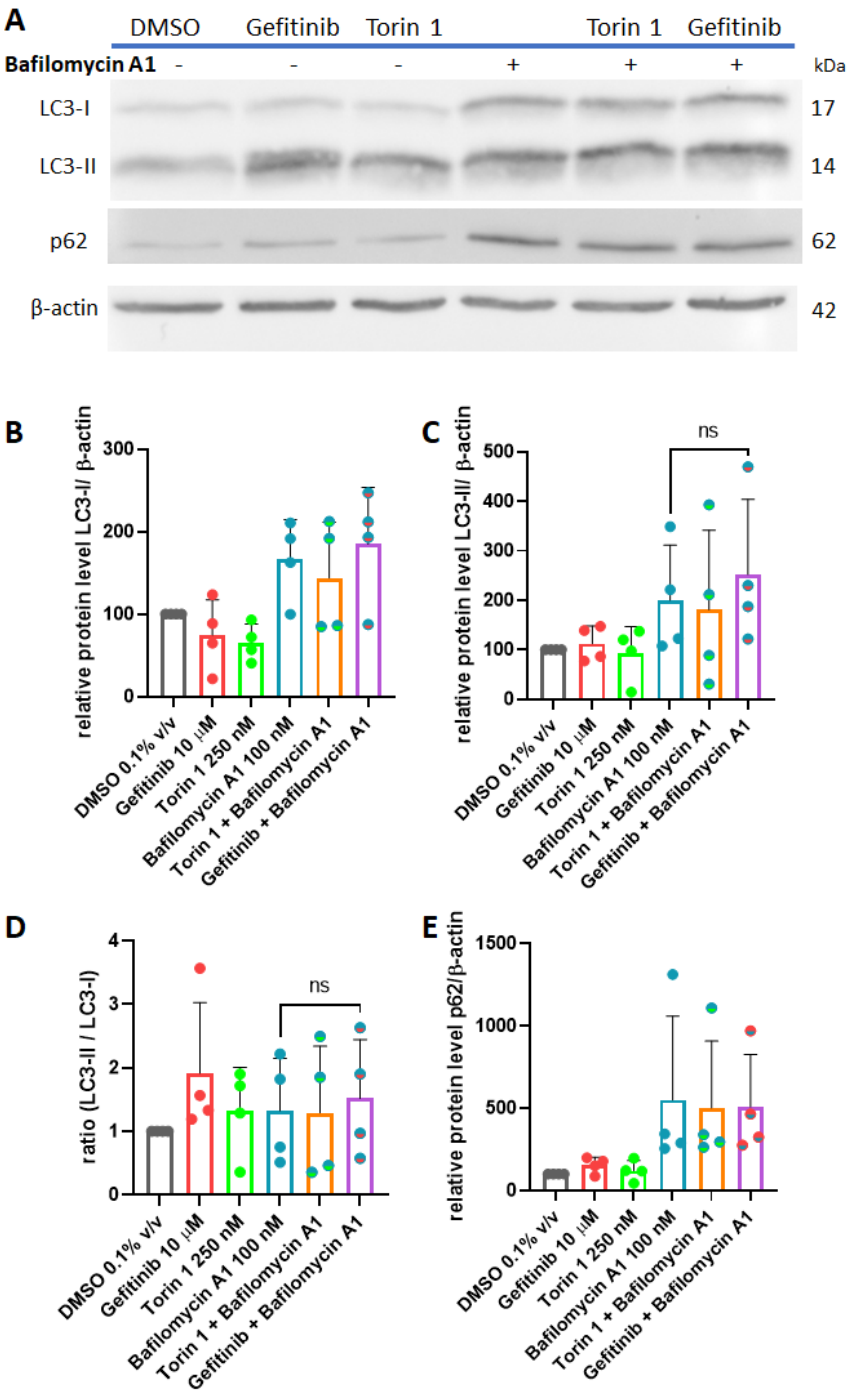

Figure 3.27 Gefitinib effect on autophagy activation in C9_78 iAstrocytes

A) Representative western blotting image obtained from C9_78 iAstrocytes. **(B)** Quantification of LC3-I levels; n=5 experimental repeats; data are mean ± SD; data relative to DMSO =100. **(C)** Quantification of LC3-II levels; n=5 experimental repeats; data are mean ± SD; data relative to DMSO =100; paired t-test, bafilomycin vs bafilomycin + gefitinib, ns. **(D)** Quantification of LC3-II/LC3-I ratio; n=5 experimental repeats; data are mean ± SD; data relative to DMSO =1; paired t-test, bafilomycin vs bafilomycin + gefitinib, ns. **(E)** Quantification of p62 levels; n=5 experimental repeats; data are mean ± SD; data relative to DMSO =100.

Considering the autophagy defect observed in C9orf72 patients, where fusion of autophagosome to lysosome is impaired (Webster et al, 2016), to further elaborate on the ability of gefitinib to induce autophagy in ALS lines, the protocol was applied to sALS iAstrocytes. LC3-I levels following a treatment with gefitinib and torin 1 were comparable and higher than in DMSO-treated cells, whereas presence of bafilomycin A1 led to an increase in LC3-I (figure 3.28 B). Levels of LC3-II were higher in all the treatment conditions compared to DMSO, albeit no robust difference was detected between them (figure 3.28 C) even after the LC3-II/LC3-I ratio was calculated (figure 3.28 D). There was no difference in p62 expression between DMSO and gefitinib or torin 1 and were elevated after treatment with bafilomycin A1 or its co-treatment (figure 3.28 E). These results suggest that, although gefitinib results alone indicate an autophagic flux, bafilomycin A1 treatment prevented a further increase in LC3-II upon autophagy activation.

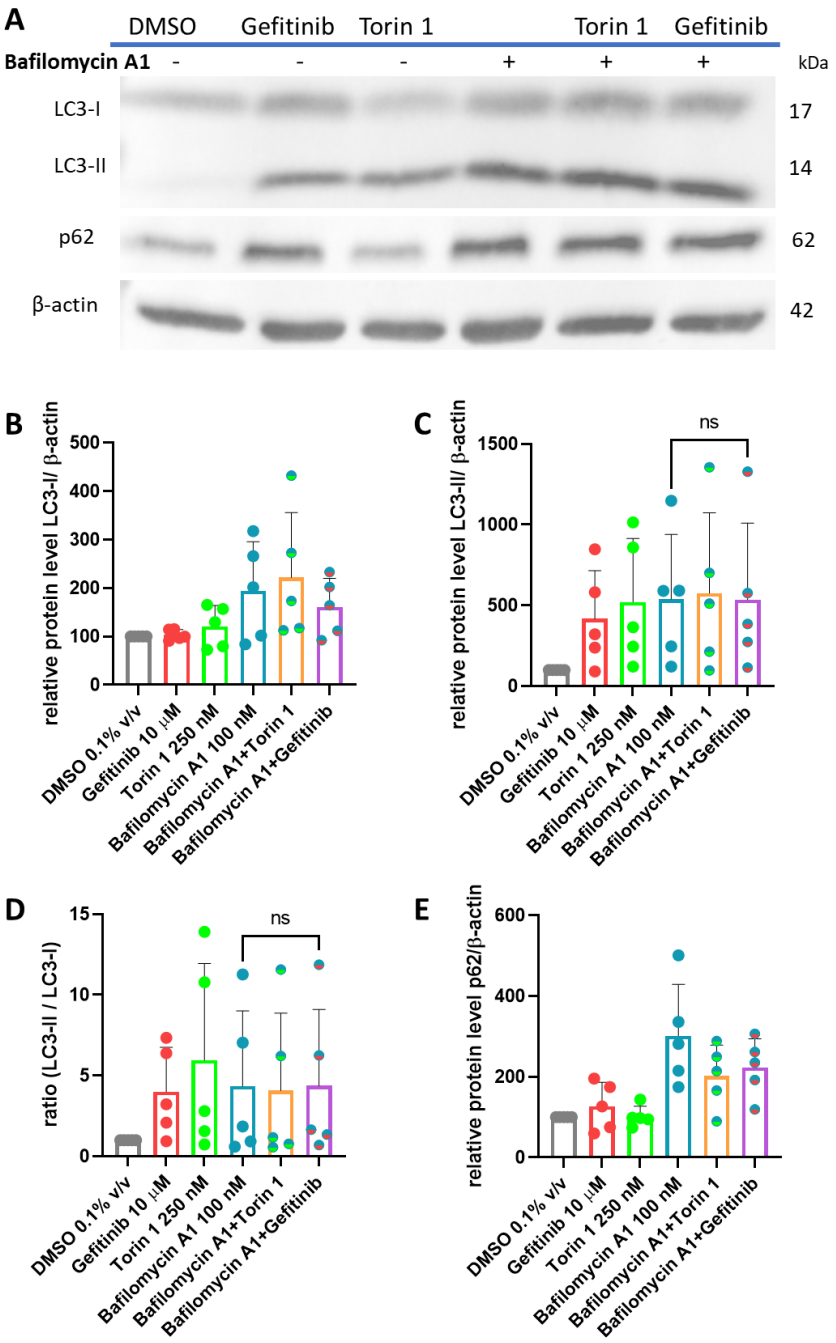

Figure 3.28 Gefitinib effect on autophagy activation in sALS iAstrocytes

(A) Representative western blotting image obtained from sALS_12 iAstrocytes. **(B)** Quantification of LC3-I levels; n=5 experimental repeats (sALS_009 n=2, sALS_17 n=2, sALS_12 n=1; applies to B-E); data are mean ± SD; data relative to DMSO =100. **(C)** Quantification of LC3-II levels; n=5 experimental repeats; data are mean ± SD; data relative to DMSO =100; paired t-test, bafilomycin vs bafilomycin + gefitinib, ns. **(D)** Quantification of LC3-II/LC3-I ratio; n=5 experimental repeats; data are mean ± SD; data relative to DMSO =1; paired t-test, bafilomycin vs bafilomycin + gefitinib, ns. **(E)** Quantification of p62 levels; n=5 experimental repeats; data are mean ± SD; data relative to DMSO =100.

Having observed conflicting results in autophagy assays conducted in iAstrocytes of different genotypes, I have decided to better visualise the LC3-p62 dynamics occurring in iAstrocytes after treatment with gefitinib. For that purpose, PLA was performed to measure the strength of the LC3-p62 interaction. This assay was originally performed as a positive control for PLA described in detail in section 3.2.2.5 and figure 3.23 (representative images in panels C and D). As before, CTR_155v2, C9_183 and sALS_009 were selected based on their responsiveness to gefitinib in the co-culture and their consistent decrease in TDP-35 after nilotinib treatment. Here, an increase in LC3-p62 interaction was observed in C9_183 and sALS_009 patient iAstrocytes, albeit no statistically significant effect was detected (figure 3.29). Nevertheless, these results confirm the finding of the autophagy assays described previously, where gefitinib treatment alone led to LC3-II elevation and had no effect on p62, which is indicative of an autophagic flux in progress. It is important to highlight that bafilomycin A1 treatment caused acute toxicity in iAstrocytes, making it challenging to appreciate any gefitinib effect in co-treatment with bafilomycin A1. For this reason, other autophagy inhibitors such as 3-Methyladenine (3-MA), which prevents autophagophore formation, could be used in future experiments. Moreover, assays investigating the autophagolysosomal fusion, and therefore a successful completion of autophagy, could be run.

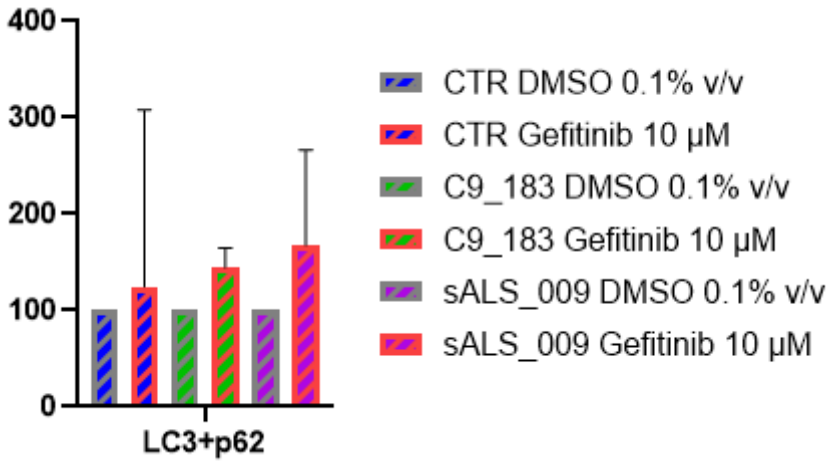

Figure 3.29 Proximity ligation assay measuring the LC3-p62 interaction

n=3 experimental repeats; data are mean ± SD; data relative to DMSO=100; Mann-Whitney test, ns.

3.2.4 Effect of gefitinib on the mitochondrial network in ALS iAstrocytes

Mitochondrial dynamics become aberrant in many neurodegenerative diseases and these dysfunctions can manifest as lack of metabolic flexibility, aberrant fragmentation (fission) or merging (fusion) of the mitochondria (Johri & Beal, 2012). Fission and fusion result in changes to the mitochondrial network and are necessary processes required for maintenance of the mitochondrial network. However, these features are exacerbated in neurodegeneration, for instance, an increase in ROS production can lead to mitochondrial fission (Hu et al., 2019). This section will describe the mitochondrial network dynamics in iAstrocytes before and after a treatment with gefitinib.

3.2.4.1 Mitochondrial numbers at baseline and after gefitinib treatment

In order to visualise the mitochondrial network, iAstrocytes were incubated with tetramethylrhodamine methyl ester (TMRM) live stain. This method allows for a thorough visualisation of the mitochondrial network. In this section we only focused on 2 patients because previous in-house studies had identified them as having mitochondrial defects (unpublished data). Briefly, CTR_155v2, C9_183, and sALS_009 iAstrocyte lines were plated into 96-well plates on day 5 of differentiation. 0.1% v/v DMSO and 10 µM gefitinib treatment was applied on day 6 and after 24 hours each treatment condition was incubated for an hour either with TMRM alone or a combination of TMRM and carbonyl cyanide m-chlorophenyl hydrazine (CCCP) negative control, an inhibitor of oxidative phosphorylation causing a collapse of the mitochondrial network. Representative images of the assay are presented in figure 3.30.

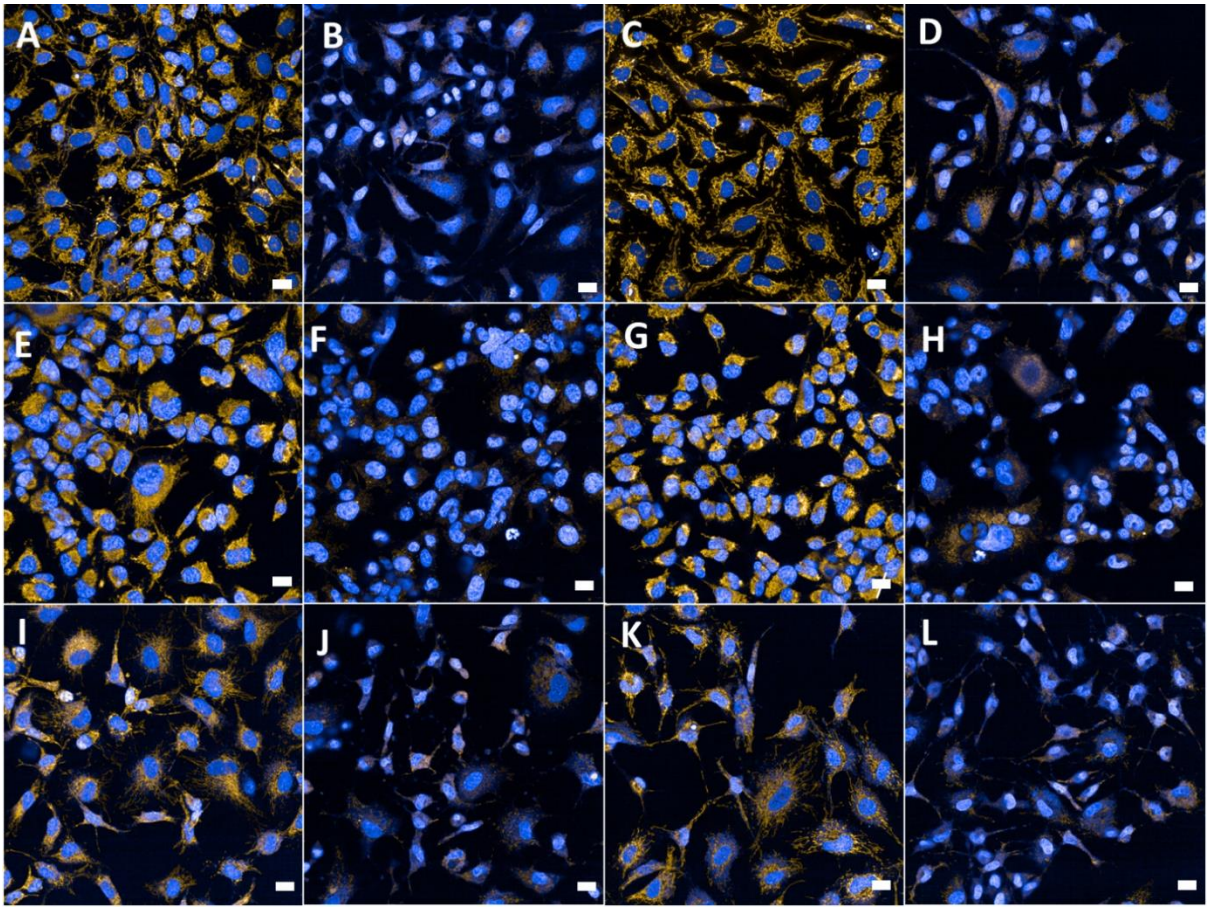

Figure 3.30 Representative images of TMRM staining

Control (**A-D**), C9_183 (**E-H**) and sALS_009 (**I-L**) stained with **TMRM** and **DAPI**. Cells treated with 0.1% v/v DMSO for 24 hours were treated for 1 hour with TMRM alone (**A, E, I**) or with TMRM+CCCP (**B, F, J**). The same treatment was applied to cells incubated with 10 µM gefitinib (**C, G, K** and **D, H, L** respectively). Scale: 20 µm

Although difficult to comment on due to high variability of the data, the number of mitochondria per area of the network did not differ between controls and ALS patient lines at baseline. However, an average sALS_009 cell had more mitochondria than the controls, whereas the opposite was true for the C9_183 line (figure 3.31 A). Interestingly, the number of mitochondria in sALS_009 dropped slightly after gefitinib administration, whereas the numbers were preserved in C9_183 before and after the CCCP challenge (figure 3.31 B). There was no difference in mitochondrial numbers per mitochondrial network area between genotypes at baseline or after gefitinib treatment (figure 3.31 C). The same was true after the CCCP challenge was applied (figure 3.31 D). TMRM intensity was significantly higher in C9_183 than the controls at baseline, with sALS_009 also showing a trend towards an increase.

Gefitinib led to a further mild increase in C9_183 TMRM intensity, whereas no change was observed in sALS_009 (figure 3.31 E). When challenged with CCCP, baseline intensity was comparable across genotypes, whilst gefitinib resulted in a mild decrease in the TMRM intensity of C9_183 compared to DMSO. Gefitinib-treated control and sALS_009 iAstrocytes showed a higher TMRM intensity than their DMSO counterparts (figure 3.31 F). In summary, compared to the mitochondrial network dynamics at baseline, gefitinib treatment caused a trend towards a decrease in mitochondrial numbers, had no discernible effect on mitochondrial network size, and showed a mild trend towards an increase in TMRM intensity of C9_183, but not sALS_009.

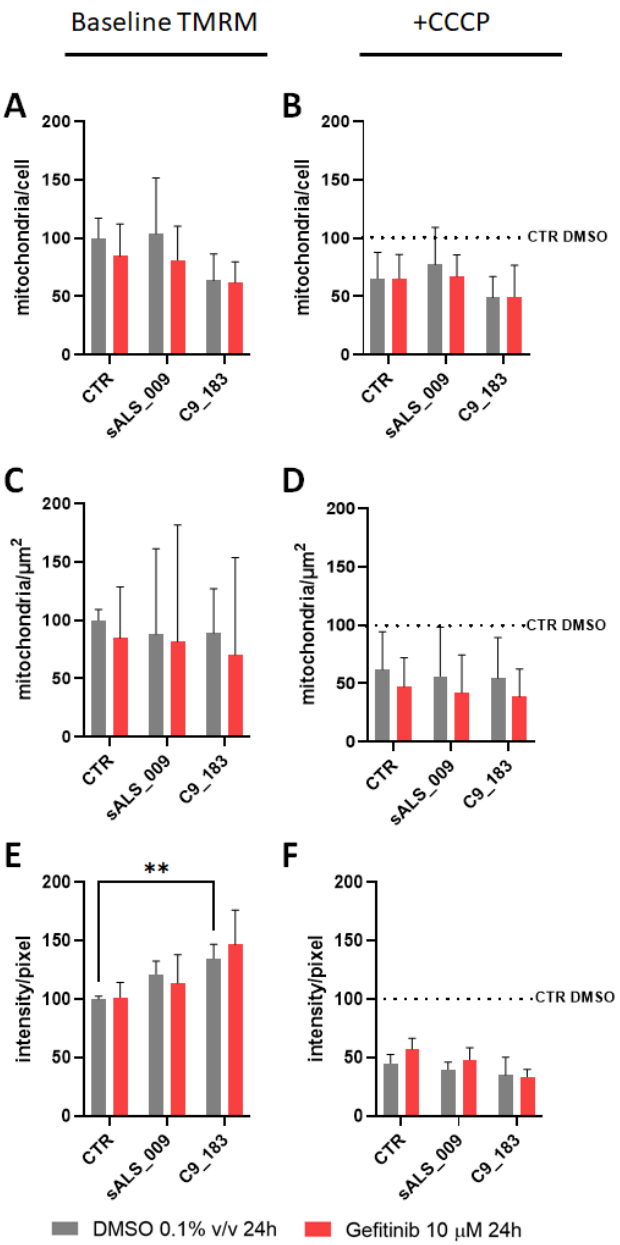

Figure 3.31 Analysis of the mitochondrial network after gefitinib treatment

(**A**) Quantification of mitochondrial numbers per cell. (**B**) Quantification of mitochondrial numbers per cell after challenge with CCCP. (**C**) Quantification of the mitochondrial numbers per mitochondrial network area (in μm^2). (**D**) Quantification of the mitochondrial numbers per mitochondrial network area (in μm^2) after challenge with CCCP. (**E**) Quantification TMRM intensity per pixel; n=4; CTR includes mean results of CTR_155v2 from n=3 experimental repeats and CTR_161 from n=1 experimental repeat; data are mean ± SD; data relative to CTR DMSO=100; two-way ANOVA with Tukey's multiple comparisons, **P<0.01. (**F**) Quantification of TMRM intensity per pixel after challenge with CCCP; n=4; CTR includes mean results of CTR_155v2 from n=3 experimental repeats and CTR_161 from n=1 experimental repeat; data are mean ± SD; data relative to CTR DMSO=100; two-way ANOVA with Tukey's multiple comparisons; unless otherwise specified, all other comparisons ns.

3.2.4.2 Mitochondrial fission vs fusion dynamics after gefitinib treatment

Due to the inconclusive results obtained using TMRM, and the dynamin 1-like protein (DRP1), a key regulator of mitochondrial fission-fusion balance, being a substrate for Abl, one of gefitinib targets, levels of DRP1 were measured in gefitinib-treated iAstrocytes. To better understand the regulation of fission in these cells, levels of DRP1 phosphorylated at serine-616 residue were also measured, as this site is key for fission orchestration (Lee & Kim, 2018). Figure 3.28 A shows a representative DRP1 blot.

During densitometry analysis, total DRP1 bands were quantified together. Levels of DRP1 after DMSO treatment showed high variability between lines, with several lines showing a trend towards a decrease in DRP1 levels after gefitinib treatment, with a notable exception of sALS_12 (figure 3.28 B). C9_183, C9_201 and sALS_12 had elevated levels of pDRP1-ser616 at baseline compared to controls, with the levels dropping significantly after gefitinib treatment in C9_201 (figure 3.28 C). The ratio of pDRP1-ser616 to total DRP1 followed a similar trend to that of pDRP1-ser616 alone, with C9_201 being significantly elevated (figure 3.28 D). No statistically significant differences between DMSO and gefitinib-treated cells were observed.

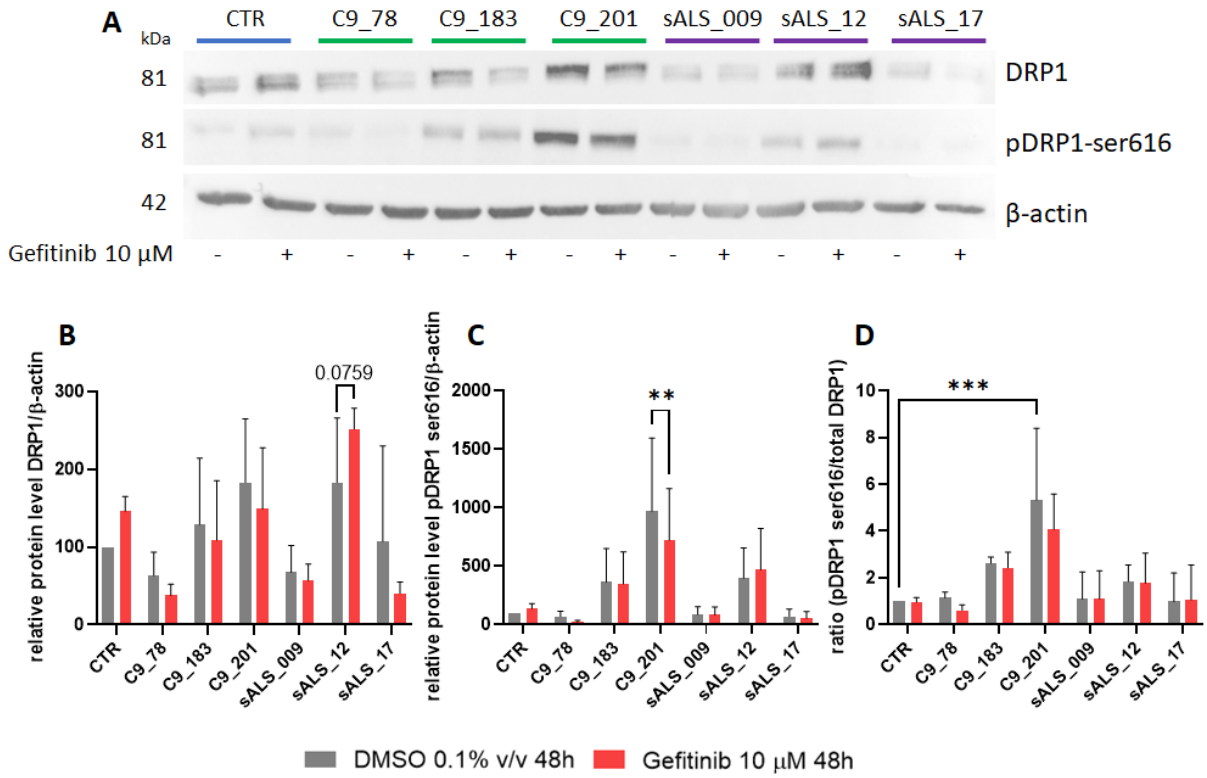

Figure 3.32 Gefitinib treatment effect on DRP1 phosphorylation at serine-616 and total DRP1 levels in iAstrocytes

(A) Representative western blot images of total DRP1 and pDRP1-ser616. **(B)** Quantification of DRP1 levels; n=3-5 experimental repeats; CTR includes mean results of CTR_155v2 from n=3 experimental repeats and CTR_161 from n=1 experimental repeat and CTR_AG08620 from n=1 experimental repeat; data relative to CTR DMSO =100; data are mean ± SD; two-way ANOVA with Tukey's multiple comparisons test, ns. **(C)** Quantification of pDRP1-ser616 levels; n=3-5 experimental repeats; CTR includes mean results of CTR_155v2 from n=3 experimental repeats and CTR_161 from n=1 experimental repeat and CTR_AG08620 from n=1 experimental repeat; data relative to CTR DMSO =100; data are mean ± SD; two-way ANOVA with Tukey's multiple comparisons test, **P<0.01. **(D)** Quantification of pDRP1-ser616 to total DRP1 ratio; n=3-5 experimental repeats; CTR includes mean results of CTR_155v2 from n=3 experimental repeats and CTR_161 from n=1 experimental repeat and CTR_AG08620 from n=1 experimental repeat; data relative to CTR DMSO =1; data are mean ± SD; two-way ANOVA with Tukey's multiple comparisons test, ***P=0.0003; all other comparisons ns unless stated otherwise.

3.2.5 Gefitinib regulation of Abl1 in ALS iAstrocytes

Having investigated some of the pathological and functional changes in iAstrocytes caused by gefitinib treatment, we have set off to deconvolute which target is crucial for gefitinib to

engage with to exert beneficial effects described in this chapter. We have concluded in section 3.2.1.3 that EGFR is unlikely to be the key modifying target of gefitinib in our model due to its low baseline expression levels in most iAstrocytes. Of all gefitinib targets unveiled in the kinome screening (table 3.1), Abl1 has been of interest to the ALS research community as a potential disease-modifying target. Conditioned media from primary astrocytes obtained from Abl1-overexpressing animals decreased the survival of primary and iPSC-derived motor neurons (Katsumata et al., 2012). Similarly, iPSC-derived motor neurons have been found to overexpress Abl1 and both genetic and pharmacological modification of its levels rescued motor neuronal survival and led to improvements in mitochondrial function (Imamura et al., 2017).

To start verifying the effect of gefitinib on Abl1 in iAstrocytes, I first investigated its transcript levels following multiple drug treatments at 1h, 6h, 12h and 24h. At baseline, C9orf72 iAstrocytes showed a convincing increase in *ABL1* compared to controls (figure 3.33 A). Neither of the gefitinib treatment timepoints had an effect on *ABL1* in controls (figure 3.33 B), whereas a trend towards a decrease in *ABL1* transcript was observed in C9_78 in gefitinib treatments of 12h and 24h (figure 3.33 C), indicating that there might be an element of transcriptional regulation of *ABL1* by gefitinib.

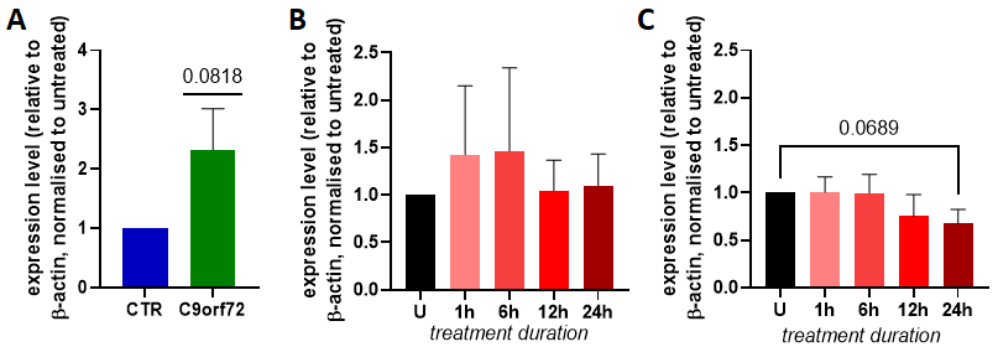

Figure 3.33 ABL1 transcript levels in iAstrocytes.

(A) Baseline *ABL1* transcript level in C9orf72 vs CTR lines; n=3 (C9orf72 includes mean values of C9_78 n=2 experimental repeats, C9_183 n=2 experimental repeats, C9_201 n=2 experimental repeats); mean ± SD; data relative to untreated control =1; one-sample t-test. **(B)** Expression of *ABL1* in CTR_3050 following a treatment with gefitinib at several time points; n=2; mean ± SD; data relative to untreated =1; **(C)** Expression of *ABL1* in C9_78 following a treatment with gefitinib at several time

points; n=3; mean ± SD; data relative to untreated =1; Kruskal-Wallis with Dunn's multiple comparisons test, *P=0.0406.

3.2.5.1 *Gefitinib reduces expression of total Abl1 protein in patient iAstrocytes*

Having interrogated the expression of *ABL1* transcript in iAstrocytes, which unveiled elevated baseline levels of *ABL1* and a trend towards a decrease in these levels after a 24h treatment with 10 µM gefitinib, I have further assessed the expression of Abl1 protein in iAstrocytes. For that purpose, 3 healthy controls, 3 C9orf72 patients and 3 sALS had their Abl1 protein expression measured via western blotting. iAstrocytes from patients expressed significantly higher levels of Abl1 compared to healthy controls (figure 3.34 A and B). Although higher than in the controls, Abl1 expression in individual ALS patient genotypes was not statistically significant (figure 3.34 C). These results are in agreement with the RNA data described in the previous section.

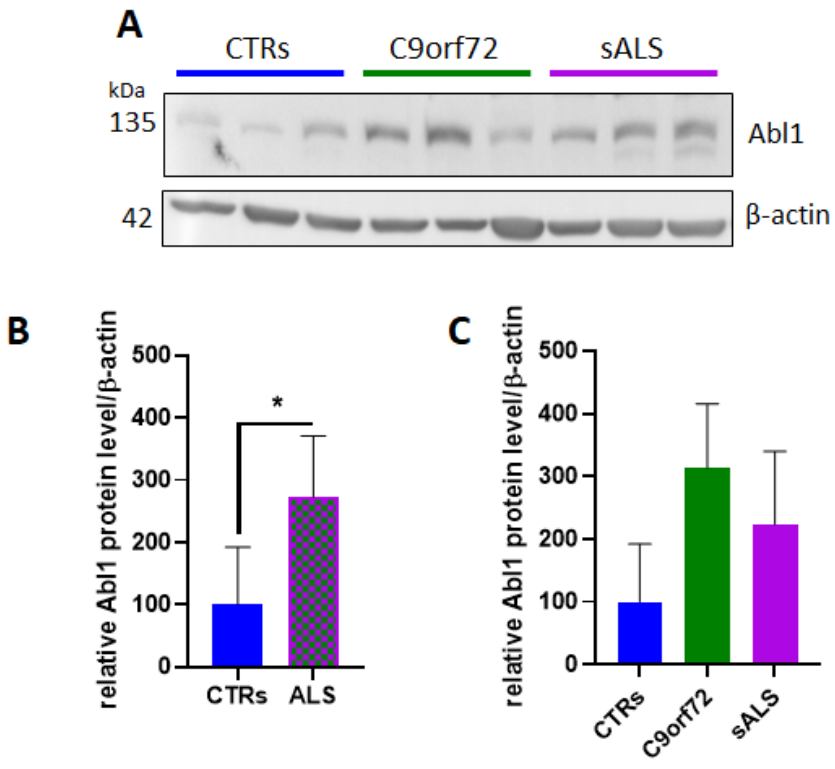

Figure 3.34 Levels of Abl1 protein in ALS iAstrocytes

(A) Representative western blot. **(B)** Comparison of all ALS iAstrocyte lines to control iAstrocytes; data relative to CTR DMSO=100; data are mean ± SD; n=3-9; CTR includes mean results of CTR_155v2 from n=3 experimental repeats; CTR_3050 mean from n=3 experimental repeats and CTR_AG08620 mean from n=3 experimental repeats; unpaired t-test, *P<0.05. **(C)** Expression of Abl1 in each ALS patient genotype; data relative to CTR DMSO=100; CTR includes mean results of CTR_155v2 from n=3

experimental repeats; CTR_3050 mean from n=3 experimental repeats and CTR_AG08620 mean from n=3 experimental repeats; data are mean ± SD; n=3, one-way ANOVA with Tukey's multiple comparisons test, all comparisons ns.

Next, I tested the effect of gefitinib on Abl1 protein expression. For that purpose, iAstrocytes were treated as before with 0.1% v/v DMSO vehicle or 10 µM gefitinib for 48h. A representative western blotting image is presented in figure 3.35 A. Compared to DMSO-treated iAstrocytes, treatment with gefitinib resulted in a significant decrease in the total Abl1 protein levels in C9orf72 iAstrocytes. The same trend was observed in sALS iAstrocytes, while levels in control iAstrocytes were unchanged (figure 3.35 B). This outcome complements the initial RNA findings and is in agreement with previously published reports on Abl1 expression in ALS motor neurons (Katsumata et al., 2012, Imamura et al., 2017).

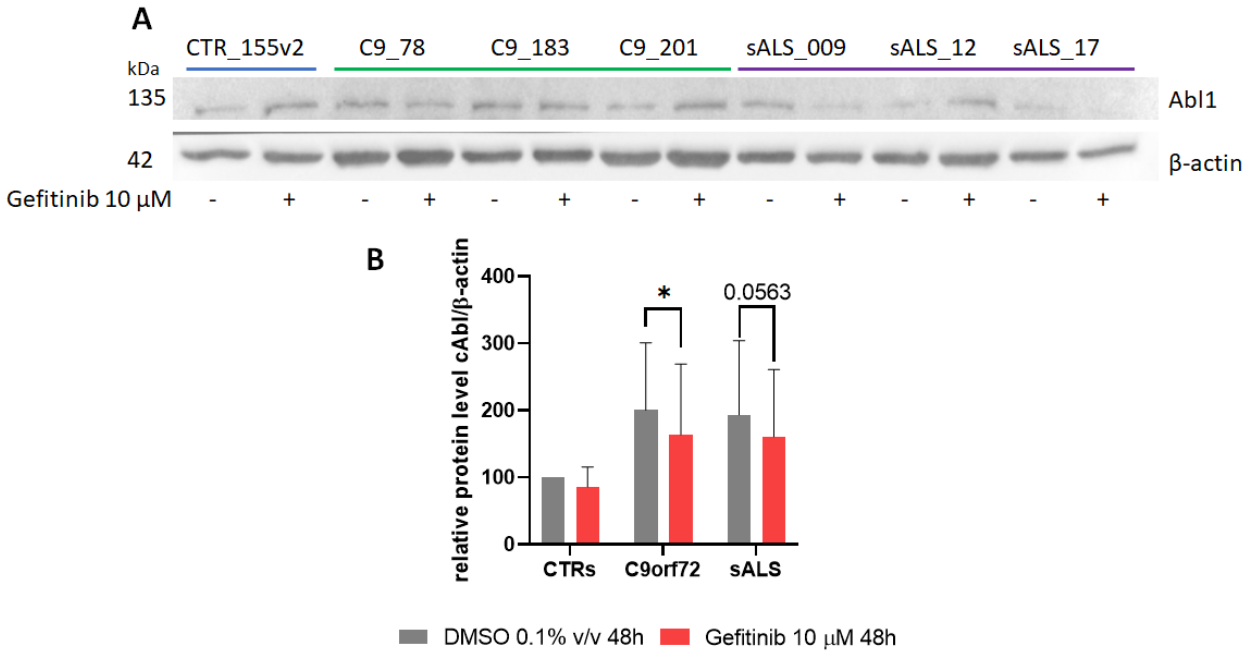

Figure 3.35 The effect of gefitinib on Abl1 expression in iAstrocytes

(A) Representative western blot showing the expression of Abl1 in iAstrocytes after treatment with DMSO 0.1% v/v or gefitinib 10 µM. **(B)** Western blot quantification; n=3 per genotype; data relative to CTR DMSO = 100; CTR includes mean results of CTR_155v2 from n=3 experimental repeats; CTR_3050 mean from n=3 experimental repeats and CTR_AG08620 mean from n=3 experimental repeats; data are mean ± SD; *P<0.05, two-way ANOVA with Šidák's multiple comparisons test.

3.2.5.2 Abl1 phosphorylation status after gefitinib treatment

Phosphorylation of Abl1 by several kinases is essential for its activation. Abl1 complex can also be constitutively active, as Abl1 is capable of autophosphorylation at the tyrosine-412. To test if the decrease in Abl1 protein levels seen after gefitinib treatment was due to changes in Abl1 phosphorylation status, we set to measure levels of phosphorylated Abl1 at all sites (panTyr-pAbl1) and at tyrosine-412 site only (pAbl1-Tyr412).

To verify the levels of active, phosphorylated Abl1 (henceforth referred to as pAbl1) in our model, iAstrocyte lysates were analysed for pAbl1 levels via western blotting.

The pAbl1 antibody used was specific for Tyr412 site. Optimisation runs to test different western blotting membranes and antibody concentrations and manufacturers, performed jointly with Dr Nora Markus, yielded poor-quality blots with unreliable signal and high levels of background noise (figure 3.36). A similar issue was encountered when testing an antibody from a different manufacturer for the same phosphorylation site (data not shown). Therefore, having tested the two different antibodies to no effect, further attempts to detect pAbl1 in iAstrocytes via western blotting were abandoned in favour of alternative methods.

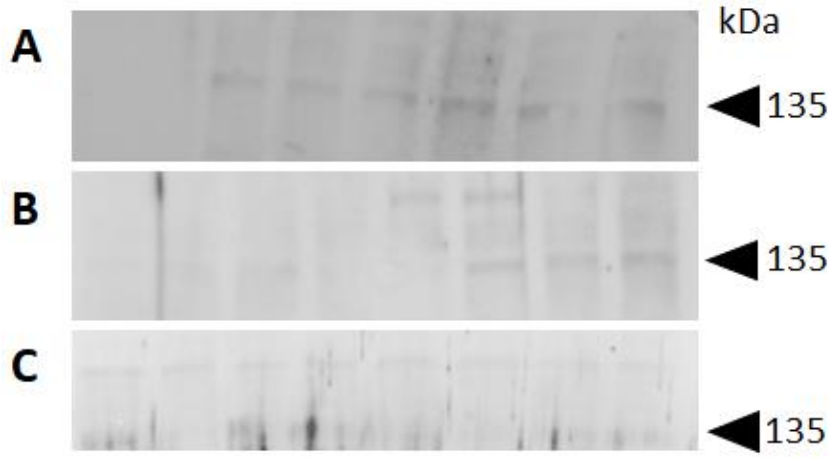

Figure 3.36 pAbl1 (Tyr412) antibody optimisation

pAbl1 (Tyr412) antibody failed to produce reliable signal in iAstrocytes in western blotting when transferred onto nitrocellulose after blocking with 5% BSA (**A**) or on PVDF with 5% BSA (**B**), even when antibody concentration was increased by 50% (**C**).

Therefore, experiments were repeated using lysates obtained from an immortalised K562 bone marrow-derived chronic myelogenous leukaemia (CML) cell line, which models

pathogenic Abl1 overexpression due to its detectable levels of BCR-Abl1 hybrid gene (Luchetti et al., 1998). Therefore, K562 cells were used as a positive control for Abl1 activation. sALS_12 iAstrocytes, which express the highest levels of total Abl1 of all patient iAstrocytes tested in this work, transfected with shRNA-Abl1 to knock down Abl1 expression were used as a negative control. The shAbl1 complex contained an RFP fluorophore, therefore cells treated with shRFP only were used as a negative control for Abl1 knockdown. Prior to conduction of the pAbl1 ELISA, both positive and negative controls had their Abl1 protein levels validated. Representative western blotting image of Abl1 expression in K562 is shown in figure 3.37 A. Compared to its DMSO vehicle control, gefitinib did not lead to a significant reduction in Abl1 (figure 3.37 B) and BCR-Abl1 (figure 3.37 C) in K562 cells. Representative western blotting image of Abl1 expression in Ad-treated sALS_12 is shown in figure 3.37 D. Compared to its shRFP counterpart, shAbl1 transduction resulted in a significant reduction in Abl1 levels in sALS_12 (figure 3.37 E).

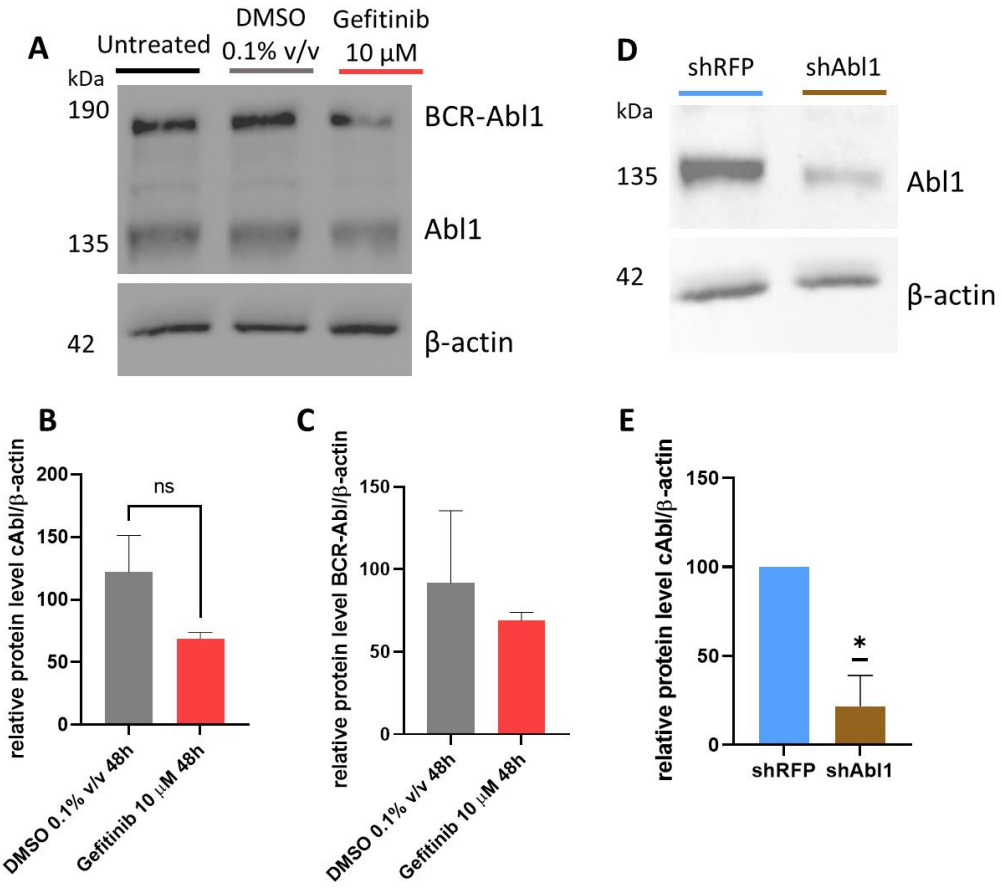

Figure 3.37 Pan-Tyr Abl1 ELISA controls validation

(**A**) Representative western blot image of Abl1 and BCR-Abl1 in K562 cells. (**B**) Quantification of Abl1 expression in DMSO- and gefitinib-treated K562 cells; n=3 experimental repeats; data relative to

untreated K562 cells = 100; mean ± SD; paired t-test, ns. (**C**) Quantification of BCR-Abl1 expression in DMSO- and gefitinib-treated K562 cells; n=2; data relative to untreated K562 cells = 100; mean ± SD. (**D**) Representative western blot image of Abl1 in sALS sALS_12 transduced with Abl1-shRNA. (**E**) Validation of Abl1 protein knockdown in sALS_12 transduced with shAbl1; n=3, data relative to shRFP control = 100; mean ± SD; one sample t-test, *P<0.05.

iAstrocytes express significantly lower levels of pAbl1 than K562 cells (figure 3.38 A). Patient iAstrocytes showed marginally elevated levels of pAbl1 compared to controls. Gefitinib did not appear to influence pAbl1. After several attempts and an increase in the total protein content loaded into assay wells, we did not detect pAbl1-Tyr412 in most iAstrocytes samples above the background signal. Although these findings would have to be evaluated with a more sensitive assay, as the levels of pAbl1 in iAstrocytes are close to detection level for this assay, gefitinib did not reduce the level of pAbl1 in K562 cells, thus confirming that gefitinib does not influence Abl1 phosphorylation, but it leads to a reduction in total Abl1 protein in iAstrocytes via transcriptional regulation.

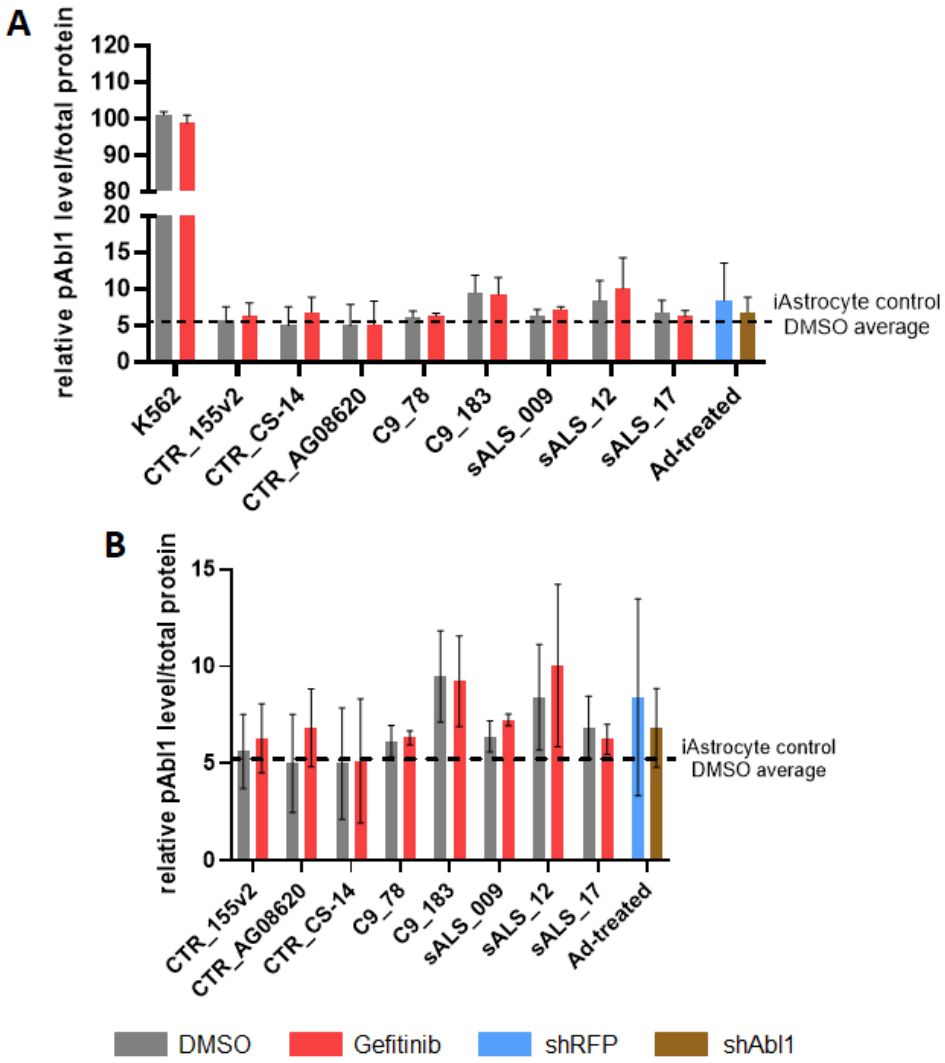

Figure 3.38 Phosphorylation status of Abl1 in gefitinib-treated iAstrocytes

(A) Quantification of pAbl1 levels; n=3 experimental repeats; data are mean ± SD; ****P<0.0001, two-way ANOVA with Šidák's multiple comparisons test. **(B)** Quantification of pAbl1 levels in iAstrocytes alone; n=3 experimental repeats; data are mean ± SD; two-way ANOVA with Šidák's multiple comparisons test, all comparisons ns. All data normalised to the total protein content and relative to panTyr-Abl1 levels in untreated K562 cells.

In summary, gefitinib administration rescued motor neuronal survival in a co-culture with ALS patient iAstrocytes. Treatment with gefitinib reduced the levels of TDP-35 cleavage product in iAstrocytes and iNeurons, whilst simultaneously increasing the levels of total TDP-43. Gefitinib-treated cells showed a trend towards an increase in the nuclear TDP-43 signal, whilst no change in the pTDP-43 cytoplasmic burden was observed. Changes in TDP-35 levels were speculated to be a result of either a decreased rate of TDP-43 cleavage by caspase-3 or an

improved clearance of this cleavage product via autophagy. The former hypothesis was tested via PLA, where no change in TDP-43-caspase-3 interaction was observed, whilst the autophagy assays showed gefitinib to be an autophagy activator in HEK293 cells and control iAstrocytes.

Although expression levels of EGFR in iAstrocytes were low (with an exception of lines obtained from female donors), gefitinib engaged with it by decreasing EGFR phosphorylation. Gefitinib also engaged with Abl1, one of its targets overexpressed in ALS iAstrocytes, by decreasing levels of total Abl1 protein, but having no effect on its phosphorylation status. In spite of its effect on Abl1, a binding partner of multiple mitochondrial protein, gefitinib had no discernible effect on mitochondrial fission or network size whilst showing a trend towards a decrease in mitochondrial numbers and an increase in MMP.

3.3 Discussion

There is a critical need for new effective therapies for ALS, as the two currently available drugs, riluzole and edarovone, offer limited improvements to patients' health (Jaiswal, 2019). The process of drug discovery for ALS has been marred by failures (Gordon & Meininger, 2011), further highlighting the need for novel approaches. In this chapter, I focus on unveiling the mechanism of action of gefitinib, a compound identified by AI-driven technologies as a potential ALS therapeutic.

High-dimensional structured and unstructured data mining for new repurposing compounds for ALS conducted by BenevolentAI has led to an identification of 5 drugs validated in the pathophysiological co-culture model of the disease. Gefitinib was the compound which consistently resulted in the highest rescue of motor neuronal survival, which qualified it for further validation.

Use of gefitinib in chemotherapies made it important to verify the effect of the drug on iAstrocyte cell numbers, as the main objective of cancer drugs is to kill tumour cells or decrease their proliferation rate. Treatment of iAstrocytes with 10 µM gefitinib for 48h has resulted in a mild, but significant decrease in control and sALS lines cell numbers. Our initial

speculation pointed towards a possible toxicity caused by the drug, which was supported by the LDH assay where an approximate 30% cytotoxicity was observed in 10 µM-treated cells. Results obtained for 30 µM gefitinib in the LDH assay, however, are unusual, since we have not expected a drug concentration to cause a higher LDH release than a positive control which consisted of a cell lysis buffer. This indicates that either the positive control has underperformed in the assays or the 30 µM gefitinib interfered with the fluorescence readout of the assay. Therefore, we might be overestimating the toxicity of gefitinib at 10 µM. It is noteworthy that the LDH assay was performed in C9_78, one of the few lines in which I have observed a decrease in the overall cell number following the gefitinib treatment. It has also shown a decrease in proliferation. If 10 µM gefitinib was indeed leading to approximately 30% cytotoxicity, this drop in cell number would have been observed across multiple cell lines, however, this result was not consistent. Furthermore, we did not observe an increase in toxicity with longer time of exposure of the cells to the drug, as the 72h treatment still led to about 30% cytotoxicity. It is not unlikely that the LDH results are C9_78-specific and further investigation of gefitinib's cytotoxicity spanning multiple cell lines would need to be performed. It is important to point out that gefitinib has been documented as an agent capable of abrogating senescent cells (Ventura et al., 2007; Zhu et al., 2015), therefore the observed cell death might also reflect the loss of senescent astrocytes. Indeed, an interesting hypothesis is that the cell death we have observed is reflective of the death of senescent cells carrying the largest pathological burden, leaving behind cells capable of supporting motor neurons in the co-culture assay. I have briefly interrogated the transcript levels of senescence-specific isoform of p53, Δ133p53 (Gong et al., 2015), after gefitinib treatment, however no conclusions could be drawn due to line to line variability (data not shown). Due to COVID-19-related timing issues I was unable to expand on that dataset by performing other assays. However, further work is currently being planned to look at the effect of gefitinib on cellular senescence and will form a part of an article manuscript currently in preparation for publication.

The changes in cell morphology and vimentin intensity observed in gefitinib-treated cells could be indicative of cytoskeleton remodelling. It is a process through which cellular organization is changed as a response to environmental cues, occurring often as a result of

chronic cellular stress or in diseases. In ALS, cytoskeleton remodelling has been described, for example, upon exacerbated ROS production (Clark et al., 2016). On the other hand, EGFR induces actin remodelling in cancer cell lines, an effect which is blocked by gefitinib, resulting in reduced cell motility, invasion and growth (Takeuchi & Ito, 2010). Increase in cell roundness observed in iAstrocytes treated with gefitinib could be used as a target engagement readout, as it was consistent across multiple cell lines and experimental repeats. A study in NSCLC cells has demonstrated that gefitinib-resistant strains of the H292 cell lines form protrusion structures, whereas gefitinib-sensitive strains appear much rounder (Bae et al., 2016). Upregulation of Serpin2B protein appears to be a key factor driving the cell roundness effect in gefitinib-sensitive cells. Of relevance to our study, a nuclear calcium-regulated neuroprotectant SerpinB2 has recently been suggested as a potential treatment for chronic neurodegenerative disorders, including ALS (Buchthal et al., 2018). Investigation of the gefitinib effect on SerpinB2 in ALS iAstrocytes could potentially contribute to the underlying mechanisms contributing to neuroprotection in our co-cultures.

Gefitinib is used as a first-line treatment in NSCLC cases driven by a mutation in EGFR. To test gefitinib's engagement with it, EGFR levels were measured at the transcript and protein levels in iAstrocytes treated with gefitinib or DMSO vehicle. Most iAstrocyte lines used in this study, particularly those obtained from male patients, do not harbour an overexpression defect in EGFR. Importantly, gefitinib treatment for 48h nevertheless resulted in a decrease in EGFR phosphorylation, thus showing an engagement with its primary target and suggesting that, regardless of target engagement, in our system, efficacy is likely to be driven by other targets. One of the important functions of gefitinib in NSCLC is its ability to inhibit cancer cell migration, which is dependent on cytoskeletal remodelling, therefore the changes in iAstrocyte morphology could be directly linked to gefitinib's inhibition of pEGFR observed here.

Gefitinib target engagement was further tested by measuring transcript levels of *CCNG2*, a non-canonical cyclin whose expression increases upon cell cycle arrest. Although not statistically significant, a pattern of gradual increase in *CCNG2* expression after 1h, 6, 12h and

24h drug treatment was observed. These results are consistent with previously published reports (Bernaudo et al., 2017).

The observed gefitinib-induced reduction in TDP-35 levels was arguably the most promising result of this study. However, the precise mechanism behind this result remains unclear. I hypothesised that the fragment is degraded via autophagy upon gefitinib treatment. Previously published reports have described gefitinib as a potent activator of autophagy in several cancer cell lines (Dragowska et al., 2013). The encouraging results obtained in HEK293 cells and control iAstrocytes did not directly translate in C9orf72 and sALS iAstrocytes. Importantly, it is known that C9orf72 hexanucleotide expansion in ALS causes defects in autophagy initiation and results in lysosomal abnormalities, preventing normal autolysosomal fusion and thus conclusion of autophagy (Boivin et al., 2020; Chitiprolu et al., 2018; Ji et al., 2017). The assays utilised in this project was useful in investigating compounds causing an autophagic flux, but not the successful autophagolysosomal fusion, as bafilomycin A1 inhibits lysosome-mediated cargo degradation by blocking the fusion of lysosomes with autophagophores (Yamamoto et al., 1998). Moreover, bafilomycin A1 caused toxicity in our cell model, thus suggesting it might have not been an optimal control for the assays. To understand if gefitinib improves autophagolysosomal fusion, a co-staining of a lysosomal marker such as lysosome-associated membrane protein 2 A (LAMP2A) with a LC3 could be performed before and after gefitinib treatment.

The question remains if autophagy activity can be restored in situations of C9orf72 haploinsufficiency. One of the functions of C9orf72 protein has been linked to regulation of endosomal trafficking (Farg et al., 2014). Given the important intersection of endosomal function and autophagy (Hansen & Johansen, 2011), restoring C9orf72 protein levels in scenarios of haploinsufficiency could therefore help boost autophagy. Moreover, loss of C9orf72 has been previously shown to impair autophagy initiation (Sellier et al., 2016). In this project, gefitinib treatment caused an autophagic flux in patient astrocytes as shown by the elevated LC3-II levels, lack of p62 upregulation and increased LC3-p62 interaction, thus showing that it can overcome the autophagy initiation impairment. Although I have not investigated the potential effect of gefitinib on C9orf72 expression and it is unlikely that it

affects the C9orf72 protein levels or targets haploinsufficiency, it might nevertheless help mitigate the autophagic dysfunction observed in patients carrying the C9orf72 expansion.

Another way in which gefitinib could decrease levels of TDP-43 fragmentation is by preventing its cleavage by caspase-3. Assays measuring caspase-3 activity could provide an answer to this question. Instead, TDP-43-caspase-3 interaction was measured in a PLA, providing information on the level of interaction between TDP-43 and capsase-3. Importantly, there is indication in the literature that the TDP-35 fragment is a result of caspase-3-mediated cleavage at TDP-43's nuclear localisation signal (NLS) domain (Winton et al., 2008; Zhang et al., 2009; Li et al., 2015). The PLA approach could be further improved by measuring the strength of the interaction between caspase-3 and pTDP-43, as TDP-43 needs to be phosphorylated prior to cleavage (Zhang et al., 2009). Improved nuclear import of TDP-43 or, indeed, lack of TDP-43 nuclear export to begin with, could be a potential mechanism that has remained untested in this project. Importantly, it remains unknown if the cell toxicity associated with TDP-43 is a result of a cytoplasmic gain-of-function or a nuclear loss-of-function. Elucidation of these dynamics would be of help for future drug discovery and repurposing efforts, as knowledge of the targets and pathways involved can allow for a synthesis of appropriate, specific therapeutic molecules. Of particular importance to this hypothesis remains the fact that gefitinib targets casein kinase epsilon, which has also been shown previously to phosphorylate TDP-43. It is not unlikely that the reduced number of pTDP-43 cytoplasmic inclusions and lower levels of TDP-35 fragment could be a result of casein kinase inhibition which could lead to reduced TDP-43 cleavage.

A trend towards a mild increase in the nuclear localisation of TDP-43, as hypothesised, could be a result of a decrease rate of TDP-43 cleavage. Alternative hypotheses not tested here point towards gefitinib's regulation of nucleocytoplasmic transport, either preventing TDP-43 from shuttling to the cytoplasm in the times of sustained cellular stress or improving the nuclear import of cytoplasmic TDP-43. To help us fully elucidate the nuclear TDP-43 dynamics after gefitinib treatment, cell fractionation protocol is currently being optimised to look independently at the levels of TDP-43 in the nucleus and the cytoplasm after the drug treatment.

Abl1 has multiple documented interactions with mitochondrial proteins, of which DRP1 is responsible for orchestration of fission vs fusion balance. Of DRP1 phosphorylation sites,

serine-616 residue has been described as a key site necessary for mitochondrial fission occurrence (Lee & Kim, 2018), whereas increased phosphorylation of DRP1 at serine-637 indicates inhibition of fission (Ko et al., 2016). Given the observed decrease in total Abl1 protein expression in iAstrocytes following the treatment with gefitinib, we hypothesised that levels of DRP1 might also be affected. There is a limited amount of published reports describing the effect of gefitinib treatment on the mitochondria, with recent studies linking gefitinib therapies to an improvement in mitochondrial functions in NSCLC mutant EGFR-positive cells (Takenaka et al., 2017). In this study, gefitinib treatment of iAstrocytes did not lead to marked changes in mitochondrial dynamics. Previous reports have demonstrated that Abl1 overexpression can lead to exacerbated mitochondrial fission driven by pDRP1-ser616 phosphorylation, which can be reversed by Abl1 knockdown (Zhou et al., 2017). Given the marginal decrease in the mitochondrial network size observed alongside an increase in TMRM intensity at basal level and upon CCCP stress and decrease in mitochondrial numbers, it is possible that gefitinib leads to an increase in mitochondrial fusion in C9orf72 iAstrocytes. As a standalone result, it could be indicative of mitochondria reacting to stress by incorporating damaged mitochondrial, hence decreasing the overall mitochondrial network surface area to preserve energy demands (Youle & Van Der Bliek, 2012).

In addition, in an in-house proof-of-concept *in vivo* study in $SOD1^{G93A}$ mice, co-treatment of gefitinib and an efflux transporter inhibitor elacridar resulted in a significant delay of neurological symptoms onset, alongside decrease of phosphorylated neurofilaments in motor neurons and neuropil (unpublished data). It has to be stressed, however, that this improvement was observed alongside severe adverse effects (alopecia, skin rash, nausea, and liver toxicity) in mice, as well as no overall improvement in their motor function. The observed side effects are consistent with adverse effects seen in NSCLC patients taking gefitinib and are synonymous with on-target EGFR inhibition (Xin et al., 2019). It is not unlikely that nausea and overall poor wellbeing of these mice were the cause of decreased motor function, as the neurofilament heavy-chain phosphorylation decrease would suggest a rescue in motor neuronal survival in the spinal cord. Interestingly, a study investigating an EGFR inhibitor erlotinib in $SOD1^{G93A}$ mice observed a similar delay in symptom onset, but without a rescue of motor neuronal survival at the NMJ (Le Pichon et al., 2013). Erlotinib, previously described as a more effective inhibitor of EGFR than gefitinib (Kim, Apetri, Luo, Settleman, & Anderson,

2015), has underperformed in the co-culture assay in comparison with gefitinib, indicating that gefitinib carries an additional neuroprotective property absent in erlotinib, which is independent of EGFR activity in our cell model. Based on our *in vitro* data, the additional protective mechanism could be the activation of autophagy. However, more work needs to be conducted in both iAstrocytes carrying a SOD1 mutation as well as in motor neurons from a range of ALS genotypes in order to fully elucidate the MOA of gefitinib globally in ALS.

Recent advances in medicinal chemistry make it possible to amend the chemical structure of a molecule in a way that can improve the general polypharmacological profile of the drug, including a decrease in the likelihood of side effects. Therefore, understanding exactly which kinases need to be engaged by gefitinib in order to observe motor neuronal rescue *in vitro* and a delay in symptoms onset *in vivo* is important. Such information could be used to refine the molecular structure of gefitinib in a way that could preserve its effect on key ALS-relevant pathways, whilst improving brain penetrance and minimising adverse reactions. Studies such as this one could also shed a light on the precise combination of pathogenic mechanisms in ALS that require modulation in order to rescue motor neurons *in vitro* and *in vivo*.

4 Assessing the repurposing potential of nilotinib in ALS

4.1 Introduction

Results of the first set of co-culture drug screenings conducted in collaboration with BenevolentAI have identified gefitinib as a potential repurposing compound for ALS. As described in chapter 3, the drug showed a lot of promise, especially since it was able to improve the hallmarks of TDP-43 proteinopathy in patient iAstrocytes. However, its inability to remain in the CNS after crossing the BBB, called for a continued search for a better compound.

Following the promising neuroprotection observed with gefitinib, an AI-powered literature search using precede and SQT (figure 3.1) was conducted on the target profile of gefitinib. In this search, Abl1 consistently emerged as a neuroprotective target. Using Abl1 as a starting point for a new wave of hypothesis generation and drug selection resulted in identification of several Abl1 inhibitor compounds which exhibited potential for repurposing in ALS. Out of all compounds tested, nilotinib (figure 4.1) yielded the highest rescue of motor neuron survival in the co-culture assays conducted by Dr Matthew Stopford (figure 4.2), therefore I have decided to characterise its neuroprotective profile and function in ALS patient astrocytes.

In order to deconvolute its mechanism of action, nilotinib was subjected to the same series of experiments as gefitinib, oftentimes side-by-side on the same set of cells. This was not only to allow for a direct comparison between the two drugs, but also because the current consensus in the literature on nilotinib and Abl1 supported the hypotheses behind these experiments.

4.1.1 Nilotinib: use, properties, and function

Nilotinib, marketed as Tasigna®, is a tyrosine kinase inhibitor used to treat chronic myelogenous leukaemia (CML) cases positive for Philadelphia chromosome (Ph+) (Ray et al., 2007). All cases of Ph+ CML carry a breakpoint cluster region-Abelson (BCR-Abl) fusion protein, which is a result of a reciprocal translocation of chromosomes 9 and 22. BCR-Abl is an example of a kinase domain mutation and is thus constitutively active, leading to CML cell hyperproliferation (Olivieri & Manzione, 2007).

Nilotinib has received FDA and EMA authorisation in 2007 and 2009 respectively as a second-generation BCR-Abl inhibitor for CML, as a result of reports describing a cohort of CML

patients developing resistance to imatinib, the initial standard of care (Ray et al., 2007). Although nilotinib's structure is largely based on imatinib's (Fouad & Elkady, 2014; figure 4.2), it is a more potent inhibitor BCR-Abl. It has since been tested as a treatment for gastric cancers, although failing to show benefit (Blay et al., 2015).

Nilotinib has also been shown to exert anti-tumour and neuroprotective effects in the peripheral nervous system, as seen in the context of plexiform neurofibromas (Wei et al., 2014).

Multiple reports have described nilotinib as a moderately CNS-permeable compound (Karuppagounder et al., 2014; Lee et al., 2017; Pagan et al., 2016). Although side effects of nilotinib treatment are not insignificant, including a black box warning for heart function, all these properties make it an attractive repurposing agent for neurodegeneration, which has been a subject of extensive investigations in the recent years.

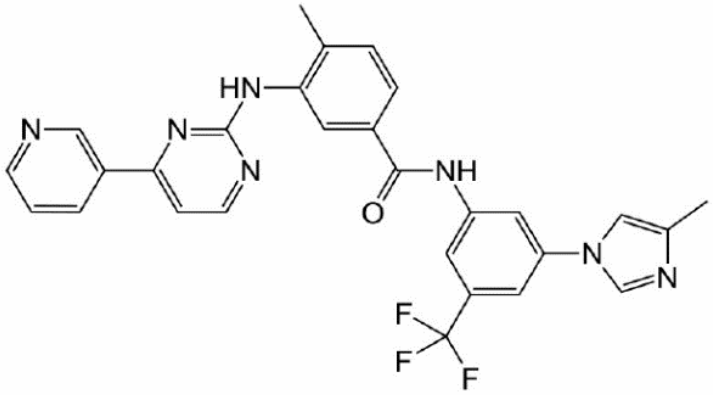

Figure 4.1 Chemical structure of nilotinib

Source: Fouad & Elkady, 2013.

Abl1 is a substrate of several mitochondrial proteins, including parkin, which is a leading cause of autosomal recessive and early onset PD (Ge et al., 2020). Considering nilotinib's reported ability to penetrate the BBB, it became a subject of extensive investigations as a therapeutic agent for PD. Two phase II clinical trials took place, showing conflicting results. One study reported a significant reduction of CSF biomarkers, such as hyperphosphorylated tau, in the nilotinib-treated group (Pagan et al., 2020), whereas others reported an absence of any evidence which might suggest a positive effect of nilotinib on PD patients (Simuni et al., 2020).

The drug was well tolerated but did not cross the BBB as efficiently as described in the reports leading up to clinical trials (Karuppagounder et al., 2014).

4.1.2 Results leading up to this study

The work described in this section was conducted by Dr Matthew Stopford.

The cohort of drugs tested in the second round of co-culture screenings was enriched in inhibitors of the Abl1 kinase. Amongst these kinase inhibitors, nilotinib was characterised by the highest increase in motor neuronal survival. Of all tested concentrations of nilotinib, the largest and most robust rescue of motor neuronal survival was observed at 1 µM. These findings were statistically significant across 2 out of 3 C9orf72 and all sALS lines, and consistent across several experimental repeats (figure 4.2).

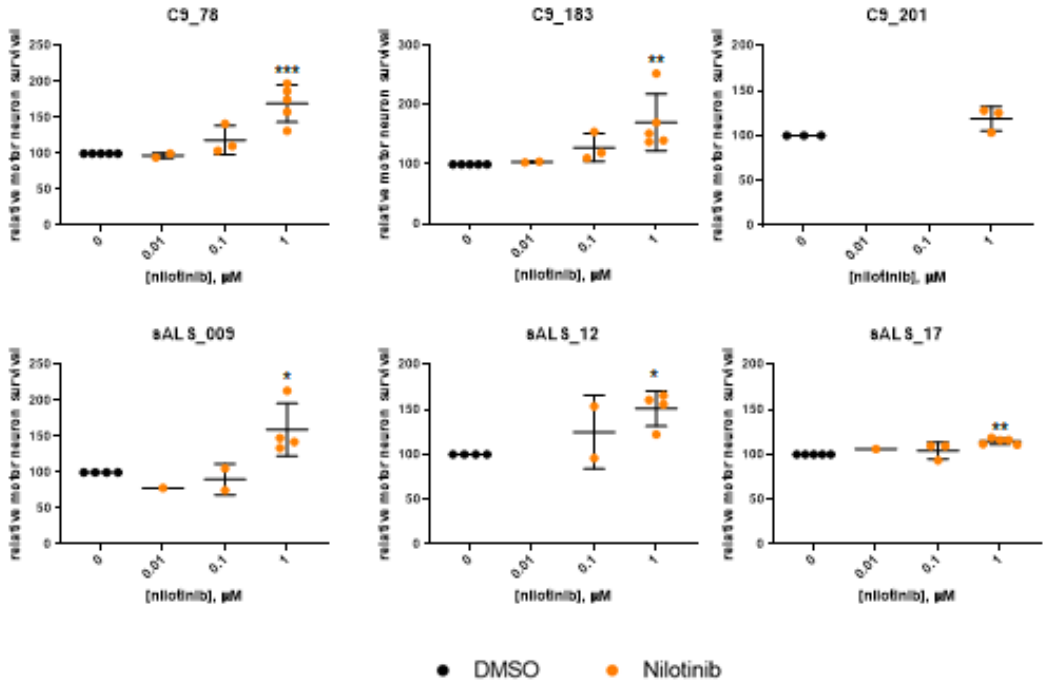

Figure 4.2 Results of the co-culture drug screening using nilotinib

Hb9-GFP motor neurons grown on ALS iAstrocytes treated with nilotinib showed a significant improvement in survival compared with a vehicle-treated controls. n=3-5, data are mean ± SD; data are relative to DMSO-treated cells =100; Kruskal-Wallis test with Dunnett's multiple comparisons post-hoc test; *P<0.05; **P<0.01; Data courtesy of Dr Matthew Stopford.

As done previously with gefitinib and described in section 3.1.3, a battery of kinases targeted by nilotinib was unveiled by BenevolentAI and Eurofins in a kinome screen. Table 4.1 summarises the top 10 kinases targeted by nilotinib most potently. Data is presented as pIC50, which is a negative log of IC_{50} values. For reference, 1 µM potency against the target = 6 on the log scale, and the higher the pIC_{50} value, the lower the concentration of the drug is required to cause 50% inhibition of the target.

Table 4.1 Top 10 kinases targeted by 10 µM nilotinib, obtained from Cerep-87 kinase panel data.

Kinase name	Kinase symbol	pIC_{50}
ABL proto-oncogene 1^{H396P}, human	Abl (H396P) (h)	8.4018
Abelson murine leukemia viral oncogene homolog 2, human	Arg (h)	8.2776
ABL proto-oncogene 1, murine	Abl (m)	8.2153
Abelson murine leukemia viral oncogene homolog 2, murine	Arg (m)	8.193
ABL proto-oncogene 1^{Y253F}, human	Abl (Y253F) (h)	8.1823
ABL proto-oncogene 1, human	Abl (h)	8.0231
ABL proto-oncogene 1^{Q252H}, human	Abl (Q252H) (h)	7.9435
Discoidin domain receptor 1, human	DDR1 (h)	7.6172
C-Kit proto-oncogene^{V560G}, human	cKit (V560G) (h)	7.4256
ABL proto-oncogene 1^{T315I}, human	Abl (T315I) (h)	7.3842

The aims of this chapter are:

1. To unveil the effect of nilotinib treatment on ALS iAstrocytes;
2. To uncover the mechanism of action of nilotinib in ALS by mapping out its effect on TDP-43 proteinopathy, autophagy dynamics and mitochondrial function;
3. To assess the viability of Abl1 as a disease-modifying target in ALS.

4.2 Results

4.2.1 Effect of nilotinib treatment on iAstrocytes

4.2.1.1 Cell number

Nilotinib is utilised in chronic myelogenous leukaemia, where it leads to cell cycle arrest by inhibiting the constitutively active BCR-Abl complex. Although the cells under study do not present chromosomal translocations and patients affected by ALS do not present an increased prevalence for the Philadelphia chromosome, it is known that Abl1 protein is capable of autophosphorylation at its tyrosine-412 residue, which leads to its sustained activation. To ensure that nilotinib does not lead to cell cycle arrest or carry undue cell toxicity, immunostained iAstrocytes treated with 0.1% v/v DMSO or 1 µM nilotinib were counted. Compared to the DMSO vehicle, nilotinib did not have an effect on iAstrocyte cell numbers after 48h treatment, with an exception of CTR_AG08620 where a significant decrease of cell numbers was observed (figure 4.3 A). Nilotinib did not appear to affect cell numbers in individual genotypes (figure 4.3 B). Altogether, I concluded that nilotinib does not influence iAstrocyte cell numbers.

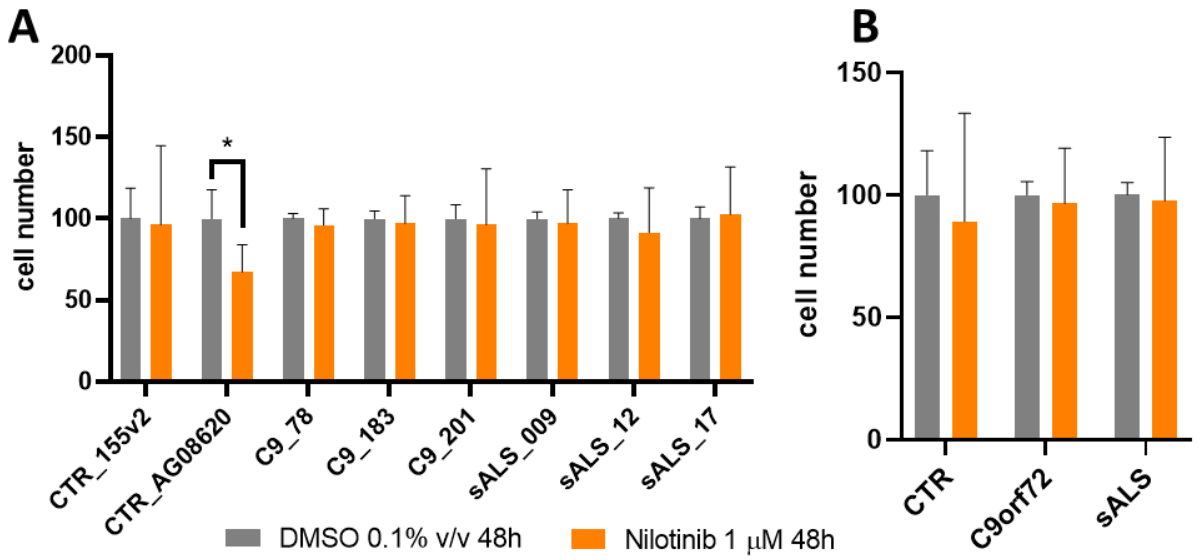

Figure 4.3 Nilotinib effect on iAstrocyte cell numbers

(A) Quantification of iAstrocyte cell numbers in individual cell lines; n=6 experimental repeats; data are mean ± SD, normalised to DMSO=100; two-way ANOVA with Tukey's multiple comparisons; *P<0.05. **(B)** Quantification of iAstrocyte cell numbers per genotype; n=3 per genotype n=3 per genotype; CTR includes CTR_155v2 mean from n=5 experimental repeats, CTR_AG08620 mean from

n=3 experimental repeats and CTR_3050 mean from n=2 experimental repeats; data are mean ± SD, normalised to DMSO=100; two-way ANOVA with Tukey's multiple comparisons, ns.

4.2.1.1.1 *LDH assay*

LDH assays to determine the levels of nilotinib-driven cell death were conducted by Dr Matthew Stopford. As described before in section 3.2.1.1.1, the absorbance values at 490nm were converted to percentage cytotoxicity relative to cell lysate value representing 100% cell death. At both 24h (figure 4.4 A) and 72h (figure 4.4 B) after treatment, the maximum nilotinib concentration tested (30 µM) produced cytotoxicity similar to that of sodium azide cytotoxin. Taken together, results of the cell number analysis and the LDH assays did not show nilotinib to be cytotoxic at 1 µM, which complements the findings of the cell number analysis.

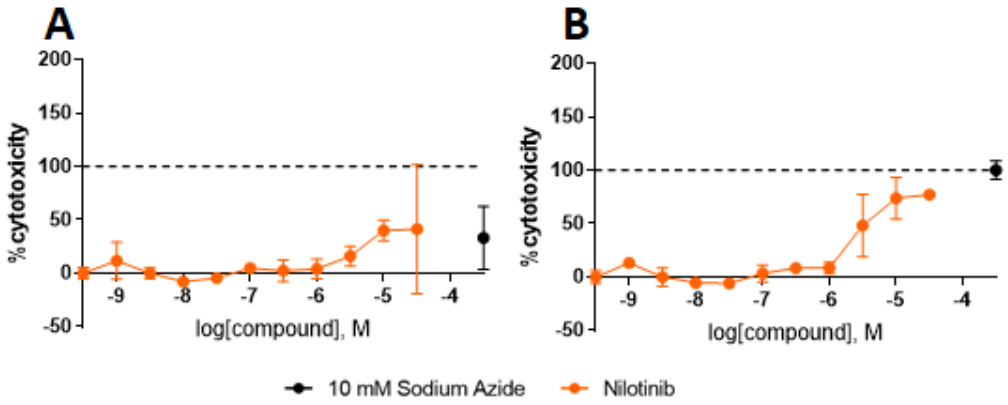

Figure 4.4 LDH cytotoxicity assay in C9_78 iAstrocytes

(A) iAstrocytes were treated with various concentrations of nilotinib for 24h or **(B)** 72h. Cell lysis buffer was applied as a positive control for cytotoxicity (i.e. 100% cytotoxicity); n= 3-7, technical replicates; data are mean ± SD.

4.2.1.1.2 *Cell proliferation*

Although iAstrocyte cell numbers did not change in the majority of iAstrocyte lines after drug treatment, the effect of nilotinib on cell numbers was clarified further by measuring their proliferation rate via immunocytochemistry staining for Ki67. Consistent with the cell number and LDH cytotoxicity data, no differences in percentages of Ki67-positive nuclei were detected between nilotinib-treated and DMSO-treated cells in individual lines (figure 4.5 A) or per genotype (figure 4.5 B), indicating no changes in the proliferation rate of iAstrocytes when treated with nilotinib.

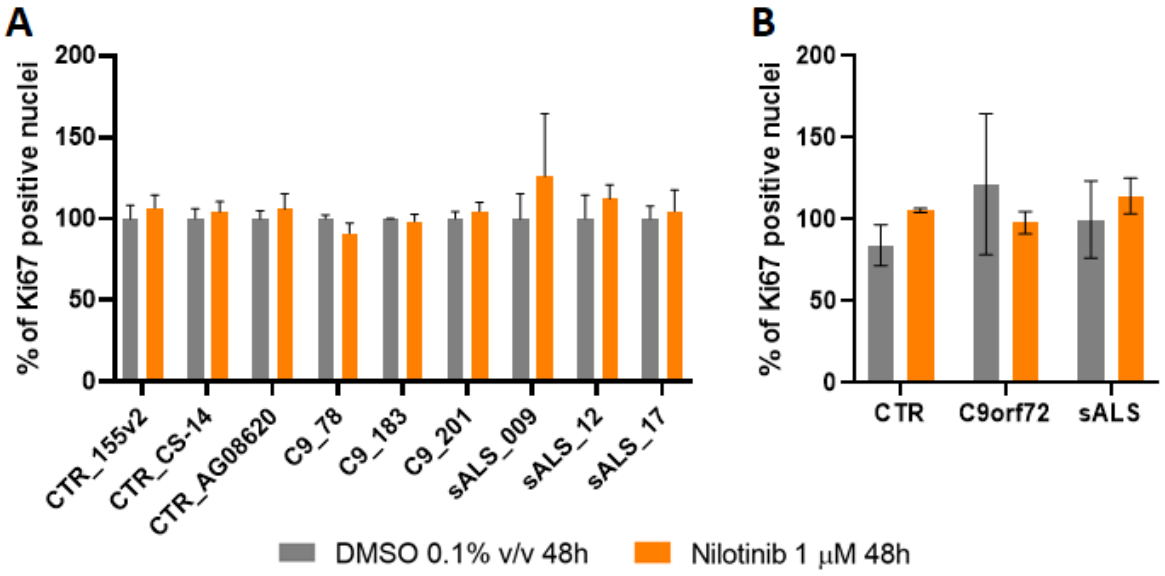

Figure 4.5 Expression of nuclear Ki67 in iAstrocytes treated with nilotinib

(A) Quantification of the percentage of Ki67-positive nuclei in individual iAstrocyte lines treated with nilotinib; n=3-6 (except CS-14 n=2); data are mean ± SD, normalised to DMSO=100; two-way ANOVA with Šidák's multiple comparisons; all comparisons ns. **(B)** Quantification of the percentage of Ki67-positive nuclei per genotype; n=3 experimental repeats; CTR includes CTR_155v2 mean from n=6 experimental repeats, CTR_AG08620 mean from n=4 experimental repeats and CTR_CS-14 mean from n=2 experimental repeats; data are mean ± SD; two-way ANOVA with Šidák's multiple comparisons; all comparisons ns.

4.2.1.2 Cell morphology

Having verified the effect of nilotinib on iAstrocyte cells numbers, I next assessed their morphology following the drug treatment. To do so, as described previously in section 3.2.1.2, iAstrocytes treated for 48h with either 0.1% (v/v) DMSO or 1 µM nilotinib were stained for the cytoskeletal marker vimentin. Captured images were analysed using Columbus image analysis software. As before, a cytoplasmic mask (figure 3.8) was applied to images to automatically analyse cell roundness (set from 0 to 1, where 1 represented a circle) and cell area (in μm^2).

Cell roundness did not change after nilotinib treatment at either individual line (figure 4.6 A) or genotype level (figure 4.6 B). Drug treatment led to a significant increase in cell area of control CTR_AG08620 and sALS_12 compared to vehicle-treated cells (figure 4.6 C).

Interestingly, analysis of cell area across genotypes unveiled a significant collective increase in the area of C9orf72 patients iAstrocytes (figure 4.6 D). Taken together, the morphology results suggest that a 48h treatment with 1 µM nilotinib does not significantly affect the morphology of iAstrocytes.

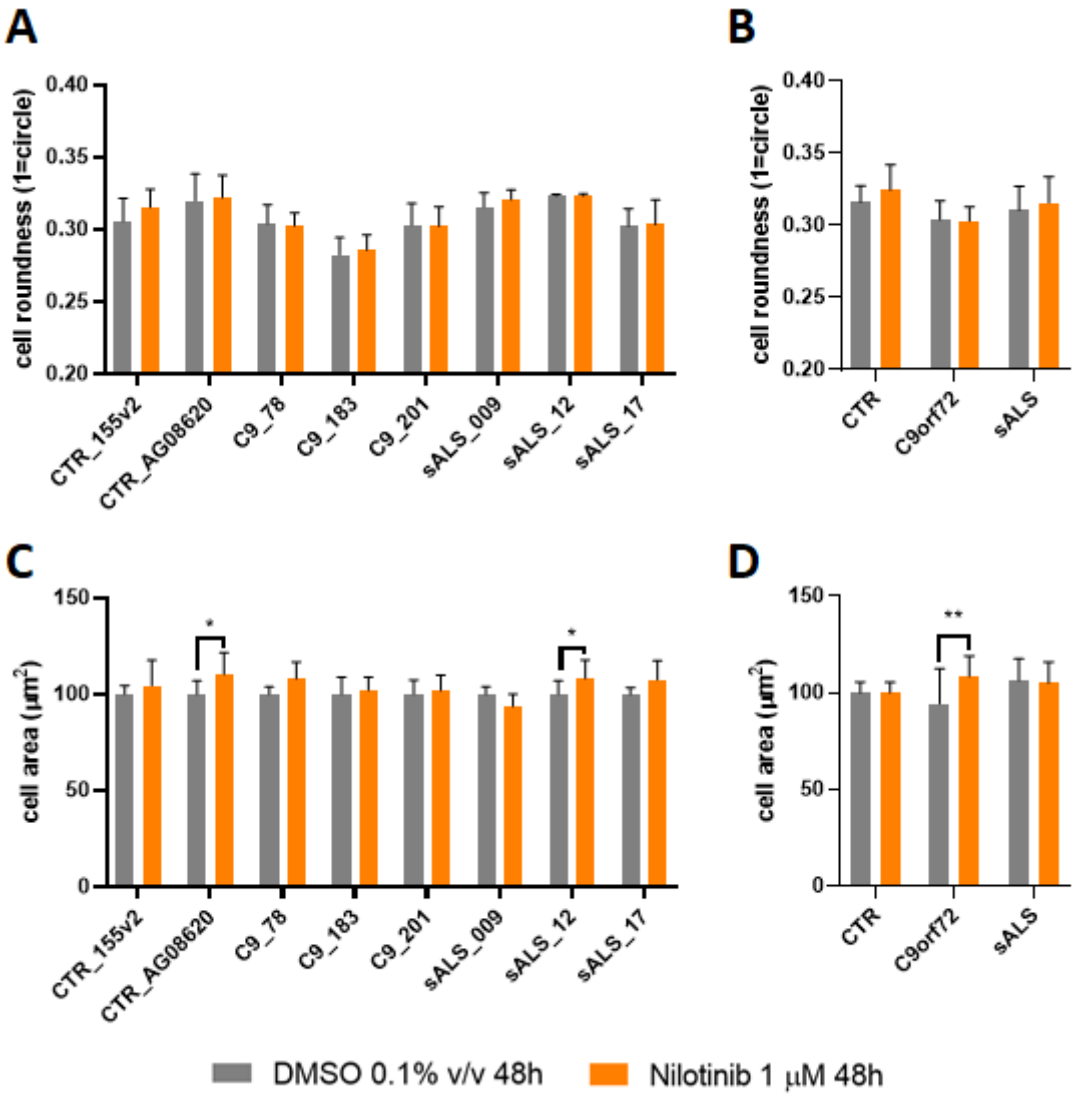

Figure 4.6 Effect of nilotinib on iAstrocyte cell morphology

(A) Quantification of the overall roundness of cell treated with nilotinib in individual lines; n=3-4 experimental repeats; data are mean ± SD; two-way ANOVA with Tukey's multiple comparisons test, ns. **(B)** Quantification of the overall roundness of cell within each genotype treated with nilotinib; n=3 per genotype; CTR includes CTR_155v2 mean from n=5 experimental repeats, CTR_AG08620 mean from n=3 experimental repeats and CTR_3050 mean from n=2 experimental repeats; data are mean ± SD; two-way ANOVA with Šidák's multiple comparisons; all comparisons ns. (**C**) Quantification of the iAstrocyte cell area in individual lines after nilotinib treatment; n=3-4 experimental repeats; data are

mean ± SD; data relative to DMSO=100; two-way ANOVA with Šidák's multiple comparisons, *P<0.05. **(D)** Quantification of the iAstrocyte cell area within each genotype after nilotinib treatment; n=3 per genotype; CTR includes CTR_155v2 mean from n=5 experimental repeats, CTR_AG08620 mean from n=3 experimental repeats and CTR_3050 mean from n=2 experimental repeats; data are mean ± SD; two-way ANOVA with Šidák's multiple comparisons, *P<0.05, **P<0.005.

4.2.2 Assessing the viability of Abl1 as a target in ALS

As described previously, Abl1 has been investigated as a potential disease modifying target in ALS. Katsumata et al. (2012) showed primary glial cultures from Abl1-overexpressing rats to be detrimental to motor neuronal survival. Conversely, a study by Imamura et al. (2017) tested a host of Abl1-targeting compounds and found them to be effective in increasing survival of iPSC-derived motor neurons. Whilst most previous studies focused on Abl1 role in diseased motor neurons, its expression in glial cells in ALS remain largely unexplored. Moreover, in *in vivo* models where constitutively active Abl1 was induced, the overexpression was targeted at neurons only, even though it has consequently resulted in astrogliosis and microgliosis (Schlatterer et al., 2011). This section will describe the Abl1 dynamics in ALS iAstrocytes at baseline and after nilotinib treatment.

4.2.2.1 Abl1 engagement by nilotinib

4.2.2.1.1 Total Abl1 mRNA

Next, I investigated the extent to which nilotinib affects the levels of Abl1 in iAstrocytes.

To measure the levels of *ABL1* transcript in iAstrocytes following nilotinib treatment, RNA was isolated from cell pellets treated for 1h, 6h, 12h and 24h with 1 µM nilotinib, or left untreated. Levels of *ABL1* were measured in C9_78, as well as controls CTR_155 and CTR_3050. As shown in section 3.2.5, baseline levels of *ABL1* transcript were elevated in C9orf72 iAstrocytes (figure 3.33 A). Nilotinib treatment had no effect on control iAstrocytes at any of the treatment timepoints, although a trend towards a decrease was observed at 6h and 12h (figure 4.7 A). Indeed, C9_78 iAstrocytes with nilotinib for 6h and 12h resulted in a similar trend towards *ABL1* decrease (figure 4.7 B). Taken together, these results suggested that 6h and 12h treatments of iAstrocytes with 1 µM nilotinib might decrease *ABL1* expression, but nilotinib's effect on Abl1 expression might not be purely transcriptional.

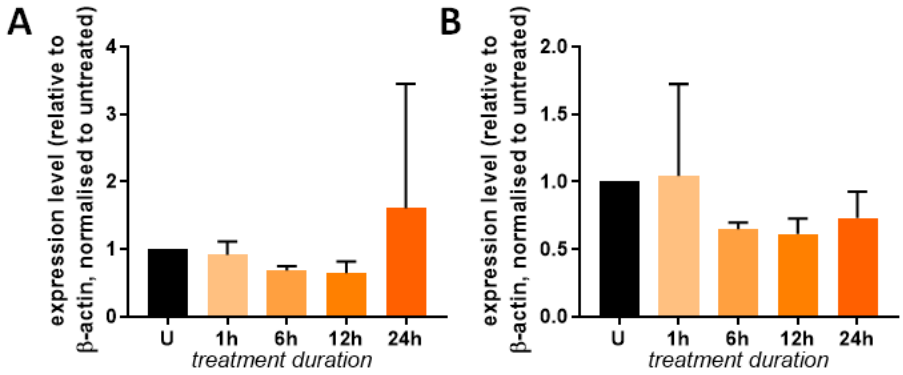

Figure 4.7 ABL1 mRNA target engagement

(A) Expression of *ABL1* in control iAstrocytes following a treatment with nilotinib at several time points; n=4 (CTR_155 n=2, CTR_3050 n=2); data are mean ± SD; data relative to untreated =1; **(B)** Expression of *ABL1* in C9_78 following a treatment with nilotinib at several time points; n=3 experimental repeats; data are mean ± SD; data relative to untreated =1; Kruskal-Wallis with Dunn's multiple comparisons test, all comparisons ns.

4.2.2.1.2 Effect of nilotinib on protein levels of total Abl1

As described in section 3.2.5.2, ALS iAstrocytes have significantly elevated levels of Abl1 compared to controls (figure 3.34). Having measured the *ABL1* dynamics in iAstrocytes following the treatment with nilotinib, I set out to measure Abl1 protein expression in all iAstrocytes lines following a treatment with nilotinib (figure 4.8 A). Having combined the cell genotypes (figure 4.8 B), the data showed a trend towards an increase in Abl1 expression after nilotinib treatment, which, likely due to variability, did not result in a statistically significant change.

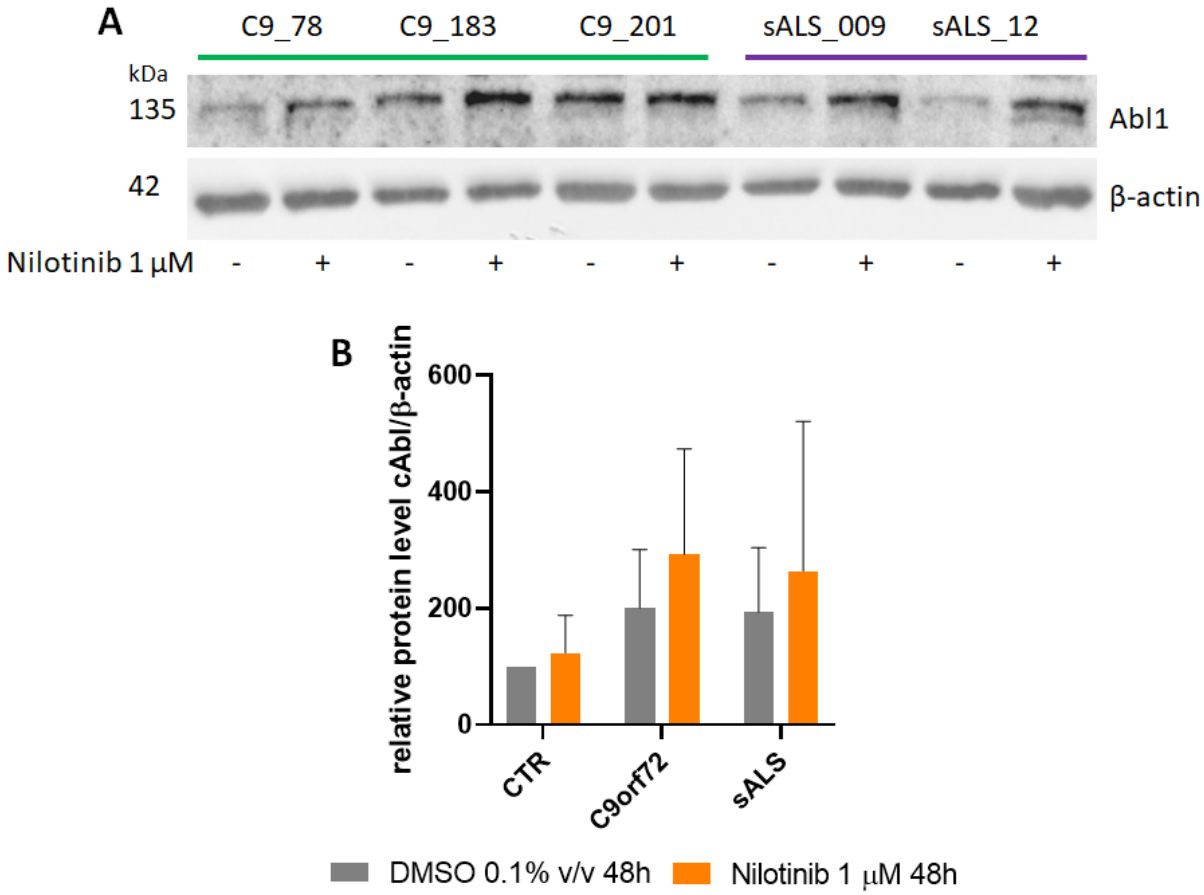

Figure 4.8 Nilotinib engagement of Abl1 in ALS patient iAstrocytes

(A) Representative western blotting image of ALS iAstrocyte Abl1 expression. **(B)** Quantification of Abl1 protein expression after treatment with nilotinib; n=3 per genotype; data are mean ± SD; data relative to CTR DMSO=100; two-way ANOVA with Šidák's multiple comparison's test, all comparisons ns.

4.2.2.1.3 Phospho-Abl1 ELISA

Having measured the effect of nilotinib on Abl1 expression in iAstrocytes, I have proceeded to verify if the Abl1 phosphorylation status is affected in iAstrocytes before and after nilotinib administration. In section 3.2.5.3 I have described the challenges we have encountered whilst optimising pAbl1 antibodies suitable for western blotting (figure 3.36). I have therefore decided to measure pAbl1 levels in iAstrocytes using a pan-tyrosine pAbl1 ELISA kit, which has been routinely used by our collaborators at BenevolentAI. As done previously with gefitinib, K562 cell line lysates, used as a positive control for Abl1 overexpression, were independently validated in western blotting for the expression of total Abl1 protein before and after nilotinib administration (figure 4.9 A). The results showed a significant reduction in Abl1 expression in

K562 cells following 1 µM nilotinib administration (figure 4.9 B). Nilotinib had a similar effect on the expression of BCR-Abl1 complex (figure 4.9 C), albeit no statistical analysis could be run as only two experimental repeats were obtained. The negative control validation is presented in figure 3.37 D-E.

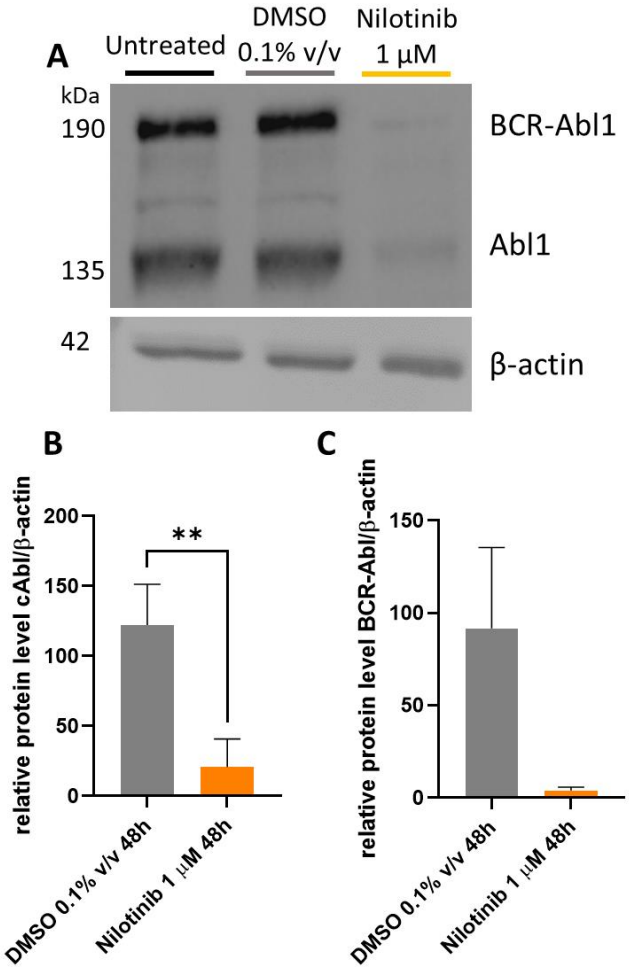

Figure 4.9 Pan-Tyr Abl1 ELISA controls validation

(**A**) Representative western blot image of Abl1 and BCR-Abl1 in K562 cells. (**B**) Quantification of Abl1 expression in DMSO- and nilotinib-treated K562 cells; n=3 experimental repeats; data relative to untreated K562 cells = 100; data are mean ± SD; paired t-test, **P<0.01. (**C**) Quantification of BCR-Abl1 expression in DMSO- and nilotinib-treated K562 cells; n=2 experimental repeats; data relative to untreated K562 cells = 100; mean ± SD.

Next, I proceeded to perform the panTyr-pAbl1 ELISA on iAstrocytes treated with DMSO or nilotinib for 48h. pAbl1 expression in nilotinib-treated K562 cells was significantly lower compared to DMSO-treated cells (figure 4.10 A). Although pre-assay validation showed a

significant reduction in Abl1 expression in shAbl1-treated cells, levels of pAbl1 in these samples were detected above the average of all control iAstrocytes treated with DMSO. As observed previously with gefitinib in section 3.2.5.3, although we have detected pAbl1 signal in iAstrocytes above the assay threshold level, the differences between DMSO and nilotinib treatments could not be detected (figure 4.10 B).

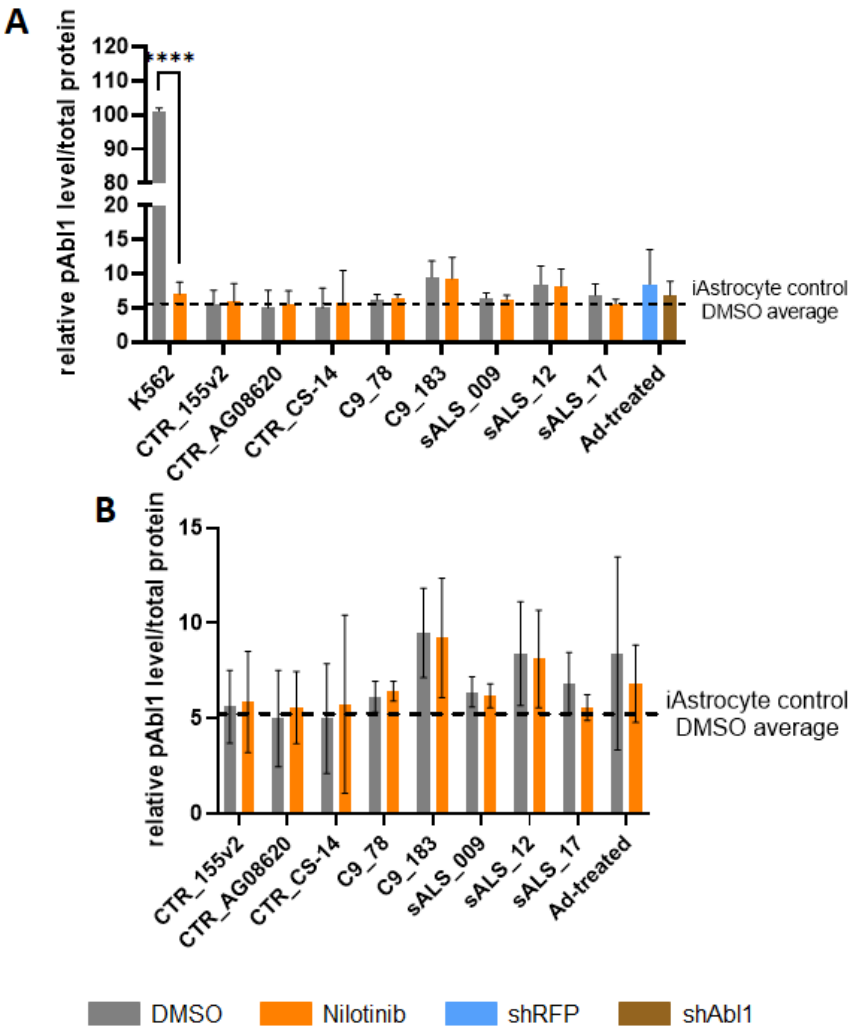

Figure 4.10 Phosphorylation status of Abl1 in nilotinib-treated iAstrocytes

(A) Quantification of pAbl1 levels; n=3 experimental repeats; data are mean ± SD; two-way ANOVA with Šidák's multiple comparisons test, ****P<0.0001. **(B)** Quantification of pAbl1 levels in iAstrocytes alone; n=3 experimental repeats; data are mean ± SD; two-way ANOVA with Šidák's multiple comparisons test, all comparisons ns. All data normalised to the total protein content and relative to panTyr-Abl1 levels in untreated K562 cells.

4.2.2.2 Knocking down Abl1 in iAstrocytes

Having observed an elevation of Abl1 protein levels in ALS patient iAstrocytes at baseline, but an unclear effect of nilotinib on this protein expression, I have tested the effect of Abl1 knockdown in the co-culture system to test the therapeutic potential of this target. This section will describe the effect of Abl1 knockdown on motor neuronal survival, iAstrocyte numbers and morphology.

4.2.2.2.1 Co-culture and motor neuronal survival

Abl1 expression was knocked down in C9_78 using an shRNA used previously to provide a negative control for the pan-Tyr-pAbl1 ELISA. An empty vector expressing RFP only was used as a control for RFP toxicity. Cells were transfected on day 2 of iAstrocyte differentiation (figure 2.1) and seeded in a co-culture plate as illustrated in figure 3.3. As performed routinely for all co-culture experiments, the plate was scanned on days 1 and 3 of co-culture.

Levels of Abl1 were measured in C9_78 iAstrocytes prior to co-culture analysis to validate the knockdown of Abl1. Western blots and their subsequent analysis were performed by Dr Matthew Stopford (figure 4.11 A). The average number of motor neurons in the co-culture plate on day 1 of the assay was similar across all treatment conditions (figure 4.11 B). As expected on day 3, the remaining cell numbers decreased in all conditions (figure 4.11 C). At day 3 the data show a dose-response effect to Abl1 shRNA treatment (figure 4.11 C). In order to normalise MN survival within the experiment and across experiments, the percentage of surviving MN at day 3 was normalised to the number of MN plated at day 1. Of all MOIs tested, MOI 10 resulted in the highest survival of motor neurons (32.97% ± 7.256) compared to the untreated iAstrocyte control (23.44% ± 4) (figure 4.11 D). The RFP-only control resulted in 11.63% survival of motor neurons, displaying elevated toxicity compared to all other conditions. Due to technical challenges and COVID-related time constraints, this assay was performed twice, therefore no statistical tests could be performed.

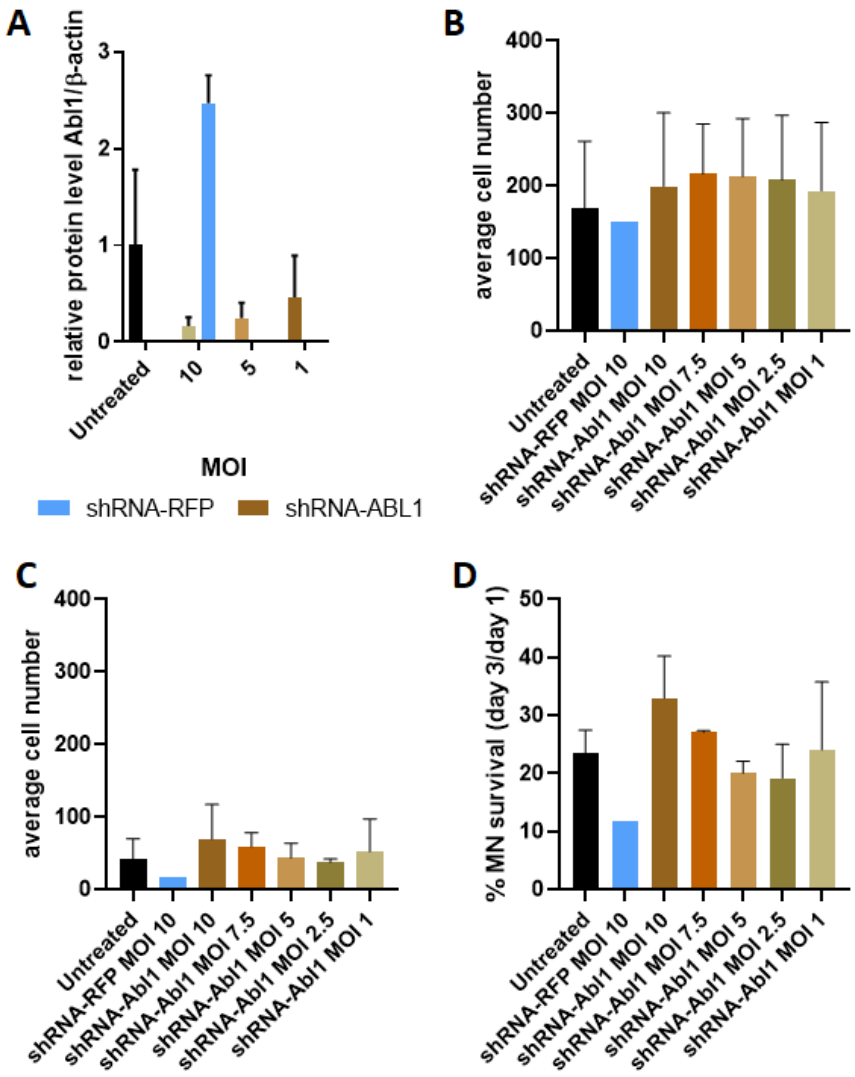

Figure 4.11 Co-culture Hb9-GFP motor neurons and shRNA-Abl1 iAstrocytes

(A) Quantification of Abl1 protein knockdown. Data courtesy of Dr Matthew Stopford. **(B)** Quantification of the average motor neuron numbers per treatment condition on day 1 of co-culture; mean ± SD, n=2 experimental repeats, except shRNA-RFP=1. **(C)** Quantification of the average motor neuron numbers per treatment condition on day 3 of co-culture; mean ± SD, n=2 experimental repeats, except shRNA-RFP=1. **(D)** Percentage of motor neuron survival (day 3 average cell numbers/ day 1 average numbers); mean ± SD, n=2, except shRNA-RFP=1.

4.2.2.2.2 iAstrocyte morphology analysis

Results obtained in the shAbl1-knockdown co-culture screenings have shown that Abl1 downregulation in C9orf72 patient iAstrocytes might rescue the survival of wild-type motor neurons. To help clarify the effect of Abl1 knockdown on iAstrocytes themselves and thus to start elucidating its mechanism of action in these cells, I have analysed the images of shRNA-

Abl1-treated cells acquired on days 1 and 3 of the co-culture screen (figure 4.12 A, B respectively). Columbus image analysis software was used to extract the following parameters: cell number, cell size (in μm^2), cell roundness (where 1= circle), and width-to-length ratio. All results were compared to C9_78 treated with shRNA-RFP only to control for the effect of the RFP contained within the shRNA-Abl1 construct.

Although the same number of cells was plated per conditions at the start of the assay, the number of cells treated with shRNA-Abl1 was significantly higher on both day 1 and day 3 of the screening in comparison to the RFP-only control (figure 4.12 C), likely reflecting the toxicity observed in the co-culture system. The overall percentage survival of C9_78 iAstrocytes after Abl1 knockdown was comparable to that of RFP-only controls (figure 4.12 D). Abl1-shRNA treated iAstrocytes on co-culture day 3 had a marginally smaller cell area than the RFP controls (figure 4.12 E). Abl1 knockdown had no effect on the cell roundness (figure 4.12 F) or width-to-length ratio (4.12 G), consistent with nilotinib treatment alone (figure 4.6).

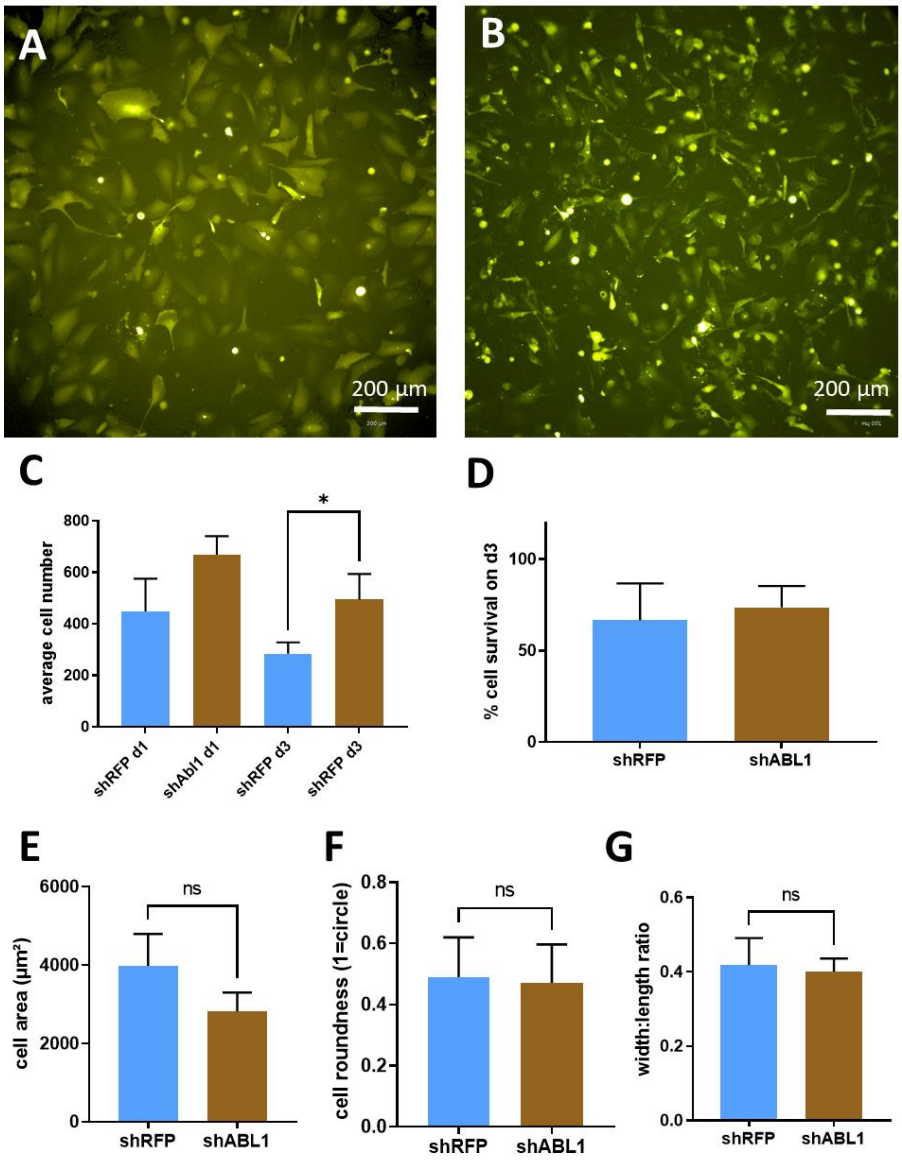

Figure 4.12 Morphological changes in C9_78 iAstrocytes after Abl1 knockdown

(A) Representative image of Abl1 shRNA-treated iAstrocytes on day 1 of the co-culture assay. Scale: 200 µm. **(B)** Representative image of Abl1 shRNA-treated iAstrocytes on day 3 of the assay. Scale: 200 µm. **(C)** Quantification of iAstrocytes cell numbers in shRNA-Abl1 and shRNA-RFP conditions on days 1 and 3 of the co-culture assay; n=4 experimental repeats; data are mean ± SD; paired t-test, *P<0.05. **(D)** Quantification of % survival of iAstrocytes in the shRNA-Abl1 and shRNA-RFP conditions; n=4 experimental repeats; data are mean ± SD; paired t-test, ns. **(E)** Quantification of the cell area in (μm^2) of iAstrocytes in the shRNA-Abl1 and shRNA-RFP conditions on day 3 of the co-culture assay; n=4 experimental repeats; data are mean ± SD; paired t-test, ns. **(F)** Quantification of cell roundness (1=circle) of iAstrocytes in the shRNA-Abl1 and shRNA-RFP conditions on day 3 of the co-culture assay; n=4 experimental repeats; data are mean ± SD; paired t-test, ns. **(G)** Quantification of the width:length

of iAstrocytes in the shRNA-Abl1 and shRNA-RFP conditions on day 3 of the co-culture assay; n=4 experimental repeats; data are mean ± SD; paired t-test, ns.

4.2.3 Nilotinib effect on TDP-43 proteinopathy and TDP-43 protein homeostasis

Studies characterising the mechanism of action of Abl1 inhibitors in ALS models often observed a decrease in the number of cytosolic protein inclusions after a drug treatment. Katsumata et al. (2012) saw a decrease in the levels of misfolded SOD1 in SC motor neurons from $SOD1^{G93A}$ mice after dasatinib treatment, whereas Imamura et al. (2017) observed decreased levels of TDP-35, as well as misfolded mutant SOD1 in iPSC-derived motor neurons treated with bosutinib. In this project, the ability of nilotinib to ameliorate TDP-43 proteinopathy in ALS iAstrocytes was investigated. As described previously in section 3.2.2, iAstrocytes recapitulate the hallmarks TDP-43 proteinopathy observed in post-mortem patient tissue, such as the expression of TDP-35 cleavage product (figure 3.15), loss of nuclear localisation of full-length TDP-43 (figure 3.16 A, B), and cytoplasmic accumulation of phosphorylated TDP-43 aggregates (figure 3.16 A, C). Here, similarly to gefitinib, nilotinib's effect on all of these mechanisms was investigated.

4.2.3.1 TDP-43 fragmentation after nilotinib treatment

To measure the levels of TDP-35, iAstrocytes treated with 1 µM nilotinib and 0.1% v/v DMSO vehicle for 48h were lysed and processed for western blotting where their C-terminal positive TDP-43 expression levels were measured (figure 4.13 A). Compared to DMSO vehicle (presented in figure 4.13 B and C as '100' to visualise the delta between DMSO and nilotinib), nilotinib had no statistically significant effect on full-length TDP-43 levels (figure 4.13 B). The drug treatment did significantly affect the levels of TDP-35 in sALS_12 and sALS_17 only, having no effect on other lines (figure 4.13 C).

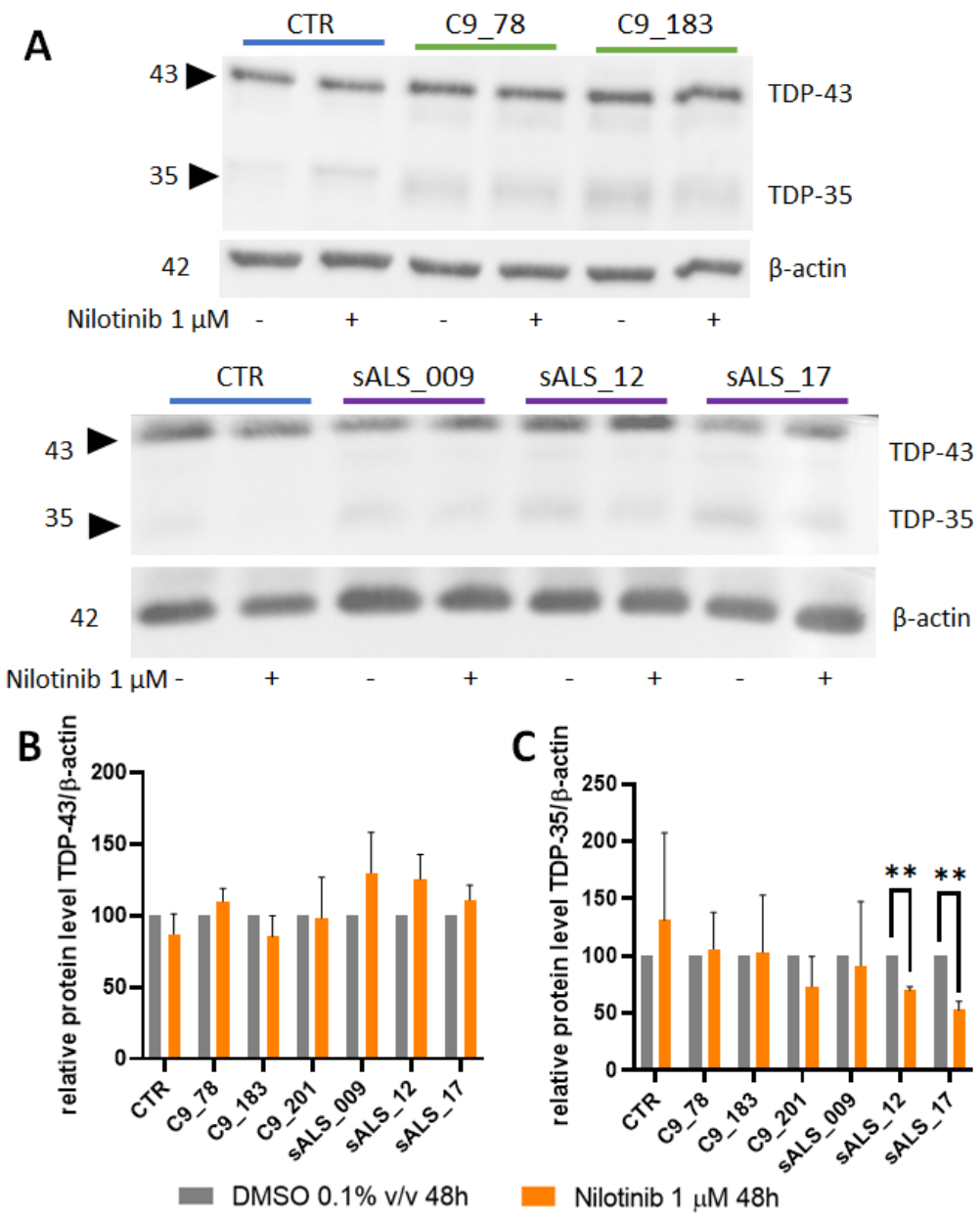

Figure 4.13 TDP-43 fragmentation after nilotinib treatment

(**A**) Representative TDP-43 western blot in ALS iAstrocytes after nilotinib treatment. (**B**) Quantification of TDP-43 levels in nilotinib-treated iAstrocytes; n=3-6 experimental repeats; CTR includes mean results of CTR_155v2 from n=2 experimental repeats; CTR_3050 mean from n=2 experimental repeats and CTR_AG08620 mean from n=2 experimental repeats; data are mean ± SD; all DMSO=100; Mann-Whitney test, ns. (**C**) Quantification of TDP-35 levels in nilotinib-treated iAstrocytes. n=3-6 experimental repeats; CTR includes mean results of CTR_155v2 from n=2 experimental repeats; CTR_3050 mean from n=2 experimental repeats and CTR_AG08620 mean from n=2 experimental repeats; data are mean ± SD; all DMSO=100; **P<0.005; Mann-Whitney test.

4.2.3.2 Localisation of TDP-43 after nilotinib treatment

As described previously in section 3.2.2.3, the levels of nuclear TDP-43 were measured via ICC, with subsequent image analysis revealing the TDP-43 levels in the nucleus as a staining intensity per pixel. Lower levels of TDP-43 expression were observed in the nuclei of the majority of ALS lines compared to controls, however, levels of nuclear TDP-43 in cells treated with nilotinib were not significantly different from the DMSO vehicle controls in any of the iAstrocyte lines (figure 4.14).

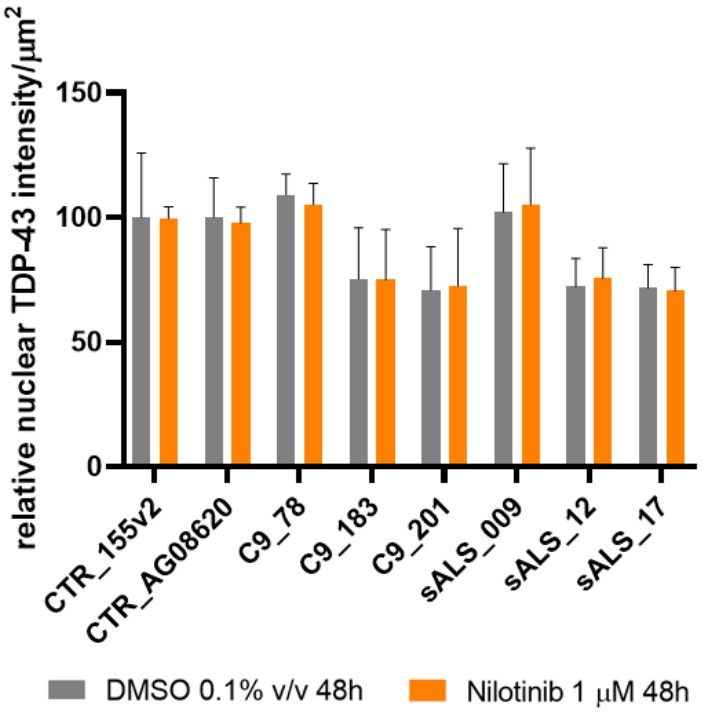

Figure 4.14 Nilotinib treatment effect on nuclear localisation of TDP-43

n=3-9 experimental repeats; data are mean ± SD; data relative to CTR DMSO=100; two-way ANOVA with Tukey's multiple comparisons; cell line factor: ***P=0.0002.

4.2.3.3 Cytoplasmic aggregation of TDP-43 after nilotinib treatment

To investigate if nilotinib is capable of decreasing pTDP-43 cytoplasmic inclusions in iAstrocytes, the numbers of pTDP-43-positive inclusions were determined via blinded manual counts from ICC images. Compared to controls, ALS patient iAstrocyte populations had a higher percentage of cells with pTDP-43 inclusions, although nilotinib did not affect these numbers at an individual cell line (figure 4.15 A) or the genotype basis (figure 4.15 B). The

number of pTDP-43 inclusions per total number of cells was less than 1 spot per cell for all genotypes and remained unaffected by nilotinib treatment (figure 4.15 C).

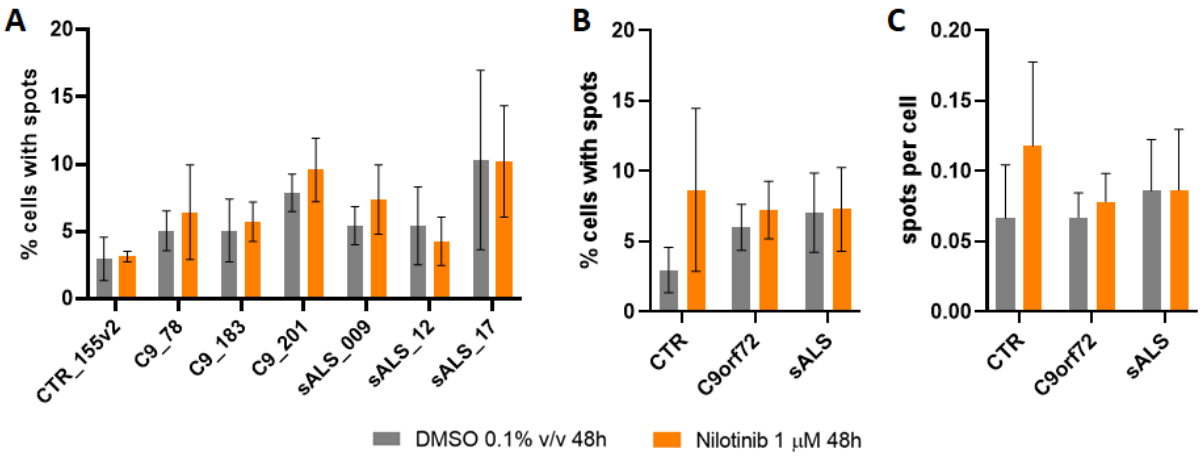

Figure 4.15 Effect of nilotinib treatment on cytoplasmic pTDP-43

(A) Quantification of cells per individual iAstrocyte line showing accumulation of pTDP-43 in the cytoplasm, presented % of total cells. n=3-5 experimental repeats; data are mean ± SD; two-way ANOVA with Šidák's multiple comparisons; all comparisons ns. (**B**) Quantification of cells per genotype showing accumulation of pTDP-43 in the cytoplasm, presented % of total cells; n=3 per genotype; CTR includes mean values of CTR_155v2 from n=4 experimental repeats, CTR_3050 mean from n=2 experimental repeats and CTR_AG08620 mean from n=2 experimental repeats; data are mean ± SD; two-way ANOVA with Šidák's multiple comparisons; all comparisons ns. (**C**) Quantification of spots per total number of cells per genotype; n=3 per genotype; CTR includes mean values of CTR_155v2 from n=4 experimental repeats, CTR_3050 mean from n=2 experimental repeats and CTR_AG08620 mean from n=2 experimental repeats. Data are mean ± SD; data relative to CTR DMSO=100; two-way ANOVA with Tukey's multiple comparisons; all comparisons ns.

4.2.4 Effect of nilotinib treatment on autophagy function

Several lines of evidence describe Abl1 as an instrumental regulator of autophagy. Overexpression of constitutively active Abl1 was described as capable of reducing LC3-I and LC3-II and leading to autophagic flux dysregulation, possibly via inhibition of autophagosome formation (Karim et al., 2020). Nilotinib treatment has also been linked to an increased autophagic degradation of α-synuclein in primary mouse cortical neurons (Mahul-Mellier et al., 2014). To test if nilotinib can be used to improve the autophagy function in disease, we

have first investigated its baseline ability to induce autophagy in healthy HEK293 cells, followed by control and patient iAstrocytes.

4.2.4.1 Autophagy activation in HEK293 cell line

Similarly to the procedure described in section 3.2.3.1., HEK293 cells were treated for 6h with nilotinib, DMSO vehicle, rapamycin as a positive control for autophagy activation, bafilomycin A1 as a negative control for autophagolysosomal fusion, or a combination of bafilomycin with either rapamycin or nilotinib (the rationale behind this treatment is summarised in figure 3.24).

After 6h of treatment (figure 4.16 A), nilotinib had no effect on LC3-I levels compared to DMSO-treated control (figure 4.16 B). Similarly, there was no difference between DMSO and nilotinib conditions in LC3-II expression, whereas rapamycin positive control led to an elevation of LC3-II, consistent with an autophagic flux. Bafilomycin A1 treatment caused a further increase in LC3-II levels, however, there was no difference between bafilomycin A1 and its co-treatment with nilotinib (figure 4.16 C). An identical trend of drug response was observed after LC3-II/LC3-I ratio was calculated (figure 4.16 D). Simultaneously, a marginal increase in p62 expression compared to DMSO was observed after nilotinib treatment, which was not observed in rapamycin-treated cells (figure 4.16 E). In contrast with what has been previously reported in the literature, in this assay, I have not detected a significant difference between bafilomycin A1 and bafilomycin A1 + nilotinib treatment, indicating a lack of autophagy activation.

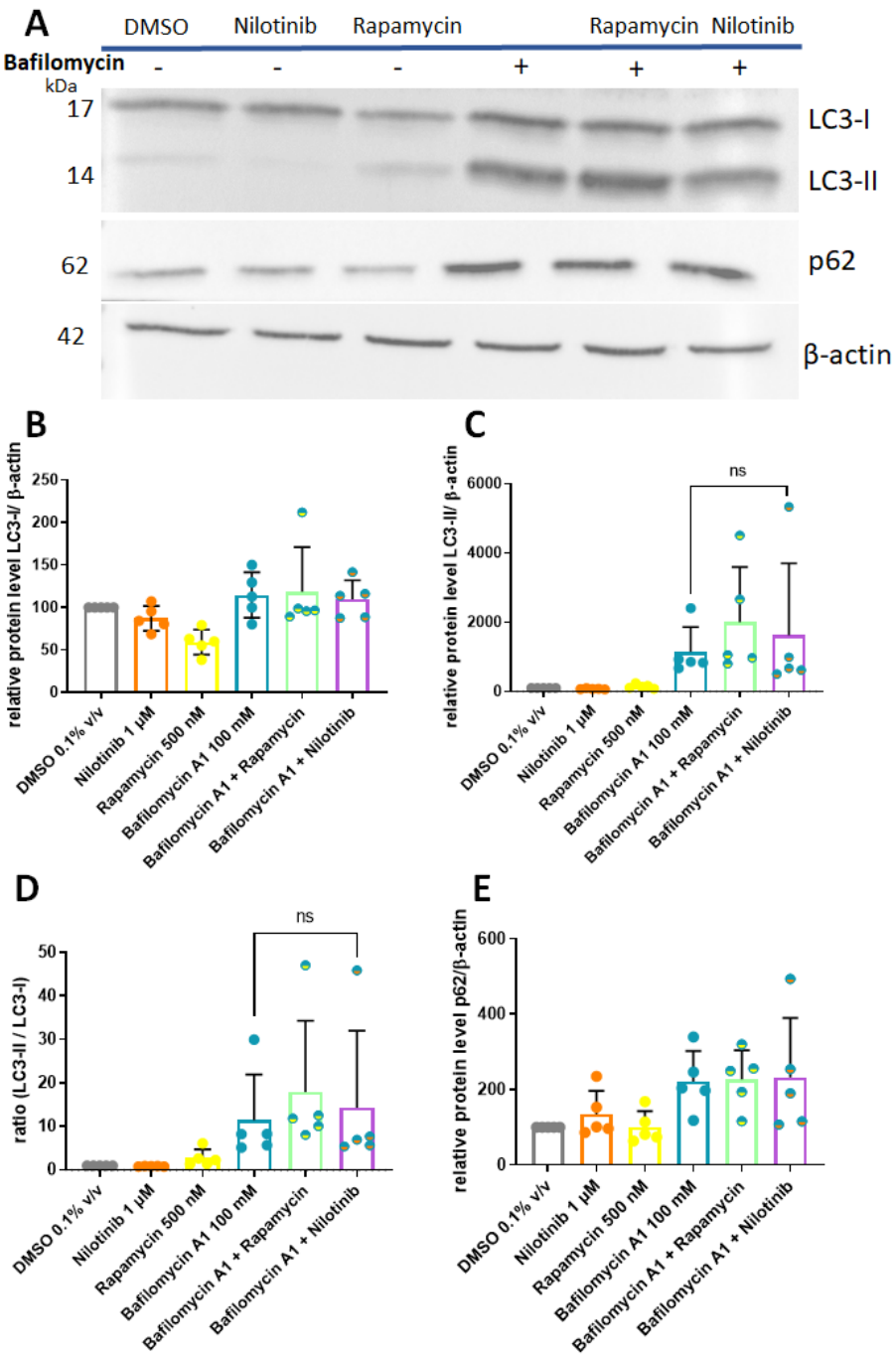

Figure 4.16 Nilotinib does not induce autophagy in HEK293 cells at 6h

(A) Representative western blotting images. **(B)** Quantification of LC3-I levels in HEK293 cells; n=5 experimental repeats; data are mean ± SD, normalised to DMSO =100. **(C)** Quantification of LC3-II levels in HEK293 cells; n=5 experimental repeats; data are mean ± SD, normalised to DMSO =100; paired t-test, bafilomycin vs gefitinib + bafilomycin, ns. **(D)** Quantification of LC3-II/LC3-I ratio; n=5 experimental repeats; data are mean ± SD, normalised to DMSO =1; paired t-test, bafilomycin vs gefitinib + bafilomycin, ns. **(E)** Quantification of p62 levels; n=5 experimental repeats; data are mean ± SD, normalised to DMSO =100.

Upon the lack of autophagy activation in HEK293 cells after 6h of treatment, I have hypothesised that this treatment duration might not be sufficient for nilotinib to exert its ability to cause autophagic flux. Therefore, the treatment duration was increased to 8 hours (figure 4.17 A). Drug concentrations remained unchanged.

Changes in LC3-I levels at 8h treatment were identical to those after 6h (figure 4.17 B). After 8h of treatment, similarly to 6h, nilotinib-only condition showed a trend towards a decrease in LC3-II levels (figure 4.17 C) and LC3-II/LC3-I ratio (figure 4.17 D). Nilotinib treatment led to no change in p62 expression after nilotinib administration, whereas a trend towards a decrease in p62 was observed in rapamycin-treated cells (figure 4.17 E). Nilotinib in combination with bafilomycin did not show a further increase in LC3-II levels when compared to bafilomycin treatment alone. Therefore, I have concluded that nilotinib treatment of 6h to 8h does not lead to an autophagic flux in healthy cell lines. The dataset presented in figure 4.17 is a result of two experimental repeats, both yielding negative results, which, in addition to the COVID-related time constraints, did not warrant a third repeat necessary to conduct statistical analysis.

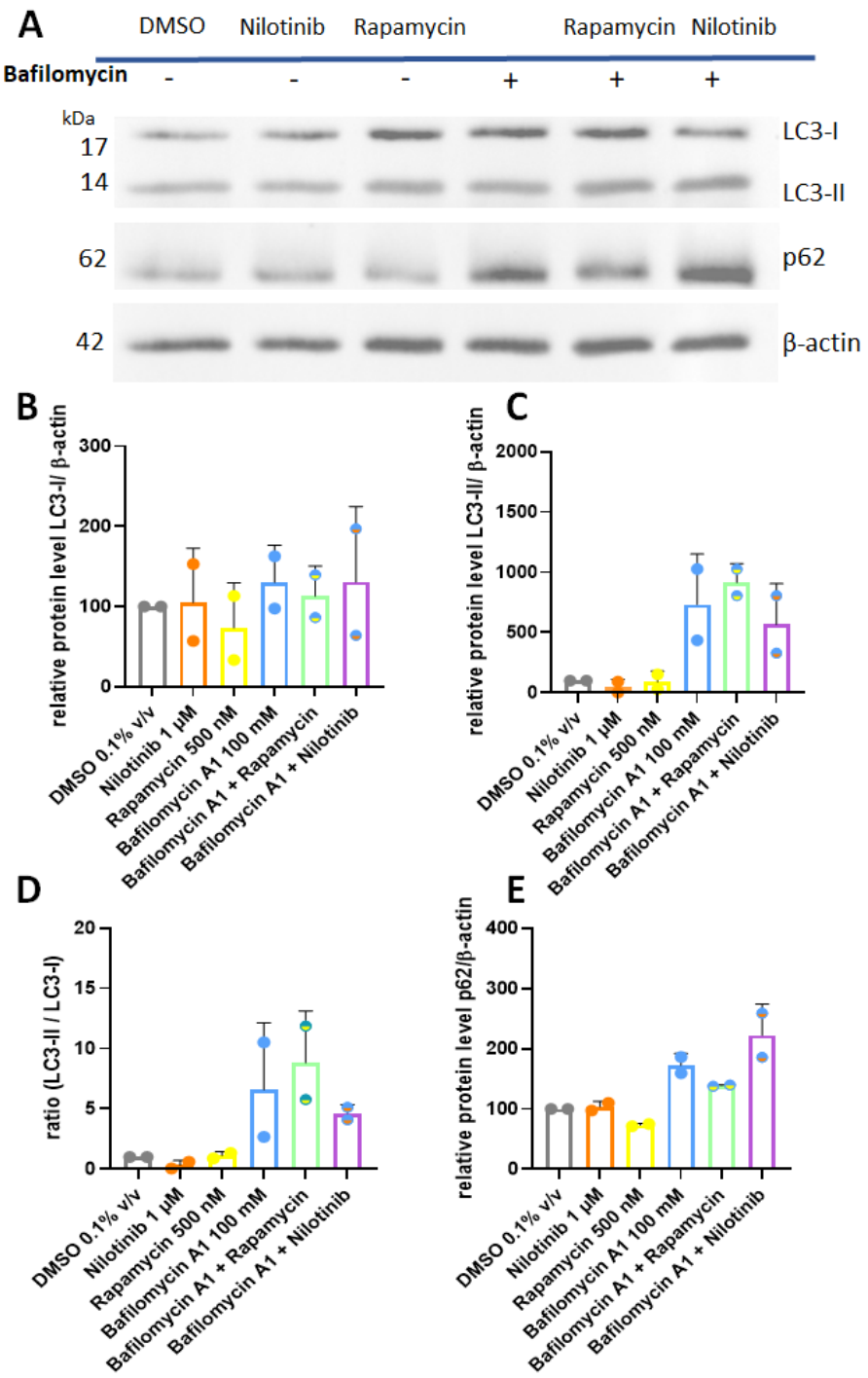

Figure 4.17 . Nilotinib does not induce autophagy in HEK293 cells at 8h

(A) Representative western blotting images. **(B)** Quantification of LC3-I levels in HEK293 cells. **(C)** Quantification of LC3-II levels in HEK293 cells. **(D)** Quantification of LC3-II/LC3-I ratio. **(E)** Quantification of p62 levels; n=2 experimental repeats; all above data are mean ± SD, normalised to DMSO =100.

4.2.4.2 Nilotinib effect in autophagy activation in iAstrocytes

The experiments in previous reports describing nilotinib and other BCR-Abl kinase inhibitors as activators of autophagy were conducted in cells carrying the BCR-Abl1 burden (Karim et al., 2020) or overexpressing Abl1. Therefore, we have elected to investigate nilotinib's ability to induce autophagy in iAstrocyte lines showing the highest levels of Abl1 expression at baseline. Due to its robust responsiveness to nilotinib treatment in the co-culture system, we have selected C9_78 iAstrocytes out of the cohort of C9orf72 patients. Treatment conditions described previously in section 3.4.2 were used for this set of assays.

Figure 4.18 A shows an example western blot obtained in the autophagy assay with C9_78. Levels of LC3-I in DMSO- and nilotinib-treated cells were identical, while torin 1 led to approximately 35% decrease in LC3-I (figure 4.18 B). As expected, bafilomycin treatment led to an increase in LC3-II expression, as well as in the LC3-II/LC3-I ratio (figure 4.18 C). There was, however, no further increase in LC3-II levels in bafilomycin + nilotinib condition compared to bafilomycin alone. This was also true for the LC3-II/LC3-I ratio. Interestingly, torin 1-treated cells showed the highest LC3-II/LC3-I ratio (figure 4.18 D). Nilotinib-treated cells showed a trend towards an increase in p62 levels, whilst bafilomycin control, as expected, resulted in a 4-fold increase in p62 expression compared to DMSO (figure 4.18 E). Although we have observed a promising trend in bafilomycin + nilotinib conditions towards an increase in LC3-II levels in some of the experimental repeats, the overall variability of this dataset, in addition to the results obtained with HEK cells, led me to conclude that nilotinib might not induce autophagy in C9_78 line.

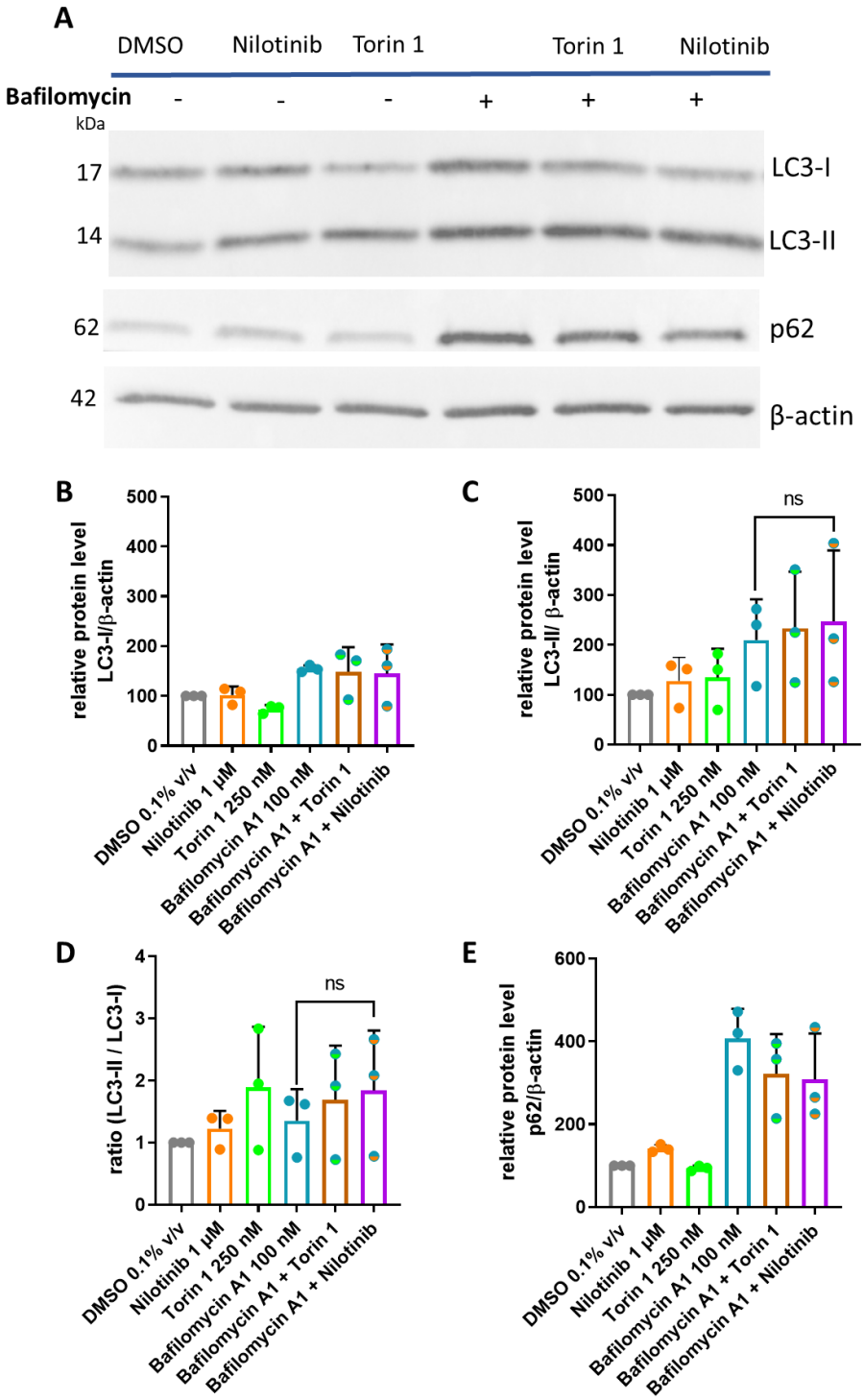

Figure 4.18 Nilotinib effect on autophagy activation in C9_78 iAstrocytes

(A) Representative western blotting images. **(B)** Quantification of LC3-I levels. **(C)** Quantification of LC3-II levels; n=3 experimental repeats; data are mean ± SD; paired t-test bafilomycin vs nilotinib + bafilomycin, ns. **(D)** Quantification of LC3-II/LC3-I ratio; n=3 experimental repeats; data are mean ± SD; DMSO vehicle = 1; paired t-test bafilomycin vs nilotinib + bafilomycin, ns. **(E)** Quantification of p62 levels. All datasets n=3 experimental repeats; data are mean ± SD, normalised to DMSO =100.

Next, I have opted to investigate nilotinib's ability to induce autophagy in sALS lines which do not possess a C9orf72 expansion-driven autophagy dysfunction (Sellier et al., 2016; Webster et al., 2016). In this set of experiments, we have included sALS_12 line, which expressed the highest levels of Abl1 expression at baseline out of all tested iAstrocytes, as well as sALS_009 and sALS_17 sALS iAstrocytes, which, although expressing lower levels of Abl1 compared to their C9orf72 counterparts, nevertheless showed elevated levels of Abl1 compared to healthy controls. A total of six experimental repeats were conducted, two repeats per each sALS line.

Figure 4.19 A shows an example western blot obtained with sALS_17. Levels of LC3-I in the sALS lines were identical in the DMSO, nilotinib, and torin 1 conditions (figure 4.19 B). Both nilotinib and torin 1 increased the LC3-II levels, which were further increased in bafilomycin-containing conditions. However, no delta between bafilomycin and either bafilomycin + nilotinib or bafilomycin + torin 1 was detected, likely due to significant variability (figure 4.19 C). This trend remained the same for LC3-II/LC3-I ratio (figure 4.19 D). Nilotinib and torin 1 treatments did not affect the p62 levels observed in DMSO-treated cells, and all bafilomycin-containing conditions resulted in an expected elevation of p62 expression (figure 4.19 E). Since the statistical comparisons did not indicate robust changes in LC3-II expression between bafilomycin and bafilomycin + nilotinib conditions, the data would exclude the hypothesis that nilotinib is an autophagy activator in iAstrocytes.

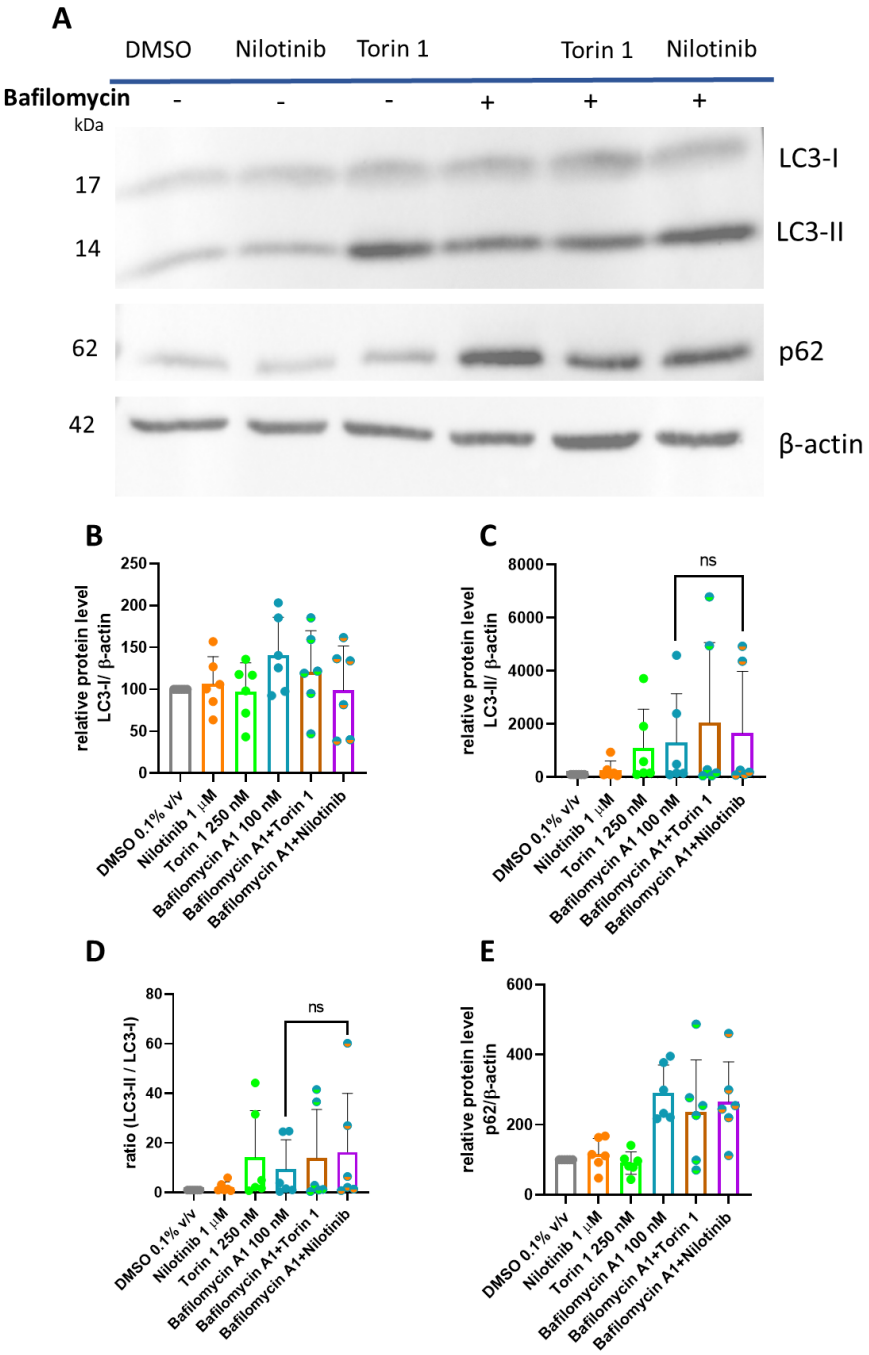

Figure 4.19 Nilotinib effect on autophagy activation in sALS patient iAstrocytes

(A) Representative western blot image of sALS_17 iAstrocytes. **(B)** Quantification of LC3-I levels. **(C)** Quantification of LC3-II levels; n=6 experimental repeats; data are mean ± SD; paired t-test bafilomycin vs nilotinib + bafilomycin, ns. **(D)** Quantification of LC3-II/LC3-I ratio; n=6 experimental repeats; data are mean ± SD; DMSO vehicle = 1; paired t-test bafilomycin vs nilotinib + bafilomycin, ns. **(E)** Quantification of p62 levels. All datasets n=6 experimental repeats; data are mean ± SD, normalised to DMSO =100.

4.2.5 Nilotinib effect on mitochondrial dynamics in ALS iAstrocytes

Among the strongest interactions Abl1 shares with other proteins is its substrate relationship with DRP1. Pathogenic Abl1 activation has been demonstrated to phosphorylate DRP1 at its serine-616 residue, which results in exacerbated mitochondrial fission and a decrease in cell survival. Abl1 is also an important upstream and downstream regulator of mitophagy. All Abl1-targeting compounds, including nilotinib, have been shown to improve mitochondrial health, drive mitophagy, and regulate DRP1 to stabilise the fission-fusion balance. This section describes the effect of nilotinib on ALS patient iAstrocyte mitochondrial network.

Mitochondrial dynamics become aberrant in many neurodegenerative diseases and these dysfunctions can manifest as lack of metabolic flexibility, aberrant fragmentation (fission) or merging (fusion) of the mitochondria. Fission and fusion result in changes to the mitochondrial network and are necessary processes required for maintenance of the mitochondrial network. However, these features are exacerbated in neurodegeneration, for instance, an increase in ROS production can lead to mitochondrial fission (Hu et al., 2019).

4.2.5.1 Mitochondrial network analysis

Having observed differential baseline levels of DRP1 and pDRP1-ser616 expression in iAstrocytes unaccompanied by clear effect of the nilotinib treatment, we have interrogated the iAstrocyte mitochondrial network further by staining DMSO- and nilotinib-treated iAstrocytes live with TMRM to visualise the mitochondrial network. To ensure that TMRM was used in a correct mode, cells were also treated with CCCP 1 hour prior to image acquisition. C9_183 and sALS_009 patient lines were selected for this experiment, alongside healthy control CTR_155v2 (figure 4.20), because previous in-house studies had identified them as having mitochondrial defects (unpublished data). The subsequent images analysis allowed for collection of the following parameters: mitochondrial numbers and mitochondrial size.

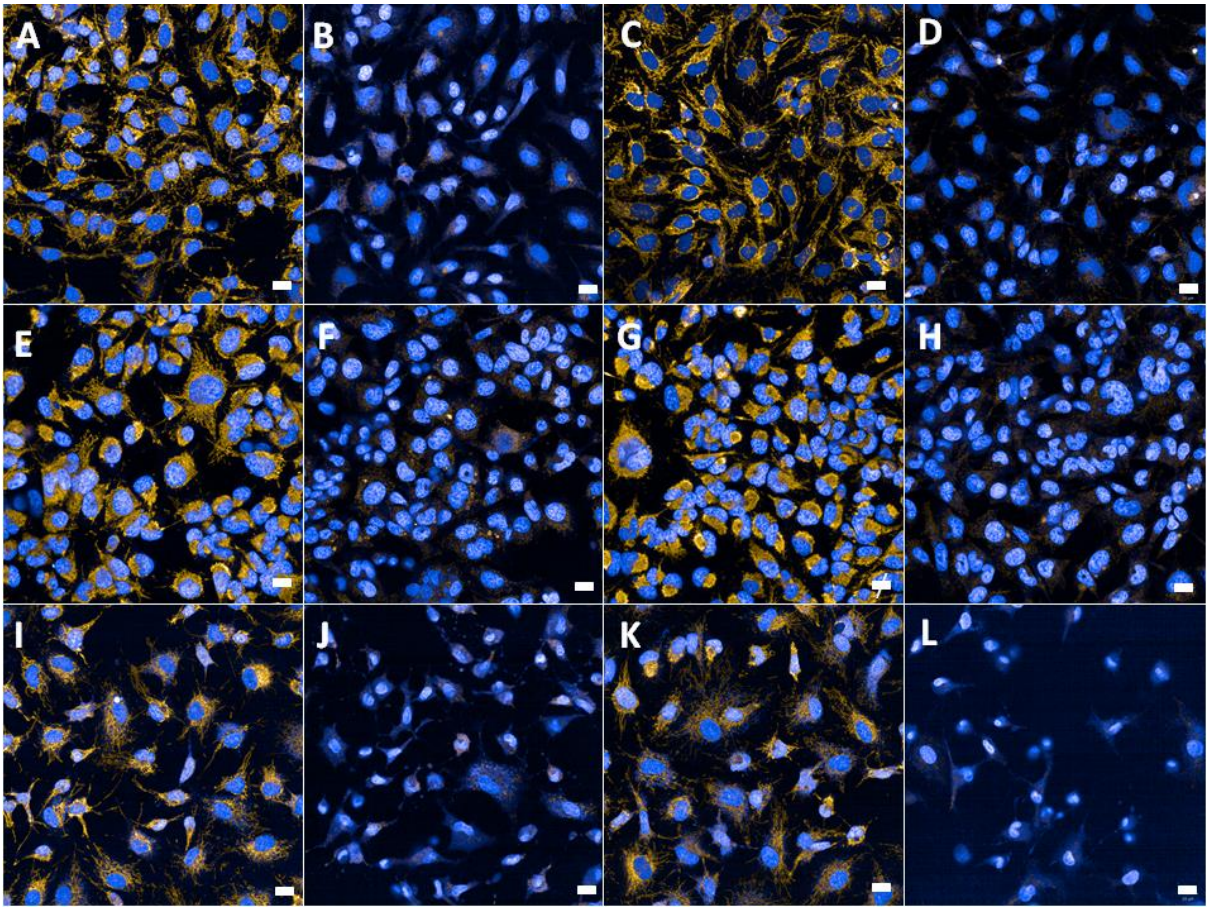

Figure 4.20 Representative images of TMRM staining

Control (**A-D**), C9_183 (**E-H**) and sALS_009 (**I-L**) stained with **TMRM** and **DAPI**. Cells treated with 0.1% v/v DMSO for 24 hours were treated for 1 hour with TMRM alone (**A, E, I**) or with TMRM+CCCP (**B, F, J**). The same treatment was applied to cells incubated with 1 µM nilotinib (**C, G, K** and **D, H, L** respectively). Scale: 20 µm

After quantification, I detected no statistical difference in the number of mitochondria per cell between the controls and patients or between DMSO and nilotinib-treated cells (figure 4.21 A). The CCCP challenge led to an expected drop in the number of mitochondria, however, we have observed a trend towards a mild preservation of mitochondrial numbers in nilotinib-treated cells (figure 4.21 B). No difference was detected in the number of mitochondria per cell area at baseline or after nilotinib administration (figure 4.21 C). The trend remained the same in the cells treated with CCCP, albeit the overall number of mitochondria has reduced as expected (figure 4.21 D). There was a trend towards a gradual increase in the TMRM intensity per pixel between control and ALS astrocytes. Moreover, the TMRM intensity was significantly lower in control and sALS_009 and significantly higher in C9_183 iAstrocytes

upon treatment with nilotinib (figure 4.21 E), potentially indicating an effect of nilotinib on mitochondrial function. CCCP challenge has reduced the TMRM intensity across all lines by approximately 55% compared to the staining intensity observed in DMSO-treated controls, and there were no further differences observed between controls and patients, or DMSO and nilotinib treatments (figure 4.21 F).

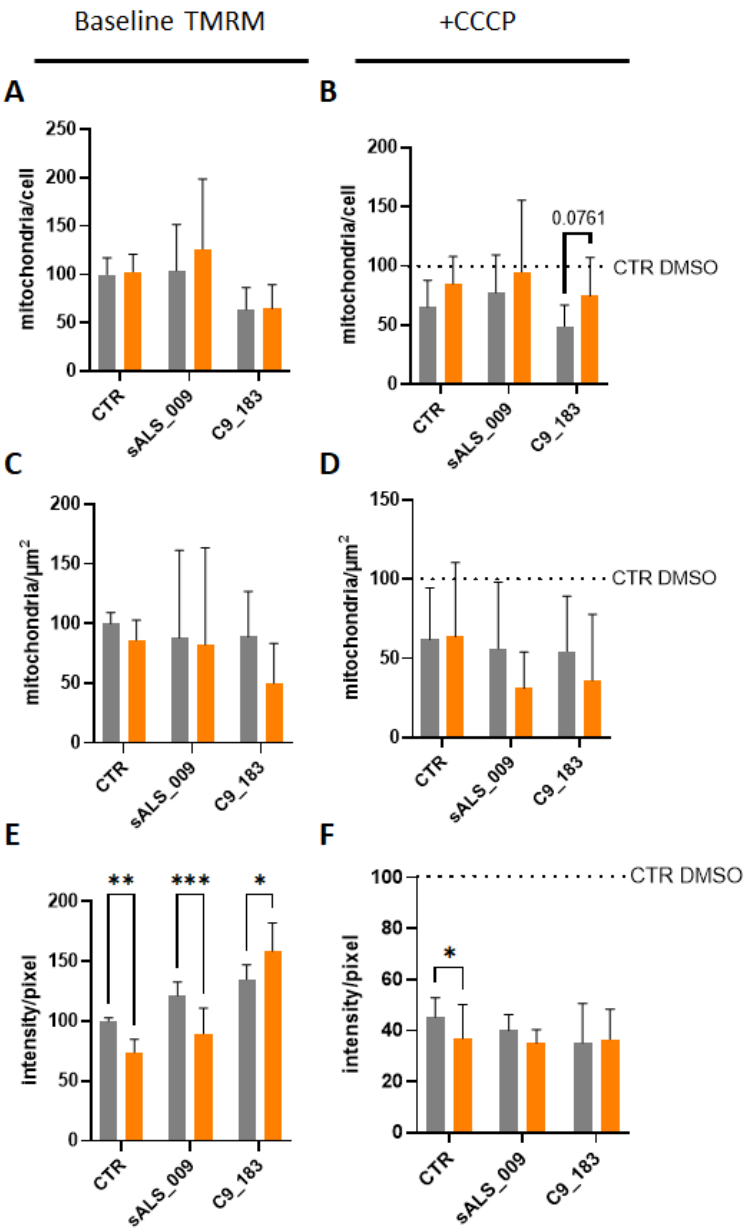

Figure 4.21 Analysis of the mitochondrial network after nilotinib treatment

(**A**) Quantification of mitochondrial numbers per cell. (**B**) Quantification of mitochondrial numbers per cell after challenge with CCCP; n=4 experimental repeats; data are mean ± SD; data relative to CTR_155v2 DMSO=100; two-way ANOVA with Tukey's multiple comparisons, ns. (**C**) Quantification of the mitochondrial numbers per mitochondrial network area (in μm^2). (**D**) Quantification of the mitochondrial numbers per mitochondrial network area (in μm^2) after challenge with CCCP. (**E**) Quantification TMRM intensity per pixel, n=4 experimental repeats; CTR includes mean results of CTR_155v2 from n=3 experimental repeats and CTR_161 from n=1 experimental repeat; data are mean ± SD; data relative to CTR DMSO=100; two-way ANOVA with Tukey's multiple comparisons, *P<0.05, **P<0.01, ***P<0.005. (**F**) Quantification of TMRM intensity per pixel after challenge with CCCP; n=4 experimental repeats; CTR includes mean results of CTR_155v2 from n=3 experimental

repeats and CTR_161 from n=1 experimental repeat; data are mean ± SD; data relative to CTR DMSO=100; two-way ANOVA with Tukey's multiple comparisons; unless otherwise specified, all comparisons ns.

4.2.5.2 Nilotinib effect on DRP1 in iAstrocytes

Abl1 has multiple documented interactions with mitochondrial proteins, of which DRP1 is responsible for orchestration of fission. Of DRP1 phosphorylation sites, serine-616 residue has been described as a key site necessary for mitochondrial fission orchestration (Lee & Kim, 2018), whereas increased phosphorylation of DRP1 at serine-637 indicates inhibition of fission (Ko et al., 2016). Here, we investigated the effect of nilotinib on total levels of DRP1 and the phosphorylation of DRP1 at serine-616 (denoted as pDRP1-ser616 thereafter).

All iAstrocytes lines carried varying levels of total DRP1 (figure 4.22 A), with nilotinib leading to no further alternation of these levels compared to DMSO vehicle-treated cells (figure 4.22 B). C9_201 expressed significantly elevated levels of pDRP-ser616 compared to DMSO-treated control iAstrocytes. However, no significant changes were observed after nilotinib treatment in this or other lines (figure 4.22 C). Ratio of pDRP1-ser616 to total DRP1 levels showed a similar trend and did not unveil any further effect of nilotinib.

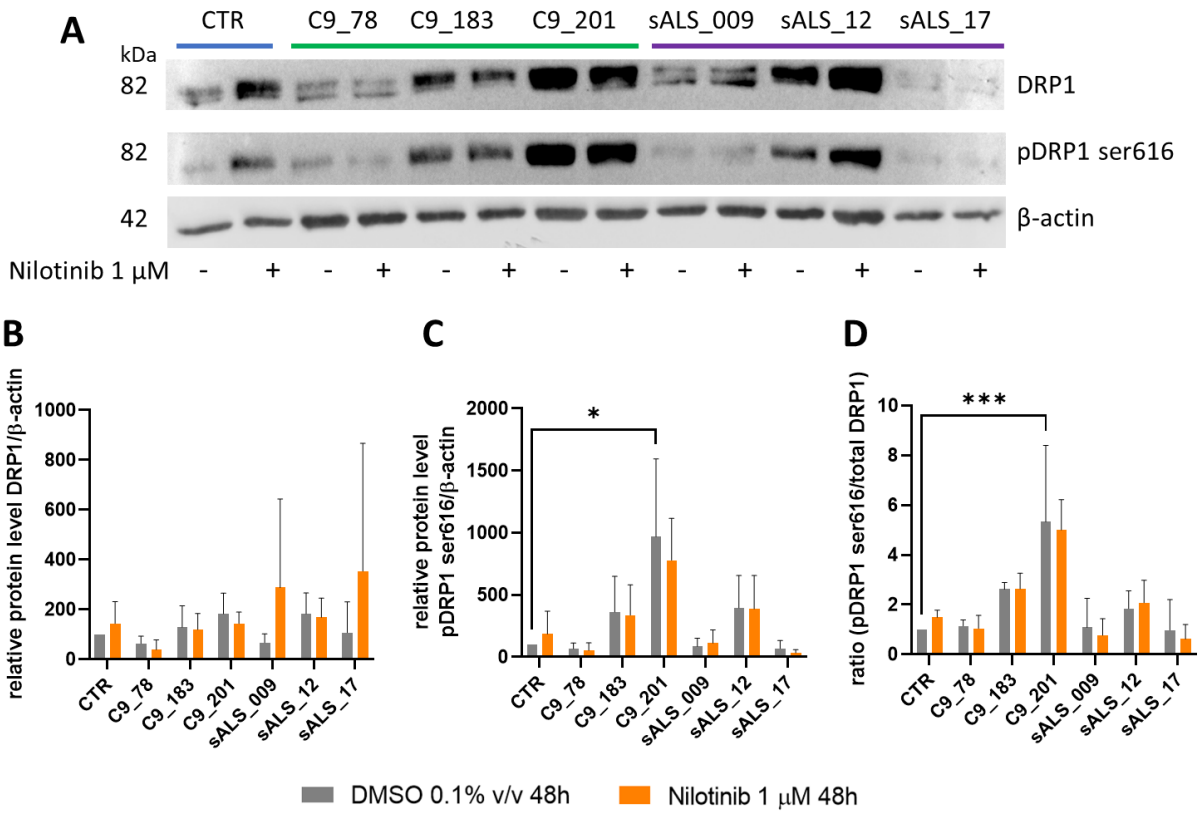

Figure 4.22 Nilotinib treatment effect on DRP1 phosphorylation at serine-616 and total DRP1 levels in iAstrocytes

(A) Representative western blot images of total DRP1 and pDRP1-ser616. **(B)** Quantification of DRP1 levels. **(C)** Quantification of pDRP1-ser616 levels; n=3-5 experimental repeats; CTR includes mean results of CTR_155v2 from n=3 experimental repeats and CTR_161 from n=1 experimental repeat and CTR_AG08620 from n=1 experimental repeat; data relative to CTR DMSO =100; data are mean ± SD; two-way ANOVA with Tukey's multiple comparisons test, *P<0.05. **(D)** Quantification of pDRP1-ser616 to total DRP1 ratio; n=3-5 experimental repeats; data relative to CTR DMSO =1; data are mean ± SD; two-way ANOVA with Tukey's multiple comparisons test, ***P=0.0003; all data n=3-5; CTR includes mean results of CTR_155v2 from n=3 experimental repeats and CTR_161 from n=1 experimental repeat and CTR_AG08620 from n=1 experimental repeat; data are mean ± SD; relative to CTR DMSO =100; two-way ANOVA with Tukey's multiple comparisons test; all comparisons ns unless stated otherwise.

In summary, nilotinib consistently rescued motor neuronal survival in the co-culture system. Nilotinib engaged with Abl1 by showing a trend towards an increase in its total levels in iAstrocytes. In spite of a robust decrease in a phosphorylation status of K562 leukaemia cell line positive control in an ELISA, no effect was observed in ALS iAstrocytes. Abl1 was

confirmed to be a potent target in ALS in a co-culture of murine motor neurons with shRNA-Abl1-treated ALS iAstrocytes, where a rescue of motor neurons upon Abl1 knockdown was observed. Nilotinib had no effect of TDP-43 fragmentation in iAstrocytes with an exception of two sALS lines where a reduction in TDP-35 was observed. No effect on TDP-43 nuclear localisation or pTDP-43 cytoplasmic inclusions was observed after nilotinib administration. Nilotinib has also underperformed in autophagy assays, in spite of the published evidence suggesting its role in autophagy activation. Nilotinib-treated cells showed a decrease in MMP in control and sALS_009 line, whilst the opposite was true in C9_183. Nilotinib had no effect on the mitochondrial numbers or the network size. Similarly, no changes in pDRP1 ser616/DRP1 were observed, indicating no effect of nilotinib on fission dynamics.

4.3 Discussion

Research efforts over the past decade have unveiled the potential of tyrosine kinase inhibitors as repurposing agents for neurodegenerative disorders. Most of these findings came as a consequence of studies identifying prominent kinases associated with other diseases as relevant in neurodegeneration. Investigations into Abl1 as a Parkinson's disease therapeutic led to a recognition of it as a crucial target for Alzheimer's disease and ALS. Most of the studies into the role of Abl1 in ALS focused on the function of this target in motor neurons, hence little is known about Abl1 expression in glial cells. Given the non-cell autonomous nature of ALS, exploration of Abl1 dynamics in astrocytes is crucial.

Nilotinib is a second-generation tyrosine kinase inhibitor used in chronic myelogenous leukaemia (CML) to target the constitutively active BCR-Abl complex that is a result of the Philadelphia chromosome (Ray et al., 2007). Since its FDA approval in 2008, nilotinib has attracted the attention of neurodegeneration researchers who unveiled Abl1 overexpression in diseases such as PD or AD. Importantly, although Abl1 has already been described in the literature as a possible target for ALS (Imamura et al., 2017; Rojas et al., 2015), BenevolentAI's Precede system validates the importance of this target in ALS. Albeit these results cannot be considered novel, they nevertheless confirm that AI can serve as a useful tool for drug

discovery and repurposing in neurodegeneration, as the most promising targets are highlighted for further study based on ongoing development in the literature.

Although utilised in chemotherapies and having a cytostatic effect on cancer cells (Liu et al., 2011; Trojani et al., 2019), no statistical difference in iAstrocyte cell numbers were observed between nilotinib and DMSO vehicle-treated cohorts. Consistently with these results, an LDH assay demonstrated 1 µM nilotinib to be non-toxic and staining for Ki67 nuclear foci indicated no changes in iAstrocyte proliferation rate upon nilotinib treatment. Therefore, this part of the study demonstrated that nilotinib could be safely administered to CNS cells, as no cytotoxicity or cytostaticity is to be expected. Moreover, previous reports have shown 1 µM nilotinib as capable of increasing the survival of ALS patient iPSC-derived motor neurons in a monoculture (Imamura et al., 2017), although no specific neuroprotective mechanism was identified.

In our ALS model, nilotinib treatment had no effect on iAstrocyte cellular morphology, thus suggesting that the motor neuron rescue observed after nilotinib treatment in the co-culture system does not result from any cytoskeletal remodelling on the iAstrocyte level. These results were further validated when a morphology of iAstrocytes whose levels of Abl1 were knocked down. Here, although the same number of cells was plated at day 0, Abl1 shRNA-treated cells displayed higher numbers than the RFP controls, as reflected by the cell number at both day 1 and day 3 post plating in the assay plate. One possible explanation is that iAstrocytes treated with Abl1-shRNA might have attached to the culture dish more efficiently than RFP controls. Indeed, LINCS describes perturbations in several different adhesion molecules across multiple cell lines after treatment with nilotinib, backing up evidence from the literature (Khatri et al., 2016). However, it needs to be pointed out that cell numbers dropped from day 1 to day 3 of the screening at the same rate of the RFP-treated cells. A possible explanation for this decrease in cell number is the overexpression of RFP. Forced expression of a foreign protein in high amounts, in fact, is likely to have toxic effects. To test this, cells can be treated with a titration of shRNA-Abl1 with and without RFP, with an empty viral vector, or with a vector containing a scrambled sequence.

An aspect of disease modelling unaddressed by this experiment is the difference in a mode of target modulation. Knockdown experiments stop target protein synthesis, whereas using compounds causes target deactivation by inhibiting its phosphorylation. Therefore, no direct parallels can be drawn between Abl1 knockdown experiments and nilotinib treatment. Moreover, nilotinib targets several other kinases, as illustrated in table 4.1, and it is therefore not unlikely that the beneficial nilotinib effect we observe in our cell model is a result of inhibition of several kinases.

Even though others have described nilotinib-mediated improvement in glial and mitochondrial function in mice expressing human wild-type TDP-43 (Heyburn et al., 2016), no robust report exists describing the ability of nilotinib to attenuate TDP-43 proteinopathy in ALS patient cells. In this study, nilotinib treatment had no effect on the nuclear localisation of TDP-43 and the numbers of pTDP-43 inclusions in the cytoplasm. However, it led to a modest decrease in TDP-35 C-terminal fragments in sALS iAstrocytes. The mechanisms behind this finding remain unclear, although the lack of improvement in TDP-43 fragmentation in C9orf72 patients indicates a genotype-specific effect. It is likely that nilotinib is a mild autophagy activator leading to reduction of proteinopathy in systems where autophagy is not impaired, though this hypothesis would require further investigation.

Despite previous reports describing nilotinib as an autophagy activator (Hebron et al., 2013; Shaker et al., 2013), autophagy assays conducted in HEK293 cells in this project failed to replicate this data. No significant increase in LC3-II or decrease in LC3-I or p62 levels were observed after nilotinib treatment at either 6h or 8h. The leading study which identified nilotinib as an autophagy activator in PD has not shown a decrease in LC3-I and a simultaneous increase in LC3-II. Instead, an increase in ubiquitin-like protein ATG12 (Atg12) and B-cell lymphoma 2 (Bcl-2) were reported (Yu et al., 2013). Moreover, others have previously measured autophagy induction in cells treated with nilotinib after much longer time periods, suggesting that neither 6h nor 8h treatment tested in this study was enough to observe an autophagic flux. On the other hand, it is not unlikely that nilotinib acts as an autophagy activator only in cells over-expressing constitutively active Abl1, as most other studies

describing Abl1 inhibition as beneficial for autophagy function investigated these dynamics in the context of overexpression (Karim et al., 2020). To our knowledge, HEK293 cells carry no defect in Abl1 expression, hence no autophagy modulation would have been observed in our immunoblotting analysis upon nilotinib treatment. However, this element of nilotinib's mechanism of action makes it somewhat less attractive for repurposing in patients which do not harbour Abl1 overexpression. Although we have observed a significant upregulation of Abl1 in ALS iAstrocytes when compared to controls, the increased levels are unlikely to translate into the constitutive activation reported in BCR-ABL models. Other Abl1 inhibitors, such as bosutinib, have been previously described as activators of autophagy in SOD1 ALS motor neurons, indicating that targeting Abl1 might be a valid strategy for modulation of autophagy dysfunction in ALS (Imamura et al., 2017). In this project, I have not interrogated the autophagy function status of SOD1 patient iAstrocytes, but this would constitute a useful strategy for further delineation of nilotinib's mode of action, to see if results obtained in our model of ALS iAstrocytes correlate with previously described data obtained from iPSC-derived SOD1 patient motor neurons (Imamura et al., 2017).

Although no difference in mitochondrial numbers was observed in nilotinib-treated cells, the TMRM staining intensity, which acts as a readout of a baseline MMP (Sakamuru et al., 2016), was decreased in control and sALS and increased in C9orf72 iAstrocytes after nilotinib administration. These changes could be indicative of a shift in ATP production, and therefore the mitochondrial function in general. Usually, loss of TMRM intensity is observed when mitochondria are depolarised and the MMP collapses (Joshi & Bakowska, 2011). In an absence of pDRP-ser616 pathology in sALS_009, and therefore no significant or pathological levels of mitochondrial fission occurring, the decrease in MMP could be attributed to a correction a hypermetabolic profile often exhibited by ALS patients (Steyn et al., 2018). On the other hand, C9_183 showed an increase in MMP after nilotinib administration, which could be indicative of an increase in ATP production. C9_183 carried a mild pDRP-ser616 upregulation that nilotinib had no effect on. Since fission-fusion balance is a dynamic process and phosphorylation of DRP1 at ser-616 could not be occurring at the same time as mitochondrial fusion, the increase in MMP could be attributed to an improvement in mitochondrial function. However, nilotinib's effect on fusion dynamics has not been studied in this work but could

constitute a line of investigation to understand the role of nilotinib in mitochondrial health. This could prove particularly useful in lines exhibiting high levels of fission, such as C9_201.

Due to its primary focus on astrocytes as drivers of toxicity in ALS, this project did not explore the effect of nilotinib on neuronal cells. The advantage of such an approach is the expansion of our current understanding of nilotinib's mode of action in ALS, as all reports published to date which investigated Abl1 inhibitors in ALS focused on motor neurons only. One of the main aspects of Abl1 activation is its phosphorylation status and, therefore, modulators of Abl1 are expected to change the levels of phosphorylated protein. Abl1 is capable of autophosphorylation at Tyr412. The pan-Tyr pAbl1 ELISA kit used in this study did not allow for a separation of this specific phosphorylation site to measure the autophosphorylation dynamics of Abl1 following the treatment with nilotinib. Moreover, I attempted to optimise a Tyr412-specific ELISA kit, however I was unable to detect a positive signal in iAstrocytes samples above the assay threshold level. Regardless of the assay limitations in iAstrocytes, the use of K562 cells convincingly confirmed that nilotinib can successfully inhibit Abl1 phosphorylation. Indeed, other members of the team have developed a target engagement assay confirming these conclusions. To our knowledge, one report exists of measuring pAbl1 and Abl1 levels in astrocytes derived from $SOD1^{L144FVX}$ patient iPSCs. No difference was detected between pAbl1 levels in these astrocytes or their isogenic control counterparts and neither did treatment with bosutinib affect them (Imamura et al., 2017).

Interestingly, recent data from our lab suggests that nilotinib exerts neuroprotection directly on motor neurons and not via astrocytes. This data, obtained by Dr Sophie Nyberg, shows that motor neurons treated with fresh media containing nilotinib show increased survival. This effect was not observed in motor neurons in co-culture with iAstrocytes pre-treated with nilotinib, but where the drug has been washed out of the culture prior to the addition of motor neurons. This would account for the positive performance of nilotinib in the co-culture screening conducted by Dr Matthew Stopford, since the drug is not removed from culture plate when motor neurons are seeded onto it. It is also in agreement with previously published reports, where modulation of Abl1 activity in iPSC-derived SOD1, C9orf72, TDP-43

and sALS motor neurons using bosutinib has resulted in increased motor neuronal survival (Imamura et al., 2017). However, the preliminary data of co-cultures of Hb9-GFP motor neurons and shAbl1-iAstrocytes indicates that knockdown of Abl1 expression in astrocytes might also exert neuroprotection on motor neurons. Indeed, recent reports have described Abl1 inhibition as capable of decreasing the chronic glial inflammation (Song et al., 2019), which can in turn result in neuroprotection. Similarly, a small clinical trial in PD patients has shown a significant decrease in phosphorylated neurofilament-heavy chain levels in the CSF after nilotinib administration (Pagan et al., 2019), which indicates neuroprotection and could also help explain this effect. However, further studies into nilotinib's ability to attenuate glial activation in ALS need to be performed.

5 Discussion

ALS is a complex neurodegenerative disorder, where a characteristic loss of upper and lower motor neurons leads to muscle weakness with subsequently muscle wasting, paralysis and death. ALS lacks effective pharmacological treatments and the only drugs currently available on the market extend patients' life expectancy by a very modest margin (Katyal & Govindarajan, 2017), making development of new ALS therapeutics a pressing need.

An estimated 10% of all ALS cases have family history of the disease, whereas the remaining 90% are termed sporadic. Several genetic mutations and mechanisms have been identified as playing a vital role in ALS pathogenesis (Ferraiuolo et al., 2011; Brown & Al-Chalabi, 2017). Though genetically and clinically heterogeneous, one factor appears to link 97% of all ALS patients, namely the presence of TDP-43 cytoplasmic aggregates combined with nuclear loss of TDP-43 expression. This feature, collectively named TDP-43 proteinopathy for its presence in several nervous system diseases, including Alzheimer's disease (Gu et al., 2017; Wilson et al., 2011), Niemann-Pick disease type C (Dardis et al., 2016), Parkinson's disease (Nakashima-Yasuda et al., 2007) and in elderly populations suffering from cognitive impairment (Deerlin et al., 2008; Nelson et al., 2019), is observed in multiple genetic subtypes of ALS, with a notable exception of SOD1 (Penndorf et al., 2017) and FUS (Farrawell et al., 2010). TDP-43 cytoplasmic inclusions have been shown to be toxic to motor neurons in ALS (Barmada et al., 2010), yet the precise mechanism of TDP-43 mislocalisation and accumulation remains unsolved, making the proteinopathy an important therapeutic target.

Since the intricacies and the interplay between the different pathogenic mechanisms of ALS are not fully understood, any progress in identifying novel drug targets or treatments offer opportunities for further progress. For that purpose, *in vitro* cell systems such as iNPCs, which can reliably model the pathophysiology ALS, can help unveil mechanisms of action of new compounds. Alongside their ability to model the non-cell autonomous aspects of ALS, our group has recently demonstrated their retention of an ageing phenotype (Gatto et al., 2021), which is important when studying diseases where age is a risk factor, such as ALS. Another approach of modelling ageing includes keeping iPCS-differentiated cells in culture for a longer period of time, a technique called *in vitro* ageing (Birger et al., 2019). Such approaches unveil disease phenotypes which are otherwise silent and remain uncharacterised, as ageing

phenotype in newly-differentiated cells is not appreciated. Cells exhibiting an ageing phenotype are transcriptionally much closer to most-mortem cells than their non-aged counterparts (Gatto et al., 2021), which translates into experimental readouts that represent the disease environment in a patient much closer. From a drug discovery and drug repurposing point of view, an appropriate model must be selected in order to gain a full insight into the precise function of a drug in a given disease scenario. Validating drugs and their mechanisms of action in target overexpressing or constitutively active systems do not reproduce the physiological scenario. To that end, iNPCs serve as a useful model, as they recapitulate many aspects of ALS pathology. Therefore, iNPCs provide a reliable platform for drug screenings and subsequent investigations of a drug's mechanism of action.

This project brings together AI technology and discovery of novel ALS therapeutics with the aim to understand the mode of action of gefitinib and nilotinib. AI algorithms are capable of scanning the entirety of published literature and publicly available data in order to build connections between a disease and a target which could play a role in the disease process. A knowledge graph built in such a way led to a discovery of Abl1 as a target of interest in this project. As described in section 3.2.5, Abl1 has previously been investigated as a target for ALS, however, its role in the disease needs to be elucidated further. The two Abl1-targeting compounds investigated in this work led to improvements of several aspects of ALS pathology, however, with little overlap, suggesting that Abl1 is not the sole crucial target via which both compounds exert their function. Nevertheless, the preliminary data in this project suggests that Abl1 knockdown in iAstrocytes could improve the survival of motor neurons. In a co-culture of wild-type motor neurons and C9orf72 iAstrocytes expressing different levels of Abl1 knockdown, we have observed an increase in motor neuronal rescue when Abl1 was downregulated by approximately 80% compared to untreated cells. These neuroprotective effects were comparable to gefitinib and nilotinib treatments, supporting the idea that Abl1 remains an important target for ALS.

Optimal performance of an AI-identified compound in an *in vitro* system helps select a candidate compound for further stages of optimisation. However, one caveat not addressed in such models is the BBB permeability of a given compound. Gefitinib does cross the BBB, however it is a substrate for both p-glycoprotein (PGP) and breast cancer resistant protein (BCRP) transporters and consequently gets constantly expelled from the CNS (Kitazaki et al.,

2005). On the other hand, nilotinib has been demonstrated to possess a moderate ability to penetrate the BBB (Karuppagounder et al., 2014). Compared to other BCR-Abl tyrosine kinase inhibitors, its BBB permeability was inferior only to bosutinib (Imamura et al., 2017). However, nilotinib has significantly underperformed in the Parkinson's disease clinical trials, despite initial results suggesting that its leads to a significant increase in dopamine metabolite levels and a decrease in α-synuclein oligomers and phosphorylated tau in the CSF (Pagan et al., 2019). Although no side effects were observed, patients' motor and cognitive functions did not improve, compared to the placebo group (Pagan et al., 2020). Moreover, another trial observed a similar lack of beneficial neurological improvement in patients, alongside a lack of dopamine metabolite biomarkers in the CSF (Simuni et al., 2020). Indeed, CSF concentration of nilotinib represented only 0.3% of the levels found in the plasma, significantly lower than the CSF concentration necessary to inhibit Abl1 (Simuni et al., 2020). To increase the CNS penetrance of a compound, AI technologies allow for a deep analysis of the compound structure to increase its polypharmacological profile and, amongst other desired properties. Therefore, although this project did not include an *in vivo* investigation into either of the drugs, the wider collaboration included an extensive chemistry programme leading to greatly improved brain exposure to the drugs at concentrations necessary for them to engage with their targets.

Gefitinib and nilotinib were identified by the AI platform as potentially neuroprotective compounds through targeting of EGFR and Abl1 respectively. Interestingly, at least in our model of human astrocytes, the neuroprotection achieved by gefitinib is unlikely to be linked to EGFR inhibition. This does not exclude a role for EGFR inhibition in motor neurons or other cell types. The failure in confirming gefitinib's primary target as responsible for the neuroprotective effect observed *in vitro* led us to interrogate the other kinases targeted by gefitinib, thus resulting in the identification of *ABL1*, which was supported by additional AI discovery-driven data, as well as further drug screening and, eventually, the literature (Imamura et al., 2017). Although the two compounds share this target, their mechanisms of action seem to be widely different. Gefitinib treatment reduced Abl1 expression at both transcript and protein levels, whereas nilotinib targeted Abl1 phosphorylation. This suggests that gefitinib targets *ABL1* transcription in the first place. Nilotinib, on the other hand, affects Abl1 post-translational modifications only. Since increased Abl1 phosphorylation was

previously observed in wild type motor neurons treated with ALS astrocyte conditioned medium (Rojas et al., 2015), understanding pAbl1 dynamics in ALS glia is important in order to understand the possible pathways needing amelioration to rescue motor neuronal survival. Abl1 is activated by a variety of stimuli, including oxidative stress, inflammation, and DNA damage (Rojas et al., 2015). Having observed elevated levels of Abl1 at baseline in ALS patient iAstrocytes, one could argue that gefitinib's activity on Abl1 transcription might be more beneficial. However, more work needs to be conducted on the Abl1 role in ALS astrocytes before and after drug treatment to fully understand how Abl1 binding partners, upstream events (such as ROS generation; Rojas et al., 2015) and downstream effectors (such as CrkL and Crk; Birger et al., 2009) are affected.

Gefitinib's ability to induce autophagy in cancer cell lines is beneficial, as it helps drive tumour cell death (Hsiao et al., 2018; Yang et al., 2019). Evidence also points towards autophagy being crucial for clearance of TDP-43 fragments as well as other pathogenic protein aggregates (Berger et al., 2006; Cascella et al., 2017; Cicardi et al., 2018; Crippa et al., 2013). However, achieving autophagy activation pharmacologically may not necessarily result in an improved disease phenotype, as observed previously, for example, with antihypertensive drug rilmenidine (Perera et al., 2018). Other conflicting reports describe beneficial effects on the disease onset and survival of $SOD1^{G93A}$ mice after pharmacological autophagy activation using trehalose (Castillo et al., 2013), whilst others described the same drug's usefulness in slowing disease progression, but not extending survival (Li et al., 2015). Moreover, previous reports using conditional knockout of the gene encoding the ubiquitin-activating enzyme E1-like protein ATG7 (Atg7) in motor neurons of $SOD1^{G93A}$ mice to inhibit autophagy, showed that autophagy inhibition might prolong survival of diseased mice, but at a cost of faster onset (Rudnick et al., 2017). Although motor neuronal numbers were unaffected by autophagy inhibition, their size and synaptic function decreased and their eventual death was not prevented (Rudnick et al., 2017). This study suggests that autophagy activation or inhibition themselves are not straightforward and viable therapy options in and of themselves, and the strength or timing of activation requires further study.

Nilotinib, on the other hand, has many important binding partners in the family of mitochondrial proteins, including DRP1 and parkin, and has been linked previously to improved mitophagy function (Rojas et al., 2015). Although we have not observed an increase

in an autophagic flux with nilotinib and did not have time to pursue its ability to induce mitophagy, it did have a beneficial effect on mitochondrial numbers following a challenge with CCCP, suggesting that it could exert neuroprotection via an improvement to mitochondrial functions. Autophagy and mitophagy pathways converge at multiple points (Ding & Yin, 2012). It would therefore be worthwhile to investigate if gefitinib had any effect on mitophagy, too. Although no decrease in mitochondrial numbers was observed after gefitinib administration, the analysis pipeline used to evaluate TMRM staining images could also take into account mitochondrial size and shape. Rounding and shortening of mitochondria is indicative of mitochondrial uncoupling and damage (Miyazono et al., 2018), therefore an insight into the compound's ability to clear defective mitochondria would be of therapeutic importance.

These differential mechanisms of the two compounds would help explain why gefitinib led to a consistent reduction in TDP-43 fragmentation, whereas nilotinib had the same effect on just two iAstrocyte lines. However, it remains to be fully explained why this reduction is being observed, since I did not manage to demonstrate a significant increase in autophagy activation in ALS iAstrocyte lines upon gefitinib treatment and nilotinib does not appear to activate autophagy in our assay. Importantly, however, autophagy is a dynamic process which is challenging to replicate *in vitro*, especially in diseased cells. Assay negative controls often result in toxicity, such as observed in this and other reports with bafilomycin A1 (Xie et al., 2014; Yuan et al., 2015), and inhibitors targeting different stages of the autophagy cascade, such as the very initiation of it, would likely also have a detrimental effect on the cell. Putting cells under extra stress in such assays is also likely to alter several other pathways, therefore making the final assay readout challenging to interpret.

In this project, we tested the hypothesis that the decrease in fragmentation might be a result of a decreased rate of TDP-43 cleavage. The proximity ligation assay we have selected as a tool to help us visualise that yielded results suggesting that gefitinib does not have an effect on the rate of TDP-43 cleavage by caspase-3. In the future, therefore, alternative hypotheses could be tested, such as the possibility that TDP-43 is retained in the nucleus and, therefore, is less exposed to cleavage, mechanisms that could be mediated by nuclear export transporters.

Although the exact mechanism via which gefitinib does lead to motor neuronal rescue in co-culture remains to be fully elucidated, findings of this project supplemented with other recent reports can help shed light on the usefulness of this drug in ALS. For example, TDP-43 mislocalisation and motor neuronal death and the neuromuscular junction health of TDP-43^{M337V} mice, has been shown to improve upon overexpression of Oxr1 (Williamson et al., 2019a), a phosphorylation of which at serine-204 can be targeted by gefitinib (Moritz et al., 2011). Oxr1 expression levels have not been measured in our model following gefitinib administration, but it would be a worthwhile strategy in order to build a picture of gefitinib's role in neuroprotection. Conversely, nilotinib and its sister compounds have previously been shown to improve the survival of iPSC-derived ALS motor neurons (Imamura et al., 2017). To that extent, this study confirmed the usefulness of Abl1 inhibitors as potential ALS therapeutics. However, the precise mechanism behind these findings needs to be investigated further. Both gefitinib and nilotinib target Abl1 and it appears that similarities between these two compounds in terms of the mechanisms of action in ALS astrocytes end there. Due to time constraints of this project and the primary focus of this project on ALS glia, the effect of the two compounds on neurons remains unexplored in this work. The present thesis focuses primarily on glia, as the aim was to investigate the mechanisms leading to neuroprotection in an assay where only the astrocytes were derived from patients. There is, however, a possibility that these compounds act by protecting the motor neurons from the insult inflicted by the astrocytes through mechanisms such as autophagy, mitophagy, oxidative stress response or mitigation of excitotoxicity. Work is currently being conducted by myself and Dr Nora Markus to unveil the precise effect of the both drugs, but especially nilotinib, on motor neuronal health and survival.

An important caveat of using gefitinib and nilotinib as new therapeutics for ALS is a host of significant side effects they cause in cancer patients. Here, as mentioned before, AI systems can be deployed to model a novel molecule based on a scaffold of the primary molecule of interest to fit the new target or identify molecules for drug repurposing which are known to engage the target of choice.

In conclusion, this study provides an important contribution to the field of drug discovery and repurposing by characterising the effect of two widely used cancer compounds on hallmarks of ALS in a pathophysiologically relevant model of the disease. The ability of iAstrocytes to

mimic the TDP-43 pathology observed in patient post-mortem tissue helped us uncover the consistent improvement in TDP-43 fragmentation in gefitinib-treated cells. To our knowledge, this is a first study to present an Abl1 pathology in ALS patient-derived astrocytes across C9orf72 and sALS patients, as the only previous report presented findings from a single SOD1 patient iPSC-derived astrocyte line.

The hypothesis behind this project was that AI can identify drugs targeting disease-relevant pathways in ALS. To that end, I have demonstrated that gefitinib affects TDP-43 proteinopathy in ALS iAstrocytes, whereas nilotinib might improve mitochondrial health. Even though the precise mechanisms and cascade of events behind these findings remain unknown, this work confirms that AI can be used as a drug discovery and repurposing tool in ALS.

6 Bibliography

Aasen, T., Raya, A., Barrero, M. J., Garreta, E., Consiglio, A., Gonzalez, F., Vassena, R., Bilić, J., Pekarik, V., Tiscornia, G., Edel, M., Boué, S., & Izpisúa Belmonte, J. C. (2008). Efficient and rapid generation of induced pluripotent stem cells from human keratinocytes. *Nature Biotechnology*, *26*(11), 1276–1284. https://doi.org/10.1038/nbt.1503

Abe, K., Aoki, M., Tsuji, S., Itoyama, Y., Sobue, G., Togo, M., Hamada, C., Tanaka, M., Akimoto, M., Nakamura, K., Takahashi, F., Kondo, K., & Yoshino, H. (2017). Safety and efficacy of edaravone in well defined patients with amyotrophic lateral sclerosis: a randomised, double-blind, placebo-controlled trial. *The Lancet Neurology*, *16*(7), 505–512.

Abushouk, A. I., Negida, A., Elshenawy, R. A., Zein, H., Hammad, A. M., Menshawy, A., & Mohamed, W. M. Y. (2018). C-Abl Inhibition; A Novel Therapeutic Target for Parkinson's Disease. *CNS & Neurological Disorders Drug Targets*, *17*(1), 14–21. https://doi.org/10.2174/1871527316666170602101538

Al-Saif, A., Al-Mohanna, F., & Bohlega, S. (2011). A mutation in sigma-1 receptor causes juvenile amyotrophic lateral sclerosis. *Annals of Neurology*. https://doi.org/10.1002/ana.22534

Al Sultan, A., Waller, R., Heath, P., & Kirby, J. (2016). The genetics of amyotrophic lateral sclerosis: current insights. *Degenerative Neurological and Neuromuscular Disease*, 49. https://doi.org/10.2147/DNND.S84956

Allen, S. P., Hall, B., Castelli, L. M., Francis, L., Woof, R., Siskos, A. P., Kouloura, E., Gray, E., Thompson, A. G., Talbot, K., Higginbottom, A., Myszczynska, M., Allen, C. F., Stopford, M. J., Hemingway, J., Bauer, C. S., Webster, C. P., De Vos, K. J., Turner, M. R., … Shaw, P. J. (2019). Astrocyte adenosine deaminase loss increases motor neuron toxicity in amyotrophic lateral sclerosis. *Brain*, *142*(3). https://doi.org/10.1093/brain/awy353

Anderson, P., & Kedersha, N. (2008). Stress granules: the Tao of RNA triage. *Trends in Biochemical Sciences*, *33*(3), 141–150. https://doi.org/10.1016/j.tibs.2007.12.003

Aoki, Y., Manzano, R., Lee, Y., Dafinca, R., Aoki, M., Douglas, A., Varela, M., Sathyaprakash, C., Scaber, J., Barbagallo, P., Vader, P., Mager, I., Ezzat, K., Turner, M., Ito, N., Gasco, S., Ohbayashi, N., El Andaloussi, S., Takeda, S., … Wood, M. (2017). C9orf72 and RAB7L1 regulate vesicle trafficking in amyotrophic lateral sclerosis and frontotemporal dementia. *Brain*, *140*(4), 887–897.

Ash, P. E. A., Bieniek, K. F., Gendron, T. F., Caulfield, T., Lin, W.-L., Dejesus-Hernandez, M., van Blitterswijk, M. M., Jansen-West, K., Paul, J. W. 3rd, Rademakers, R., Boylan, K. B., Dickson, D. W., & Petrucelli, L. (2013). Unconventional translation of C9ORF72 GGGGCC expansion generates insoluble polypeptides specific to c9FTD/ALS. *Neuron*, *77*(4), 639–646. https://doi.org/10.1016/j.neuron.2013.02.004

Ashburn, T. T., & Thor, K. B. (2004). Drug repositioning: identifying and developing new uses for existing drugs. *Nature Reviews. Drug Discovery*, *3*(8), 673–683. https://doi.org/10.1038/nrd1468

Atsumi, T. (1981). The ultrastructure of intramuscular nerves in amyotrophic lateral sclerosis. *Acta Neuropathologica*, *55*(1), 193–198.

Bae, S. Y., Park, H. J., Hong, J. Y., Lee, H. J., & Lee, S. K. (2016). Down-regulation of SerpinB2 is associated with gefitinib resistance in non-small cell lung cancer and enhances invadopodia-like structure protrusions. *Scientific Reports*, *6*(February), 1–15. https://doi.org/10.1038/srep32258

Baghaei, B., Saeb, M. R., Jafari, S. H., Khonakdar, H. A., Rezaee, B., Goodarzi, V., & Mohammadi, Y. (2017). Modeling and closed-loop control of particle size and initial burst of PLGA biodegradable nanoparticles for targeted drug delivery. *Journal of Applied Polymer Science*, *134*(33), 1–12. https://doi.org/10.1002/app.45145

Bakkar, N., Kovalik, T., Lorenzini, I., Spangler, S., Lacoste, A., Sponaugle, K., Ferrante, P., Argentinis, E., Sattler, R., & Bowser, R. (2018). Artificial intelligence in neurodegenerative disease research: use of IBM Watson to identify additional RNA-binding proteins altered in amyotrophic lateral sclerosis. *Acta Neuropathologica*, *135*(2), 227–247.

Bannwarth, S., Ait-El-Mkadem, S., Chaussenot, A., Genin, E., Lacas-Gervais, S., Fragako, K., Berg-Alonso, L., Kageyama, Y., Serre, V., Moore, D., Verschueren, A., Rouzier, C., Le Ber, I., Augé, G., Cochaud, C., Lespinasse, F., N'Guyen, K., de Septenville, A., Brice, A., … Paquis-Flucklinger, V. (2014). A mitochondrial origin for frontotemporal dementia and amyotrophic lateral sclerosis through CHCHD10 involvement. *Brain*, *137*(8), 2329–2345.

Barmada, S. J., Skibinski, G., Korb, E., Rao, E. J., & Wu, J. Y. (2010). Cytoplasmic mislocalization of TDP-43 is toxic to neurons and enhanced by a mutation associated with familial ALS. *The Journal of Neuroscience*, *30*(2), 639–665. https://doi.org/10.1523/JNEUROSCI.4988-09.2010.Cytoplasmic

Bentmann, E., Neumann, M., Tahirovic, S., Rodde, R., Dormann, D., & Haass, C. (2012). Requirements for stress granule recruitment of fused in sarcoma (FUS) and TAR DNA-binding protein of 43 kDa (TDP-43). *Journal of Biological Chemistry*, *287*(27), 23079–23094. https://doi.org/10.1074/jbc.M111.328757

Berger, Z., Ravikumar, B., Menzies, F., Garcia-Oroz, L., Underwood, B., Pangalos, M., Schmitt, I., Wullner, U., Evert, B., O'Kane, C., & Rubinsztein, D. (2006). Rapamycin alleviates toxicity of different aggregate-prone proteins. *Human Molecular Genetics*, *15*(3), 433–442.

Bernaudo, S., Khazai, S., Honarparvar, E., Kopteva, A., & Peng, C. (2017). Epidermal growth factor promotes cyclin G2 degradation via calpain-mediated proteolysis in gynaecological cancer cells. *PLoS ONE*, *12*(6), 1–15.

Berning, B. A., & Walker, A. K. (2019). The pathobiology of TDP-43 C-terminal fragments in ALS and FTLD. *Frontiers in Neuroscience*, *13*(APR), 1–27. https://doi.org/10.3389/fnins.2019.00335

Bilican, B., Serio, A., Barmada, S. J., Nishimura, A. L., Sullivan, G. J., Carrasco, M., Phatnani, H. P., Puddifoot, C. A., Story, D., Fletcher, J., Park, I.-H., Friedman, B. A., Daley, G. Q., Wyllie, D. J. A., Hardingham, G. E., Wilmut, I., Finkbeiner, S., Maniatis, T., Shaw, C. E., & Chandran, S. (2012). Mutant induced pluripotent stem cell lines recapitulate aspects of TDP-43 proteinopathies and reveal cell-specific vulnerability. *Proceedings of the National Academy of Sciences of the United States of America*, *109*(15), 5803–5808. https://doi.org/10.1073/pnas.1202922109

Birger, A., Ben-Dor, I., Ottolenghi, M., Turetsky, T., Gil, Y., Sweetat, S., Perez, L., Belzer, V., Casden, N., Steiner, D., Izrael, M., Galun, E., Feldman, E., Behar, O., & Reubinoff, B. (2019). Human iPSC-derived astrocytes from ALS patients with mutated C9ORF72 show increased oxidative stress and neurotoxicity. *EBioMedicine*, *50*(1), 274–289.

Birger, R., Kalodimos, C., Inagaki, F., & Tanaka, S. (2009). Crk and CrkL adaptor proteins: networks for physiological and pathological signaling. *Cell Communication and Signaling*, *7*(13).

Blay, J.-Y., Shen, L., Kang, Y.-K., Rutkowski, P., Qin, S., Nosov, D., Wan, D., Trent, J., Srimuninnimit, V., Pápai, Z., Le Cesne, A., Novick, S., Taningco, L., Mo, S., Green, S., Reichardt, P., & Demetri, G. D. (2015). Nilotinib versus imatinib as first-line therapy for patients with unresectable or metastatic gastrointestinal stromal tumours (ENESTg1): a randomised phase 3 trial. *The Lancet. Oncology*, *16*(5), 550–560. https://doi.org/10.1016/S1470-2045(15)70105-1

Blokhuis, A. M., Koppers, M., Groen, E. J. N., van den Heuvel, D. M. A., Dini Modigliani, S., Anink, J. J.,

Fumoto, K., van Diggelen, F., Snelting, A., Sodaar, P., Verheijen, B. M., Demmers, J. A. A., Veldink, J. H., Aronica, E., Bozzoni, I., den Hertog, J., van den Berg, L. H., & Pasterkamp, R. J. (2016). Comparative interactomics analysis of different ALS-associated proteins identifies converging molecular pathways. *Acta Neuropathologica*, *132*(2), 175–196. https://doi.org/10.1007/s00401-016-1575-8

Bogdanov, M., Brown Jr, R., Matson, W., Smart, R., Hayden, D., O'Donnell, H., Beal, M., & Cudkowicz, M. (2000). Increased oxidative damage to DNA in ALS patients. *Free Radical Biology and Medicine*, *29*(7), 652–658.

Boillée, S., Yamanaka, K., Lobsiger, C. S., Copeland, N. G., Jenkins, N. A., Kassiotis, G., Kollias, G., & Cleveland, D. W. (2006). Onset and progression in inherited ALS determined by motor neurons and microglia. *Science*, *312*(5778), 1389–1392. https://doi.org/10.1126/science.1123511

Boivin, M., Pfister, V., Gaucherot, A., Ruffenach, F., Negroni, L., Sellier, C., & Charlet-Berguerand, N. (2020). Reduced autophagy upon C9ORF72 loss synergizes with dipeptide repeat protein toxicity in G4C2 repeat expansion disorders. *The EMBO Journal*, *39*(4), 1–15. https://doi.org/10.15252/embj.2018100574

Borthwick, G., Johnson, M., Ince, P., Shaw, P., & Turnbull, D. (1999). Mitochondrial enzyme activity in amyotrophic lateral sclerosis: implications for the role of mitochondria in neuronal cell death. *Annals of Neurology*, *46*(5), 787–790.

Brady, O. A., Meng, P., Zheng, Y., Mao, Y., & Hu, F. (2011). Regulation of TDP-43 aggregation by phosphorylation andp62/SQSTM1. *Journal of Neurochemistry*, *116*(2), 248–259. https://doi.org/10.1111/j.1471-4159.2010.07098.x

Brettschneider, J., Libon, D. J., Toledo, J. B., Xie, S. X., McCluskey, L., Elman, L., Geser, F., Lee, V. M. Y., Grossman, M., & Trojanowski, J. Q. (2012). Microglial activation and TDP-43 pathology correlate with executive dysfunction in amyotrophic lateral sclerosis. *Acta Neuropathologica*, *123*(3), 395–407. https://doi.org/10.1007/s00401-011-0932-x

Brown, G. C., & Vilalta, A. (2015). How microglia kill neurons. *Brain Research*, *1628*, 288–297. https://doi.org/10.1016/j.brainres.2015.08.031

Brown, R. H., & Al-Chalabi, A. (2017). Amyotrophic Lateral Sclerosis. *New England Journal of Medicine*, *377*(2), 162–172. https://doi.org/10.1056/NEJMra1603471

Bruijn, L., Miller, T., & Cleveland, D. (2004). Unraveling the mechanisms involved in motor neuron degeneration in ALS. *Annual Review of Neuroscience*, *27*(1), 723–749.

Buchthal, B., Weiss, U., & Bading, H. (2018). Post-injury Nose-to-Brain Delivery of Activin A and SerpinB2 Reduces Brain Damage in a Mouse Stroke Model. *Molecular Therapy*, *26*(10), 2357–2365. https://doi.org/10.1016/j.ymthe.2018.07.018

Budini, M., Romano, V., Quadri, Z., Buratti, E., & Baralle, F. (2015). TDP-43 loss of cellular function through aggregation requires additional structural determinants beyond its C-terminal Q/N prion-like domain. *Human Molecular Genetics*, *24*(1), 9–20.

Cai, R., Liu, M., Hu, Y., Melton, B. L., Matheny, M. E., Xu, H., Duan, L., & Waitman, L. R. (2017). Identification of adverse drug-drug interactions through causal association rule discovery from spontaneous adverse event reports. *Artificial Intelligence in Medicine*, *76*, 7–15. https://doi.org/10.1016/j.artmed.2017.01.004

Cascella, R., Fani, G., Capitini, C., Rusmini, P., Poletti, A., Cecchi, C., & Chiti, F. (2017). Quantitative assessment of the degradation of aggregated TDP-43 mediated by the ubiquitin proteasome system and macroautophagy. *FASEB Journal*, *31*(12). https://doi.org/10.1096/fj.201700292RR

Castillo, K., Nassif, M., Valenzuela, V., Rojas, F., Matus, S., Mercado, G., Courtr, F., van Zundert, B., & Hetz, C. (2013). Trehalose delays the progression of amyotrophic lateral sclerosis by enhancing autophagy in motoneurons. *Autophagy*, *9*(9), 1308–1320.

Chang, Y., Kong, Q., Shan, X., Tian, G., Ilieva, H., Clevelad, D., Rothstein, J., Borchelt, D., Wong, P., & Lin, C. (2008). Messenger RNA Oxidation Occurs Early in Disease Pathogenesis and Promotes Motor Neuron Degeneration in ALS. *PLoS ONE*, *3*(8), e2849.

Chao, J., Liu, H., Su, S., Wang, L., Huang, W., & Fan, C. (2014). Structural DNA nanotechnology for intelligent drug delivery. *Small*, *10*(22), 4626–4635. https://doi.org/10.1002/smll.201401309

Che, M. X., Jiang, L. L., Li, H. Y., Jiang, Y. J., & Hu, H. Y. (2015). TDP-35 sequesters TDP-43 into cytoplasmic inclusions through binding with RNA. *FEBS Letters*, *589*(15), 1920–1928. https://doi.org/10.1016/j.febslet.2015.06.009

Chen, H.-J., Anagnostou, G., Chai, A., Withers, J., Morris, A., Adhikaree, J., Pennetta, G., & de Belleroche, J. S. (2010). Characterisation of the properties of a novel mutation in VAPB in familial ALS. *The Journal of Biological Chemistry*.

Chew, J., Gendron, T., Prudencio, M., Sasaguri, H., Zhang, J., Castanedes-Casey, M., Lee, C., Jansen-West, K., Kurti, A., Murray, M., Bieniek, K., O Bauer, P., Whitelaw, E., Rousseau, L., Stankowski, J., Stetler, C., Daughrity, L., Perkerson, E., Desaro, P., … Petrucelli, L. (2015). Neurodegeneration. C9ORF72 repeat expansions in mice cause TDP-43 pathology, neuronal loss, and behavioral deficits. *Science*, *348*(6239), 1151–1154.

Chiang, C. H., Grauffel, C., Wu, L. S., Kuo, P. H., Doudeva, L. G., Lim, C., Shen, C. K. J., & Yuan, H. S. (2016). Structural analysis of disease-related TDP-43 D169G mutation: Linking enhanced stability and caspase cleavage efficiency to protein accumulation. *Scientific Reports*, *6*(September 2015), 1–14. https://doi.org/10.1038/srep21581

Chitiprolu, M., Jagow, C., Tremblay, V., Bondy-Chorney, E., Paris, G., Savard, A., Palidwor, G., Barry, F. A., Zinman, L., Keith, J., Rogaeva, E., Robertson, J., Lavallée-Adam, M., Woulfe, J., Couture, J. F., Côté, J., & Gibbings, D. (2018). A complex of C9ORF72 and p62 uses arginine methylation to eliminate stress granules by autophagy. *Nature Communications*, *9*(1). https://doi.org/10.1038/s41467-018-05273-7

Chow, C. Y., Landers, J. E., Bergren, S. K., Sapp, P. C., Grant, A. E., Jones, J. M., Everett, L., Lenk, G. M., McKenna-Yasek, D. M., Weisman, L. S., Figlewicz, D., Brown, R. H., & Meisler, M. H. (2009). Deleterious Variants of FIG4, a Phosphoinositide Phosphatase, in Patients with ALS. *American Journal of Human Genetics*. https://doi.org/10.1016/j.ajhg.2008.12.010

Cicardi, M. E., Cristofani, R., Rusmini, P., Meroni, M., Ferrari, V., Vezzoli, G., Tedesco, B., Piccolella, M., Messi, E., Galbiati, M., Boncoraglio, A., Carra, S., Crippa, V., & Poletti, A. (2018). Tdp-25 Routing to Autophagy and Proteasome Ameliorates its Aggregation in Amyotrophic Lateral Sclerosis Target Cells. *Scientific Reports*, *8*(1), 1–16. https://doi.org/10.1038/s41598-018-29658-2

Cirillo, D., Agostini, F., Klus, P., Marchese, D., Rodriguez, S., Bolognesi, B., & Tartaglia, G. G. (2013). Neurodegenerative diseases : Quantitative predictions of protein – RNA interactions. *Bioinformatics*, 129–140. https://doi.org/10.1261/rna.034777.112.4

Clark, K. C., Josephson, A., Benusa, S. D., Hartley, R. K., Baer, M., Thummala, S., Joslyn, M., Sword, B. A., Elford, H., Oh, U., Dilsizoglu-Senol, A., Lubetzki, C., Davenne, M., DeVries, G. H., & Dupree, J. L. (2016). Compromised axon initial segment integrity in EAE is preceded by microglial reactivity and contact. *Glia*, *64*(7), 1190–1209. https://doi.org/10.1002/glia.22991

Clarke, P. A., te Poele, R., Wooster, R., & Workman, P. (2001). Gene expression microarray analysis in cancer biology, pharmacology, and drug development: progress and potential. *Biochemical Pharmacology*, *62*(10), 1311–1336. https://doi.org/10.1016/s0006-2952(01)00785-7

Clement, A. M., Nguyen, M. D., Roberts, E. A., Garcia, M. L., Boillée, S., Rule, M., McMahon, A. P., Doucette, W., Siwek, D., Ferrante, R. J., Brown, R. H., Julien, J. P., Goldstein, L. S. B., & Cleveland, D. W. (2003). Wild-type nonneuronal cells extend survival of SOD1 mutant motor neurons in ALS mice. *Science*, *302*(5642), 113–117. https://doi.org/10.1126/science.1086071

Conlon, E. G., Lu, L., Sharma, A., Yamazaki, T., Tang, T., Shneider, N. A., & Manley, J. L. (2016). The C9ORF72 GGGGCC expansion forms RNA G-quadruplex inclusions and sequesters hnRNP H to disrupt splicing in ALS brains. *ELife*, *5*(September2016), 1–28. https://doi.org/10.7554/eLife.17820

Correia, A. S., Patel, P., Dutta, K., & Julien, J. P. (2015). Inflammation induces TDP-43 mislocalization and aggregation. *PLoS ONE*, *10*(10), 1–19. https://doi.org/10.1371/journal.pone.0140248

Couratier, P., Corcia, P., Lautrette, G., Nicol, M., & Marin, B. (2017). ALS and frontotemporal dementia belong to a common disease spectrum. *Revue Neurologique*, *173*(5), 273–279. https://doi.org/10.1016/j.neurol.2017.04.001

Cox, L. E., Ferraiuolo, L., Goodall, E. F., Heath, P. R., Higginbottom, A., Mortiboys, H., Hollinger, H. C., Hartley, J. A., Brockington, A., Burness, C. E., Morrison, K. E., Wharton, S. B., Grierson, A. J., Ince, P. G., Kirby, J., & Shaw, P. J. (2010). Mutations in CHMP2B in lower motor neuron predominant amyotrophic lateral sclerosis (ALS). *PLoS ONE*. https://doi.org/10.1371/journal.pone.0009872

Crippa, V., Boncoraglio, A., Galbiati, M., Aggarwal, T., Rusmini, P., Giorgetti, E., Cristofani, R., Carra, S., Pennuto, M., & Poletti, A. (2013). Differential autophagy power in the spinal cord and muscle of transgenic ALS mice. *Frontiers in Cellular Neuroscience*, *7*(NOV), 1–12. https://doi.org/10.3389/fncel.2013.00234

Cummings, J. (2018). Lessons learned from Alzheimer disease: clinical trials with negative outcomes. *Clinical and Translational Science*, *11*(2), 147–152. https://doi.org/10.1111/cts.12491

Cummings, J. L., Morstorf, T., & Zhong, K. (2014). Alzheimer's disease drug-development pipeline: few candidates, frequent failures. *Alzheimer's Research & Therapy*, *6*(37), 1–7.

Cykowski, M. D., Powell, S. Z., Peterson, L. E., Appel, J. W., Rivera, A. L., Takei, H., Chang, E., & Appel, S. H. (2017). Clinical significance of TDP-43 neuropathology in amyotrophic lateral sclerosis. *Journal of Neuropathology and Experimental Neurology*, *76*(5), 402–413. https://doi.org/10.1093/jnen/nlx025

Dafinca, R., Scaber, J., Ababneh, N., Lalic, T., Weir, G., Christian, H., Vowles, J., Douglas, A. G. L., Fletcher-Jones, A., Browne, C., Nakanishi, M., Turner, M. R., Wade-Martins, R., Cowley, S. A., & Talbot, K. (2016). C9orf72 Hexanucleotide Expansions Are Associated with Altered Endoplasmic Reticulum Calcium Homeostasis and Stress Granule Formation in Induced Pluripotent Stem Cell-Derived Neurons from Patients with Amyotrophic Lateral Sclerosis and Frontotemporal Demen. *Stem Cells*, *34*(8), 2063–2078. https://doi.org/10.1002/stem.2388

Dardis, A., Zampieri, S., Canterini, S., Newell, K. L., Stuani, C., Murrell, J. R., Ghetti, B., Fiorenza, M. T., Bembi, B., & Buratti, E. (2016). Altered localization and functionality of TAR DNA Binding Protein 43 (TDP-43) in niemann- pick disease type C. *Acta Neuropathologica Communications*, *4*(1), 52. https://doi.org/10.1186/s40478-016-0325-4

De Vos, K., Chapman, A., Tennant, M., Manser, C., Tudor, E., Lau, K., Brownlees, J., Ackerley, S., Shaw, P., McLoughlin, D., Shaw, C., Leigh, P., Miller, C., & Grierson, A. (2007). Familial amyotrophic lateral sclerosis-linked SOD1 mutants perturb fast axonal transport to reduce axonal mitochondria content. *Human Molecular Genetics*, *16*(22), 2720–2728.

Deerlin, V. M. Van, Leverenz, J. B., Bekris, L. M., Bird, T. D., Yuan, W., Elman, L. B., Clay, D., Wood, E. M., Chen-plotkin, A. S., Martinez-lage, M., Steinbart, E., Mccluskey, L., Grossman, M., Neumann, M., Wu, I., Yang, W., Kalb, R., Galasko, D. R., Montine, T. J., … Yu, C. (2008). TARDBP mutations in amyotrophic lateral sclerosis with TDP-43 neuropathology : a genetic and histopathological analysis. *Lancet Neurology*, *7*(1), 409–416. https://doi.org/10.1016/S1474-4422(08)70071-1

DeJesus-Hernandez, M., Mackenzie, I. R., Boeve, B. F., Boxer, A. L., Baker, M., Rutherford, N. J., Nicholson, A. M., Finch, N. C. A., Flynn, H., Adamson, J., Kouri, N., Wojtas, A., Sengdy, P., Hsiung, G. Y. R., Karydas, A., Seeley, W. W., Josephs, K. A., Coppola, G., Geschwind, D. H., … Rademakers, R. (2011). Expanded GGGGCC Hexanucleotide Repeat in Noncoding Region of C9ORF72 Causes Chromosome 9p-Linked FTD and ALS. *Neuron*, *72*(2), 245–256. https://doi.org/10.1016/j.neuron.2011.09.011

Deng, H. X., Chen, W., Hong, S. T., Boycott, K. M., Gorrie, G. H., Siddique, N., Yang, Y., Fecto, F., Shi,

Y., Zhai, H., Jiang, H., Hirano, M., Rampersaud, E., Jansen, G. H., Donkervoort, S., Bigio, E. H., Brooks, B. R., Ajroud, K., Sufit, R. L., … Siddique, T. (2011). Mutations in UBQLN2 cause dominant X-linked juvenile and adult-onset ALS and ALS/dementia. *Nature*. https://doi.org/10.1038/nature10353

Deng, J., Yang, M., Chen, Y., Chen, X., Liu, J., Sun, S., Cheng, H., Li, Y., Bigio, E., Mesulam, M., Xu, Q., Du, S., Fushimi, K., Zhu, L., & Wu, J. (2015). FUS interacts with HSP60 to promote mitochondrial damage. *PLoS Genetics*, *11*(1), e1005357.

Di Giorgio, F. P., Carrasco, M. A., Siao, M. C., Maniatis, T., & Eggan, K. (2007). Non-cell autonomous effect of glia on motor neurons in an embryonic stem cell-based ALS model. *Nature Neuroscience*, *10*(5), 608–614. https://doi.org/10.1038/nn1885

Dimos, J. T., Rodolfa, K. T., Niakan, K. K., Weisenthal, L. M., Mitsumoto, H., Chung, W., Croft, G. F., Saphier, G., Leibel, R., Goland, R., Wichterle, H., Henderson, C. E., & Eggan, K. (2008). Induced pluripotent stem cells generated from patients with ALS can be differentiated into motor neurons. *Science (New York, N.Y.)*, *321*(5893), 1218–1221. https://doi.org/10.1126/science.1158799

Ding, W., & Yin, X. (2012). Mitophagy: mechanisms, pathophysiological roles, and analysis. *Biological Chemistry*, *383*(7), 547–564.

Donnelly, C. J., Zhang, P. W., Pham, J. T., Heusler, A. R., Mistry, N. A., Vidensky, S., Daley, E. L., Poth, E. M., Hoover, B., Fines, D. M., Maragakis, N., Tienari, P. J., Petrucelli, L., Traynor, B. J., Wang, J., Rigo, F., Bennett, C. F., Blackshaw, S., Sattler, R., & Rothstein, J. D. (2013). RNA Toxicity from the ALS/FTD C9ORF72 Expansion Is Mitigated by Antisense Intervention. *Neuron*, *80*(2), 415–428. https://doi.org/10.1016/j.neuron.2013.10.015

Drachman, D. B., Frank, K., Dykes-Hoberg, M., Teismann, P., Almer, G., Przedborski, S., & Rothstein, J. D. (2002). Cyclooxygenase 2 inhibition protects motor neurons and prolongs survival in a transgenic mouse model of ALS. *Annals of Neurology*, *52*(6), 771–778. https://doi.org/10.1002/ana.10374

Dragowska, W. H., Weppler, S. A., Wang, J. C., Wong, L. Y., Kapanen, A. I., Rawji, J. S., Warburton, C., Qadir, M. A., Donohue, E., Roberge, M., Gorski, S. M., Gelmon, K. A., & Bally, M. B. (2013). Induction of autophagy is an early response to gefitinib and a potential therapeutic target in breast cancer. *PloS One*, *8*(10), e76503. https://doi.org/10.1371/journal.pone.0076503

Ebstein, S. Y., Yagudayeva, I., & Shneider, N. A. (2019). Mutant TDP-43 Causes Early-Stage Dose-Dependent Motor Neuron Degeneration in a TARDBP Knockin Mouse Model of ALS. *Cell Reports*, *26*(2), 364-373.e4. https://doi.org/10.1016/j.celrep.2018.12.045

Elden, A. C., Kim, H.-J., Hart, M. P., Chen-Plotkin, A. S., Johnson, B. S., Fang, X., Armakola, M., Geser, F., Greene, R., Lu, M. M., Padmanabhan, A., Clay-Falcone, D., McCluskey, L., Elman, L., Juhr, D., Gruber, P. J., Rüb, U., Auburger, G., Trojanowski, J. Q., … Gitler, A. D. (2010). Ataxin-2 intermediate-length polyglutamine expansions are associated with increased risk for ALS. *Nature*, *466*(7310), 1069–1075. https://doi.org/10.1038/nature09320

Estrada, L. D., Chamorro, D., Yañez, M. J., Gonzalez, M., Leal, N., Von Bernhardi, R., Dulcey, A. E., Marugan, J., Ferrer, M., Soto, C., Zanlungo, S., Inestrosa, N. C., & Alvarez, A. R. (2016). Reduction of Blood Amyloid-β Oligomers in Alzheimer's Disease Transgenic Mice by c-Abl Kinase Inhibition. *Journal of Alzheimer's Disease*, *54*(3), 1193–1205. https://doi.org/10.3233/JAD-151087

Farg, M. A., Sundaramoorthy, V., Sultana, J. M., Yang, S., Atkinson, R. A. K., Levina, V., Halloran, M. A., Gleeson, P. A., Blair, I. P., Soo, K. Y., King, A. E., & Atkin, J. D. (2014). C9ORF72, implicated in amytrophic lateral sclerosis and frontotemporal dementia, regulates endosomal trafficking. *Human Molecular Genetics*, *23*(13), 3579–3595. https://doi.org/10.1093/hmg/ddu068

Farrawell, N. E., Lambert-smith, I. A., Warraich, S. T., Blair, I. P., Saunders, D. N., Hatters, D. M., & Yerbury, J. J. (2010). Distinct partitioning of ALS associated TDP-43 , FUS and SOD1 mutants into cellular inclusions. *Nature Publishing Group*, 1–14. https://doi.org/10.1038/srep13416

Fecto, F., Yan, J., Vemula, S. P., Liu, E., Yang, Y., Chen, W., Zheng, J. G., Shi, Y., Siddique, N., Arrat, H., Donkervoort, S., Ajroud-Driss, S., Sufit, R. L., Heller, S. L., Deng, H. X., & Siddique, T. (2011). SQSTM1 mutations in familial and sporadic amyotrophic lateral sclerosis. *Archives of Neurology*. https://doi.org/10.1001/archneurol.2011.250

Felbecker, A., Camu, W., Valdmanis, P., Sperfeld, A., Waibel, S., Rouleau, G., Ludolph, A., & Andersen, P. (2010). Four familial ALS pedigrees discordant for two SOD1 mutations: are all SOD1 mutations pathogenic? *Journal of Neurology, Neurosurgery, and Psychiatry*, *81*(5), 572–577.

Ferraiuolo, L, Kirby, J., Grierson, A. J., Sendtner, M., & Shaw, P. J. (2011). Molecular pathways of motor neuron injury in amyotrophic lateral sclerosis. *Nature Reviews. Neurology*, *7*(11), 616–

630. https://doi.org/10.1038/nrneurol.2011.152

Ferraiuolo, Laura, Heath, P. R., Holden, H., Kasher, P., Kirby, J., & Shaw, P. J. (2007). Microarray analysis of the cellular pathways involved in the adaptation to and progression of motor neuron injury in the SOD1 G93A mouse model of familial ALS. *The Journal of Neuroscience : The Official Journal of the Society for Neuroscience*, *27*(34), 9201–9219. https://doi.org/10.1523/JNEUROSCI.1470-07.2007

Ferraiuolo, Laura, Meyer, K., Sherwood, T. W., Vick, J., Likhite, S., Frakes, A., Miranda, C. J., Braun, L., Heath, P. R., Pineda, R., Beattie, C. E., Shaw, P. J., Askwith, C. C., McTigue, D., & Kaspar, B. K. (2016). Oligodendrocytes contribute to motor neuron death in ALS via SOD1-dependent mechanism. *Proceedings of the National Academy of Sciences of the United States of America*, *113*(42), E6496–E6505. https://doi.org/10.1073/pnas.1607496113

Ferri, A., Cozzolino, M., Crosio, C., Nencini, M., Cascati, A., Butler Gralla, E., Rotilio, G., Selverstone Valentine, J., & Carri, M. (2006). Familial ALS-superoxide dismutases associate with mitochondria and shift their redox potentials. *PNAS*, *103*(37), 13860–13865.

Ferri, A., Fiorenzo, P., Nencini, M., Cozzolino, M., Pesaresi, M., Valle, C., Sepe, S., Moreno, S., & Carri, M. (2010). Increased reactive oxygen species in familial amyotrophic lateral sclerosis with mutations in SOD1. *Human Molecular Genetics*, *19*(22), 4529–4542.

Fouad, M. A., & Elkady, E. F. (2014). Forced degradation study and validated stability-indicating RP-LC method for determination of nilotinib in bulk and capsules. *Acta Chromatographica*, *26*(4), 637–647. https://doi.org/10.1556/AChrom.26.2014.4.6

Frakes, A. E., Braun, L., Ferraiuolo, L., Guttridge, D. C., & Kaspar, B. K. (2017). Additive amelioration of ALS by co-targeting independent pathogenic mechanisms. *Annals of Clinical and Translational Neurology*, *4*(2), 76–86. https://doi.org/10.1002/acn3.375

Frakes, A. E., Ferraiuolo, L., Haidet-Phillips, A. M., Schmelzer, L., Braun, L., Miranda, C. J., Ladner, K. J., Bevan, A. K., Foust, K. D., Godbout, J. P., Popovich, P. G., Guttridge, D. C., & Kaspar, B. K. (2014). Microglia induce motor neuron death via the classical NF-κB pathway in amyotrophic lateral sclerosis. *Neuron*, *81*(5), 1009–1023. https://doi.org/10.1016/j.neuron.2014.01.013

Freibaum, B. D., & Taylor, J. P. (2017). The role of dipeptide repeats in C9ORF72-related ALS-FTD. *Frontiers in Molecular Neuroscience*, *10*(February), 1–9. https://doi.org/10.3389/fnmol.2017.00035

Freischmidt, A., Moeller, K., Zondler, L., Weydt, P., Mayer, B., von Arnim, C. A. F., H??bers, A., Dorst, J., Otto, M., Holzmann, K., Ludolph, A. C., Danzer, K. M., & Weishaupt, J. H. (2015). Serum microRNAs in sporadic amyotrophic lateral sclerosis. *Neurobiology of Aging*, *36*(9), 2660.e15-2660.e20. https://doi.org/10.1016/j.neurobiolaging.2015.06.003

Freischmidt, A., Wieland, T., Richter, B., Ruf, W., Schaeffer, V., Müller, K., Marroquin, N., Nordin, F., Hübers, A., Weydt, P., Pinto, S., Press, R., Millecamps, S., Molko, N., Bernard, E., Desnuelle, C., Soriani, M.-H., Dorst, J., Graf, E., … Weishaupt, J. H. (2015). Haploinsufficiency of TBK1 causes familial ALS and fronto-temporal dementia. *Nature Neuroscience*, *18*(5), 631–636. https://doi.org/10.1038/nn.4000

Furukawa, Y., Kaneko, K., & Nukina, N. (2011). Molecular properties of TAR DNA binding protein-43 fragments are dependent upon its cleavage site. *Biochimica et Biophysica Acta - Molecular Basis of Disease*, *1812*(12), 1577–1583. https://doi.org/10.1016/j.bbadis.2011.09.005

Garcia-Vaquero, M., Gama-Carvalho, M., De Las Rivas, J., & Pinto, F. (2018). Searching the overlap between network modules with specific betweeness (S2B) and its application to cross-disease analysis. *Scientific Reports*, *8*(1), 1–10. https://doi.org/10.1038/s41598-018-29990-7

Gasset-Rosa, F., Lu, S., Yu, H., C, C., Melamed, Z., Guo, L., Shorter, J., Da Cruz, S., & Cleveland, D. W. (2019). Cytoplasmic TDP-43 De-mixing Independent of Stress Granules Drives Inhibition of Nuclear Import, Loss of Nuclear TDP-43, and Cell Death. *Neuron*, *102*(2), 339–357.

Gatto, N., Dos Santos Souza, C., Shaw, A., Bell, S., Myszczynska, M., Powers, S., Meyer, K., Castelli, L., Karyka, E., Mortiboys, H., Azzouz, M., Hautbergue, G., Markus, N., Shaw, P., & Ferraiuolo, L. (2021). Directly converted astrocytes retain the ageing features of the donor fibroblasts and elucidate the astrocytic contribution to human CNS health and disease. *Ageing Cell*, *20*(1), e13281.

Ge, P., Dawson, V. L., & Dawson, T. M. (2020). PINK1 and Parkin mitochondrial quality control: a source of regional vulnerability in Parkinson's disease. *Molecular Neurodegeneration*, *15*(1), 20. https://doi.org/10.1186/s13024-020-00367-7

Gendron, T., Bieniek, K., Zhang, Y., Jansen-West, K., Ash, P., Caulfield, T., Daughrity, L., Dunmore, J., Castanedes-Casey, M., Chew, J., Cosio, D., van Blitterswijk, M., Lee, W., Rademakers, R., Boylan, K., Dickson, D., & Petrucelli, L. (2013). Antisense transcripts of the expanded C9ORF72 hexanucleotide repeat form nuclear RNA foci and undergo repeat-associated non-ATG

translation in c9FTD/ALS. *Acta Neuropathologica*, *126*(6), 829–844.

Genin, E., Plutino, M., Bannwarth, S., Villa, E., Cisneros-Barroso, E., Roy, M., Ortega-Vila, B., Fragaki, K., Lespinasse, F., Pinero-Martos, E., Augé, G., Moore, D., Burté, F., Lacas-Gervais, S., Kageyama, Y., Itoh, K., Yu-Wai-Man, P., Sesaki, H., Ricci, J., … Paquis-Flucklinger, V. (2016). CHCHD10 mutations promote loss of mitochondrial cristae junctions with impaired mitochondrial genome maintenance and inhibition of apoptosis. *EMBO Molecular Medicine*, *8*(1), 58–72.

Geser, F., Robinson, J. L., Malunda, J. A., Moore, E. M., Deerlin, V. M. Van, & Lee, V. M. (2011). Pathological 43-kDa Transactivation Response DNA-Binding Protein in Older Adults With and Without Severe Mental Illness. *Pathology*, *67*(10), 1238–1250. https://doi.org/10.1001/archneurol.2010.254.Pathological

Gitcho, M. a, Baloh, R. H., Chakraverty, S., Norton, J. B., Levitch, D., Hatanpaa, K. J., Iii, C. L. W., Bigio, E. H., Caselli, R., Baker, M., Al-lozi, M. T., Morris, J. C., Pestronk, A., Goate, A. M., & Cairns, N. J. (2009). TDP-43 A315T Mutation in Familial Motor Neuron Disease Michael. *Neuron*, *63*(4), 535–538. https://doi.org/10.1002/ana.21344.TDP-43

Gkogkas, C., Middleton, S., Kremer, A. M., Wardrope, C., Hannah, M., Gillingwater, T. H., & Skehel, P. (2008). VAPB interacts with and modulates the activity of ATF6. *Human Molecular Genetics*. https://doi.org/10.1093/hmg/ddn040

Gong, L., Gong, H., Pan, X., Chang, C., Ou, Z., Ye, S., Yin, L., Yang, L., Tao, T., Zhang, Z., Liu, C., Lane, D., Peng, J., & Chen, J. (2015). p53 isoform Δ113p53/Δ133p53 promotes DNA double-strand break repair to protect cell from death and senescence in response to DNA damage. *Cell Research*, *25*(3), 351–369.

Gordon, P. H., & Meininger, V. (2011). How can we improve clinical trials in amyotrophic lateral sclerosis ? *Nature Reviews Neurology*, *7*(11), 650–654. https://doi.org/10.1038/nrneurol.2011.147

Gottlieb, A., Stein, G. Y., Ruppin, E., & Sharan, R. (2011). PREDICT: A method for inferring novel drug indications with application to personalized medicine. *Molecular Systems Biology*, *7*(496), 1–9. https://doi.org/10.1038/msb.2011.26

Green, K. M., Glineburg, M. R., Kearse, M. G., Flores, B. N., Linsalata, A. E., Fedak, S. J., Goldstrohm, A. C., Barmada, S. J., & Todd, P. K. (2017). RAN translation at C9orf72-associated repeat

expansions is selectively enhanced by the integrated stress response. *Nature Communications*, *8*(1). https://doi.org/10.1038/s41467-017-02200-0

Greenway, M. J., Andersen, P. M., Russ, G., Ennis, S., Cashman, S., Donaghy, C., Patterson, V., Swingler, R., Kieran, D., Prehn, J., Morrison, K. E., Green, A., Acharya, K. R., Brown, R. H., & Hardiman, O. (2006). ANG mutations segregate with familial and "sporadic" amyotrophic lateral sclerosis. *Nature Genetics*. https://doi.org/10.1038/ng1742

Gu, J., Chen, F., Iqbal, K., Gong, C. X., Wang, X., & Liu, F. (2017). Transactive response DNA-binding protein 43 (TDP-43) regulates alternative splicing of tau exon 10: Implications for the pathogenesis of tauopathies. *Journal of Biological Chemistry*, *292*(25), 10600–10612. https://doi.org/10.1074/jbc.M117.783498

Guilbert, S. M., Lambert, H., Rodrigue, M. A., Fuchs, M., Landry, J., & Lavoie, J. N. (2018). Hspb8 and bag3 cooperate to promote spatial sequestration of ubiquitinated proteins and coordinate the cellular adaptive response to proteasome insufficiency. *FASEB Journal*, *32*(7), 3518–3535. https://doi.org/10.1096/fj.201700558RR

Hadano, S, Hand, C. K., Osuga, H., Yanagisawa, Y., Otomo, a, Devon, R. S., Miyamoto, N., Showguchi-Miyata, J., Okada, Y., Singaraja, R., Figlewicz, D. a, Kwiatkowski, T., Hosler, B. a, Sagie, T., Skaug, J., Nasir, J., Brown, R. H., Scherer, S. W., Rouleau, G. a, … Ikeda, J. E. (2001). A gene encoding a putative GTPase regulator is mutated in familial amyotrophic lateral sclerosis 2. *Nature Genetics*, *29*(october), 166–173. https://doi.org/10.1038/ng1001-166

Hadano, Shinji, Otomo, A., Kunita, R., Suzuki-Utsunomiya, K., Akatsuka, A., Koike, M., Aoki, M., Uchiyama, Y., Itoyama, Y., & Ikeda, J. E. (2010). Loss of ALS2/Alsin exacerbates motor dysfunction in a SOD1H46R-expressing mouse ALS model by disturbing endolysosomal trafficking. *PLoS ONE*. https://doi.org/10.1371/journal.pone.0009805

Han, W., Pan, H., Chen, Y., Sun, J., Wang, Y., Li, J., Ge, W., Feng, L., Lin, X., Wang, X., Wang, X., & Jin, H. (2011). EGFR tyrosine kinase inhibitors activate autophagy as a cytoprotective response in human lung cancer cells. *PloS One*, *6*(6), e18691. https://doi.org/10.1371/journal.pone.0018691

Hansch, C., Maloney, P., Fujita, T., & Muir, R. (1962). Correlation of Biological Activity of Phenoxyacetic Acids with Hammett Substituent Constants and Partition Coefficients. *Nature*, *194*, 178–180.

Hansen, T. E., & Johansen, T. (2011). Following autophagy step by step. *BMC Biology*, *9*, 2–5. https://doi.org/10.1186/1741-7007-9-39

Hanspal, M. A., Dobson, C. M., Yerbury, J. J., & Kumita, J. R. (2017). The relevance of contact-independent cell-to-cell transfer of TDP-43 and SOD1 in amyotrophic lateral sclerosis. *Biochimica et Biophysica Acta - Molecular Basis of Disease*, *1863*(11), 2762–2771. https://doi.org/10.1016/j.bbadis.2017.07.007

Hardiman, O., & van den Berg, L. H. (2017). Edaravone: a new treatment for ALS on the horizon? *The Lancet Neurology*, *16*(7), 490–491.

Harraz, M., Marden, J., Zhou, W., Zhang, Y., Williams, A., Sharov, V., Nelson, K., Luo, M., Paulson, H., Schoeneich, C., & Engelhardt, J. (2008). SOD1 mutations disrupt redox-sensitive Rac regulation of NADPH oxidase in a familial ALS model. *Journal of Clinical Investigations*, *118*(2), 659–670.

Harrison, A. F., & Shorter, J. (2017). RNA-binding proteins with prion-like domains in health and disease. *Biochemical Journal*, *474*(8), 1417–1438. https://doi.org/10.1042/BCJ20160499

Harrison, R. K. (2016). Phase II and phase III failures: 2013-2015. *Nature Reviews Drug Discovery*, *15*(12), 817–818. https://doi.org/10.1038/nrd.2016.184

Hebron, M. L., Lonskaya, I., & Moussa, C. E. H. (2013). Nilotinib reverses loss of dopamine neurons and improvesmotorbehavior via autophagic degradation of α-synuclein in parkinson's disease models. *Human Molecular Genetics*, *22*(16), 3315–3328. https://doi.org/10.1093/hmg/ddt192

Hester, M. E., Murtha, M. J., Song, S., Rao, M., Miranda, C. J., Meyer, K., Tian, J., Boulting, G., Schaffer, D. V., Zhu, M. X., Pfaff, S. L., Gage, F. H., & Kaspar, B. K. (2011). Rapid and efficient generation of functional motor neurons from human pluripotent stem cells using gene delivered transcription factor codes. *Molecular Therapy*, *19*(10), 1905–1912. https://doi.org/10.1038/mt.2011.135

Heyburn, L., Hebron, M. L., Smith, J., Winston, C., Bechara, J., Li, Z., Lonskaya, I., Burns, M. P., Harris, B. T., & Moussa, C. E. H. (2016). Tyrosine kinase inhibition reverses TDP-43 effects on synaptic protein expression, astrocytic function and amino acid dis-homeostasis. *Journal of Neurochemistry*, *139*(4), 610–623. https://doi.org/10.1111/jnc.13763

Hicks, D. A., Cross, L. L., Williamson, R., & Rattray, M. (2020a). Endoplasmic Reticulum Stress Signalling Induces Casein Kinase 1-Dependent Formation of Cytosolic TDP-43 Inclusions in

Motor Neuron-Like Cells. *Neurochemical Research*, *45*(6), 1354–1364. https://doi.org/10.1007/s11064-019-02832-2

Hicks, D. A., Cross, L. L., Williamson, R., & Rattray, M. (2020b). Endoplasmic Reticulum Stress Signalling Induces Casein Kinase 1-Dependent Formation of Cytosolic TDP-43 Inclusions in Motor Neuron-Like Cells. *Neurochemical Research*, *45*(6), 1354–1364. https://doi.org/10.1007/s11064-019-02832-2

Highley, J. R., Kirby, J., Jansweijer, J. A., Webb, P. S., Hewamadduma, C. A., Heath, P. R., Higginbottom, A., Raman, R., Ferraiuolo, L., Cooper-Knock, J., Mcdermott, C. J., Wharton, S. B., Shaw, P. J., & Ince, P. G. (2014). Loss of nuclear TDP-43 in amyotrophic lateral sclerosis (ALS) causes altered expression of splicing machinery and widespread dysregulation of RNA splicing in motor neurones. *Neuropathology and Applied Neurobiology*, *40*(6), 670–685. https://doi.org/10.1111/nan.12148

Hu, J., Zhang, Y., Jiang, X., Zhang, H., Gao, Z., Li, Y., Fu, R., Li, L., Li, J., Cui, H., & Gao, N. (2019). ROS-mediated activation and mitochondrial translocation of CaMKII contributes to Drp1-dependent mitochondrial fission and apoptosis in triple-negative breast cancer cells by isorhamnetin and chloroquine. *Journal of Experimental and Clinical Cancer Research*, *38*(1), 1–16. https://doi.org/10.1186/s13046-019-1201-4

Hutten, S., Usluer, S., Bourgeois, B., Simonetti, F., Odeh, H. M., Fare, C. M., Czuppa, M., Hruska-Plochan, M., Hofweber, M., Polymenidou, M., Shorter, J., Edbauer, D., Madl, T., & Dormann, D. (2020). Nuclear Import Receptors Directly Bind to Arginine-Rich Dipeptide Repeat Proteins and Suppress Their Pathological Interactions. *Cell Reports*, *33*(12), 108538. https://doi.org/10.1016/j.celrep.2020.108538

Iguchi, Y., Katsuno, M., Niwa, J. I., Takagi, S., Ishigaki, S., Ikenaka, K., Kawai, K., Watanabe, H., Yamanaka, K., Takahashi, R., Misawa, H., Sasaki, S., Tanaka, F., & Sobue, G. (2013). Loss of TDP-43 causes age-dependent progressive motor neuron degeneration. *Brain*, *136*(5), 1371–1382. https://doi.org/10.1093/brain/awt029

Imamura, K., Izumi, Y., Watanabe, A., Tsukita, K., Woltjen, K., Yamamoto, T., Hotta, A., Kondo, T., Kitaoka, S., Ohta, A., Tanaka, A., Watanabe, D., Morita, M., Takuma, H., Tamaoka, A., & Kunath, T. (2017). The Src / c-Abl pathway is a potential therapeutic target in amyotrophic lateral sclerosis. *Science Translational Medicine*, *9*(1), 1–11.

Israelson, A., Arbel, N., Da Cruz, S., Ilieva, H., Yamanaka, K., Shoshan-Barmatz, V., & Cleveland, D. (2010). Misfolded mutant SOD1 directly inhibits VDAC1 conductance in a mouse model of inherited ALS. *Neuron*, *67*(4), 575–587.

Issa, N. T., Kruger, J., Wathieu, H., Raja, R., Byers, S. W., & Dakshanamurthy, S. (2016). DrugGenEx-Net: A novel computational platform for systems pharmacology and gene expression-based drug repurposing. *BMC Bioinformatics*, *17*(1), 1–18. https://doi.org/10.1186/s12859-016-1065-y

Iyer, S., Subramanian, V., & Acharya, K. (2018). C9orf72, a protein associated with amyotrophic lateral sclerosis (ALS) is a guanine nucleotide exchange factor. *PeerJ*, *6*(1), e5815.

Jaiswal, M. K. (2019). Riluzole and edaravone: A tale of two amyotrophic lateral sclerosis drugs. *Medicinal Research Reviews*, *39*(2), 733–748. https://doi.org/10.1002/med.21528

Ji, Y. J., Ugolino, J., Brady, N. R., Hamacher-Brady, A., & Wang, J. (2017). Systemic deregulation of autophagy upon loss of ALS- and FTD-linked C9orf72. *Autophagy*, *13*(7), 1254–1255. https://doi.org/10.1080/15548627.2017.1299312

Jiang, J., Zhu, Q., Gendron, T., Saberi, S., McAlonis-Downes, M., Seelman, A., Stauffer, J., Jafar-Nejad, P., Drenner, K., Schulte, D., Chun, S., Sun, S., Ling, S., Myers, B., Engelhardt, J., Katz, M., Baughn, M., Platoshyn, O., Marsala, M., … Lagier-Tourenne, C. (2016). Gain of toxicity from ALS/FTD-linked repeat expansions in C9ORF72 is alleviated by antisense oligonucleotides targeting GGGGCC-containing RNAs. *Neuron*, *90*(3), 535–550.

Johnson, J. O., Glynn, S. M., Raphael Gibbs, J., Nalls, M. A., Sabatelli, M., Restagno, G., Drory, V. E., Chiò, A., Rogaeva, E., & Traynor, B. J. (2014). Mutations in the CHCHD10 gene are a common cause of familial amyotrophic lateral sclerosis. In *Brain*. https://doi.org/10.1093/brain/awu265

Johnson, J. O., Mandrioli, J., Benatar, M., Abramzon, Y., Van Deerlin, V. M., Trojanowski, J. Q., Gibbs, J. R., Brunetti, M., Gronka, S., Wuu, J., Ding, J., McCluskey, L., Martinez-Lage, M., Falcone, D., Hernandez, D. G., Arepalli, S., Chong, S., Schymick, J. C., Rothstein, J., … Traynor, B. J. (2010). Exome Sequencing Reveals VCP Mutations as a Cause of Familial ALS. *Neuron*. https://doi.org/10.1016/j.neuron.2010.11.036

Johnson, J. O., Pioro, E. P., Boehringer, A., Chia, R., Feit, H., Renton, A. E., Pliner, H. A., Abramzon, Y., Marangi, G., Winborn, B. J., Gibbs, J. R., Nalls, M. A., Morgan, S., Shoai, M., Hardy, J., Pittman, A., Orrell, R. W., Malaspina, A., Sidle, K. C., … Pirisi, A. (2014). Mutations in the Matrin 3 gene

cause familial amyotrophic lateral sclerosis. *Nature Neuroscience*. https://doi.org/10.1038/nn.3688

Johnston, C. A., Stanton, B. R., Turner, M. R., Gray, R., Blunt, A. H. M., Butt, D., Ampong, M. A., Shaw, C. E., Leigh, P. N., & Al-Chalabi, A. (2006). Amyotrophic lateral sclerosis in an urban setting: A population based study of inner city London. *Journal of Neurology*, *253*(12), 1642–1643. https://doi.org/10.1007/s00415-006-0195-y

Johnston, J. A., Ward, C. L., & Kopito, R. R. (2012). Aggresomes: A Cellular Response to Misfolded Proteins. *Cell*, *143*(7), 1883–1898. http://www.jcb.org

Johri, A., & Beal, M. F. (2012). Mitochondrial dysfunction in neurodegenerative diseases. *The Journal of Pharmacology and Experimental Therapeutics*, *342*(3), 619–630. https://doi.org/10.1124/jpet.112.192138

Joshi, D. C., & Bakowska, J. C. (2011). Determination of mitochondrial membrane potential and reactive oxygen species in live rat cortical neurons. *Journal of Visualized Experiments*, *51*, 2–5. https://doi.org/10.3791/2704

Kabashi, E., Agar, J. N., Strong, M. J., & Durham, H. D. (2012). Impaired proteasome function in sporadic amyotrophic lateral sclerosis. *Amyotrophic Lateral Sclerosis*, *13*(4), 367–371. https://doi.org/10.3109/17482968.2012.686511

Kabashi, E., Lin, L., Tradewell, M. L., Dion, P. A., Bercier, V., Bourgouin, P., Rochefort, D., Bel Hadj, S., Durham, H. D., Velde, C. Vande, Rouleau, G. A., & Drapeau, P. (2009). Gain and loss of function of ALS-related mutations of TARDBP (TDP-43) cause motor deficits in vivo. *Human Molecular Genetics*. https://doi.org/10.1093/hmg/ddp534

Kametani, F., Nonaka, T., Suzuki, T., Arai, T., Dohmae, N., Akiyama, H., & Hasegawa, M. (2009). Identification of casein kinase-1 phosphorylation sites on TDP-43. *Biochemical and Biophysical Research Communications*, *382*(2), 405–409. https://doi.org/10.1016/j.bbrc.2009.03.038

Kametani, F., Obi, T., Shishido, T., Akatsu, H., Murayama, S., Saito, Y., Yoshida, M., & Hasegawa, M. (2016). Mass spectrometric analysis of accumulated TDP-43 in amyotrophic lateral sclerosis brains. *Scientific Reports*, *6*(March), 1–15. https://doi.org/10.1038/srep23281

Kang, S. H., Li, Y., Fukaya, M., Lorenzini, I., Cleveland, D. W., Ostrow, L. W., Rothstein, J. D., & Bergles, D. E. (2013). Degeneration and impaired regeneration of gray matter oligodendrocytes in

amyotrophic lateral sclerosis. *Nature Neuroscience*, *16*(5), 571–579. https://doi.org/10.1038/nn.3357

Karim, M. R., Liao, E. E., Kim, J., Meints, J., Martinez, H. M., Pletnikova, O., Troncoso, J. C., & Lee, M. K. (2020). α-Synucleinopathy associated c-Abl activation causes p53-dependent autophagy impairment. *Molecular Neurodegeneration*, *15*(1), 1–18. https://doi.org/10.1186/s13024-020-00364-w

Karuppagounder, S. S., Brahmachari, S., Lee, Y., Dawson, V. L., Dawson, T. M., & Ko, H. S. (2014). The c-Abl inhibitor, nilotinib, protects dopaminergic neurons in a preclinical animal model of Parkinson's disease. *Scientific Reports*, *4*, 1–8. https://doi.org/10.1038/srep04874

Katsumata, R., Ishigaki, S., Katsuno, M., Kawai, K., Sone, J., Huang, Z., Adachi, H., Tanaka, F., Urano, F., & Sobue, G. (2012). c-Abl Inhibition Delays Motor Neuron Degeneration in the G93A Mouse, an Animal Model of Amyotrophic Lateral Sclerosis. *PLoS ONE*, *7*(9). https://doi.org/10.1371/journal.pone.0046185

Katyal, N., & Govindarajan, R. (2017). Shortcomings in the Current Amyotrophic Lateral Sclerosis Trials and Potential Solutions for improvement. *Frontiers in Neurology*, *8*(September), 1–9. https://doi.org/10.3389/fneur.2017.00521

Kazandjian, D., Blumenthal, G. M., Yuan, W., He, K., Keegan, P., & Pazdur, R. (2016). FDA Approval of Gefitinib for the Treatment of Patients with Metastatic EGFR Mutation-Positive Non-Small Cell Lung Cancer. *Clinical Cancer Research : An Official Journal of the American Association for Cancer Research*, *22*(6), 1307–1312. https://doi.org/10.1158/1078-0432.CCR-15-2266

Khalfallah, Y., Kuta, R., Grasmuck, C., Prat, A., Durham, H. D., & Vande Velde, C. (2018). TDP-43 regulation of stress granule dynamics in neurodegenerative disease-relevant cell types /631/80/304 /631/378/87 /13/1 /13/31 /13/51 /13/109 /13/106 /13/89 /14/19 /14/32 /82/80 article. *Scientific Reports*, *8*(1), 1–13. https://doi.org/10.1038/s41598-018-25767-0

Khatri, A., Wang, J., & Pendergast, A. M. (2016). Multifunctional Abl kinases in health and disease. *Journal of Cell Science*, *129*(1), 9–16. https://doi.org/10.1242/jcs.175521

Khosravi, B., Hartmann, H., May, S., Möhl, C., Ederle, H., Michaelsen, M., Schludi, M. H., Dormann, D., & Edbauer, D. (2017). Cytoplasmic poly-GA aggregates impair nuclear import of TDP-43 in C9orf72 ALS/FTLD. *Human Molecular Genetics*, *26*(4), 790–800. https://doi.org/10.1093/hmg/ddw432

Kiernan, M. C., Vucic, S., Talbot, K., McDermott, C. J., Hardiman, O., Shefner, J. M., Al-Chalabi, A., Huynh, W., Cudkowicz, M., Talman, P., Van den Berg, L. H., Dharmadasa, T., Wicks, P., Reilly, C., & Turner, M. R. (2021). Improving clinical trial outcomes in amyotrophic lateral sclerosis. *Nature Reviews Neurology*, *17*(2), 104–118. https://doi.org/10.1038/s41582-020-00434-z

Kilicoglu, H., Shin, D., Fiszman, M., Rosemblat, G., & Rindflesch, T. C. (2012). SemMedDB: A PubMed-scale repository of biomedical semantic predications. *Bioinformatics*, *28*(23), 3158–3160. https://doi.org/10.1093/bioinformatics/bts591

Kim, H. J., Kim, N. C., Wang, Y. D., Scarborough, E. A., Moore, J., Diaz, Z., MacLea, K. S., Freibaum, B., Li, S., Molliex, A., Kanagaraj, A. P., Carter, R., Boylan, K. B., Wojtas, A. M., Rademakers, R., Pinkus, J. L., Greenberg, S. A., Trojanowski, J. Q., Traynor, B. J., … Taylor, J. P. (2013). Mutations in prion-like domains in hnRNPA2B1 and hnRNPA1 cause multisystem proteinopathy and ALS. *Nature*. https://doi.org/10.1038/nature11922

Kim, Y., Apetri, M., Luo, B. B., Settleman, J. E., & Anderson, K. S. (2015). Differential effects of tyrosine kinase inhibitors on normal and oncogenic EGFR signaling and downstream effectors. *Molecular Cancer Research*, *13*(4), 765–774. https://doi.org/10.1158/1541-7786.MCR-14-0326

King, R. D., Muggleton, S., Lewis, R. a, & Sternberg, M. J. (1992). Drug design by machine learning: the use of inductive logic programming to model the structure-activity relationships of trimethoprim analogues binding to dihydrofolate reductase. *Proceedings of the National Academy of Sciences of the United States of America*, *89*(23), 11322–11326. https://doi.org/10.1073/pnas.89.23.11322

Kirk, K., Gennings, C., Hupf, J., Tadesse, S., D'Aurelio, M., Kawamata, H., Valsecchi, F., Mitsumoto, H., & Manfredi, G. (2014). Bioenergetic markers in skin fibroblasts of sporadic amyotrophic lateral sclerosis and progressive lateral sclerosis patients. *Annals of Neurology*, *76*(4), 620–624.

Kitamura, A., Inada, N., Kubota, H., Matsumoto, G., Kinjo, M., Morimoto, R. I., & Nagata, K. (2014). Dysregulation of the proteasome increases the toxicity of ALS-linked mutant SOD1. *Genes to Cells*, *19*(3), 209–224. https://doi.org/10.1111/gtc.12125

Kitazaki, T., Oka, M., Nakamura, Y., Tsurutani, J., Doi, S., Yasunaga, M., Takemura, M., Yabuuchi, H., Soda, H., & Kohno, S. (2005). Gefitinib, an EGFR tyrosine kinase inhibitor, directly inhibits the function of P-glycoprotein in multidrug resistant cancer cells. *Lung Cancer (Amsterdam, Netherlands)*, *49*(3), 337–343. https://doi.org/10.1016/j.lungcan.2005.03.035

Klucznik, T., Mikulak-Klucznik, B., McCormack, M. P., Lima, H., Szymkuć, S., Bhowmick, M., Molga, K., Zhou, Y., Rickershauser, L., Gajewska, E. P., Toutchkine, A., Dittwald, P., Startek, M. P., Kirkovits, G. J., Roszak, R., Adamski, A., Sieredzińska, B., Mrksich, M., Trice, S. L. J., & Grzybowski, B. A. (2018). Efficient Syntheses of Diverse, Medicinally Relevant Targets Planned by Computer and Executed in the Laboratory. *Chem*, *4*(3), 522–532. https://doi.org/10.1016/j.chempr.2018.02.002

Ko, H. S., Lee, Y., Shin, J.-H., Karuppagounder, S. S., Gadad, B. S., Koleske, A. J., Pletnikova, O., Troncoso, J. C., Dawson, V. L., & Dawson, T. M. (2010). Phosphorylation by the c-Abl protein tyrosine kinase inhibits parkin's ubiquitination and protective function. *Proceedings of the National Academy of Sciences of the United States of America*, *107*(38), 16691–16696. https://doi.org/10.1073/pnas.1006083107

Koppers, M., Blokhuis, A. M., Westeneng, H. J., Terpstra, M. L., Zundel, C. A. C., Vieira De Sá, R., Schellevis, R. D., Waite, A. J., Blake, D. J., Veldink, J. H., Van Den Berg, L. H., & Pasterkamp, R. J. (2015). C9orf72 ablation in mice does not cause motor neuron degeneration or motor deficits. *Annals of Neurology*, *78*(3), 426–438. https://doi.org/10.1002/ana.24453

Kovalevich, J., & Langford, D. (2013). Considerations for the use of SH-SY5Y neuroblastoma cells in neurobiology. *Methods in Molecular Biology (Clifton, N.J.)*, *1078*, 9–21. https://doi.org/10.1007/978-1-62703-640-5_2

Kreutzberg, G. W. (1996). Microglia: A sensor for pathological events in the CNS. *Trends in Neurosciences*, *19*(8), 312–318. https://doi.org/10.1016/0166-2236(96)10049-7

Kriz, J., Nguyen, M. D., & Julien, J. P. (2002). Minocycline slows disease progression in a mouse model of amyotrophic lateral sclerosis. *Neurobiology of Disease*, *10*(3), 268–278. https://doi.org/10.1006/nbdi.2002.0487

Kwiatkowski, T. J., Bosco, D. A., LeClerc, A. L., Tamrazian, E., Vanderburg, C. R., Russ, C., Davis, A., Gilchrist, J., Kasarskis, E. J., Munsat, T., Valdmanis, P., Rouleau, G. A., Hosler, B. A., Cortelli, P., De Jong, P. J., Yoshinaga, Y., Haines, J. L., Pericak-Vance, M. A., Yan, J., … Brown, R. H. (2009). Mutations in the FUS/TLS gene on chromosome 16 cause familial amyotrophic lateral sclerosis. *Science*. https://doi.org/10.1126/science.1166066

Kwon, I., Xiang, S., Kato, M., Wu, L., Theodoropoulos, P., Wang, T., Kim, J., Yun, J., Xie, Y., & McKnight, S. (2014). Poly-dipeptides encoded by the C9orf72 repeats bind nucleoli, impede

RNA biogenesis, and kill cells. *Science*, *345*(6201), 1139–1145.

Lagier-Tourenne, C., Polymenidou, M., Hutt, K., Vu, A., Baughn, M., Huelga, S., Clutario, K., Ling, S., Liang, T., Mazur, C., Wancewicz, E., Kim, A., Watt, A., Freier, S., Hicks, G., Donohue, J., Shiue, L., Bennett, C., Ravits, J., … Yeo, G. (2012). Divergent roles of ALS-linked proteins FUS/TLS and TDP-43 intersect in processing long pre-mRNAs. *Nature Neuroscience*, *15*(1), 1488–1497.

Le Pichon, C. E., Dominguez, S. L., Solanoy, H., Ngu, H., Lewin-Koh, N., Chen, M., Eastham-Anderson, J., Watts, R., & Scearce-Levie, K. (2013). EGFR Inhibitor Erlotinib Delays Disease Progression but Does Not Extend Survival in the SOD1 Mouse Model of ALS. *PLoS ONE*, *8*(4). https://doi.org/10.1371/journal.pone.0062342

Lee, D. shin, & Kim, J. E. (2018). PDI-mediated S-nitrosylation of DRP1 facilitates DRP1-S616 phosphorylation and mitochondrial fission in CA1 neurons. *Cell Death and Disease*, *9*(9). https://doi.org/10.1038/s41419-018-0910-5

Lee, S. M., Asress, S., Hales, C. M., Gearing, M., Vizcarra, J. C., Fournier, C. N., Gutman, D. A., Chin, L.-S., Li, L., & Glass, J. D. (2019). TDP-43 cytoplasmic inclusion formation is disrupted in C9orf72-associated amyotrophic lateral sclerosis/frontotemporal lobar degeneration. *Brain Communications*, *1*(1). https://doi.org/10.1093/braincomms/fcz014

Lee, W. J., Moon, J., Kim, T. J., Jun, J. S., Lee, H. S., Ryu, Y. J., Lee, S. T., Jung, K. H., Park, K. Il, Jung, K. Y., Kim, M., Lee, S. K., & Chu, K. (2017). The c-Abl inhibitor, nilotinib, as a potential therapeutic agent for chronic cerebellar ataxia. *Journal of Neuroimmunology*, *309*(April), 82–87. https://doi.org/10.1016/j.jneuroim.2017.05.015

Lee, Y., Chen, H., Peres, J., Gomez-Deza, J., Attig, J., Stalekar, M., Troakes, C., Nishimura, A., Scotter, E., Vance, C., Adachi, Y., Saradone, V., Miller, J., Smith, B., Gallo, J., Ule, J., Hirth, F., Rogelj, B., Houart, C., & Shaw, C. (2013). Hexanucleotide Repeats in ALS/FTD Form Length-Dependent RNA Foci, Sequester RNA Binding Proteins, and Are Neurotoxic. *Cell Reports*, *5*(5), 1178–1186.

Li, G., Taljaard, M., Van den Heuvel, E. R., Levine, M. A., Cook, D. J., Wells, G. A., Devereaux, P. J., & Thabane, L. (2017). An introduction to multiplicity issues in clinical trials: the what, why, when and how. *International Journal of Epidemiology*, *46*(2), 746–755. https://doi.org/10.1093/ije/dyw320

Li, Qingliang, & Shah, S. (2017). Structure-Based Virtual Screening. *Methods in Molecular Biology (Clifton, N.J.)*, *1558*, 111–124. https://doi.org/10.1007/978-1-4939-6783-4_5

Li, Quan, Velde, C. Vande, Israelson, A., Xie, J., Bailey, A. O., Dong, M. Q., Chun, S. J., Roy, T., Winer, L., Yates, J. R., Capaldi, R. A., Cleveland, D. W., & Miller, T. M. (2010). ALS-linked mutant superoxide dismutase 1 (SOD1) alters mitochondrial protein composition and decreases protein import. *Proceedings of the National Academy of Sciences of the United States of America*, *107*(49), 21146–21151. https://doi.org/10.1073/pnas.1014862107

Li, Quan, Yokoshi, M., Okada, H., & Kawahara, Y. (2015a). The cleavage pattern of TDP-43 determines its rate of clearance and cytotoxicity. *Nature Communications*, *6*, 1–12. https://doi.org/10.1038/ncomms7183

Li, Quan, Yokoshi, M., Okada, H., & Kawahara, Y. (2015b). The cleavage pattern of TDP-43 determines its rate of clearance and cytotoxicity. *Nature Communications*, *6*. https://doi.org/10.1038/ncomms7183

Li, T., Tong, W., Roberts, R., Liu, Z., & Thakkar, S. (2020). Deep Learning on High-Throughput Transcriptomics to Predict Drug-Induced Liver Injury. *Frontiers in Bioengineering and Biotechnology*, *8*(November), 1–14. https://doi.org/10.3389/fbioe.2020.562677

Li, W., Reeb, A. N., Lin, B., Subramanian, P., Fey, E. E., Knoverek, C. R., French, R. L., Bigio, E. H., & Ayala, Y. M. (2017). Heat shock-induced phosphorylation of TAR DNA-binding protein 43 (TDP-43) by MAPK/ERK kinase regulates TDP-43 function. *Journal of Biological Chemistry*, *292*(12), 5089–5100. https://doi.org/10.1074/jbc.M116.753913

Li, Y., Guo, Y., Wang, X., Yu, X., Duan, W., Hong, K., Wang, J., Han, H., & Li, C. (2015). Trehalose decreases mutant SOD1 expression and alleviates motor deficiency in early but not end-stage amyotrophic lateral sclerosis in a SOD1-G93A mouse model. *Neuroscience*, *298*(1), 12–25.

Lin, Y. C., Boone, M., Meuris, L., Lemmens, I., Van Roy, N., Soete, A., Reumers, J., Moisse, M., Plaisance, S., Drmanac, R., Chen, J., Speleman, F., Lambrechts, D., Van De Peer, Y., Tavernier, J., & Callewaert, N. (2014). Genome dynamics of the human embryonic kidney 293 lineage in response to cell biology manipulations. *Nature Communications*, *5*(11). https://doi.org/10.1038/ncomms5767

Liu, B., Teschemacher, A. G., & Kasparov, S. (2017). Astroglia as a cellular target for neuroprotection and treatment of neuro-psychiatric disorders. *Glia*, *65*(8), 1205–1226. https://doi.org/10.1002/glia.23136

Liu, W., Yamashita, T., Tian, F., Morimoto, N., Ikeda, Y., Deguchi, K., & Abe, K. (2013). Mitochondrial

Fusion and Fission Proteins Expression Dynamically Change in a Murine Model of Amyotrophic Lateral Sclerosis. *Current Neurovascular Research*, *10*(3), 222–230.

Liu, Y., Wang, Z., Kwong, S. Q., Lui, E. L. H., Friedman, S. L., Li, F. R., Lam, R. W. C., Zhang, G. C., Zhang, H., & Ye, T. (2011). Inhibition of PDGF, TGF-β, and Abl signaling and reduction of liver fibrosis by the small molecule Bcr-Abl tyrosine kinase antagonist Nilotinib. *Journal of Hepatology*, *55*(3), 612–625. https://doi.org/10.1016/j.jhep.2010.11.035

Lobsiger, C. S., Boillee, S., McAlonis-Downes, M., Khan, A. M., Feltri, M. L., Yamanaka, K., & Cleveland, D. W. (2009). Schwann cells expressing dismutase active mutant SOD1 unexpectedly slow disease progression in ALS mice. *Proceedings of the National Academy of Sciences of the United States of America*, *106*(11), 4465–4470. https://doi.org/10.1073/pnas.0813339106

Logroscino, G., Traynor, B. J., Hardiman, O., Chió, A., Mitchell, D., Swingler, R. J., Millul, A., Benn, E., & Beghi, E. (2010). Incidence of amyotrophic lateral sclerosis in Europe. *Journal of Neurology, Neurosurgery and Psychiatry*, *81*(4), 385–390. https://doi.org/10.1136/jnnp.2009.183525

Lopez-Gonzalez, R., Lu, Y., Gendron, T., Karydas, A., Tran, H., Yang, D., Petrucelli, L., Miller, L., Almeida, S., & Gao, F. (2016). Poly(GR) in C9ORF72-Related ALS/FTD Compromises Mitochondrial Function and Increases Oxidative Stress and DNA Damage in iPSC-Derived Motor Neurons. *Neuron*, *92*(2), 383–391.

Lötsch, J., & Ultsch, A. (2016). Process Pharmacology: A Pharmacological Data Science Approach to Drug Development and Therapy. *CPT: Pharmacometrics and Systems Pharmacology*, *5*(4), 192–200. https://doi.org/10.1002/psp4.12072

Luchetti, F., Gregorini, A., Papa, S., Burattini, S., Canonico, B., Valentini, M., & Falcieri, E. (1998). The K562 chronic myeloid leukemia cell line undergoes apoptosis in response to interferon-α. *Haematologica*, *83*(11), 974–980.

Luty, A. A., Kwok, J. B. J., Dobson-Stone, C., Loy, C. T., Coupland, K. G., Karlström, H., Sobow, T., Tchorzewska, J., Maruszak, A., Barcikowska, M., Panegyres, P. K., Zekanowski, C., Brooks, W. S., Williams, K. L., Blair, I. P., Mather, K. A., Sachdev, P. S., Halliday, G. M., & Schofield, P. R. (2010). Sigma nonopioid intracellular receptor 1 mutations cause frontotemporal lobar degeneration-motor neuron disease. *Annals of Neurology*. https://doi.org/10.1002/ana.22274

Madill, M., McDonagh, K., Ma, J., Vajda, A., McLoughlin, P., O'Brien, T., Hardiman, O., & Shen, S. (2017). Amyotrophic lateral sclerosis patient iPSC-derived astrocytes impair autophagy via non-

cell autonomous mechanisms. *Molecular Brain*, *10*(1), 1–12. https://doi.org/10.1186/s13041-017-0300-4

Magrané, J, Cortez, C., Gan, W., & Manfredi, G. (2014). Abnormal mitochondrial transport and morphology are common pathological denominators in SOD1 and TDP43 ALS mouse models. *Human Molecular Genetics*, *23*(6), 1413–1424.

Magrané, Jordi, Sahawneh, M. A., Przedborski, S., Estévez, Á. G., & Manfredi, G. (2012). Mitochondrial dynamics and bioenergetic dysfunction is associated with synaptic alterations in mutant SOD1 motor neurons. *The Journal of Neuroscience : The Official Journal of the Society for Neuroscience*, *32*(1), 229–242. https://doi.org/10.1523/JNEUROSCI.1233-11.2012

Mahul-Mellier, A. L., Fauvet, B., Gysbers, A., Dikiy, I., Oueslati, A., Georgeon, S., Lamontanara, A. J., Bisquertt, A., Eliezer, D., Masliah, E., Halliday, G., Hantschel, O., & Lashuel, H. A. (2014). C-Abl phosphorylates α-synuclein and regulates its degradation: Implication for α-synuclein clearance and contribution to the pathogenesis of parkinson's disease. *Human Molecular Genetics*, *23*(11), 2858–2879. https://doi.org/10.1093/hmg/ddt674

Marat, A., Dokainish, H., & McPherson, P. (2011). DENN domain proteins: regulators of Rab GTPases. *Journal of Biological Chemistry*, *286*(16), 13791–13800.

Marchetto, M. C. N., Muotri, A. R., Mu, Y., Smith, A. M., Cezar, G. G., & Gage, F. H. (2008). Non-cell-autonomous effect of human SOD1 G37R astrocytes on motor neurons derived from human embryonic stem cells. *Cell Stem Cell*, *3*(6), 649–657. https://doi.org/10.1016/j.stem.2008.10.001

Maruyama, H., Morino, H., Ito, H., Izumi, Y., Kato, H., Watanabe, Y., Kinoshita, Y., Kamada, M., Nodera, H., Suzuki, H., Komure, O., Matsuura, S., Kobatake, K., Morimoto, N., Abe, K., Suzuki, N., Aoki, M., Kawata, A., Hirai, T., … Kawakami, H. (2010). Mutations of optineurin in amyotrophic lateral sclerosis. *Nature*. https://doi.org/10.1038/nature08971

Matus, S., Medinas, D., & Hetz, C. (2014). Common ground: stem cell approaches find shared pathways underlying ALS. *Cell Stem Cell*, *14*(6), 697–699.

May, S., Hornburg, D., Schludi, M. H., Arzberger, T., Rentzsch, K., Schwenk, B. M., Grässer, F. A., Mori, K., Kremmer, E., Banzhaf-Strathmann, J., Mann, M., Meissner, F., & Edbauer, D. (2014). C9orf72 FTLD/ALS-associated Gly-Ala dipeptide repeat proteins cause neuronal toxicity and Unc119 sequestration. *Acta Neuropathologica*, *128*(4), 485–503. https://doi.org/10.1007/s00401-014-

1329-4

Mayers, M., Li, T. S., Queralt-Rosinach, N., & Su, A. I. (2019). Time-resolved evaluation of compound repositioning predictions on a text-mined knowledge network. *BMC Bioinformatics*, *20*(1), 1–12. https://doi.org/10.1186/s12859-019-3297-0

Mertens, J., Paquola, A. C. M., Ku, M., Hatch, E., Böhnke, L., Ladjevardi, S., McGrath, S., Campbell, B., Lee, H., Herdy, J. R., Gonçalves, J. T., Toda, T., Kim, Y., Winkler, J., Yao, J., Hetzer, M. W., & Gage, F. H. (2015). Directly Reprogrammed Human Neurons Retain Aging-Associated Transcriptomic Signatures and Reveal Age-Related Nucleocytoplasmic Defects. *Cell Stem Cell*, *17*(6), 705–718. https://doi.org/10.1016/j.stem.2015.09.001

Meyer, K., Ferraiuolo, L., Miranda, C. J., Likhite, S., McElroy, S., Renusch, S., Ditsworth, D., Lagier-Tourenne, C., Smith, R. A., Ravits, J., Burghes, A. H., Shaw, P. J., Cleveland, D. W., Kolb, S. J., & Kaspar, B. K. (2014). Direct conversion of patient fibroblasts demonstrates non-cell autonomous toxicity of astrocytes to motor neurons in familial and sporadic ALS. *Proceedings of the National Academy of Sciences*, *111*(2), 829–832. https://doi.org/10.1073/pnas.1314085111

Meyerowitz, J., Parker, S. J., Vella, L. J., Ng, D. C., Price, K. A., Liddell, J. R., Caragounis, A., Li, Q.-X., Masters, C. L., Nonaka, T., Hasegawa, M., Bogoyevitch, M. A., Kanninen, K. M., Crouch, P. J., & White, A. R. (2011). C-Jun N-terminal kinase controls TDP-43 accumulation in stress granules induced by oxidative stress. *Molecular Neurodegeneration*, *6*(1), 57. https://doi.org/10.1186/1750-1326-6-57

Miller, R. G., Mitchell, J. D., & Moore, D. H. (2012). Riluzole for amyotrophic lateral sclerosis (ALS)/motor neuron disease (MND). *Cochrane Database of Systematic Reviews*, *3*. https://doi.org/10.1002/14651858.CD001447.pub2

Mitne-Neto, M., Machado-Costa, M., Marchetto, M. C. N., Bengtson, M. H., Joazeiro, C. A., Tsuda, H., Bellen, H. J., Silva, H. C. A., Oliveira, A. S. B., Lazar, M., Muotri, A. R., & Zatz, M. (2011). Downregulation of VAPB expression in motor neurons derived from induced pluripotent stem cells of ALS8 patients. *Human Molecular Genetics*, *20*(18), 3642–3652. https://doi.org/10.1093/hmg/ddr284

Mitra, J., Guerrero, E., Hegde, P., Liachko, N., Wang, H., Vasquez, V., Gao, J., Pandey, A., Taylor, J., Kraemer, B., Wu, P., Boldogh, I., Garruto, R., Mitra, S., Rao, K., & Hegde, M. (2019). Motor

neuron disease-associated loss of nuclear TDP-43 is linked to DNA double-strand break repair defects. *PNAS*, *116*(10), 4696–4705.

Mitsumoto, H, Santella, R., Liu, X., Bogdanov, M., Zipprich, J., Wu, H., Mahata, J., Kilty, M., Bednarz, K., Bell, D., Gordon, P., Horing, M., Mehrazin, M., Naini, A., Beal, M., & Factor-Litvak, P. (2008). Oxidative stress biomarkers in sporadic ALS. *Amyotrophic Lateral Sclerosis*, *9*(3), 177–183.

Mitsumoto, Hiroshi, Brooks, B. R., & Silani, V. (2014). Clinical trials in amyotrophic lateral sclerosis: Why so many negative trials and how can trials be improved? *The Lancet Neurology*, *13*(11), 1127–1138. https://doi.org/10.1016/S1474-4422(14)70129-2

Miyazono, Y., Hirashima, S., Ishihara, N., Kusukawa, J., Nakamura, K., & Ohta, K. (2018). Uncoupled mitochondria quickly shorten along their long axis to form indented spheroids, instead of rings, in a fission-independent manner. *Scientific Reports*, *8*(350).

Mizielinska, S., Lashley, T., Norona, F. E., Clayton, E. L., Ridler, C. E., Fratta, P., & Isaacs, A. M. (2013). C9orf72 frontotemporal lobar degeneration is characterised by frequent neuronal sense and antisense RNA foci. *Acta Neuropathologica*, *126*(6), 845–857. https://doi.org/10.1007/s00401-013-1200-z

Mompeán, M., Romano, V., Pantoja-Uceda, D., Stuani, C., Baralle, F. E., Buratti, E., & Laurents, D. V. (2017). Point mutations in the N-terminal domain of transactive response DNA-binding protein 43 kDa (TDP-43) compromise its stability, dimerization, and functions. *Journal of Biological Chemistry*, *292*(28), 11992–12006. https://doi.org/10.1074/jbc.M117.775965

Moore, A. S., & Holzbaur, E. L. F. (2016). Dynamic recruitment and activation of ALS-associated TBK1 with its target optineurin are required for efficient mitophagy. *Proceedings of the National Academy of Sciences of the United States of America*, *113*(24), E3349–E3358. https://doi.org/10.1073/pnas.1523810113

Mori, K., Nihei, Y., Arzberger, T., Zhou, Q., Mackenzie, I. R., Hermann, A., Hanisch, F., Consortium, G., Degeneration, L., Brain, B., Alliance, B., Kamp, F., Nuscher, B., Orozco, D., & Edbauer, D. (2016). *Reduced hnRNPA 3 increases C 9 orf 72 repeat RNA levels and dipeptide-repeat protein deposition*. *17*(9), 1314–1325.

Moritz, A., Li, Y., Guo, A., VilléN, J., Wang, Y., MavNeill, J., Kornhauser, J., Sprott, K., Zhou, J., Possemato, A., Ren, J., Hornbeck, P., Cantley, L., Gygi, S., Rush, J., & Comb, M. (2011). Akt-RSK-S6-kinase Signaling Networks Activated by Oncogenic Receptor Tyrosine Kinases. *Science*

Signaling, *3*(136), 1–7. https://doi.org/10.1161/CIRCULATIONAHA.110.956839

Nagai, M., Re, D. B., Nagata, T., Chalazonitis, A., Jessell, T. M., Wichterle, H., & Przedborski, S. (2007). Astrocytes expressing ALS-linked mutated SOD1 release factors selectively toxic to motor neurons. *Nature Neuroscience*, *10*(5), 615–622. https://doi.org/10.1038/nn1876

Nakashima-Yasuda, H., Uryu, K., Robinson, J., Xie, S. X., Hurtig, H., Duda, Jo. E., Arnold, S. E., Siderowf, A., Grossman, M., Leverenz, J. B., Woltjer, R., Lopez, O. L., Hamilton, R., Tsuang, D. W., Galasko, D., Masliah, E., Kaye, J., Clark, C. M., Montine, T. J., … Trojanowski, J. Q. (2007). Co-morbidity of TDP-43 proteinopathy in Lewy body related diseases. *Acta Neuropathologica*, *114*(1), 221–229. https://doi.org/10.1007/s00401-007-0261-2

Nelson, P., Gal, Z., Wang, W., Niedowicz, D., Artiushin, S., Wycoff, S., Wei, A., Jicha, G., & Fardo, D. (2019). TDP-43 proteinopathy in aging: Associations with risk-associated gene variants and with brain parenchymal thyroid hormone levels. *Neurobiology of Disease*, *125*(1), 67–76.

Neumann, M., Sampathu, D. M., Kwong, L. K., Truax, A. C., Micsenyi, M. C., Chou, T. T., Bruce, J., Schuck, T., Grossman, M., Clark, C. M., McCluskey, L. F., Miller, B. L., Masliah, E., Mackenzie, I. R., Feldman, H., Feiden, W., Kretzschmar, H. A., Trojanowski, J. Q., & Lee, V. M.-Y. (2006). Ubiquitinated TDP-43 in frontotemporal lobar degeneration and amyotrophic lateral sclerosis. *Science (New York, N.Y.)*, *314*(5796), 130–133. https://doi.org/10.1126/science.1134108

Nikkhah, G., Olsson, M., Eberhard, J., Bentlage, C., Cunningham, M. G., & Björklund, A. (1994). A microtransplantation approach for cell suspension grafting in the rat Parkinson model: a detailed account of the methodology. *Neuroscience*, *63*(1), 57–72. https://doi.org/10.1016/0306-4522(94)90007-8

Nishimura, A. L., Mitne-Neto, M., Silva, H. C. A., Richieri-Costa, A., Middleton, S., Cascio, D., Kok, F., Oliveira, J. R. M., Gillingwater, T., Webb, J., Skehel, P., & Zatz, M. (2004). A mutation in the vesicle-trafficking protein VAPB causes late-onset spinal muscular atrophy and amyotrophic lateral sclerosis. *American Journal of Human Genetics*. https://doi.org/10.1086/425287

Nishiyama, K. (2017). Exploration of peptides that fit into the thermally vibrating active site of cathepsin K protease by alternating artificial intelligence and molecular simulation. *Chemical Physics Letters*, *682*, 26–29. https://doi.org/10.1016/j.cplett.2017.06.004

Nonaka, T., Masuda-Suzukake, M., Arai, T., Hasegawa, Y., Akatsu, H., Obi, T., Yoshida, M., Murayama, S., Mann, D. M. A., Akiyama, H., & Hasegawa, M. (2013). Prion-like Properties of Pathological

TDP-43 Aggregates from Diseased Brains. *Cell Reports*, *4*(1), 124–134. https://doi.org/10.1016/j.celrep.2013.06.007

Nonaka, T., Suzuki, G., Tanaka, Y., Kametani, F., Hirai, S., Okado, H., Miyashita, T., Saitoe, M., Akiyama, H., Masai, H., & Hasegawa, M. (2016). Phosphorylation of TAR DNA-binding protein of 43 kDa (TDP-43) by truncated casein kinase 1 triggers mislocalization and accumulation of TDP-43. *Journal of Biological Chemistry*, *291*(11), 5473–5483. https://doi.org/10.1074/jbc.M115.695379

Olivieri, A., & Manzione, L. (2007). Dasatinib: a new step in molecular target therapy. *Annals of Oncology : Official Journal of the European Society for Medical Oncology*, *18 Suppl 6*, vi42-6. https://doi.org/10.1093/annonc/mdm223

Onesto, E., Colombrita, C., Gumina, V., Borghi, M., Dusi, S., Doretti, A., Fagiolari, G., Invernizzi, F., Moggio, M., Tiranti, V., Silani, V., & Ratti, A. (2016). Gene-specific mitochondria dysfunctions in human TARDBP and C9ORF72 fibroblasts. *Acta Neuropathologica Communications*, *4*(1), 47.

Otomo, A., Hadano, S., Okada, T., Mizumura, H., Kunita, R., Nishijima, H., Showguchi-Miyata, J., Yanagisawa, Y., Kohiki, E., Suga, E., Yasuda, M., Osuga, H., Nishimoto, T., Narumiya, S., & Ikeda, J. E. (2003). ALS2, a novel guanine nucleotide exchange factor for the small GTPase Rab5, is implicated in endosomal dynamics. *Human Molecular Genetics*, *12*(14), 1671–1687. https://doi.org/10.1093/hmg/ddg184

Ou, S. H., Wu, F., Harrich, D., García-Martínez, L. F., & Gaynor, R. B. (1995). Cloning and characterization of a novel cellular protein, TDP-43, that binds to human immunodeficiency virus type 1 TAR DNA sequence motifs. *Journal of Virology*, *69*(6), 3584–3596. https://doi.org/10.1128/JVI.69.6.3584-3596.1995

Pagan, F., Hebron, M., Valadez, E. H., Torres-Yaghi, Y., Huang, X., Mills, R. R., Wilmarth, B. M., Howard, H., Dunn, C., Carlson, A., Lawler, A., Rogers, S. L., Falconer, R. A., Ahn, J., Li, Z., & Moussa, C. (2016). Nilotinib effects in Parkinson's disease and dementia with lewy bodies. *Journal of Parkinson's Disease*, *6*(3), 503–517. https://doi.org/10.3233/JPD-160867

Pagan, F. L., Hebron, M. L., Wilmarth, B., Torres-Yaghi, Y., Lawler, A., Mundel, E. E., Yusuf, N., Starr, N. J., Anjum, M., Arellano, J., Howard, H. H., Shi, W., Mulki, S., Kurd-Misto, T., Matar, S., Liu, X., Ahn, J., & Moussa, C. (2020). Nilotinib Effects on Safety, Tolerability, and Potential Biomarkers in Parkinson Disease: A Phase 2 Randomized Clinical Trial. *JAMA Neurology*, *77*(3), 309–317.

https://doi.org/https://doi.org/10.1001/jamaneurol.2019.4200

Pagan, Fernando L., Hebron, M. L., Wilmarth, B., Torres-Yaghi, Y., Lawler, A., Mundel, E. E., Yusuf, N., Starr, N. J., Arellano, J., Howard, H. H., Peyton, M., Matar, S., Liu, X., Fowler, A. J., Schwartz, S. L., Ahn, J., & Moussa, C. (2019). Pharmacokinetics and pharmacodynamics of a single dose Nilotinib in individuals with Parkinson's disease. *Pharmacology Research and Perspectives*, *7*(2), 1–12. https://doi.org/10.1002/prp2.470

Pahikkala, T., Airola, A., Pietilä, S., Shakyawar, S., Szwajda, A., Tang, J., & Aittokallio, T. (2015). Toward more realistic drug-target interaction predictions. *Briefings in Bioinformatics*, *16*(2), 325–337. https://doi.org/10.1093/bib/bbu010

Pan, Y., Li, X., Li, X., Duan, J., Yuan, L., Fan, S., Fan, J., Xiaokaiti, Y., Yang, H., & Wang, Y. (2015). Enoxaparin sensitizes human non -small-cell lung carcinomas to gefitinib by inhibiting DOCK1 expression, vimentin phosphorylation, and akt activation. *Molecular Pharmacology*, *87*(3), 378–390. https://doi.org/10.1124/mol.114.094425

Parakh, S., & Atkin, J. D. (2016). Protein folding alterations in amyotrophic lateral sclerosis. *Brain Research*, *1648*, 633–649. https://doi.org/10.1016/j.brainres.2016.04.010

Pasinelli, P., Borchelt, D. R., Houseweart, M. K., Cleveland, D. W., & Brown, R. H. J. (1998). Caspase-1 is activated in neural cells and tissue with amyotrophic lateral sclerosis-associated mutations in copper-zinc superoxide dismutase. *Proceedings of the National Academy of Sciences of the United States of America*, *95*(26), 15763–15768. https://doi.org/10.1073/pnas.95.26.15763

Payne, A. G. (2009). Experimental regimen targeting the ependyma slows disease progression in four patients with amyotrophic lateral sclerosis. *Medical Hypotheses*, *72*(5), 548–550. https://doi.org/10.1016/j.mehy.2008.12.032

Penndorf, D., Tadi, V., Witte, O. W., Grosskreutz, J., & Kretz, A. (2017). DNA strand breaks and TDP-43 mislocation are absent in the murine hSOD1 G93A model of amyotrophic lateral sclerosis in vivo and in vitro. *PLoS ONE*, *12*(8), 1–22.

Perera, N. D., Sheean, R. K., Lau, C. L., Shin, Y. S., Beart, P. M., Horne, M. K., & Turner, B. J. (2018). Rilmenidine promotes MTOR-independent autophagy in the mutant SOD1 mouse model of amyotrophic lateral sclerosis without slowing disease progression. *Autophagy*, *14*(3), 534–551. https://doi.org/10.1080/15548627.2017.1385674

Petrov, D., Mansfield, C., Moussy, A., & Hermine, O. (2017). ALS Clinical Trials Review: 20 Years of Failure. Are We Any Closer to Registering a New Treatment? *Frontiers in Aging Neuroscience*, *9*, 68. https://doi.org/10.3389/fnagi.2017.00068

Philips, T., Bento-Abreu, A., Nonneman, A., Haeck, W., Staats, K., Geelen, V., Hersmus, N., Küsters, B., Van Den Bosch, L., Van Damme, P., Richardson, W. D., & Robberecht, W. (2013). Oligodendrocyte dysfunction in the pathogenesis of amyotrophic lateral sclerosis. *Brain*, *136*(2), 471–482. https://doi.org/10.1093/brain/aws339

Pickrell, A., & Youle, R. (2015). The roles of PINK1, parkin, and mitochondrial fidelity in Parkinson's disease. *Neuron*, *85*(2), 257–273.

Qian, K., Huang, H., Peterson, A., Hu, B., Maragakis, N., Ming, G., Chen, H., & Zhang, S. (2017). Sporadic ALS Astrocytes Induce Neuronal Degeneration In Vivo. *Stem Cell Reports*, *8*(4), 843–855.

Raiteri, L., Zappettini, S., Stigliani, S., Paluzzi, S., Raiteri, M., & Bonanno, G. (2005). Glutamate release induced by activation of glycine and GABA transporters in spinal cord is enhanced in a mouse model of amyotrophic lateral sclerosis. *NeuroToxicology*, *26*(5), 883–892. https://doi.org/10.1016/j.neuro.2005.01.015

Ray, A., Cowan-Jacob, S. W., Manley, P. W., Mestan, J., & Griffin, J. D. (2007). Identification of BCR-ABL point mutations conferring resistance to the Abl kinase inhibitor AMN107 (nilotinib) by a random mutagenesis study. *Blood*, *109*(11), 5011–5015. https://doi.org/10.1182/blood-2006-01-015347

Reaume, A., Elliott, J., Hoffman, E., Kowall, N., Ferrante, R., Siwek, D., Wilcox, H., Flood, D., Beal, M., Brown Jr, R., Scott, R., & Snider, W. (1996). Motor neurons in Cu/Zn superoxide dismutase-deficient mice develop normally but exhibit enhanced cell death after axonal injury. *Nature Genetics*, *13*(1), 43–47.

Renton, A. E., Majounie, E., Waite, A., Simón-Sánchez, J., Rollinson, S., Gibbs, J. R., Schymick, J. C., Laaksovirta, H., van Swieten, J. C., Myllykangas, L., Kalimo, H., Paetau, A., Abramzon, Y., Remes, A. M., Kaganovich, A., Scholz, S. W., Duckworth, J., Ding, J., Harmer, D. W., … Traynor, B. J. (2011). A hexanucleotide repeat expansion in C9ORF72 is the cause of chromosome 9p21-linked ALS-FTD. *Neuron*. https://doi.org/10.1016/j.neuron.2011.09.010

Rindflesch, T. C., & Fiszman, M. (2003). The interaction of domain knowledge and linguistic structure

in natural language processing: interpreting hypernymic propositions in biomedical text. *Journal of Biomedical Informatics*, *36*(6), 462–477. https://doi.org/10.1016/j.jbi.2003.11.003

Rizzu, P., Blauwendraat, C., Heetveld, S., Lynes, E. M., Castillo-Lizardo, M., Dhingra, A., Pyz, E., Hobert, M., Synofzik, M., Simón-Sánchez, J., Francescatto, M., Heutink, P., Jesus-Hernandez, M., Mackenzie, I., Boeve, B., Boxer, A., Baker, M., Rutherford, N., Renton, A., … Liu, Z. (2016). C9orf72 is differentially expressed in the central nervous system and myeloid cells and consistently reduced in C9orf72, MAPT and GRN mutation carriers. *Acta Neuropathologica Communications*, *4*(1), 37. https://doi.org/10.1186/s40478-016-0306-7

Rojas, F., Gonzalez, D., Cortes, N., Ampuero, E., Hernández, D. E., Fritz, E., Abarzua, S., Martinez, A., Elorza, A. A., Alvarez, A., Court, F., & Van Zundert, B. (2015). Reactive oxygen species trigger motoneuron death in non-cell-autonomous models of als through activation of c-Abl signaling. *Frontiers in Cellular Neuroscience*, *9*(June), 1–20. https://doi.org/10.3389/fncel.2015.00203

Romeo-Guitart, D., Forés, J., Herrando-Grabulosa, M., Valls, R., Leiva-Rodríguez, T., Galea, E., González-Pérez, F., Navarro, X., Petegnief, V., Bosch, A., Coma, M., Mas, J. M., & Casas, C. (2018). Neuroprotective Drug for Nerve Trauma Revealed Using Artificial Intelligence. *Scientific Reports*, *8*(1), 1–15. https://doi.org/10.1038/s41598-018-19767-3

Rosen, D. R., Siddique, T., Patterson, D., Figlewicz, D. A., Sapp, P., Hentati, A., Donaldson, D., Goto, J., O'Regan, J. P., Deng, H. X., Rahmani, Z., Krizus, A., McKenna-Yasek, D., Cayabyab, A., Gaston, S. M., Berger, R., Tanzi, R. E., Halperin, J. J., Herzfeldt, B., … Brown, R. H. (1993). Mutations in Cu/Zn superoxide dismutase gene are associated with familial amyotrophic lateral sclerosis. *Nature*. https://doi.org/10.1038/362059a0

Rosen, D., Siddique, T., Patterson, D., Figlewicz, D., Sapp, P., Hentati, A., Donaldson, D., Goto, J., Deng, H., & O'Regan, J. (1993). Mutations in Cu/Zn superoxide dismutase gene are associated with familial amyotrophic lateral sclerosis. *Nature*, *362*(6415), 59–62.

Rothschild, B. L., Shim, A. H., Ammer, A. G., Kelley, L. C., Irby, K. B., Head, J. A., Chen, L., Varella-Garcia, M., Sacks, P. G., Frederick, B., Raben, D., & Weed, S. A. (2006). Cortactin overexpression regulates actin-related protein 2/3 complex activity, motility, and invasion in carcinomas with chromosome 11q13 amplification. *Cancer Research*, *66*(16), 8017–8025. https://doi.org/10.1158/0008-5472.CAN-05-4490

Rowland, L., & Shneider, N. (2001). The clinical diagnosis of ALS is probably correct in more than 95

percent of cases. 1 However, because. *English Journal*, *344*(22), 1688–1700.

Rudnick, N., Griffey, C., Guarnieri, P., Gerbino, V., Wang, X., Piersaint, J., Tapia, J., Rich, M., & Maniatis, T. (2017). Distinct roles for motor neuron autophagy early and late in the SOD1G93A mouse model of ALS. *PNAS*, *114*(39), E8284–E8303.

Rué, L., Oeckl, P., Timmers, M., Lenaerts, A., van der Vos, J., Smolders, S., Poppe, L., de Boer, A., Van Den Bosch, L., Van Damme, P., Weishaupt, J. H., Ludolph, A. C., Otto, M., Robberecht, W., & Lemmens, R. (2019). Reduction of ephrin-A5 aggravates disease progression in amyotrophic lateral sclerosis. *Acta Neuropathologica Communications*, *7*(1), 114. https://doi.org/10.1186/s40478-019-0759-6

Rutherford, N. J., Zhang, Y. J., Baker, M., Gass, J. M., Finch, N. C. A., Xu, Y. F., Stewart, H., Kelley, B. J., Kuntz, K., Crook, R. J. P., Sreedharan, J., Vance, C., Sorenson, E., Lippa, C., Bigio, E. H., Geschwind, D. H., Knopman, D. S., Mitsumoto, H., Petersen, R. C., … Rademakers, R. (2008). Novel mutations in TARDBP(TDP-43) in patients with familial amyotrophic lateral sclerosis. *PLoS Genetics*. https://doi.org/10.1371/journal.pgen.1000193

Sakamuru, S., Attene-Ramos, M., & Xia, M. (2016). Mitochondrial Membrane Potential Assay. *Methods in Molecular Biology*, *1473*(5), 17–22. https://doi.org/10.1007/978-1-4939-6346-1

Sareen, D., O'Rourke, J. G., Meera, P., Muhammad, A. K. M. G., Grant, S., Simpkinson, M., Bell, S., Carmona, S., Ornelas, L., Sahabian, A., Gendron, T., Petrucelli, L., Baughn, M., Ravits, J., Harms, M. B., Rigo, F., Frank Bennett, C., Otis, T. S., Svendsen, C. N., & Baloh, R. H. (2013). Targeting RNA foci in iPSC-derived motor neurons from ALS patients with a C9ORF72 repeat expansion. *Science Translational Medicine*, *5*(208). https://doi.org/10.1126/scitranslmed.3007529

Sasaki, S., & Iwata, M. (2007). Mitochondrial alterations in the spinal cord of patients with sporadic amyotrophic lateral sclerosis. *Journal of Neuropathology and Experimental Neurology*, *66*(1), 10–16.

Scarpino, A., Ferenczy, G. G., & Keserű, G. M. (2018). Comparative Evaluation of Covalent Docking Tools. *Journal of Chemical Information and Modeling*, *58*(7), 1441–1458. https://doi.org/10.1021/acs.jcim.8b00228

Schlatterer, S. D., Tremblay, M. A., Acker, C. M., & Davies, P. (2011). Neuronal c-Abl overexpression leads to neuronal loss and neuroinflammation in the mouse forebrain. *Journal of Alzheimer's Disease*, *25*(1), 119–133. https://doi.org/10.3233/JAD-2011-102025

Scotter, E. L., Chen, H. J., & Shaw, C. E. (2015). TDP-43 Proteinopathy and ALS: Insights into Disease Mechanisms and Therapeutic Targets. *Neurotherapeutics*, *12*(2), 352–363. https://doi.org/10.1007/s13311-015-0338-x

Segler, M. H. S., Preuss, M., & Waller, M. P. (2018). Planning chemical syntheses with deep neural networks and symbolic AI. *Nature*, *555*(7698), 604–610. https://doi.org/10.1038/nature25978

Sellier, C., Campanari, M., Corbier, C., Gaucherot, A., Kolb-Cheynel, I., Oulad-Abdelghani, M., Ruffenach, F., Page, A., Ciura, S., Kabashi, E., & Charlet-Berguerand, N. (2016). Loss of C9ORF72 impairs autophagy and synergizes with polyQ Ataxin-2 to induce motor neuron dysfunction and cell death. *The EMBO Journal*, *35*(12), 1276–1297.

Sellwood, M., Ahmed, M., Segler, M., & Brown, N. (2018). Artificial intelligence in drug discovery. *Future Medicinal Chemistry*, *10*(17), 2025–2028.

Serio, A., Bilican, B., Barmada, S. J., Ando, D. M., Zhao, C., Siller, R., Burr, K., Haghi, G., Story, D., Nishimura, A. L., Carrasco, M. A., Phatnani, H. P., Shum, C., Wilmut, I., Maniatis, T., Shaw, C. E., Finkbeiner, S., & Chandran, S. (2013). Astrocyte pathology and the absence of non-cell autonomy in an induced pluripotent stem cell model of TDP-43 proteinopathy. *Proceedings of the National Academy of Sciences*, *110*(12), 4697–4702. https://doi.org/10.1073/pnas.1300398110

Shaker, M. E., Ghani, A., Shiha, G. E., Ibrahim, T. M., & Mehal, W. Z. (2013). Nilotinib induces apoptosis and autophagic cell death of activated hepatic stellate cells via inhibition of histone deacetylases. *Biochimica et Biophysica Acta - Molecular Cell Research*, *1833*(8), 1992–2003. https://doi.org/10.1016/j.bbamcr.2013.02.033

Shaw, G., Morse, S., Ararat, M., & Graham, F. L. (2002). Preferential transformation of human neuronal cells by human adenoviruses and the origin of HEK 293 cells. *The FASEB Journal : Official Publication of the Federation of American Societies for Experimental Biology*, *16*(8), 869–871. https://doi.org/10.1096/fj.01-0995fje

Sheng, Y., Chattopadhyay, M., Whitelegge, J., & Valentine, J. S. (2012). SOD1 aggregation and ALS: role of metallation states and disulfide status. *Current Topics in Medicinal Chemistry*, *12*(22), 2560–2572. https://doi.org/http://dx.doi.org.ezproxy.lib.monash.edu.au/10.2174/1568026611212220010

Shimonaka, S., Nonaka, T., Suzuki, G., Hisanaga, S. I., & Hasegawa, M. (2016). Templated aggregation

of TAR DNA-binding protein of 43 kDa (TDP-43) by seeding with TDP-43 peptide fibrils. *Journal of Biological Chemistry*, *291*(17), 8896–8907. https://doi.org/10.1074/jbc.M115.713552

Simpson, E., Henry, Y., Henkel, J., Smith, R., & Appel, S. (2004). Increased lipid peroxidation in sera of ALS patients: A potential biomarker of disease burden. *Neurology*, *62*(10), 1758–1765.

Simuni, T., Fiske, B., Merchant, K., Coffey, C. S., Klingner, E., Caspell-Garcia, C., Lafontant, D.-E., Matthews, H., Wyse, R. K., Brundin, P., Simon, D. K., Schwarzschild, M., Weiner, D., Adams, J., Venuto, C., Dawson, T. M., Baker, L., Kostrzebski, M., Ward, T., … Collaborators, P. S. G. N.-P. I. and. (2020). Efficacy of Nilotinib in Patients With Moderately Advanced Parkinson Disease: A Randomized Clinical Trial. *JAMA Neurology*. https://doi.org/10.1001/jamaneurol.2020.4725

Sirota, M., Dudley, J. T., Kim, J., Chiang, A. P., Morgan, A. A., Sweet-Cordero, A., Sage, J., & Butte, A. J. (2011). Discovery and preclinical validation of drug indications using compendia of public gene expression data. *Science Translational Medicine*, *3*(96), 96ra77. https://doi.org/10.1126/scitranslmed.3001318

Smith, B. N., Ticozzi, N., Fallini, C., Gkazi, A. S., Topp, S., Kenna, K. P., Scotter, E. L., Kost, J., Keagle, P., Miller, J. W., Calini, D., Vance, C., Danielson, E. W., Troakes, C., Tiloca, C., Al-Sarraj, S., Lewis, E. A., King, A., Colombrita, C., … Bertolin, C. (2014). Exome-wide rare variant analysis identifies TUBA4A mutations associated with familial ALS. *Neuron*. https://doi.org/10.1016/j.neuron.2014.09.027

Smith, E., Shaw, P., & De Vos, K. (2019). The role of mitochondria in amyotrophic lateral sclerosis. *Neuroscience Letters*, *710*(1), 132933.

Smith, RG, Henry, Y., Mattson, M., & Appel, S. (1998). Presence of 4-hydroxynonenal in cerebrospinal fluid of patients with sporadic amyotrophic lateral sclerosis. *Annals of Neurology*, *44*(4), 696–699.

Smith, Richard, Myers, K., Ravits, J., & Bowser, R. (2015). Amyotrophic lateral sclerosis: Is the spinal fluid pathway involved in seeding and spread? *Medical Hypotheses*, *85*(5), 576–583. https://doi.org/10.1016/j.mehy.2015.07.014

Song, G. J., Rahman, M. H., Jha, M. K., Gupta, D. P., Park, S. H., Kim, J. H., Lee, S. H., Lee, I. K., Sim, T., Bae, Y. C., Lee, W. H., & Suk, K. (2019). A BCR-ABL inhibitor GNF-2 attenuates inflammatory activation of glia and chronic pain. *Frontiers in Pharmacology*, *10*(MAY), 1–13. https://doi.org/10.3389/fphar.2019.00543

Sonobe, Y., Ghadge, G., Masaki, K., Sendoel, A., Fuchs, E., & Roos, R. P. (2018). Translation of dipeptide repeat proteins from the C9ORF72 expanded repeat is associated with cellular stress. *Neurobiology of Disease*, *116*, 155–165. https://doi.org/10.1016/j.nbd.2018.05.009

Sreedharan, J., Blair, I. P., Tripathi, V. B., Hu, X., Vance, C., Rogelj, B., Ackerley, S., Durnall, J. C., Williams, K. L., Buratti, E., Baralle, F., De Belleroche, J., Mitchell, J. D., Leigh, P. N., Al-Chalabi, A., Miller, C. C., Nicholson, G., & Shaw, C. E. (2008). TDP-43 mutations in familial and sporadic amyotrophic lateral sclerosis. *Science*. https://doi.org/10.1126/science.1154584

Steyn, F. J., Ioannides, Z. A., Van Eijk, R. P. A., Heggie, S., Thorpe, K. A., Ceslis, A., Heshmat, S., Henders, A. K., Wray, N. R., Van Den Berg, L. H., Henderson, R. D., McCombe, P. A., & Ngo, S. T. (2018). Hypermetabolism in ALS is associated with greater functional decline and shorter survival. *Journal of Neurology, Neurosurgery and Psychiatry*, *89*(10), 1016–1023. https://doi.org/10.1136/jnnp-2017-317887

Stopford, M. J., Allen, S. P., & Ferraiuolo, L. (2019). A High-throughput and Pathophysiologically Relevant Astrocyte-motor Neuron Co-culture Assay for Amyotrophic Lateral Sclerosis Therapeutic Discovery. *Bio-Protocol*, *9*(17). https://doi.org/10.21769/BioProtoc.3353

Sweeney, P., Park, H., Baumann, M., Dunlop, J., Frydman, J., Kopito, R., McCampbell, A., Leblanc, G., Venkateswaran, A., Nurmi, A., & Hodgson, R. (2017). Protein misfolding in neurodegenerative diseases: implications and strategies. *Translational Neurodegeneration*, *6*, 6. https://doi.org/10.1186/s40035-017-0077-5

Swinnen, B., & Robberecht, W. (2014). The phenotypic variability of amyotrophic lateral sclerosis. *Nature Reviews Neurology*, *10*(11), 661–670. https://doi.org/10.1038/nrneurol.2014.184

Tak, Y. J., Park, J. H., Rhim, H., & Kang, S. (2020). ALS-related mutant SOD1 aggregates interfere with mitophagy by sequestering the autophagy receptor optineurin. *International Journal of Molecular Sciences*, *21*(20), 1–17. https://doi.org/10.3390/ijms21207525

Takahashi, K., Tanabe, K., Ohnuki, M., Narita, M., Ichisaka, T., Tomoda, K., & Yamanaka, S. (2007). Induction of pluripotent stem cells from adult human fibroblasts by defined factors. *Cell*, *131*(5), 861–872. https://doi.org/10.1016/j.cell.2007.11.019

Takahashi, Y., Fukuda, Y., Yoshimura, J., Toyoda, A., Kurppa, K., Moritoyo, H., Belzil, V. V., Dion, P. A., Higasa, K., Doi, K., Ishiura, H., Mitsui, J., Date, H., Ahsan, B., Matsukawa, T., Ichikawa, Y., Moritoyo, T., Ikoma, M., Hashimoto, T., … Tsuji, S. (2013). Erbb4 mutations that disrupt the

neuregulin-erbb4 pathway cause amyotrophic lateral sclerosis type 19. *American Journal of Human Genetics*. https://doi.org/10.1016/j.ajhg.2013.09.008

Takenaka, T., Katayama, M., Sugiyama, A., Hagiwara, M., Fujii, I., Takatani-Nakase, T., Kobayashi, S. S., & Nakase, I. (2017). Gefitinib enhances mitochondrial biological functions in NSCLCs with EGFR mutations at a high cell density. *Anticancer Research*, *37*(9), 4779–4788. https://doi.org/10.21873/anticanres.11884

Takeuchi, K., & Ito, F. (2010). EGF receptor in relation to tumor development: molecular basis of responsiveness of cancer cells to EGFR-targeting tyrosine kinase inhibitors. *The FEBS Journal*, *277*(2), 316–326. https://doi.org/10.1111/j.1742-4658.2009.07450.x

Tanaka, Y., Nonaka, T., Suzuki, G., Kametani, F., & Hasegawa, M. (2016). Gain-of-function profilin 1 mutations linked to familial amyotrophic lateral sclerosis cause seed-dependent intracellular TDP-43 aggregation. *Human Molecular Genetics*, *25*(7), 1420–1433. https://doi.org/10.1093/hmg/ddw024

Taura, D., Noguchi, M., Sone, M., Hosoda, K., Mori, E., Okada, Y., Takahashi, K., Homma, K., Oyamada, N., Inuzuka, M., Sonoyama, T., Ebihara, K., Tamura, N., Itoh, H., Suemori, H., Nakatsuji, N., Okano, H., Yamanaka, S., & Nakao, K. (2009). Adipogenic differentiation of human induced pluripotent stem cells: comparison with that of human embryonic stem cells. *FEBS Letters*, *583*(6), 1029–1033. https://doi.org/10.1016/j.febslet.2009.02.031

Therrien, M., Rouleau, G., Dion, P., & Parker, J. (2013). Deletion of C9ORF72 Results in Motor Neuron Degeneration and Stress Sensitivity in C. elegans. *Plos One*, *8*(12), e83450.

Townsend, M. J., & Arron, J. R. (2016). Reducing the risk of failure: Biomarker-guided trial design. *Nature Reviews Drug Discovery*, *15*(8), 517–518. https://doi.org/10.1038/nrd.2016.124

Toyama, B. H., Savas, J. N., Park, S. K., Harris, M. S., Ingolia, T., Yates, J. R., & Hetzer, M. W. (2014). Identification of long-lived proteins reveals exceptional stability of essential cellular structures. *Cell*, *154*(5), 971–982. https://doi.org/10.1016/j.cell.2013.07.037.Identification

Tran, H., Almeida, S., Moore, J., Gendron, T., Chalasani, U., Lu, Y., Du, X., Nickerson, J., Petrucelli, L., Weng, Z., & Gao, F. (2015). Differential Toxicity of Nuclear RNA Foci versus Dipeptide Repeat Proteins in a Drosophila Model of C9ORF72 FTD/ALS. *Neuron*, *87*(6), 1207–1214.

Trojani, A., Pungolino, E., Molin, A. D., Lodola, M., Rossi, G., D'Adda, M., Perego, A., Elena, C., Turrini,

M., Borin, L., Bucelli, C., Malato, S., Carraro, M. C., Spina, F., Latargia, M. L., Artale, S., Spedini, P., Anghilieri, M., Camillo, B. Di, … Cairoli, R. (2019). Nilotinib interferes with cell cycle, ABC transporters and JAK-STAT signaling pathway in CD34+/lin- cells of patients with chronic phase chronic myeloid leukemia after 12 months of treatment. *PLoS ONE*, *14*(7), 1–15. https://doi.org/10.1371/journal.pone.0218444

Tsang, C. K., Liu, Y., Thomas, J., Zhang, Y., & Zheng, X. F. S. (2014). Superoxide dismutase 1 acts as a nuclear transcription factor to regulate oxidative stress resistance. *Nature Communications*, *5*, 3446. https://doi.org/10.1038/ncomms4446

Tyzack, G. E., Hall, C. E., Sibley, C. R., Cymes, T., Forostyak, S., Carlino, G., Meyer, I. F., Schiavo, G., Zhang, S. C., Gibbons, G. M., Newcombe, J., Patani, R., & Lakatos, A. (2017). A neuroprotective astrocyte state is induced by neuronal signal EphB1 but fails in ALS models. *Nature Communications*, *8*(1). https://doi.org/10.1038/s41467-017-01283-z

Uchino, A., Takao, M., Hatsuta, H., Sumikura, H., Nakano, Y., Nogami, A., Saito, Y., Arai, T., Nishiyama, K., & Murayama, S. (2015). Incidence and extent of TDP-43 accumulation in aging human brain. *Acta Neuropathologica Communications*, *3*(1), 35. https://doi.org/10.1186/s40478-015-0215-1

Urushitani, M., Kurisu, J., Tsukita, K., & Takahashi, R. (2002). Proteasomal inhibition by misfolded mutant superoxide dismutase 1 induces selective motor neuron death in familial amyotrophic lateral sclerosis. *Journal of Neurochemistry*, *83*(5), 1030–1042.

Ustyantseva, E. I., Medvedev, S. P., Vetchinova, A. S., Illarioshkin, S. N., Leonov, S. V., & Zakian, S. M. (2020). Generation of an induced pluripotent stem cell line, ICGi014-A, by reprogramming peripheral blood mononuclear cells from a patient with homozygous D90A mutation in SOD1 causing Amyotrophic lateral sclerosis. *Stem Cell Research*, *42*(September 2019), 101675. https://doi.org/10.1016/j.scr.2019.101675

Van Damme, P., Robberecht, W., & Van Den Bosch, L. (2017). Modelling amyotrophic lateral sclerosis: progress and possibilities. *Disease Models & Mechanisms*, *10*(5), 537–549.

van de Waterbeemd, H., & Gifford, E. (2003). ADMET in silico modelling: towards prediction paradise? *Nature Reviews. Drug Discovery*, *2*(3), 192–204. https://doi.org/10.1038/nrd1032

Van Den Bosch, L., Tilkin, P., Lemmens, G., & Robberecht, W. (2002). Minocycline delays disease onset and mortality in a transgenic model of ALS. *NeuroReport*, *13*(8), 1067–1070.

https://doi.org/10.1097/00001756-200206120-00018

Van Mossevelde, S., van der Zee, J., Cruts, M., & Van Broeckhoven, C. (2017). Relationship between C9orf72 repeat size and clinical phenotype. *Current Opinion in Genetics and Development*, *44*(1), 117–124. https://doi.org/10.1016/j.gde.2017.02.008

van Rheenen, W., Shatunov, A., Dekker, A. M., McLaughlin, R. L., Diekstra, F. P., Pulit, S. L., van der Spek, R. A. A., Võsa, U., de Jong, S., Robinson, M. R., Yang, J., Fogh, I., van Doormaal, P. T., Tazelaar, G. H. P., Koppers, M., Blokhuis, A. M., Sproviero, W., Jones, A. R., Kenna, K. P., … Veldink, J. H. (2016). Genome-wide association analyses identify new risk variants and the genetic architecture of amyotrophic lateral sclerosis. *Nature Genetics*, *48*(9), 1043–1048. https://doi.org/10.1038/ng.3622

Vance, C., Rogelj, B., Hortobágyi, T., De Vos, K. J., Nishimura, A. L., Sreedharan, J., Hu, X., Smith, B., Ruddy, D., Wright, P., Ganesalingam, J., Williams, K. L., Tripathi, V., Al-Saraj, S., Al-Chalabi, A., Leigh, P. N., Blair, I. P., Nicholson, G., De Belleroche, J., … Shaw, C. E. (2009). Mutations in FUS, an RNA processing protein, cause familial amyotrophic lateral sclerosis type 6. *Science*. https://doi.org/10.1126/science.1165942

Vande Velde, C., McDonald, K., Boukhedimi, Y., McAlonis-Downes, M., Lobsiger, C., Bel Hadj, S., Zandona, A., Julien, J., Shah, S., & Cleveland, D. (2011). Misfolded SOD1 Associated with Motor Neuron Mitochondria Alters Mitochondrial Shape and Distribution Prior to Clinical Onset. *PLoS ONE*, *6*(7), e22031.

Varcianna, A., Myszczynska, M. A., Castelli, L. M., O'Neill, B., Kim, Y., Talbot, J., Nyberg, S., Nyamali, I., Heath, P. R., Stopford, M. J., Hautbergue, G. M., & Ferraiuolo, L. (2019). Micro-RNAs secreted through astrocyte-derived extracellular vesicles cause neuronal network degeneration in C9orf72 ALS. *EBioMedicine*, *40*. https://doi.org/10.1016/j.ebiom.2018.11.067

Vargas, L. M., Leal, N., Estrada, L. D., González, A., Serrano, F., Araya, K., Gysling, K., Inestrosa, N. C., Pasquale, E. B., & Alvarez, A. R. (2014). EphA4 activation of c-Abl mediates synaptic loss and LTP blockade caused by amyloid-β oligomers. *PLoS ONE*, *9*(3). https://doi.org/10.1371/journal.pone.0092309

Ventura, A., Kirsch, D. G., McLaughlin, M. E., Tuveson, D. A., Grimm, J., Lintault, L., Newman, J., Reczek, E. E., Weissleder, R., & Jacks, T. (2007). Restoration of p53 function leads to tumour regression in vivo. *Nature*, *445*(7128), 661–665. https://doi.org/10.1038/nature05541

Verkhratsky, A., & Butt, A. (2013). Numbers: how many glial cells are in the brain? In *Glial Physiology and Pathophysiology* (1st ed., pp. 93–95). Wiley-Blackwell.

Vijayvergiya, C., Beal, M., Buck, J., & Manfredi, G. (2005). Mutant Superoxide Dismutase 1 Forms Aggregates in the Brain Mitochondrial Matrix of Amyotrophic Lateral Sclerosis Mice. *Journal of Neuroscience*, *25*(10), 2463–2470.

Vléduts, G. É. (1963). Concerning one system of classification and codification of organic reactions. *Information Storage and Retrieval*, *1*(2–3), 117–146. https://doi.org/10.1016/0020-0271(63)90013-5

von Bartheld, C., Bahne, J., & Herculano-Houzel, S. (2017). The Search for True Numbers of Neurons and Glial Cells in the Human Brain. *Physiology & Behavior*, *176*(12), 139–148. https://doi.org/10.1002/cne.24040.The

Walsh, M. J., Cooper-Knock, J., Dodd, J. E., Stopford, M. J., Mihaylov, S. R., Kirby, J., Shaw, P. J., & Hautbergue, G. M. (2015). Invited Review: Decoding the pathophysiological mechanisms that underlie RNA dysregulation in neurodegenerative disorders: A review of the current state of the art. *Neuropathology and Applied Neurobiology*, *41*(2), 109–134. https://doi.org/10.1111/nan.12187

Wang, S. J., Wang, K. Y., & Wang, W. C. (2004). Mechanisms underlying the riluzole inhibition of glutamate release from rat cerebral cortex nerve terminals (synaptosomes). *Neuroscience*, *125*(1), 191–201. https://doi.org/10.1016/j.neuroscience.2004.01.019

Wang, W., Wang, L., Lu, J., Siedlak, S. L., Fujioka, H., Liang, J., Jiang, S., Ma, X., Jiang, Z., da Rocha, E. L., Sheng, M., Choi, H., Lerou, P. H., Li, H., & Wang, X. (2016). The inhibition of TDP-43 mitochondrial localization blocks its neuronal toxicity. *Nature Medicine*, *22*(8), 869–878. https://doi.org/10.1038/nm.4130

Watanabe, S., Oiwa, K., Murata, Y., Komine, O., Sobue, A., Endo, F., Takahashi, E., & Yamanaka, K. (2020). ALS-linked TDP-43M337V knock-in mice exhibit splicing deregulation without neurodegeneration. *Molecular Brain*, *13*(1), 13–16. https://doi.org/10.1186/s13041-020-0550-4

Webster, C. P., Smith, E. F., Bauer, C. S., Moller, A., Hautbergue, G. M., Ferraiuolo, L., Myszczynska, M. A., Higginbottom, A., Walsh, M. J., Whitworth, A. J., Kaspar, B. K., Meyer, K., Shaw, P. J., Grierson, A. J., & De Vos, K. J. (2016). The C9orf72 protein interacts with Rab1a and the ULK1

complex to regulate initiation of autophagy. *EMBO Journal*, *35*(15). https://doi.org/10.15252/embj.201694401

Wei, J., Freytag, M., Schober, Y., Nockher, W. A., Mautner, V. F., Friedrich, R. E., Manley, P. W., Kluwe, L., & Kurtz, A. (2014). Nilotinib is more potent than imatinib for treating plexiform neurofibroma in vitroand in vivo. *PLoS ONE*, *9*(10), 5–10. https://doi.org/10.1371/journal.pone.0107760

White, M. A., Lin, Z., Kim, E., Henstridge, C. M., Pena Altamira, E., Hunt, C. K., Burchill, E., Callaghan, I., Loreto, A., Brown-Wright, H., Mead, R., Simmons, C., Cash, D., Coleman, M. P., & Sreedharan, J. (2019). Sarm1 deletion suppresses TDP-43-linked motor neuron degeneration and cortical spine loss. *Acta Neuropathologica Communications*, *7*(1), 1–16. https://doi.org/10.1186/s40478-019-0800-9

Wiedemann, F., Manfredi, G., Mawrin, C., Beal, M., & Schon, E. (2002). Mitochondrial DNA and respiratory chain function in spinal cords of ALS patients. *Journal of Neurochemistry*, *80*(4), 616–625.

Williams, K., Bilsland, E., Sparkes, A., Aubrey, W., Young, M., Soldatova, L. N., De Grave, K., Ramon, J., de Clare, M., Sirawaraporn, W., Oliver, S. G., & King, R. D. (2015). Cheaper faster drug development validated by the repositioning of drugs against neglected tropical diseases. *Journal of The Royal Society Interface*, *12*(104), 20141289–20141289. https://doi.org/10.1098/rsif.2014.1289

Williamson, M. G., Finelli, M. J., Sleigh, J. N., Reddington, A., Gordon, D., Talbot, K., Davies, K. E., & Oliver, P. L. (2019a). Neuronal over-expression of Oxr1 is protective against ALS-associated mutant TDP-43 mislocalisation in motor neurons and neuromuscular defects in vivo. *Human Molecular Genetics*, *28*(21), 3584–3599. https://doi.org/10.1093/hmg/ddz190

Williamson, M. G., Finelli, M. J., Sleigh, J. N., Reddington, A., Gordon, D., Talbot, K., Davies, K. E., & Oliver, P. L. (2019b). Neuronal over-expression of Oxr1 is protective against ALS-associated mutant TDP-43 mislocalisation in motor neurons and neuromuscular defects in vivo. *Human Molecular Genetics*, *28*(21), 3584–3599. https://doi.org/10.1093/hmg/ddz190

Wilson, A. C., Dugger, B. N., Dickson, D. W., & Wang, D.-S. (2011). TDP-43 in aging and Alzheimer's disease - A review. *International Journal of Clinical and Experimental Pathology*, *4*(2), 147–155.

Winograd, T. (1971). *Procedures as a representation for data in a computer program for*

understanding natural language. Massachusetts Institute of Technology.

Winton, M. J., Igaz, L. M., Wong, M. M., Kwong, L. K., Trojanowski, J. Q., & Lee, V. M. Y. (2008). Disturbance of nuclear and cytoplasmic TAR DNA-binding protein (TDP-43) induces disease-like redistribution, sequestration, and aggregate formation. *Journal of Biological Chemistry*, *283*(19), 13302–13309. https://doi.org/10.1074/jbc.M800342200

Wobst, H. J., Delsing, L., Brandon, N. J., & Moss, S. J. (2017). Truncation of the TAR DNA-binding protein 43 is not a prerequisite for cytoplasmic relocalization, and is suppressed by caspase inhibition and by introduction of the A90V sequence variant. *PLoS ONE*, *12*(5), 1–20. https://doi.org/10.1371/journal.pone.0177181

Wu, C. H., Fallini, C., Ticozzi, N., Keagle, P. J., Sapp, P. C., Piotrowska, K., Lowe, P., Koppers, M., McKenna-Yasek, D., Baron, D. M., Kost, J. E., Gonzalez-Perez, P., Fox, A. D., Adams, J., Taroni, F., Tiloca, C., Leclerc, A. L., Chafe, S. C., Mangroo, D., … Landers, J. E. (2012). Mutations in the profilin 1 gene cause familial amyotrophic lateral sclerosis. *Nature*. https://doi.org/10.1038/nature11280

Xie, Z., Xie, Y., Xu, Y., Zhou, H., Xu, W., & Dong, Q. (2014). Bafilomycin A1 inhibits autophagy and induces apoptosis in MG63 osteosarcoma cells. *Molecular Medicine Reports*, *10*(2), 1103–1107. https://doi.org/10.3892/mmr.2014.2281

Xin, S., Zhao, Y., Wang, C., Huang, Y., Zhuang, W., Ma, Y., Huang, M., Xu, X., Wang, X., & Zhang, L. (2020). Polymorphisms of NF-κB pathway genes influence adverse drug reactions of gefitinib in NSCLC patients. *Pharmacogenomics Journal*, *20*(2), 285–293. https://doi.org/10.1038/s41397-019-0115-z

Yamamoto, A., Tagawa, Y., Yoshimori, T., Moriyama, Y., Masaki, R., & Tashiro, Y. (1998). Bafilomycin A1 prevents maturation of autophagic vacuoles by inhibiting fusion between autophagosomes and lysosomes in rat hepatoma cell line, H-4-II-E cells. *Cell Structure and Function*, *23*(1), 33–42. https://doi.org/10.1247/csf.23.33

Yamanaka, K., Miller, T. M., McAlonis-Downes, M., Chun, S. J., & Cleveland, D. W. (2006). Progressive spinal axonal degeneration and slowness in ALS2-deficient mice. *Annals of Neurology*, *60*(1), 95–104. https://doi.org/10.1002/ana.20888

Yang, L., Ying, S., Hu, S., Zhao, X., Li, M., Chen, M., Zhu, Y., Song, P., Zhu, L., Jiang, T., An, H., Yousafzai, N. A., Xu, W., Zhang, Z., Wang, X., Feng, L., & Jin, H. (2019). EGFR TKIs impair

lysosome-dependent degradation of SQSTM1 to compromise the effectiveness in lung cancer. *Signal Transduction and Targeted Therapy*, *4*(1). https://doi.org/10.1038/s41392-019-0059-4

Ye, C., Ho, D. J., Neri, M., Yang, C., Kulkarni, T., Randhawa, R., Henault, M., Mostacci, N., Farmer, P., Renner, S., Ihry, R., Mansur, L., Keller, C. G., McAllister, G., Hild, M., Jenkins, J., & Kaykas, A. (2018). DRUG-seq for miniaturized high-throughput transcriptome profiling in drug discovery. *Nature Communications*, *9*(1), 1–9. https://doi.org/10.1038/s41467-018-06500-x

Youle, R. J., & Van Der Bliek, A. M. (2012). Mitochondrial Fission, Fusion, and Stress. *Science*, *337*(6098), 1062–1065. https://doi.org/10.1126/science.1219855.Mitochondrial

Young, P. E., Jew, S. K., Buckland, M. E., Pamphlett, R., & Suter, C. M. (2017). Epigenetic differences between monozygotic twins discordant for amyotrophic lateral sclerosis (ALS) provide clues to disease pathogenesis. *PLoS ONE*, *12*(8), 1–19. https://doi.org/10.1371/journal.pone.0182638

Yu, H. C., Lin, C. S., Tai, W. T., Liu, C. Y., Shiau, C. W., & Chen, K. F. (2013). Nilotinib induces autophagy in hepatocellular carcinoma through AMPK activation. *Journal of Biological Chemistry*, *288*(25), 18249–18259. https://doi.org/10.1074/jbc.M112.446385

Yuan, N., Song, L., Zhang, S., Lin, W., Cao, Y., Xu, F., Fang, Y., Wang, Z., Zhang, H., Li, X., Wang, Z., Cai, J., Wang, J., Zhang, Y., Mao, X., Zhao, W., Hu, S., Chen, S., & Wang, J. (2015). Bafilomycin A1 targets both autophagy and apoptosis pathways in pediatric B-cell acute lymphoblastic leukemia. *Haematologica*, *100*(3), 345–356. https://doi.org/10.3324/haematol.2014.113324

Yuan, Y., Li, X. F., Chen, J. Q., Dong, C. X., Weng, S. S., & Huang, J. J. (2014). Critical appraisal of the role of gefitinib in the management of locally advanced or metastatic non-small cell lung cancer. *OncoTargets and Therapy*, *7*, 841–852. https://doi.org/10.2147/OTT.S34124

Zhang, D., Iyer, L., He, F., & Aravind, L. (2012). Discovery of Novel DENN Proteins: Implications for the Evolution of Eukaryotic Intracellular Membrane Structures and Human Disease. *Frontiers in Genetics*, *3*(1), 283.

Zhang, S. C., Wernig, M., Duncan, I. D., Brüstle, O., & Thomson, J. A. (2001). In vitro differentiation of transplantable neural precursors from human embryonic stem cells. *Nature Biotechnology*, *19*(12), 1129–1133. https://doi.org/10.1038/nbt1201-1129

Zhang, Y. J., Xu, Y. F., Cook, C., Gendron, T. F., Roettges, P., Link, C. D., Lin, W. L., Tong, J., Castanedes-Casey, M., Ash, P., Gass, J., Rangachari, V., Buratti, E., Baralle, F., Golde, T. E.,

Dickson, D. W., & Petrucelli, L. (2009). Aberrant cleavage of TDP-43 enhances aggregation and cellular toxicity. *Proceedings of the National Academy of Sciences of the United States of America*, *106*(18), 7607–7612. https://doi.org/10.1073/pnas.0900688106

Zhao, J., Cooper, L. T., Boyd, A. W., & Bartlett, P. F. (2018). Decreased signalling of EphA4 improves functional performance and motor neuron survival in the SOD1G93A ALS mouse model. *Scientific Reports*, *8*(1), 1–10. https://doi.org/10.1038/s41598-018-29845-1

Zhao, K., & So, H. C. (2018). Drug repositioning for schizophrenia and depression/anxiety disorders: A machine learning approach leveraging expression data. *IEEE Journal of Biomedical and Health Informatics*, *PP*(c), 1. https://doi.org/10.1109/JBHI.2018.2856535

Zhou, L., Zhang, Q., Zhang, P., Sun, L., Peng, C., Yuan, Z., & Cheng, J. (2017). C-Abl-mediated Drp1 phosphorylation promotes oxidative stress-induced mitochondrial fragmentation and neuronal cell death. *Cell Death and Disease*, *8*(10), 1–11. https://doi.org/10.1038/cddis.2017.524

Zhu, Y., He, W., Gao, X., Li, B., Mei, C., Xu, R., & Chen, H. (2015). Resveratrol overcomes gefitinib resistance by increasing the intracellular gefitinib concentration and triggering apoptosis, autophagy and senescence in PC9/G NSCLC cells. *Scientific Reports*, *5*(December), 1–12. https://doi.org/10.1038/srep17730

7 Outcomes of the PhD

7.1 Awards

Neuronus IBRO Neuroscience Forum 2020, December 2020 – award for the best biological oral presentation

7.2 Communications at national and international scientific meetings

Platform presentation Neuronus IBRO Neuroscience Forum 2020 – "*Uncovering new drug therapies and targets for ALS using machine learning approaches*", December 2020

Invited workshop Sheffield NeuroSoc National Conference – "*Use of Artificial Intelligence in Neurology and Neuroscience Research*", March 2020

Platform presentation European Network to Cure ALS (ENCALS) 2019 (Tours, France) – "*Using AI to uncover novel drug therapies and targets for ALS*", May 2019

Platform presentation Medical School Research Meeting (University of Sheffield, 2018) – "*Using AI to uncover novel drug therapies and targets for ALS*", June 2018

Poster Presentation Sheffield Neuroscience Conference (2017) – "*A novel human* in vitro *model of motor neuron disease uncovers individual patient response to antioxidant drugs*", July 2017

Poster presentation Medical School Research Meeting (University of Sheffield, 2017) – "*A novel human* in vitro *model of motor neuron disease uncovers individual patient response to antioxidant drugs*", June 2017

Poster presentation European Network to Cure ALS (ENCALS) 2017 (Ljubljana, Slovenia) – "*A novel human* in vitro *model of motor neuron disease uncovers individual patient response to antioxidant drugs*", May 2017

7.3 Publications

Gatto N, Dos Santos Souza C, Shaw AC, Bell SM, **Myszczynska MA**, Powers S, Meyer K, Castelli LM, Karyka E, Mortiboys H, Azzouz M, Hautbergue GM, Márkus NM, Shaw PJ, Ferraiuolo L. (2021). Directly converted astrocytes retain the ageing features of the donor fibroblasts and elucidate the astrocytic contribution to human CNS health and disease. *Ageing Cell.* 20**(1)**: e13281 doi: https://doi.org/10.1111/acel.13281

Myszczynska MA, Ojamies PN, Lacoste AMB, Neil D, Saffari A, Mead R, Hautbergue GM, Holbrook JD, Ferraiuolo. (2020). Applications of machine learning to diagnosis and treatment of neurodegenerative diseases. *Nature Reviews Neurology*. 16**(8)**: 440-456. doi: https://doi.org/10.1038/s41582-020-0377-8

Schwartzentruber A, Boschian C, Lopes F, **Myszczynska M**, New E, Beyrath J, Smeitnik J, Ferraiuolo L, Mortiboys HJ. (2020). Oxidative switch drives mitophagy defects in dopaminergic parkin mutant patient neurons. *Scientific Reports*. 10**(1)**: 15485. doi: 10.1038/s41598-020-72345-4

Allen SP, Hall B, Woof R, Francis L, Gatto N, Shaw AC, **Myszczynska MA**, Hemingway J, Coldicott I, Wilcock A, Job L, Hughes RM, Boschian C, Bayatti N, Heath PR, Bandmann O, Mortiboys H, Ferraiuolo L, Shaw PJ. (2019). C9orf72 expansion within astrocytes reduces metabolic flexibility in amyotrophic lateral sclerosis. *Brain*. 142**(12)**. 3771-3790. https://doi.org/10.1093/brain/awz302

Allen SP, Hall B, Castelli LM, Francis L, Woof R, Siskos AP, Kouloura E, Gray E, Thompson AG, Talbot K, Higginbottom A, **Myszczynska M**, Allen CF, Stopford MJ, Hemingway J, Bauer CS, Webster CP, De Vos KJ, Turner MR, Keun HC, Hautbergue GM, Ferraiuolo L, Shaw PJ. (2019). Astrocyte adenosine deaminase loss increases motor neuron toxicity in amyotrophic lateral sclerosis. *Brain*. 142**(3)**. 586-605. https://doi.org/10.1093/brain/awy353

Varcianna A*, **Myszczynska MA***, Castelli LM, O'Neill B, Kim Y, Talbot J, Nyberg S, Nyamali I, Heath PR, Stopford MJ, Hautbergue GM, Ferraiuolo L. (2019). Micro-RNAs secreted through astrocyte-derived extracellular vesicles cause neuronal network degeneration in

C9orf72 ALS. *EBioMedicine.* 40. 626-635. https://doi.org/10.1016/j.ebiom.2018.11.067 ***Joint first authors**

Allen SP, Hall B, Castelli L, Francis L, Woof R, Higginbottom A, **Myszczynska M**, Allen CF, Stopford MJ, Webster CP, De Vos K, Hautbergue GM, Ferraiuolo L, Shaw PJ. (2018). Inosine reverses motor neuron toxicity observed in amyotrophic lateral sclerosis patient astrocytes with an adenosine deaminase deficiency. *Biochimica et Biophysica Acta (BBA) – Bioenergetics*. 1859. e23. doi: 10.1016/j.bbabio.2018.09.071

Iannitti T, Scarrott JM, Likhite S, Coldicott IRP, Lewis KE, Heath PR, Higginbottom A, **Myszczynska MA**, Milo M, Hautbergue GM, Meyer K, Kaspar BK, Ferraiuolo L, Shaw PJ, Azzouz M. (2018). Translating SOD1 Gene Silencing toward the Clinic: A Highly Efficacious, Off-Target-free, and Biomarker-Supported Strategy for fALS. *Molecular therapy. Nucleic acids.* 12. 75-88. doi: 10.1016/j.omtn.2018.04.015.